NUCLEAR REACTOR LABORATORY

AN INTERDEPARTMENTAL CENTER OF
MASSACHUSETTS INSTITUTE OF TECHNOLOGY

John A. Bernard
Director of Reactor Operations

Mail Stop: NW12-208A
138 Albany Street
Cambridge, MA 02139

Phone: 617 253-4202
Fax: 617 253-7300
Email: bernardj@mit.edu

August 15, 2008

U.S. Nuclear Regulatory Commission
Attn: Document Control Room
Washington, DC 20555

Re: Massachusetts Institute of Technology – Request for Additional Information License Renewal Request (TAC No. MA6084); License No. R-37; Docket No. 50-20

Dear Sir or Madam:

The Massachusetts Institute of Technology hereby replies to the above request which consisted of 39 questions. Responses to all of those, (except #13.1, #13.2, and #14.1) are hereby provided. The response for #13.1 and #14.1 will be provided shortly. We do not as yet have an estimated time of submission for #13.2.

Please contact the undersigned with any questions.

Sincerely,

John Bernard, Ph.D., PE, CHP
Director of Reactor Operations

I declare under the penalty of perjury that the foregoing is true and correct.

Executed on 8-15-08 ____________________
Date Signature

cc:

w/enclosures	Stephen Pierce, Project Manager Research and Test Reactors Branch A Division of Policy and Rulemaking Office of Nuclear Reactor Regulation
w/o enclosures	Senior Project Manager Research and Test Reactors Branch A Division of Policy and Rulemaking Office of Nuclear Reactor Regulation
w/o enclosure	Senior Reactor Inspector Research and Test Reactors Branch B Division of Policy and Rulemaking Office of Nuclear Reactor Regulation
w/o enclosure	Document Control Desk

2.1 The new runway, which is designated as 14-32, opened for regular use on November 23, 2006. As predicted, its use reduced delays for incoming flights and therefore decreased the likelihood of an incident involving aircraft that are awaiting clearance to land. Hence, there is no "additional risk" to the MITR from this new runway.

4.1 Please refer to Figure 4-12, "Core Cross-Section" which shows the hexagonal and radial spider that is part of the core structural support. (Note: The word "strut" is used in the figure instead of "spider.") The core was designed so that fixed absorbers could be attached to the upper twelve inches of both the hexagonal and radial spider. The original idea, as put forth in the early 1970s when the MITR-II was being designed, was to poison the upper half of the core thereby generating most of the power in the lower half and thus maximizing flux to the beam ports. The initial core for the MITR-II, which was operated in 1975, did contain twelve inch cadmium inserts in both the hexagonal and radial spider. The idea did work as confirmed by experimental measurement. However, the research mission of the MITR changed shortly thereafter from one involving beam port experiments to one involving in-core loops. This in turn meant that a more uniform axial power (and hence flux) distribution was preferred. As a result, all of the hexagonal inserts were removed. The ones in the radial spider were reduced in length to four inches. That is, the inserts extend from the top of the core downward by four inches. Also, because the shim blades were changed from cadmium to 1% boron-impregnated stainless steel, so were the inserts at that time.

The principal purpose of the retained four-inch radial fixed absorbers in the original core (all fresh fuel) was to reduce power peaking in the B and C-ring elements by displacing water that would otherwise fill the slot in the spider. The boron-10 was allowed to deplete and is now gone. The inserts are modeled for purposes of core analysis as stainless steel with boron-11. The absence of swelling of the inserts as a result of boron-10 fission was verified through both visual inspections (quarterly) and fuel element movement (5-6 times per year on average) since 1975. None has been observed.

The radial inserts slots are 4-5/8 x 13-1/8 x 0.165 inches with the absorber currently occupying only the upper 4.0 inches. The absorbers are fastened to the spider with capture screws.

4.2 The last paragraph of section 4.2 "Reactor Core" will be modified as follows to include a more detailed description of the flow path within the core tank: "Heat generated by the fission of U-235 is removed from the core by means of the light-water primary cooling system. Coolant enters the reactor through the inlet plenum, flows into the annular region between the core tank and the core shroud, and then moves downward to the bottom of the core tank through the six coolant inlet channels formed by the hexagonal core support housing assembly as shown in Figure 4-2. The coolant is then directed upward through the fuel elements which are held in the core support housing assembly. <u>It was determined during the MITR-II start up testing that a small portion of the primary flow bypasses the fuel elements through the natural convection valves. The coolant flow exiting the core then enters the core tank through a hexagonal flow guide that is about 39 cm from flat to flat and 76 cm high. The flow guide protects the shim blades from flow-induced</u>

vibration. Water then moves at lower velocity upwards within the space contained by the core shroud to the three exit ports which form the outlet plenum. This plenum is located above the level of the inlet plenum. The coolant passes out of the reactor and flows through two parallel pumps and the primary heat exchangers to form a common line back to the reactor, thereby forming a closed loop. A detailed description of the flow system is given in Chapter 5 of this report." (Note: Figure 4 (p. 7) in the paper "Validation of the MULCH-II Code for the Thermal-Hydraulic Safety Analysis of the MIT Research Reactor Conversion to LEU" may be of assistance in visualizing the preceding information. A copy of that paper is included in Appendix F.)

4.3 Prior to assembly of a fuel element, each fuel plate is inspected, radiographically tested for content and loading. These are used to assure the meeting of specifications of fuel loading, fuel and cladding thickness, fin height, bond integrity, void volume, and fuel homogeneity, as well as testing for stray fuel particles. After assembly, the elements are tested for mechanical integrity. Welding integrity and final assembled dimensions are also checked. This testing is done at the manufacturer according to the following specifications:

TRTR-3 Specification for Massachusetts Institute of Technology Fuel Elements.

TRTR-10 Specification for High Enriched U Metal for Reactor Fuel Plates.

TRTR-12 Specification for Reactor Grade High Enriched Uranium Aluminide (UALx) Powder.

TRTR-14 Specification for Aluminum Powder for Fuel Plate Core matrixes for Fuel Elements.

Other Standards (ASTM, ANSI, AWS, and military specifications) also apply, as specified in TRTR-3.

Acceptance testing of fuel after arrival at MIT includes detailed visual inspections, dimensional checks, and radiation and contamination surveys.

4.4 References 4-1 "J.L. Snelgrove and G.L. Hofman, Evaluation of Existing Technology Base for Candidate Fuels for the HWR-NPR, Argonne National Laboratory ANL/NPR-93/002, Feb. 1993." and 4-2 "R.W. Cahn, P. Haasen, and E.J. Kramer, Materials Science and Technology - A Comprehensive Treatment, Published by VCH, Germany." are included in Appendix A. A paper authored by Beeston et al., which summarizes the results of post irradiation examination results of UAlx dispersion fuel irradiated at the ATR up to $2.3 \cdot 10^{21}$ fissions/cc, is also included in Appendix A

4.5 Aluminum (Al-6061) conductivity and heat capacity values (at 50°C) can be found in IAEA-TECDOC-643.

These values are listed on p. 4-7 for information only. They are not used in calculation of the steady-state thermal limits. Uncertainties in their values therefore do not play a role.

4.6 As stated in RAI #25, CITATION is currently the program being used for fuel management. The MCNP calculations referred to in section 4.6.1.2 were only used to generate axial and radial flux profiles in the core for derivation of the safety limits. Validation of the MCNP model can be found in the following references:

E. Redmond, J. Yanch, and O. Harling, "Monte Carlo Simulation of the MIT Research Reactor," *Nuclear Technology*, **106**, pp. 1-14 (1994).

T. Newton, Jr., Z. Xu, E. Pilat, and M. Kazimi, "Modeling the MIT Reactor Neutronics for LEU Conversion Studies," PHYSOR-2004, Chicago, IL, April, 2004.

T. Newton, M. Kazimi, and E. Pilat, "Development of a Low Enrichment Uranium Core for the MIT Reactor," MIT-NFC-TR-83, Center for Advanced Nuclear Energy Systems, Department of Nuclear Science and Engineering Massachusetts Institute of Technology, 2006.

4.7 The studies in question refer to the effect of the position of the shim blades and/or fixed absorbers on the core power distribution. These studies were done via computer modeling with the results confirmed by experimental measurement for selected blade/absorber positions. The core housing (hexagonal and radial spider) contains slots that allow fixed absorbers of up to 12 inches. (Note: The zero position for the fixed absorbers is taken as the top of the core; a 12-inch fixed absorber would extend downwards by a distance of 12 inches from the core top.) The term "raised" as used in these studies refers to a change in length of the absorber in the computer model or to a possible repositioning of the absorbers while shut down. Thus, "raise" would means shortening the absorber while "lower" would mean lengthening it.

4.8 Fuel burnup is tracked using Depletion Code 2, as discussed in reference 4-8. This code calculates the burnup in fissions/cm^3 in each radial, azimuthal, and axial node for each fuel element. The fission density in each node is evaluated prior to each refueling, so that the limit in any fuel element will not be exceeded. Fuel is discharged when the peak node in an element reaches 90-95% of the fission (1.8×10^{21} fissions/ cm^3) limit. Historically, other than the few elements discharged for reasons other than burnup, all discharged elements have had peak fission densities in this range. None has exceeded 95% of the limit.

4.9 Equilibrium Xe worth for the MITR-II at 4.9 MW has been measured at 3.9 β several times throughout its operating history. Xenon reactivity worth is given by:

$$\Delta\rho_{Xe} = -f(\gamma_{Te} + \gamma_{Xe})\, \Phi\, \sigma_{aXe}\, \Sigma_{fu} / (\lambda_{Xe} + \Phi\, \sigma_{aXe})\, \Sigma_{au}\, K_{eff} \quad [1]$$

When comparing identical reactors, this reduces to:

$\Delta\rho_{Xe} = C\, \Phi / (\lambda_{Xe} + \Phi\, \sigma_{aXe})$, where λ_{Xe} is 2.1×10^{-5} sec^{-1}, and σ_{aXe} is approximately 2.72×10^6 barns.

Given that with a power increase from 4.9 MW to 6 MW, the only change will be that Φ will become 1.22 Φ. Taking a ratio between the two equations, the change in $\Delta\rho_{Xe}$ for 6 MW becomes 1.12. Multiplying 3.9 β by 1.12 gives 4.37 β. (Note: The 4.37 β figure should be used on p. 4-40 of the SAR.)

[1] Foster and Wright, *Basic Nuclear Engineering*, 3rd edition. p. 306.

4.10 Data taken in determining the prompt neutron lifetime (via noise analysis, the most reliable method) show results varying from 1.04E-4 s to 1.25E-4s. Thus, there is about a 20% uncertainty in the value, with the 100 μs value being used as the most conservative. The 1.0E-4 figure is the value reported to the U.S. NRC in the startup report for the MITR-II Research Reactor, 19 February 1977. It is also the value used for operation of the MITR for the past three decades.

4.11 Our practice is, and has always been, to include both movable and non-secured experiments in the shutdown margin calculation. Therefore, both section 4.5.3.3 (p. 4-51) and TS 3.1.2 will be changed to reflect this. The language will be "...with all moveable and non-secured experiments in their most reactive state."

4.12 Self-sustained combustion of the graphite that forms part of the MITR's reflector is not possible because the peak operating temperature of the graphite is ~150 °C, allowing a small but continuous annealing process. Additionally, the graphite's neutron exposure is low (flux no more than 8×10^{12} n/cm^2 –s at 5 MW) and mostly thermal (cadmium ratio >110). (Note: This was confirmed experimentally by the MITR staff in 1987 when tests were performed on graphite specimens.)

4.13 The de Walsche report is enclosed in Appendix B.

5.1 The following description is provided for the make-up water system:

The make-up water system supplies de-ionized water to any of the light water process systems and to the fuel storage pool.

City water first passes through a pre-filter, an activated-charcoal column which removes organic material, and two mixed-bed ion columns. The product water flows into a storage tank. During idle periods, the auxiliary pump maintains a recirculation flow through the ion columns to prevent their degradation.

The storage tank, main pump, another ion column, and the associated piping comprise three flow loops. A recirculation flow from the tank, but bypassing the ion column, is available to circulate the contents of the tank. The second loop includes the ion column and a pre- and post-filter to maintain tank water purity. The last loop is the supply header to the various tanks in the reactor basement. The primary coolant storage tank has a permanent connection for filling. A hose must be used to fill the shield and fuel pool systems.

Water requirements are such that the makeup system tank need be filled only once every month or two. Replenishing of the tank is accomplished by means of a solenoid fill valve that is controlled by a timer set to stop flow at the time of calculated full level.

A "Make-up Water System" SCAM alarm is activated by the following conditions: low water purity as read by the selected probe, high level storage tank, low level storage tank, and low flow through either the main pump or cleanup ion column. Also, low flow in the inlet de-ionizer system or a detected leak will cause an alarm. All alarm conditions are displayed on a local control panel and, after a short time delay, will cause a control room alarm. A conductivity probe continuously monitors the purity of water as it is supplied to the storage tank and will shut the solenoid fill valve should the resistance drop below a pre-set value. A high level storage tank alarm or a leak will also close the fill valve.

6.1 The statement that "either three out of the four natural convection values" would be adequate for removing decay heat should have been referenced to the MITR-II SAR. The exact wording in the MITR-II SAR was "The failure of one of four valves is not predicted to significantly reduce the effectiveness of the system." The second part of the sentence "... the anti-siphon valves alone are enough to remove decay heat from 6 MW steady-state operation" is demonstrated in reference 6-1. The text will be revised to reflect the correct references.

4.14 The OFI correlation uncertainty was not quantified in the original references and therefore not included in the safety limits calculation. However, as shown in Table 4-6, OFI correlations are generally more conservative in predicting flow rates leading to flow instability than the OFI flow rates calculated by pressure drops using the MULCH code.

Furthermore, as shown in the comparison of CHF and OFI in section 4.6.6.1, there is an additional margin of about 70% between OFI and CHF. Therefore, there exists a significant safety margin by adopting OFI as the safety limit criterion. The ratio between the *best-estimate* CHF to calculated OFI is approximately 1.5 (MCHFR) x 1.7 (q''_{CHF} / q''_{OFI}) = 2.55. This translates to a safety margin of about 155% between calculated OFI and CHF.

4.15 a) As explained in SAR section 4.6.6.3, the CHF correlation adopted for the safety limits calculation for natural convection operation was derived for a counter-current flooding condition at zero flow. This correlation was developed for a narrow rectangular coolant channel heated on both sides. The flooding limit is based on the total channel power (or corresponding channel average heat flux). Therefore, no axial peaking factor is used in the calculation.

b) The thermal physical properties used in the safety limits calculation correspond to 107 °C, which is the saturation temperature in the core region. Using liquid and vapor densities of $\rho_f = 953$ kg/m^3, $\rho_g = 0.75$ kg/m^3 ; density ratio is obtained for ρ_f / ρ_g =1270.7

The calculation shown in Ref (6-1) used temperature-dependent coolant properties at lower temperatures. Detailed calculation for critical heat flux based on counter-current flooding limit, $q''_{CHF} = 2.353\text{x}10^4\ \text{W}/\text{m}^2$ using Eq. (4-30), is shown in the MathCAD worksheet given in Appendix C. (Note that it is a very conservative assumption to adopt the counter-current flow flooding limit. This correlation was developed for research reactors using MTR-type fuel elements that have either upflow or downflow flow configuration, and for the latter the transition to upflow natural circulation condition a brief no-flow condition may be encountered during a loss of flow transient.)

To obtain a more realistic OFI limit, a series of RELAP5 simulations were performed to calculate the peak cladding temperatures that represent the "best estimate" of this mode of operation. As shown in Figure 4.15-1, at 300 kW there is some flow oscillation in the hot channel that resulted in the clad temperature fluctuation. At 600 kW, as shown in Figure 4.15-2, the maximum clad temperature has a higher fluctuating frequency and seems to increase toward the end of the simultation time of 150 s. Table 4.15-1 summarizes the maximum clad temperature in the hot channel for corresponding reactor power during natural convection operation. Because the maximum clad temperature remains about the same up to 600 kW, it is concluded that the best estimate safety limit based on the flow instability criterion is 600 kW.

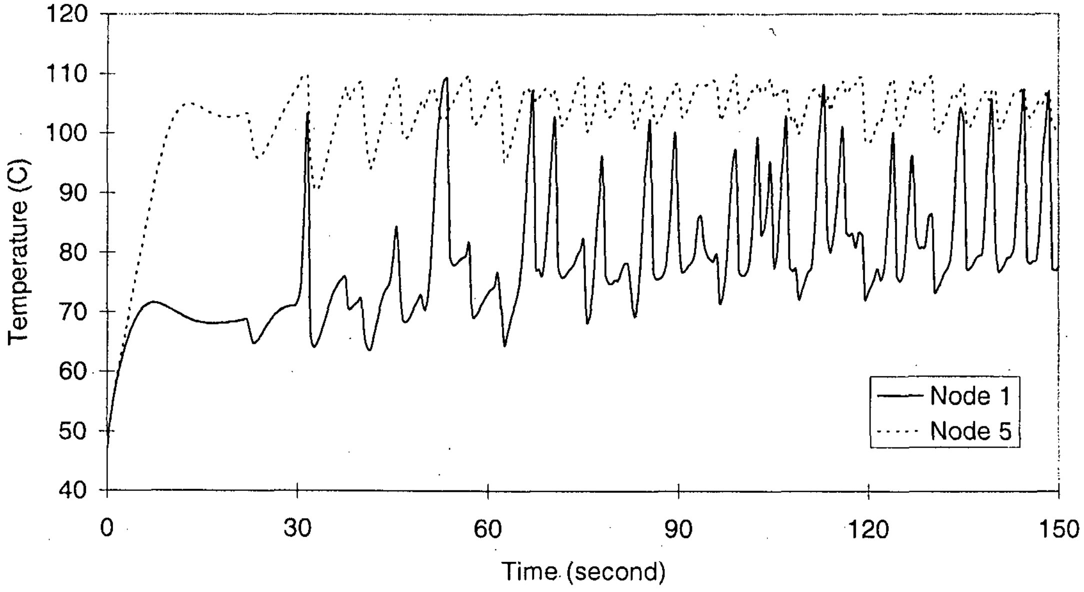

Figure 4.15-1 Hot channel clad temperature oscillation during natural convection (reactor power=300 kW, HCF=2.0)

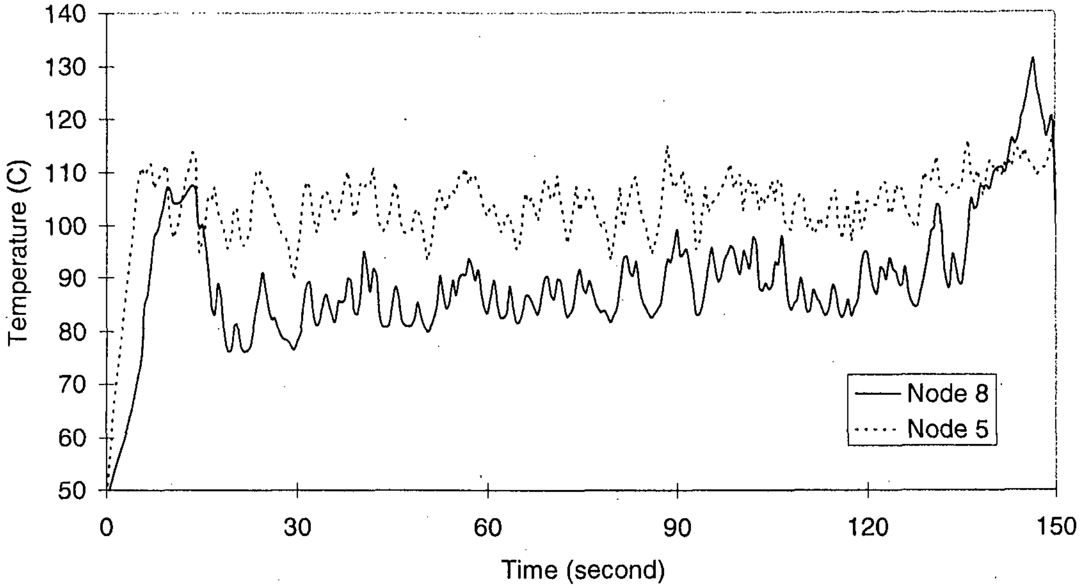

Figure 4.15-2 Hot channel clad temperature oscillation during natural convection (reactor power=600 kW, HCF=2.0)

Table 4.15-1. Predicted maximum clad temperature during natural convection

Reactor power (kW)	The maximum clad temperature (°C)
300	109.4
400	111.3
500	112.6
580	113.8
600	131.2

c) Although the aspect ratio of our coolant channel (L/De=260) is a little larger than the experiment geometry used in Ref. 4-20, this correlation is, in our opinion, the best suited in the literature for the modeling of our coolant channel.

4.16 (a) The correlation used for the heat transfer coefficient is Dittus-Boelter where

$$\mathrm{Nu} = \frac{hD_e}{\mu} = 0.023\,\mathrm{Re}^{0.8}\,\mathrm{Pr}^{0.4} = 0.023\left(\frac{\rho V D_e}{\mu}\right)^{0.8}\left(\frac{\mu c_p}{k}\right)^{0.4}$$

Based on total core flow rate of 1800 gpm, core coolant flow factor $F_f = 0.921$ and flow disparity factor $d_f = 0.864$, the heat transfer coefficient for the hot channel

(Eq. 4-35) is calculated to be 2.08 x 10^4 W/m^{2}K. The effect of fins is accounted for by applying a fin effectiveness of 1.9 to the calculation of heat flux.

(b) The calculation of ΔT_{ONB} does not require a subcooling assumption. The words "a hot channel subcooling of 10 °C..." will be deleted from Section 4.6.7.

(c) The uncertainty associated with the prediction of ONB is accounted for in the engineering hot channel factor for film temperature rise $F_{\Delta T}$, as part of the sub-factor for heat transfer coefficient, in Table 4-8. The Bergles and Rohensow correlation was determined experimentally to be conservative in predicting the lower limits of ONB temperatures, as demonstrated in the paper titled, "Experimental Study of Incipient Nucleate Boiling in Narrow Vertical Rectangular Channel Simulating Subchannel of Upgraded JRR-3," by Y. Sudo, et al. A copy is attached as Appendix D.

4.17 The core flow distribution is taken into account when calculating the mass flow rate through the hot channel . As indicated in section 4.6.6.2, it is assumed conservatively that the hot channel (one with maximum radial peaking factor) also receives the minimum amount of flow among all the coolant channels. The hot channel flow rate is thus derived using Eq. (4-26) in which the core coolant flow factor (F_f) and flow disparity factor (d_f) are accounted for (definitions of these factors are given in section 4.6.3.2). The LSSS limits are determined based on the hot channel power and flow disparity.

11.1 The information requested by this question is more appropriate to Chapter 10, "Experimental Facilities and Utilization," and our response (see below) will be added as Section 10.2.11, "Utilization Activities."

10.2.11 Utilization Activities

The MIT-NRL Silicon Program irradiates silicon material for the semiconductor industry for its use in the manufacture of microcircuits and switches. MIT's responsibility is to treat the silicon material, provided by the customer, per the customer's requirements. The program utilizes the 4TH1-3 and 6TH1-2 horizontal through ports (see Fig. 10-1) for Neutron Transmutation Doping (NTD) of single crystal silicon. These through ports are tangent to the D2O Reflector Tank. The 4TH1-3 port can accommodate the 4-inch crystals and the 6TH1-2 port can accommodate 4, 5 and 6-inch crystals.

The NTD process takes place when undoped (high purity) silicon is irradiated in a thermal neutron flux. The purpose of semiconductor doping is to create free electrons (low resistivity). The thermal neutron is captured by the Si-30 atom, which has a 3% abundance in pure Silicon. Because of the high neutron/proton ratio of Si-31, the capture causes release of a beta and, by converting a neutron to a proton, the Si-31 atom transmutes to a P-31 atom. Overall the result is a lower resistivity with little variance from the target resistivity. The doped Silicon is used in a variety of electronic devices, such as transistors, diodes, and IC chips.

The silicon crystals are loaded into 400 mm long cans and then placed on the loading conveyor. These cans are then transferred to the port's entrance and pushed through the rotated throughport to the unload side. The cans are then placed on another conveyor for radioactive decay. The speed at which the crystals are pushed through the port is determined by the reactor power, the final and initial ingot resistivity, and the port in which the silicon is processed.

Typical dose should be from 50-200 mR/hr. Radiation levels of the irradiated ingots are measured using both wall-mounted and portable detectors. Radiation levels in the work area where the ingots are unloaded are monitored by area radiation monitors that indicate and alarm locally in the work area. The work area can also be placed under video surveillance from the control room.

13.1 Response being prepared.

13.2 Response being prepared.

13.3 Loss of Primary Coolant Flow:

a) The flow coastdown data was obtained from measurements. The measurement error is within 5%. To validate the MULCH-II calculation in order to quantify all error sources, such as decay heat model, thermal hydraulics correlations etc., a benchmark analysis was performed using RELAP5. The results are summarized in Appendix F. Because MULCH predicted a slightly lower hot channel temperature than RELAP5, another LOF analysis was performed using RELAP5 and the results are given below.

The initial conditions for this calculation are P=7.4 MW, Tout=60 °C, W=1800 gpm. Figures 13.3-1 and 13.3-2 are the predicted clad temperature for the average and hot channels. Note that the max cladding temperature in the hot channel is ~ 125 °C, much lower than the softening temperature of Al alloy.

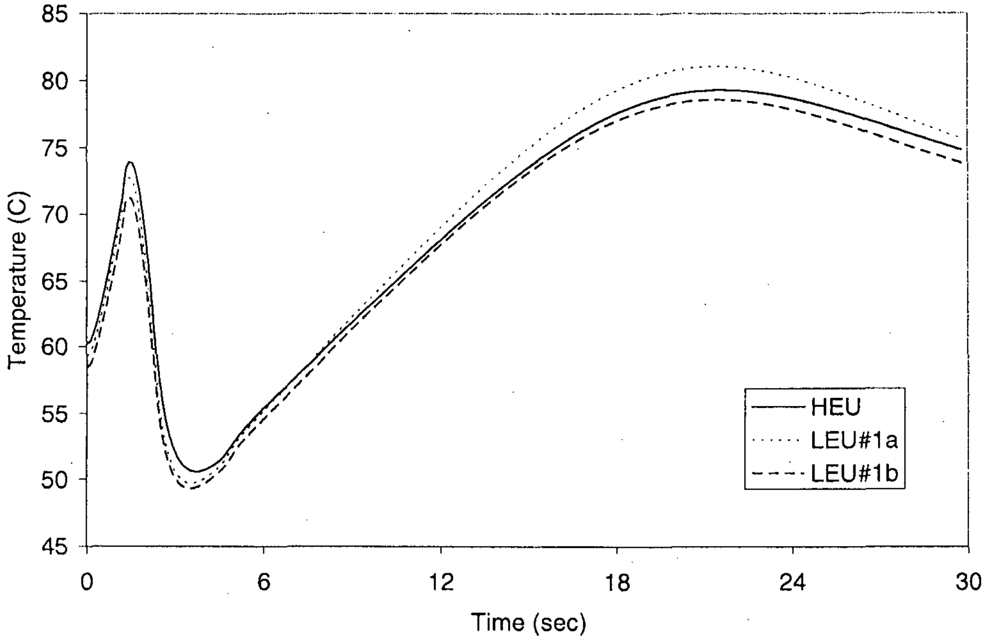

Figure 13.3-1 Comparison of Cladding Temperature (Average Channel, Node#5)

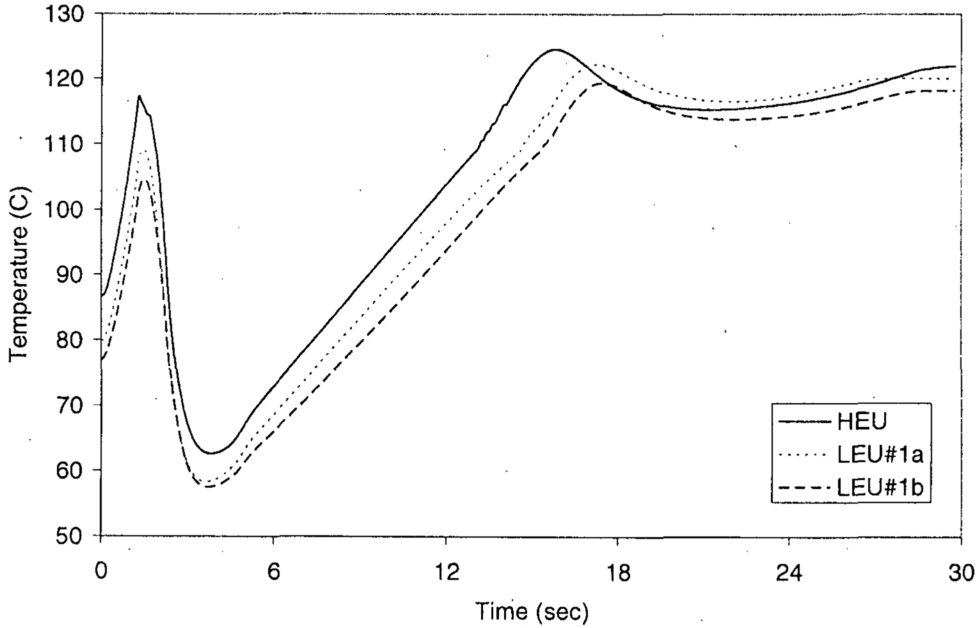

Figure 13.3-2 Comparison of Cladding Temperature (Hot Channel. Node#5)

b) The analysis above shows that during a LOF transient, even assuming the most conservative initial conditions (LSSS), the maximum fuel clad temperature is predicted to be ~125 °C and a very large safety margin exists to the fuel cladding softening temperature. The decay power, which decreases exponentially during this transient, should not be directly compared to the SL power established for NC because the former is a transient and the latter is steady-state.

13.4 The MITR core has been operated with 24 fuel elements since the 1980's. It may be possible to use 23 fuel elements in the future to increase the number of in-core experiments. The minimum fuel element configuration (23 elements) is more limiting because core power is constant and hence the power per element is higher for 23 elements than for 24. Also, for natural convection, the total core flow is driven by the core pressure drop and therefore the total core flow increases if the number of fuel elements increases (i.e., decay heat removal is improved). However, the effect is small and the LSSS power for forced convection at constant primary flow is roughly the same for 23 and 24 elements configurations.

Therefore all thermal hydraulic limits calculations and the LOF calculation are performed assuming 23 fuel elements in the core. RAI response#28 uses 24 elements to illustrate the margin between OFI to CHF. Section 4.6.6.1 will be modified for 23 elements for consistency.

13.5 All the thermal hydraulics limits calculations shown in the SAR (chapter 4) assume a hot channel which consists of (1) the highest radial power peaking, (2) the highest axial peaking, and (3) the lowest flow disparity factor. For the purpose of establishing the average core condition, all other channels are assumed identical to the average coolant channel which provides the core outlet temperature. The hot channel assumption is very conservative in that the highest radial power peaking, axial power peaking, and lowest flow disparity normally occur in different locations of the core region.

The coolant channels next to the edge fuel plates are slightly different from the inner coolant channels. There are two possible configurations. The first is that one edge fuel plate is placed next to another (of another fuel element). The second is that an edge plate is next to a solid aluminum alloy support plate. The coolant channel diameters of these are documented in a file memo by T. Newton (see Appendix G) and listed in the table below. In both cases, flow velocities are higher (based on constant pressure drop boundary condition) because the coolant channel equivalent diameters are slightly larger than an inner channel. The velocity and heat transfer coefficient (HTC) ratios are derived as follows:

$$\Delta P = f\frac{L}{D}\frac{1}{2}\rho v^2$$

For turbulent flow: $f = 0.316\,Re^{-0.25}$ (Blausis correlation) and, using a constant pressure drop, the velocity ratio can be derived as $\frac{V_1}{V_2} = \left(\frac{D_1}{D_2}\right)^{0.714}$

Using the Dittus-Boelter correlation for HTC:

$$Nu = \frac{hD}{\mu} \propto \left(\frac{\rho VD}{\mu}\right)^{0.8} \text{, therefore } h \propto V^{0.8} D^{-0.2}$$

As shown in the table, the two configurations of the edge plate would fall within the envelope of the hot channel assumption for MITR's thermal hydraulics analysis.

	Case 1 Two edge plates next to each other	**Case 2 Edge plate next to support plate**	**Hot channel**
Heat removal	Both sides	One side	Both sides
Coolant channel equivalent diameter De (cm)*	0.295	0.246	0.219
Flow velocity ratio to avg. channel	1.82	1.266	0.864
HTC ratio	1.52	1.163	0.864

* See file memo "End coolant channel equivalent diameter" by T. Newton (Appendix G)

5.2 The core outlet temperature sensors, MTS-1 and MTS-1A, are located in the core tank near the outlet pipes. Both provide high temperature alarms as well as automatic scram signals. Because the natural circulation flow would reach the upper region of the core tank, these temperature sensors will detect the core outlet temperature with some delay time. Therefore, to take into account the delay time conservatively, the LSSS calculations were performed assuming the core inlet coolant temperature is the same as the mixture coolant temperature in the upper core tank region. This corresponds to the outlet temperature as measured by MTS-1 and MTS-1A, as shown in SAR Table 4-1. The figure below illustrates the primary coolant control volumes as modeled by MULCH and RELAP5 in the transient analysis. The elevation of MTS-1 and MTS-1A is about 10 cm higher than that of the anti-syphon valves.

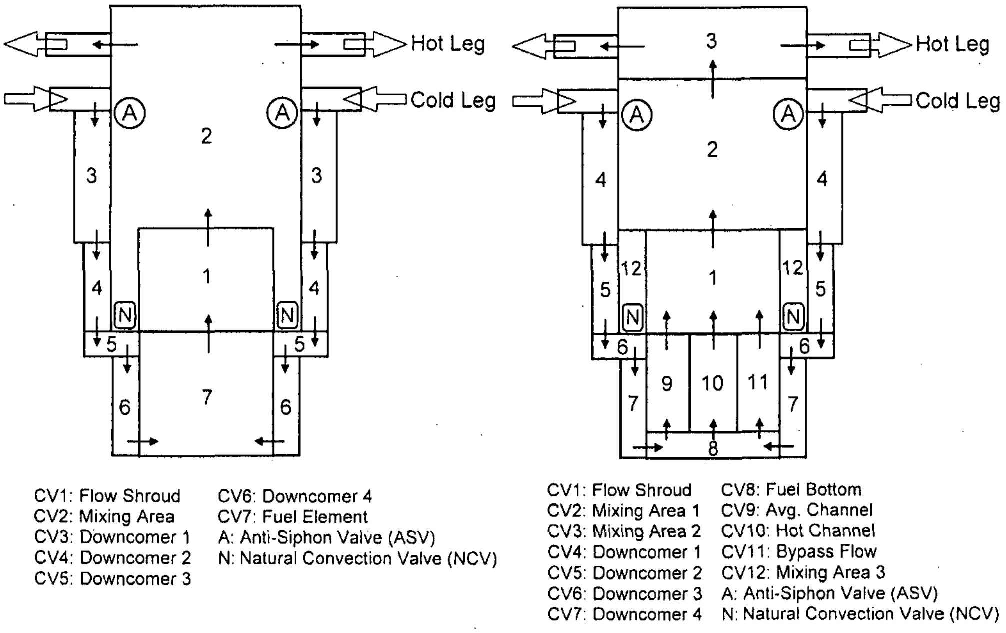

(a) MULCH-II Code

(b) RELAP5 Code

Figure 5.2-1. Primary loop control volumes for MIT reactor

12.1 The major steps in the startup plan are:

1. Once there are no further RAIs, we will consolidate the technical specifications so that there is a single document that contains the original submission together with the changes that resulted from the RAIs and the changes that have been made since submission of the original relicensing package.

2. MITR procedures (test/calibration as well as operating) will be reviewed and revised as necessary to ensure compliance with the new technical specifications. This is a major task that will require several months.

3. Training will be conducted on the new procedures and specifications.

4. The new operating license will be initially implemented for operation at the existing power level of 5 MW.

5. Preparations will be made for the upgrade to 6 MW. This will involve a second revision of the operating procedures as well as issuance of a special procedure for the upgrade. This latter procedure would cover such items as the adjustment of instrument setpoints, especially those for the nuclear detectors. The shielding, coolant flows, and instrumentation ranges as now installed are adequate for 6 MW operation.

6. A power ascent to 6 MW would be done in steps of 0.50 MW using various methods (calorimetrics, foil activation, instrument readings) to verify the increases. The objective in using these multiple and independent methods would be to ensure that the detector response is, as predicted, linear in the range 5-6 MW.

14.1 Response being prepared.

14.2 A sixth paragraph will be added to TS #3.4., "Reactor Containment Integrity and Pressure Relief System." It will state the following:

6. The following is the minimum equipment required to establish containment integrity.

   a) The main and basement personnel locks are either operable or at least one door is closed.

   b) The truck airlock inner door is closed.

   c) All containment penetrations (ventilation, pneumatic, gas supply, electrical) are either sealed or equipped with an operable isolation device. (<u>Note</u>: If an isolation device is redundant, then only one set of the redundant devices is required.)

   d) All piping penetrations within the reactor building are capable of withstanding containment building test pressure.

   e) Initiation system for containment isolation is operable.

   f) At least one set of the redundant vacuum relief breakers is operable.

   g) Pressure relief system is operable.

14.3 A fourth paragraph will be added to TS #3.5, "Ventilation System." It will state the following:

4. The following is the minimum equipment required for operability of the ventilation system:

   a) Intake and exhaust fans.

   b) Auxiliary fans if needed to maintain building differential pressure.

   c) Vacuum relief system.

d) Controls (manual or remote actuator plus damper) to adjust building differential pressure.

e) Exhaust filters.

f) Ventilation system interlocks listed in Specification 4.5.

g) One gaseous, particulate, and area radiation monitor located in the ventilation effluent.

14.4 A third paragraph will be added to TS #3.6, "Emergency Power." It will state the following:

3. The following is the minimum equipment needed for operability of the emergency power system:

a) Batteries sufficient to fulfill the requirement of paragraph (1) above.

b) A motor-generator set.
c) Startup circuitry and automatic transfer switches to fulfill the requirement of paragraph (2) above.

d) A manual transfer switch for the primary coolant auxiliary pump.

14.5 10CFR20.1301 states in part that the dose to individual members of the public shall not exceed 0.1 rem in a year and that compliance with this part is detailed within 20.1302.

Effluents from the MIT's 150 foot stack exhibit large dilutions such that the ground concentration is a small fraction of the effluent (stack) concentration. It is for this reason that a dilution factor was included within this technical specification such that a reasonable determination of the effective concentration and resultant dose to a member of the public could be made.

The current technical specification's permissible dilution factor was set conservative and as a result has led to confusion. For example, within the annual report to the NRC, an effective offsite concentration is calculated at 40-50% of Technical Specification which is obtained by comparison to Table 2 of Appendix B. This in theory would imply an offsite dose consequence of 25 mrem. In evaluating against the constraint criteria of 20.1101(d), a calculated off site dose of less than 1 mrem is realized. To avoid this confusion, a more realistic dilution factor was included in this re-licensing effort such that the effective concentration is consistent with the dose calculations. Implicit therefore is that the criteria for effluents are dose based. Please refer to the response *"Item 66 of the second partial request for additional information"* for additional detail.

In addition to the above, a study to determine the affect to elevated receptors was made and it was determined that the dose from routine operations is less than 1 mrem/y.

Although, the methodology cite above is dose based, a comparison to Table 2, Appendix B will continued to be made for purpose of reporting

11.2 The radiation protection organization as described in Section 12.1.2.2 includes one officer, one assistant officer, two technicians, and part-time support staff. Although this describes the nominal complement, the actual numbers may vary depending on the operational needs of the facility. For example, during large anticipated projects, contract technicians have been used as well as support from the allied campus radiation protection program as needed.

The minimum requirement pursuant to the technical specifications for an unsecured condition is that a member of the radiation protection staff either be on site or on-call.

11.3 The training requirements are described in Section 12.10 of the SAR.

12.2 The requalification program that will be observed upon issuance of the new license for the MITR is as described in Section 12.10 of the SAR. (Note: This has been discussed with NRC's Research and Test Reactor Branch B and confusion between the plan in this submittal (Section 12.10) and an earlier requalification program has been resolved. The one in Section 12.10 will be observed.)

4.18 The statement in Section 4.2.1, pages 4-5, is correct. There is an error in RAI response #17(b). The width of the fuel plate in RAI 17(b) should be 5.288 cm. This changes the fission density calculation in that response from 1.46 x 10^{21} fissions/cm^3 to 1.50 x 10^{21} fissions/cm^3.

13.6 The statement on page 13-38 (Section 13.2.9.1) is a typo. It will be changed to read, "Specifically, the subcritical interlock, which is described in Section 7.3.1.2 of this report, blocks blade withdrawal beyond five inches unless all blades are first brought to the five inch position. Once all blades are above five inches, satisfaction of the requirement to maintain a uniform bank height is achieved by administrative procedure." This statement is now consistent with TS 3.2.4 and with Section 7.2.2.1(4).

14.6 ANSI/ANS-15.1 (1990) has been replaced by ANSI/ANS-15.1 (2007). The 2007 definition has deleted the words, "that is in the normally closed position." Our definition of containment (number 1.3.5) will be revised to use the wording of the 2007 definition. Specifically, the new definition will be:

1.3.5 Containment

Containment is an enclosure of the facility designed to (1) be at a negative internal pressure to ensure in-leakage, (2) control the release of effluents to the environment, and (3) mitigate the consequences of certain analyzed accidents or events.

Appendix A

- Snelgove and Hofman (*relevant pages only*)
- Caho
- Beeston

Distribution Category:
Nuclear Energy
(UC-940)

ANL/NPR-93/002

EVALUATION OF EXISTING TECHNOLOGY BASE FOR CANDIDATE FUELS FOR THE HWR-NPR

by

J. L. Snelgrove and G. L. Hofman
Argonne National Laboratory

R. L. Frontroth, W. R. McDonell, and H. B. Peacock
Westinghouse Savannah River Company

R. F. Whitacre
EG&G Idaho, Inc.

G. L. Copeland
Oak Ridge National Laboratory

ARGONNE NATIONAL LABORATORY
9700 South Cass Avenue
Argonne, Illinois 60439

February 1993

FOREWORD

This report was originally published, with a restricted distribution, in March 1990 as part of a more general assessment of candidate materials for a new heavy water-moderated production reactor. The compilation and evaluation of data for aluminum-based dispersion fuels performed during 1989 and early 1990 were by far the most comprehensive to date. Therefore, the fuel materials portion of the original report is being republished with an unrestricted distribution. Because of time and funding restrictions only minor editorial changes, such as adding references to the sources of the data in Table XI, have been made. Consequently, the examples and discussions still refer to the new production reactor. However, similar issues also apply to research and test reactors, and we believe that sufficient information is included in the report to allow one to modify the illustrations to suit any particular reactor.

The development, testing, and study of aluminum-based dispersion fuels has continued during the past three years, primarily at the Argonne National Laboratory (ANL) and the Japan Atomic Energy Research Institute (JAERI). At ANL the emphasis is currently on high-temperature, high-fission rate performance of U_3Si_2, U_3Si, U_3O_8, and UAl_x fuels for possible application in the Advanced Neutron Source reactor. At JAERI the emphasis has been on fission product release from uranium silicide fuels and on the behavior of these fuels when subjected to energetic pulses. As these studies proceed, new insights are being gained, and, in some instances, the information in this report may become obsolete. Those needing up-to-date information are encouraged to closely follow current work. The work on this report prompted one of the authors to perform an even-more-comprehensive review of the U_3O_8-aluminum exothermic reaction. Both this review and a report on the JAERI fission product release experiments are being published in *Nuclear Safety*.

Table of Contents

APPENDICES

A. H. B. Peacock and R. L. Frontroth, "Properties of Aluminum-Uranium Alloys," Westinghouse Savannah River Company Report WSRC-RP-89-489 (August 1989)

B. H. B. Peacock, "Properties of U_3O_8-Aluminum Cermet Fuel," Westinghouse Savannah River Company Report WSRC-RP-89-981 (October 1989)

C. R. F. Whitacre, "The UAl_x Fuel Dispersion System," EG&G Idaho, Inc., Report EGG-PRP-8783 (November 1989)

D1. J. L. Snelgrove, R. F. Domagala, G. L. Hofman, T. C. Wiencek, G. L. Copeland, R. W. Hobbs, and R. L. Senn, "The Use of U_3Si_2 Dispersed in Aluminum in Plate-Type Fuel Elements for Research and Test Reactors," Argonne National Laboratory Report ANL/RERTR/TM-11 (October 1987)

D2. G. L. Hofman, "Some Recent Observations on the Radiation Behavior of Uranium Silicide Dispersion Fuel," Proc. 1988 Int. Mtg. on Reduced Enrichment for Research and Test Reactors, San Diego, California, September 19-22, 1988, Argonne National Laboratory Report ANL/RERTR/TM-13 (CONF-8809221), pp. 92-110 (June 1993)

D3. G. L. Hofman and W.-S. Ryu, "Detailed Analysis of Uranium Silicide Dispersion Fuel Swelling," Proc. XIIth Int. Mtg. on Reduced Enrichment for Research and Test Reactors, Berlin, Germany, September 10-14, 1989, G. Thamm and M. Brandt, Eds., Forschungszentrum Jülich GmbH, pp. 115-135 (1991)

List of Tables

List of Figures

Page

tion and accident conditions; and Sections 8 and 9 discuss the pre- and postirradiation issues of fabricability and reprocessibility. An overall summary is presented in Section 10.

2. CANDIDATE FUELS AND ANTICIPATED REACTOR OPERATING CONDITIONS

2.1 Candidate Fuels

The current SRS reactors have successfully used a highly enriched U-Al alloy fuel clad in aluminum since the late 1950s. Many other research and materials testing reactors have also successfully used this type of fuel. As will become apparent, a considerable base of fuel properties and behavior data exists for U-Al alloy fuel. Its major drawback is the relatively low uranium content (~35 wt% U, ~1.3 g U/cm^3) beyond which production yields become intolerably low, which puts a lower limit on the enrichment to achieve a given ^{235}U loading in an assembly of a particular design. Such a limitation might restrict the amount of recycle uranium which could be used in the HWR-NPR fuel cycle. In addition, the production of U-Al alloy fuel requires uranium metal, which must be obtained from the Y-12 Plant in Oak Ridge, as a feed material. However, because of the good experience with U-Al alloy fuel at SRS during more than 30 years, the U-Al alloy fuel is considered to be the primary candidate fuel for the HWR-NPR.

Because of the possibilities to achieve a significantly increased fuel loading (to >1.9 g U/cm^3 at 60 wt% U_3O_8), direct on-site uranium recycle at SRS, improved fabrication yields, reduced waste, and improved fabrication safety, a major effort to develop the fabrication process for and to test an alternative fuel, a dispersion of U_3O_8 in Al produced by a powder-metallurgy technique, was carried out at SRS during the 1970s. Considerable development work on U_3O_8 dispersion plate-type fuel had been carried out during the 1960s for the Advanced Test Reactor (ATR) at INEL and for the High Flux Isotope Reactor (HFIR) at ORNL. Although the ATR subsequently switched to the uranium aluminide dispersion fuel (see below), the HFIR and three other U.S. Government-owned reactors are currently using U_3O_8 dispersion fuel. The results of the SRS work were positive, and a project to convert to the use of U_3O_8 dispersion fuel in the existing SRS reactors was started. However, the conversion project is currently on hold because of concerns about the effect of the exothermic reactions between the uranium oxides and aluminum which were raised during a National Academy of Sciences review of the SRS reactors following the Chernobyl accident. Nevertheless, the attractiveness of this fuel cycle is such that the U_3O_8 dispersion fuel is considered to be the primary backup fuel for the HWR-NPR. The exothermic reaction is addressed explicitly in Section 4.1.2 of this report.

The fuel selection study performed by ANL and reported elsewhere (see, for example, Ref. 1) addresses the question of whether the additional prompt negative feedback from the Doppler effect in ^{236}U and ^{238}U might provide a significant advantage to avoid or mitigate the effects of a severe accident. If a design based on much lower enrichment were found to be advantageous, a high-density fuel might be needed to allow inclusion of sufficient diluent. The high-density fuel developed by the Reduced Enrichment Research and Test Reactor (RERTR) Program[2] at ANL to make the operation of research and test reactors feasible with low-enriched uranium (LEU), U_3Si_2 dispersed in aluminum, should allow at least a three-fold increase in uranium loading over that possible with the 35-wt%-U alloy in an HWR-NPR fuel tube. Approximately two cores of plate-type fuel with a uranium loading of 4.8 g LEU/cm^3 were successfully commercially fabricated and subsequently tested in the Oak Ridge Research Reactor (ORR) at ORNL,[3] and the U.S. Nuclear Regulatory Commission gave its approval for the use of this fuel in licensed nonpower reactors.[4] A number of U.S. and foreign reactors are converting to use the U_3Si_2 dispersion fuel. In addition, U_3Si_2 dispersion fuel, with highly enriched uranium (HEU), is currently the primary candidate fuel for the Advanced Neutron Source Reactor being designed by ORNL.[5]

Uranium-aluminum alloy fuel has been superseded in many reactors by a dispersion of uranium aluminide compounds in aluminum. Today it is the predominant HEU fuel type for research and test reactors around the world. Since U-Al alloy is actually a dispersion of UAl_4 and UAl_3 particles in aluminum, the so-called UAl_x (denoting a mixture of UAl_2, UAl_3, and UAl_4) dispersion fuel has many of the same characteristics as the alloy; however, it can be fabricated to higher loadings if temperatures are low enough to prevent conversion of the UAl_3 into UAl_4 during the fabrication process (see Section 3.1.1). Should a somewhat higher density than 1.3 g U/cm^3 be needed for the HWR-NPR and should neither the U_3O_8 nor the U_3Si_2 dispersions be considered acceptable, the UAl_x fuel could be a viable alternative to the U-Al alloy fuel (up to 1.6 g U/cm^3 at 35 vol% UAl_x).

Other high-density uranium compounds (including UO_2, UC, UC_2, UN, and U_3Si) were tested as dispersants in an aluminum matrix during the late 1950s and early 1960s. These fuels were abandoned either because of excessive reaction with the aluminum matrix during fabrication or because of excessive swelling during irradiation.[6,7] No other candidate fuels were identified for the HWR-NPR.

2.2 Reactor Design and Anticipated Operating Conditions

In order to properly evaluate whether the existing data for each of the fuels are adequate to support use in the HWR-NPR, it is necessary to compare the expected service conditions to the test conditions under which the data were obtained. Although conceptual design of the HWR-NPR is just beginning, preliminary work at SRS on a concept similar to the present reactors provides some guidance.

In the preconceptual studies, the reactor core consisted of 438 fuel/target assemblies on a 203-mm (8-in.) triangular pitch. The fuel assemblies consisted of three fuel tubes and an inner and an outer target tube. The reactor was moderated and cooled with heavy water. The fuel assemblies were similar to the Mark 22 assembly shown in Appendix 1 of Appendix A of this report. The fuel tubes ranged from 4.06 to 4.24 m (160 to 167 in.) in length, with 3.81-m-long fuel meat. Two fuel tube designs emerged from the preconceptual studies and have been used in the fuel selection support study at ANL[1]—one having fuel meat thicknesses of 1.08, 1.64, and 1.21 mm (0.0425, 0.0645, and 0.0475 in.) in the outer, middle, and inner tubes, respectively (called geometry A in this report), and the other having fuel meat thicknesses of 1.97, 2.74, and 2.13 mm (0.0775, 0.108, and 0.084 in.) in the outer, middle, and inner tubes, respectively (called geometry B). The total fuel meat volume in the three tubes is 3678 cm^3 for geometry A and 6310 cm^3 for geometry B.

The most important reactor parameters are the power density, temperature, and fission density (or uranium burnup) in the fuel meat. The values of these quantities from the preconceptual study are given in Table I.[8] Also listed are estimated values of the fast neutron exposure for an HWR-NPR assembly irradiated for an average of 200 full-power days (fpd).

In order to characterize the behavior of the fuels under irradiation, it is often desirable to convert the power density in the fuel meat to fission rate in the fuel particle and the fission density in the fuel meat to fission density in the fuel particle. To convert from meat values to fuel particle values one divides by the volume fraction of fuel in the meat, which, of course, depends on the density of the fuel. As used in this report, burnup refers to the total depletion of ^{235}U (including both fissions and captures).* A useful formula relating burnup to fission density (FD) in the fuel meat (particle) is:

$$FD = (2.10 \times 10^{21})\, \rho_u\, e\, B / X \ \ cm^{-3}, \qquad (1)$$

where ρ_u = the uranium density in the meat (particle);

e = the weight fraction of ^{235}U in the U, i.e, the enrichment;

B = the fractional depletion of ^{235}U;

---

*It should be noted that this definition of burnup is not universal in the literature. Care must be exercised when interpreting and comparing burnup values. Fission density, on the other hand, appears to be used consistently throughout the literature.

Table I. Anticipated Operating Conditions of the HWR-NPR

Parameter	Value
Power Density in Fuel Meat, W/cm^3	
Average	2030
Peak	2900
Fuel Centerline Temperature, °C	
Average	166
Peak	175
Uranium Burnup, at.% ^{235}U Depletion	
Average	44
Peak	62
Fast Neutron Exposure in 200 fpd, 10^{21} n/cm^3	
(>0.1 MeV)	
Average	1.3
Peak	1.9
(>1.0 MeV)	
Average	0.45
Peak	0.64

and X = the fraction of all fissions resulting from ^{235}U.

A ^{235}U capture-to-fission ratio of 0.22, based on recent cell calculations for the HWR-NPR at ANL[9], was used in deriving the constant in Eq. (1). The factor X is a function of the enrichment and the burnup because of fissions in the non-^{235}U isotopes and in the Pu produced during irradiation of the fuel. Values of X calculated for an ORR-type (light-water-moderated) reactor are given in Table II. Over the range of burnups expected for the HWR-NPR, use of the ORR values should result in only small (no more than a few percent) errors in fission densities. These values can be checked and new values calculated if needed during the design studies.

Table II. Values of the ^{235}U Fission Fraction, X, in Equation (1)

	X, for Enrichment		
Burnup, %	20%	45%	93%
0	0.996	0.998	1.000
10	0.987	0.992	0.999
20	0.977	0.986	0.998
30	0.968	0.981	0.998
40	0.958	0.975	0.997
50	0.947	0.968	0.996
60	0.935	0.962	0.995
70	0.921	0.954	0.994
80	0.904	0.944	0.993
85	0.894	0.938	0.992
90	0.897	0.931	0.991
95	0.862	0.921	0.990
100	0.831	0.902	0.988

3. PHYSICAL AND MECHANICAL PROPERTIES OF THE FUELS

3.1 Constituent Phases

3.1.1 U-Al Alloy and UAl_x

The phase diagram of the uranium-aluminum system is shown in Fig. 2, p. 7, of Appendix C. Three uranium aluminide compounds exist: UAl_2, UAl_3, and UAl_4. In Mondolfo's diagram, UAl_4 is shown to exist over a range of compositions between $UAl_{4.5}$ and $UAl_{4.9}$, as first indicated by Borie.[10] He determined the density to be 5.7 ± 0.3 g/cm^3 and the formula to be UAl_4, indicating a defect structure deficient in U atoms. Work at Chalk River[11] and at INEL[12] supported this position. Other workers, however, found no evidence to support a range of homogeneity[13] or a lower than theoretical density.[14] Gibson's work, where high-purity, single-phase crystals of UAl_x were produced, appears to provide incontrovertible evidence of the defect structure of UAl_4. Therefore, it is recommended that a uranium weight fraction of 0.651 and a density of 5.7 g/cm^3 be used for UAl_4, corresponding to $U_{0.853}Al_4$.[*] For UAl_3 and UAl_2 the uranium weight frac-

---

[*] The theoretical density of 50%-enriched UAl_4 is 6.0 g/cm^3, and its uranium weight fraction is 0.687.

5. IRRADIATION PERFORMANCE

Each of the candidate fuels for the HWR-NPR has been extensively tested under irradiation and has been demonstrated to perform well through use in fuel elements in research and test reactors and, in the case of the U-Al alloy and U_3O_8-Al fuels, in the SRS production reactors, as indicated in Section 2.1. The most important characteristics of a fuel determined by irradiation testing are the swelling, the changes in microstructure, and the blister temperature of the fuel meat. As used in this report, swelling is defined as a volume change of the fuel meat, which, due to physical constraint, occurs in the thickness direction only in plate-type fuels and can affect both the thickness and diameter of fuel tubes.* Blistering is typically a high-temperature phenomenon in which gas pressure causes local separations of the meat and cladding. In some instances in the literature, however, the terms breakaway swelling (accelerated, large-scale swelling of the fuel meat caused by interconnection and consequent rapid growth of fission gas bubbles) and blistering have been used to describe the same phenomenon.

Fuel meat swelling and blister temperature are macroscopic quantities which can be determined by external measurements; a study of the microstructure is necessary to understand the mechanism of swelling and blistering and to indicate conditions of incipient failure. The microstructures of the candidate fuels will be discussed in conjunction with swelling and blistering.

5.1 Swelling and Microstructural Characteristics

Swelling can occur from a combination of phenomena, but the result is the same as far as operation of the reactor is concerned—a change in the thickness of a fuel tube or plate and a change in diameter of a fuel tube which causes a change in the area of a cooling channel. The primary cause of swelling is the accumulation in the fuel particles of fission products which occupy more volume than the uranium atoms from which they were produced. Of special concern are gaseous fission products, which might collect in bubbles which grow to a size where gas pressure is larger than the restraint provided by the fuel particles or fuel meat, resulting in rapid (breakaway) swelling. Other sources of gas are (n,α) reactions with burnable poisons or impurities, α decay of fission products, and adsorbed gases present at the time of fabrication. Two additional mechanisms for volume change of the fuel meat are reactions of the fuel particles with the matrix aluminum and sintering of the as-fabricated voids in the fuel meat. The latter is especially important for the dispersion fuels. To aid in the understanding of the swelling data, a brief discussion of the swelling process follows.

---

*Sometimes, however, data in the literature are recorded as percentages of plate volume rather than as percentages of fuel meat volume; therefore, one must determine the basis of percentage swelling data from different sources before comparing them. In one instance plate swelling data were found to be mistakenly labeled as meat swelling.

The amount of fuel meat swelling measured after a given amount of burnup is the algebraic sum of the volume changes due to the phenomena listed above. Radiation-induced sintering causes a consolidation of the as-fabricated voids and reduction in their volume. Negative fuel meat volume changes have been measured in many instances, especially when the fuel meat of the as-fabricated plate contained a large amount of porosity. This phenomenon occurs regardless of the temperature of the fuel plate or tube or even the fission rate, as evidenced by its occurrence in fuel plates containing fuels made from depleted uranium. Chemical reactions also occur during irradiation. Their rates may be temperature dependent, and the volume changes associated with them may be either positive or negative. The fuel particles also begin to swell as a result of accumulated fission products. The swelling due to solid fission products is linear with fission density, but fission gas swelling will become nonlinear if gas pressure exceeds the strength of the irradiated fuel particles (which may be chemical reaction products). As fuel particles swell they begin to fill adjacent voids and to exert pressure on the aluminum matrix, causing radiation-enhanced creep. The creeping matrix material will tend to compress voids and to move out of the fuel meat toward the cladding. If, however, the voids have become pressurized with gas, they will resist the creeping matrix aluminum, and their rate of closure will be reduced. In fact, if the matrix temperature is high enough, the gas pressure may cause the voids to expand. The most likely source of gas to pressurize the voids is helium from (n,α) reactions with burnable poison. Helium atoms can diffuse much more readily in aluminum than can the much larger fission gas atoms. As will be discussed below, experimental observations have shown that the as-fabricated voids tend to disappear in highly irradiated fuels except when B_4C poison was dispersed in the fuel meat.

Swelling is measured in various ways, the most accurate being the use of Archimedes' principle to determine the volume of the fuel meat (including voids) before and after irradiation (often called immersion density measurements) and the least accurate being plate thickness measurements. Plate thickness measurements, which invariably overestimate the swelling because measurements are made between high points on the plate or tube surfaces, are perfectly adequate to assure that swelling is within reasonable limits. However, more accurate measurements are needed when studying the swelling mechanism. Correlations have been developed to relate the amount of meat swelling to the fission density and the as-fabricated porosity in the meat of UAl_x and U_3O_8 dispersion fuels (see Section 4.2.2, pp. 50-58, of Appendix C and Ref. 25).

During the RERTR Program it was recognized that most of the swelling of intermetallic dispersion fuels occurred in the fuel particles, so similar correlations were developed to determine meat swelling as a function of fission density in the fuel particles and of the as-fabricated porosity, or, most recently, of the actual decrease in as-fabricated porosity during irradiation. Such correlations have the advantage of taking into account the volume fraction of fuel in the meat. In earlier studies with relatively low-volume-fraction fuels, the fuel volume fraction was not such an important parameter.

Completely satisfactory correlations have not yet been developed for UAl_x and, especially, for U_3O_8 fuels because of complications related to volume changes resulting from reaction of the fuel and the matrix during fabrication and irradiation.

Even though U-Al alloy fuel was extensively tested during the 1950s and very early 1960s, few quantitative data on swelling during irradiation have been found. References 39 and 41 report that 18-wt% and 23-wt%, fully-enriched U-Al alloy fuel plates irradiated to 13 to 83% burnup showed thickness changes in the range of -1 to 4%. It is not known to what extent oxidation of the cladding was taken into account in the quoted thickness changes. Reference 41 indicates that tests of up to 50-wt% U-Al alloy fuels at temperatures up to 177°C and burnups up to 50% produced no apparent dimensional or microstructural changes. Reference 41 reports density change data for fully enriched 45-wt%-U, 3-wt%-Si plates irradiated in the MTR. After $\sim 3.0 \times 10^{21}$ f/cm^3 ($\sim$80% ^{235}U burnup), the plate density had decreased by ~2.4%, indicating ~12% swelling of the meat.

Over the years considerable emphasis has been placed on postirradiation annealing tests of U-Al alloy fuel plates, and swelling data obtained during such tests are plotted in Figs. 18 and 19, pp. 38-39, of Appendix A. Little, if any, microstructural change occurred during 400°C anneals; however, extensive cracking of the fuel meat led to significant swelling after ~9 h at 475°C and after <2 h at 550°C. Reference 41 reports that a 4-h, 340°C anneal of an 18-wt% U-Al alloy fuel plate irradiated to 50% burnup caused minor microstructural changes but no significant dimensional changes. Fuel tubes irradiated at SRS at temperatures apparently higher than 400°C swelled during irradiation in a manner similar to that seen during postirradiation anneals. The swelling was attributed to fission gas bubbles in and subsequent cracking of the Al matrix. The presence of substantial amounts of fission gas in the matrix of U-Al alloy fuel is plausible because the uranium is likely to be rather finely dispersed in the matrix, both in solution and as small UAl_4 fuel particles from which high percentages of fission products would recoil into the matrix.

All of the swelling data and qualitative evidence from extensive operating experience in the SRS reactors and other research and test reactors, as well as data for the similar UAl_x dispersion fuel discussed later, indicate that, when used at temperatures comfortably below 400°C, U-Al alloy fuel is extremely stable under irradiation. The highest burnup achieved in U-Al alloy fuel, albeit with a silicon addition, was $\sim 3.0 \times 10^{21}$ f/cm^3 in 45-wt%-U alloy. In order to provide additional conservatism because the HWR-NPR fuel will operate at a higher temperature than that in the test plates and because of the silicon addition in the 45%-wt%-U fuel tested, a limit of 2.4×10^{21} f/cm^3 is recommended for U-Al alloy dispersion fuel in the HWR-NPR. Based on preconceptual design information, such a limit is well beyond the peak fission density of 1.4×10^{21} f/cm^3 to be expected in the HWR-NPR (see Table VI).

Many more data have been found for the dispersion fuels because most of their development occurred during the 1960s and 1980s. The U_3O_8-Al dispersion fuel is the most complicated because of the extensive reaction of the U_3O_8 with the aluminum during fabrication and irradiation to form a number of reaction products, as discussed earlier in Section 4.1. Because substantial amounts of aluminum are consumed during these reactions, they result in a net negative volume change (e.g., see Ref. 25). This effectively adds to the already-high void fraction for U_3O_8 plates, increasing the accommodation for swelling, but at the same time significantly reducing the amount of matrix Al, as shown in Figs. 25-26, pp. 48-49, of Appendix B. Examinations of irradiated HFIR elements indicated that the extent of reaction was a function principally of irradiation temperature and not of burnup (see Fig. 27, p. 51, of Appendix B). Somewhat higher fuel meat temperatures and much longer irradiation times (compared to 21 days for a HFIR element) result in the almost complete reaction of the U_3O_8 seen in the tubes irradiated at SRS. The HWR-NPR fuel is expected to be operated under similar temperature and burnup conditions.

Immersion density techniques could not be used to determine swelling of the 15-ft-long U_3O_8-Al fuel tubes irradiated at SRS. However, thickness measurements are available for a number of sections of tubes containing from 18 to 59 wt% U_3O_8. As discussed in Section 4.3.1, pp. 53-58, of Appendix B, estimated corrections for cladding oxidation and for the thickness change/volume change bias have been applied to the thickness data to derive volumetric swelling values. The fuel meat swelling for these sections and for a number of U_3O_8-Al miniature fuel plates (miniplates) is plotted as a function of fuel meat fission density in Fig. 29, p. 57, of Appendix B. The data exhibit significant scatter because effects of as-fabricated void and fuel-matrix reaction have not been taken into account. The data for the SRS tubes appear to be consistent with previous miniplate data, however, and the swelling appears stable up to the 1.1×10^{21} f/cm^3 exposure* achieved in the central sections of the 59-wt%-U_3O_8 tubes and up to the 1.2×10^{21} f/cm^3 exposure achieved in the 42-wt%-U_3O_8 tubes. Although further work is needed to determine the proper way to account for voids and reactions and to justify the estimated corrections applied to the thickness change data, preliminary analysis of the data tends to confirm the stable nature of the swelling of the SRS tubes up to 1.1×10^{21} f/cm^3 (1.2×10^{21} f/cm^3) in fuel meat containing 59 wt% (42 wt%) U_3O_8.

Twenty-one fuel assemblies, consisting of three fuel tubes each which contained 62-wt%-U_3O_8 fuel meat, were subsequently irradiated at SRS as a demonstration of acceptable behavior of tubes produced under production-like conditions. Peak fission densities achieved were 1.4×10^{21}, 1.5×10^{21}, and 1.6×10^{21} f/cm^3 in the inner, middle,

---

*The fission densities quoted for SRS tubes are determined from measured assembly power production (flow and temperature change for each assembly), calculated tube power fractions, measured "typical" axial power shapes, and nominal tube fuel meat volumes. The assembly powers are believed to be accurate to ±1% and the axial power distribution to ±5%.

and outer tubes, respectively. The tubes were easily removed from their assemblies following irradiation, indicating that gross swelling or warping had not occurred, and underwater visual inspection revealed no anomalies.

A considerable number of swelling measurements have been reported for U_3O_8-Al dispersion fuel plates. Data from plates containing from 40 to 50 wt% (17 to 24 vol%) U_3O_8 irradiated in the ETR and HFIR to fission densities ranging from 1.2×10^{21} to 2.2×10^{21} f/cm^3 of fuel meat indicated stable swelling for the high-fired and the burned U_3O_8.[25] During the RERTR Program miniplates containing high-fired U_3O_8 at densities from 65 to 75 wt% (35 to 44 vol%) U_3O_8 were irradiated to fission densities ranging from 0.9×10^{21} to 2.8×10^{21} f/cm^3 of fuel meat. After achieving fission densities of ~2.5×10^{21} f/cm^3 or higher, several fuel plates containing 70 or 75 wt% U_3O_8 had experienced breakaway swelling. Microstructural examination of failed plates showed that U_3O_8-Al reactions had consumed virtually all of the matrix and that the meat had experienced severe cracking and separation. Apparently, the reaction products are not particularly strong; therefore, when little or no Al remains between the fuel-containing particles, fission gas pressure can cause cracks which easily propagate. Breakaway swelling was not encountered in the plates containing 65 wt% U_3O_8 even though they were irradiated to fission densities as high as 2.2×10^{21} f/cm^3 of meat. Based on these data the RERTR Program recommended a fission density limit of 1.8×10^{21} f/cm^3 of meat for highly loaded U_3O_8 dispersion fuels irradiated under conditions similar to those in the ORR.[58] Fuel meat temperatures of the U_3O_8 miniplates in the ORR are estimated to have ranged from 100 to 125°C for low-burnup plates to perhaps as low as 75°C for highly burned plates at the time when breakaway swelling occurred.

As discussed in the preceding paragraph, the presence of large amounts of fission gas in fuel meat where most of the aluminum matrix has been consumed by reaction with the U_3O_8 induces cracking and breakaway swelling of the meat. Complete reaction of the U_3O_8 in fuel meat containing at least 64 wt% U_3O_8 will result in virtual elimination of the matrix aluminum; therefore, one must expect breakaway swelling to occur if fission densities become high enough. As the U_3O_8 loading is reduced below 64 wt%, the amount of matrix aluminum remaining after complete reaction of the U_3O_8 will increase, and, at some loading, sufficient matrix will remain to inhibit large-scale propagation of cracks in the reacted fuel and, hence, breakaway swelling. Although no firm basis now exists for determining a U_3O_8 loading below which breakaway swelling will not occur, even for 100% ^{235}U burnup, some very simple, but preliminary, analyses indicate that such a loading might be in the range of 35 to 40 wt% U_3O_8. Thus, it is clear that breakaway swelling must be considered possible at some fission density for U_3O_8 loadings of interest for the HWR-NPR and, therefore, that a fission density limit must be established for the use of this fuel in the HWR-NPR.

In the absence of irradiation data to high fission densities for SRS U_3O_8 fuel tubes, the data discussed above for U_3O_8 miniplates will be used to estimate a limit for HWR-

NPR tubes. To do so one must consider differences between the as-fabricated tubes and the miniplates and differences in the irradiation conditions. The RERTR-type plates, for which the fission density limit was set, were fabricated using high-fired U_3O_8 whereas HWR-NPR tubes would be fabricated with a less-dense, low-fired oxide. However, the data obtained by Martin et al.[25] showed that the swelling was not strongly influenced by the type of U_3O_8 used. In any case, since breakaway swelling only occurs after reaction of the U_3O_8 and Al, one would not expect the initial characteristics of the U_3O_8 to be important. For the same reason, differences due to extrusion of tubes versus rolling of plates should not be important. Since external restraint of the fuel meat would most likely increase the fission gas pressure required to initiate breakaway swelling, one might expect the tubular geometry to offer an advantage over the flat-plate geometry. In the absence of measurements or mechanical analysis, however, one cannot claim credit for cladding restraint.

The only significant difference in irradiation conditions would appear to be the fuel meat temperature. The RERTR miniplates in the ORR were estimated to operate at peak temperatures in the 100 to 125°C range, and, since they had achieved high burnups, they were probably operating at temperatures perhaps as low as 75°C when breakaway swelling occurred. The HWR-NPR tubes, on the other hand, are likely to operate at more nearly constant temperatures (of the order of 175 to 200°C) during their entire residence in the reactor since the average power density in the reactor core will remain constant and large changes in the spatial power distribution are not anticipated. Since fission gas pressure is apparently the driving force for breakaway swelling, an increase in temperature would be expected to decrease the fission density limit (i.e., the total number of fission gas atoms allowed) according to the ideal gas law, assuming no other temperature effects. For example, a fission density limit of $(348/448)(1.8 \times 10^{21}) = 1.4 \times 10^{21}$ f/cm^3 is predicted for operation at 175°C. An increase in temperature may also decrease the strength of the reacted phases, but the magnitude of such an effect is expected to be negligible at these relatively low temperatures. This lower limit would have the same conservatism, i.e., margin to failure, as existed for the RERTR fuel (20 to 25%) if indeed the similarities and differences between the tubes and the miniplates are exactly as stated above.

Based on these arguments, the working group believes that a fission density limit for SRS U_3O_8 tubes of the order of 1.4×10^{21} f/cm^3 can ultimately be established. If it can be shown that the cylindrical cladding provides some external restraint to the swelling fuel, perhaps an even higher limit can be justified. Traditionally, fission density limits are set to provide a margin between the limit and the highest fission density attained in fuel demonstrated to have performed acceptably under operating conditions typical of the reactor in question. For example, the current fission density limit for the UAl_x-Al fuel used in the ATR was set after tests of miniplates in the ATR to ~20%-higher fission densities showed that the fuel was behaving stably with no evidence of incipient failure.

As discussed earlier, tube thickness measurements and metallography on one 59-wt%-U_3O_8 tube section irradiated at SRS to 1.1×10^{21} f/cm^3 indicate stable swelling. In addition, 63 tubes containing 62 wt% U_3O_8 were irradiated to peak fission densities ranging between 1.4×10^{21} and 1.6×10^{21} f/cm^3 with no evidence of excessive swelling during disassembly or visual inspection; however, no thickness measurements were made on these tubes. For SRS conditions no swelling data have been obtained for fission densities higher than 1.1×10^{21} f/cm^3 in fuel containing more than 42 wt% U_3O_8. Although the fuel apparently performs acceptably at 1.6×10^{21} f/cm^3, above the 1.4×10^{21} f/cm^3 limit derived on the basis of temperature considerations, there are no swelling or microstructural data from which to judge whether or not swelling had begun to accelerate at that exposure. Therefore, the working group believes that additional information, either swelling data at higher fission densities and/or more sophisticated and conclusive analyses of the existing data, must be obtained in order to confirm a 1.4×10^{21} f/cm^3 or higher limit. Until such additional information becomes available, a limit of 1.2×10^{21} f/cm^3, 25% below the highest fission densities attained under SRS conditions, is recommended for large-scale use of the fuel. However, the working group also is confident that the existing data are sufficient to allow any irradiations which might be needed to firmly establish an appropriate fission density limit for SRS U_3O_8 fuel. For consideration of U_3O_8 fuel during the design of the HWR-NPR, the working group is comfortable with a provisional limit of 1.4×10^{21} f/cm^3 until a firm limit can be established. Based on preconceptual design information, such a limit is coincident with the peak fission density expected in an HWR-NPR fuel assembly with type A geometry and is well above the peak fission density expected in a fuel assembly with type B geometry (see Table VI).

Dispersion fuels containing the intermetallic compounds UAl_x and U_3Si_2 are considerably simpler to analyze than the U_3O_8 dispersions because the effect of reactions is much smaller. In UAl_x dispersion fuel with an average composition close to that of UAl_3, transformation of the UAl_3 to UAl_4 results in a volume change of only a few tenths of a percent; however, the matrix volume fraction is reduced. So little reaction is seen in U_3Si_2 dispersion fuel that it can be neglected. It should be noted that transformation of the fuel phases undoubtedly would occur even in the absence of Al as the ^{235}U is burned. In highly enriched fuels burnup removes a large fraction of the total uranium. Fortunately, UAl_4 and USi (and probably U_3Si_5, also) show stable swelling under irradiation.

The irradiation testing of uranium silicide dispersion fuels is discussed in detail in Sections 5.1 and 5.2, pp. 23-44, of Appendix D1. Significant recent additions to the understanding of the swelling behavior of U_3Si_2 dispersion fuels are discussed in Appendices D2 and D3. The most important feature of U_3Si_2 is its ability to contain fission gases in small stable bubbles to very high fission densities (see Figs. 5-7, pp. 13-15, of Appendix D3). In contrast, U_3Si apparently becomes amorphous during the early stages of irradiation, which allows fission gas bubbles to grow rapidly if external restraint is not applied to the fuel particles, e.g., by using the U_3Si dispersion fuel in a rod rather than in a thin plate.[59] Since it is difficult to avoid the formation of some U_3Si during fabrication or irradiation due to inhomogeneities in the as-cast product, small regions of larger bubbles are frequently found in nominally pure U_3Si_2 fuel particles. However, these areas are small enough not to contribute significantly to the swelling. The changes in the microstructure of the meat as irradiation progresses are illustrated in Figs. 24-26, pp. 40-41, of Appendix D1. Complete closure of the as-fabricated porosity at high burnup is evident; the pores seen at 96% burnup are actually fission gas bubbles in U_3Si, as discussed above. No evidence of reaction with the matrix is seen except in the recoil zone surrounding the fuel particles, but the particle sizes have increased and the amount of matrix has decreased.

Swelling data for ANL U_3Si_2 miniplates irradiated in the ORR are listed in Table V, p. 28, of Appendix D1. Originally, fuel particle swelling was calculated assuming complete closure of the as-fabricated porosity, and the linear relationship (with slope 6.2 vol% fuel per 10^{21} f/cm^3) shown in Fig. 9, p. 30, of Appendix D1 was derived. A more careful analysis of the residual porosity at the end of irradiation (and discovery that a minus sign had been inadvertently dropped from the fuel meat swelling values for plates A125M and A126M at some stage of data transmittal) has led to a new interpretation of the swelling data. As shown in Fig. 3, p. 11, of Appendix D3, the swelling of U_3Si_2 now appears to depend on the fission rate. (Average fission rates during the first 60 days of irradiation in the LEU, MEU, and HEU plates were estimated to be $\sim 2 \times 10^{14}$, $\sim 3 \times 10^{14}$, and $\sim 7 \times 10^{14}$ fissions/s per cm^3 of fuel particle, respectively.) Until bubbles of ~0.05-µm diameter begin to form, the fuel particle swelling rate is ~3 vol% per 10^{21} f/cm^3; then it quickly changes to ~10 vol% per 10^{21} f/cm^3. In both regimes the swelling appears to be approximately a linear function of the fission density up to the fission densities achieved during the tests.

The peak power density of 2900 W/cm^3 of fuel meat anticipated for the HWR-NPR (see Table III) in a 30%-enriched, 30-vol% U_3Si_2 fuel assembly corresponds to $\sim 3 \times 10^{14}$ fissions/s per cm^3 of fuel particle. Therefore, 30%-enriched fuel particles in an HWR-NPR assembly might be expected to swell at the lower rate until the fission density in the meat reaches $\sim 1.2 \times 10^{21}$ f/cm^3 (30% of 4.0×10^{21}) and then at the higher rate until discharge. At the point of peak burnup (see Table VI), corresponding to $\sim 1.4 \times 10^{21}$ f/cm^3 of fuel meat (4.7×10^{21} f/cm^3 of fuel particle), U_3Si_2 particle swelling of ~19% would be predicted. This corresponds to ~6% of the volume of the fuel meat. However, since the ~4% as-fabricated porosity would be expected to accommodate at least one-half of this swelling, net swelling of only a few percent would be predicted in the region of peak burnup. Should U_3Si_2 dispersion fuel be used at higher enrichments, with increased fission rates in the fuel particles, the onset of the higher rate of swelling would be further delayed.

The swelling data discussed above were obtained from plates irradiated at temperatures of 125°C or lower; however, long-term (hundreds of hours) high-temperature (400 to 450°C) anneals of U_3Si_2 miniplates produced no swelling or microstructural changes. Although these out-of-reactor data may not be directly applicable to fuel under irradiation at high temperatures, the extreme postirradiation stability of the U_3Si_2-Al fuel at elevated temperatures gives high confidence that the stable performance of the fuel at ~100°C will be maintained at HWR-NPR temperatures.

The results of the miniplate tests discussed above were confirmed for production fuel elements during a whole-core demonstration of 19.8%-enriched U_3Si_2-Al fuel in the ORR. Sixty-eight 4.8-g U/cm^3 elements were irradiated to average burnups ranging from 5 and 52%, and eight 3.5-g U/cm^3 fuel followers were irradiated to average burnups ranging between 10 and 75%. Postirradiation examinations were performed on six of the ~50%-burnup elements and on one 75%-burnup follower. At a peak fission density of $\sim 1.5 \times 10^{21}$ f/cm^3, reached both in the elements and in the follower, the swelling and microstructural characteristics of the meat were found to be consistent with the miniplate and test element results summarized in Appendix D1.[3]

As indicated in Table XI and by the preceding discussion, fission densities as high as 2.4×10^{21} f/cm^3 have been attained in 40%-enriched, 3.95 g U/cm^3 U_3Si_2 miniplates with no indication of unstable swelling. In order to provide additional conservatism because of the higher-temperature operation of the HWR-NPR fuel than of the test plates, a limit of 2.0×10^{21} f/cm^3 is recommended for U_3Si_2 dispersion fuel in the HWR-NPR until experience under more typical conditions is available. Based on preconceptual design information, such a limit is well beyond the peak fission density of 1.4×10^{21} f/cm^3 to be expected in the HWR-NPR (see Table VI).

There are many similarities between the behavior of the U_3Si_2 and UAl_x dispersion fuels, and the understanding of dispersion fuel swelling gained during the RERTR Program can be applied to the UAl_x data from the 1960s. Most of the development work on UAl_x dispersions in the U.S. was directly related to its use in the ATR, and, as a result, many of the irradiation test plates contained B_4C dispersed in the fuel meat as a burnable poison. As discussed in Appendix D2, it has been found that He gas produced by the $^{10}B(n,\alpha)$ reaction prevents the closure of the as-fabricated porosity during irradiation and, consequently, results in higher fuel meat swelling than if no He were present. Therefore, as for the U_3Si_2 dispersion swelling data discussed above, the residual as-fabricated porosity must be determined if the fuel particle swelling is to be determined.

Uranium aluminide fuel particles, specifically UAl_4 and UAl_3, appear to be more stable than any other fuel compound tested for use in an aluminum-matrix dispersion system. No report of unstable swelling of UAl_x dispersion fuel was found in the literature. It appears that fission gas is accommodated in the fuel particles (principally UAl_4

Table XI. Summary of Swelling and Blister Threshold Temperature Data for Dispersion Fuels Irradiated in the MTR, ETR, HFIR, FR 2, ATR, ORR, JMTR, and FRJ-2 (from PIE of Miniature Fuel Plates).

Fuel Type	Uranium Density, g/cm^3		U Enr.[a]	No. of Plates	Irrad. Temp., °C	Fission Density, 10^{21}/cm^3		Meat Swelling, % $\Delta V/V_m$		Blister Threshold Temp., °C	References
	Low	High				Low	High	Low	High		
UAl_x[b]	0.98	1.04	H	4	100-210	0.4	1.8	-1.8	4.7	565->600	60,61
UAl_x[b]	1.17	1.20	H	7	110-250	0.3	1.5	-2.5	4.4	—	62
UAl_x[b]	1.22	1.35	H	32	88-290	0.3	2.4	-2.4	7.4	440-590	60,61,63
UAl_x[b]	1.41	1.48	H	8	130-200	0.5	2.1	-4.2	2.5	450-540	60,63
UAl_x[b]	1.64	1.65	H	2	150-200	2.5	2.7	2.0	4.7	565	61
UAl_x[b]	1.97	1.99	H	3	120	1.0	1.7	4.3	5.4	470-530	19
UAl_x	1.33	1.42	H	7	80-165	1.6	2.0	4.8	8.8	—	64
UAl_x	1.38	1.38	H	11	70-180	0.6	2.2	2.0	21.0	—	17
UAl_x	1.57	1.82	H	7	85-170	0.9	2.2	1.2	6.1	600	60,64
UAl_x	2.22	2.26	H	2	150-170	1.3	2.4	-1.9	1.1	430-600[c]	60
UAl_x	1.47	1.47	M	1	75-125	1.3	1.3	4.3	4.3	—	65
UAl_x	1.88	1.95	M	4	75-125	1.1	1.5	-0.3	0.6	550-565	66,U[d]
UAl_x	2.13	2.31	M	6	75-125	1.3	1.8	1.9	3.4	550-561	66,67,U
UAl_x	1.88	1.99	L	3	75-125	0.8	0.9	0.7	2.9	>550	66,U
UAl_x	2.14	2.33	L[e]	6	75-125	1.0	1.1	-1.7	4.0	≥550	65,66,67,U
UAl_x	2.48	2.52	L	2	75-125	1.1	1.1	-3.9	-3.3	550	65
U_3O_8	0.71	0.71	H	1	75-125	1.1	1.1	3.3	3.3	—	68
U_3O_8	1.22	1.41	H	9	80	0.3	1.8	-2.2	6.2	—	62,64
U_3O_8	1.52	1.89	H	12	80	1.3	2.2	-1.4	7.6	—	64
U_3O_8	2.34	2.46	M	5	75-130	1.7	2.0	2.9	13.8	470	67,68,69,U
U_3O_8	2.77	2.77	M	1	75-125	2.3	2.3	P[f]	P[f]	—	68,U
U_3O_8	3.10	3.10	M	3	75-125	2.1	2.5	11.2	P[f]	—	68,U

Table XI. (Continued)

Fuel Type	Uranium Density, g/cm^3		U Enr.	No. of Plates	Irrad. Temp., °C	Fission Density, 10^{21}/cm^3		Meat Swelling, % $\Delta V/V_m$		Blister Threshold Temp., °C	References
	Low	High				Low	High	Low	High		
U_3O_8	2.30	2.48	L[e]	9	75-125	0.8	1.1	0.0	2.0	490->550	65,67,68,U
U_3O_8	2.76	2.79	L	11	75-125	0.9	1.2	-0.7	1.3	>550	68
U_3O_8	2.91	3.13	L[e]	16	75-125	1.0	1.6	-3.8	12.6	478-550	18,65,67,68,U
U_3O_8	3.49	3.58	L	3	75-125	1.5	1.5	-5.4	-3.4	450	18
U_3Si_2	1.30	1.34	H	3	110-130	1.1	1.3	4.4	6.6	-	62
U_3Si_2	1.66	1.66	H	2	75-125	1.4	2.1	4.9	11.6	-	U
U_3Si_2	3.94	3.95	M	2	75-125	1.5	2.4	0.7	10.6	-	U
U_3Si_2	4.95	4.95	M	1	75-125	1.4	1.4	~0	~0	-	U
U_3Si_2	5.13	5.18	M	2	75-125	1.6	1.6	-2.1	-1.1	-	U
U_3Si_2	3.72	3.76	L	4	75-125	1.6	1.7	3.7	7.0	530	U
U_3Si_2	4.75	4.88	L	12	75-130	0.7	1.9	-0.2	8.0	529-550	69,70,71,72
U_3Si_2	4.92	4.99	L	4	75-125	1.2	1.3	0.2	0.8	-	U
U_3Si_2	5.04	5.30	L	10	75-130	0.6	2.3	-0.7	5.3	525-550	69,70,72,U
U_3Si_2	5.10	5.13	L	4	75-125	1.5	2.3	3.7	9.6	425	U, App. D2
U_3Si_2	5.60	5.67	L	7	75-125	2.2	2.5	0.1	2.7	515	U

[a] Enrichment: H = ~93%; M = 40 to 45%; L = ~19.8%, except as indicated in note e.

[b] Contains B_4C dispersed in fuel meat.

[c] Higher burnup plate split open at 430°C.

[d] U indicates unpublished RERTR Program data.

[e] One or more plates enriched to 27% included in group.

[f] Indicates that plates "pillowed" during irradiation.

due to transformation of any UAl_3 by reactions with Al or by U depletion) in solution or in very small (<0.01-μm-diam) bubbles. However, fission gas bubbles have been found to be associated with uranium oxide inclusions in UAl_x particles.[73] In addition, there is strong evidence that fission gases are retained in the fuel particle and do not diffuse into the matrix to any extent. Of course, some fission gases undoubtedly reach the region adjacent to fuel particles by recoil and by being released during reactions with the Al. Since no evidence has been found that fuel particle size affects the swelling of UAl_x fuel meat, it is concluded that the small bubbles seen in the recoil zones do not contribute significantly to the meat swelling.

The irradiation behavior of UAl_x dispersion fuel is discussed in Section 4.2.2, pp. 50-58, of Appendix C, where the emphasis is on ATR-type fuel, which contains B_4C in the meat. Swelling data for non-B_4C-containing fuel plates found in Refs. 17, 25, and 60 are summarized in Table XI. Hofman has analyzed those data for which estimates of the residual porosity could be made from photomicrographs, and the results are shown in Fig. 14. Although there is considerably more spread in the data than for the U_3Si_2 fuel, one might interpret the data as showing the same type of dependence on fission rate as do the U_3Si_2 data. Data for B_4C-containing UAl_x dispersion fuels are listed in Table 16, p. 52, and Fig. 17, p. 53, of Appendix C and are summarized, along with additional data, in Table XI. It is interesting to note that two of the data points lying well below the fit were from plates (169-4 and 169-5) with low initial B_4C content. The fit shown indicates that, on the average, the as-fabricated porosity was not effective in accommodating swelling. However, as stated before, the presence of B_4C most likely has kept the pores from closing to any great extent. There has been extensive operating experience in the ATR with 1.6-g U/cm^3 UAl_x-Al fuel up to a fission density of 2.3×10^{21} f/cm^3 at temperatures similar to those anticipated for the HWR-NPR.

Based upon the stable swelling exhibited by ATR-type UAl_x dispersions at fission densities as high as 2.9×10^{21} f/cm^3 under temperature conditions typical of those expected in the HWR-NPR, a fission density limit of 2.6×10^{21} f/cm^3 is recommended for UAl_x dispersion fuel used under HWR-NPR conditions. Based on preconceptual design information, such a limit is well beyond the peak fission density of 1.4×10^{21} f/cm^3 to be expected in the HWR-NPR (see Table VI).

In summary, the U-Al alloy fuel and the UAl_x and U_3Si_2 dispersion fuels show similar microstructural and swelling characteristics. For each of these fuels the swelling appears to increase linearly with fission density up to the highest exposures achieved thus far. Although there is no evidence that a fission density limit would be required for any of these fuels, a conservative limit 10 to 20% below the highest recorded fission density, depending on temperature conditions of the test irradiations, has been recommended for use of these fuels in the HWR-NPR, namely, 2.4×10^{21}, 2.6×10^{21}, and 2.0×10^{21} f/cm^3 for U-Al alloy, UAl_x, and U_3Si_2, respectively. The U_3O_8 dispersion fuel, however, is believed to be vulnerable to breakaway swelling at some fission density for

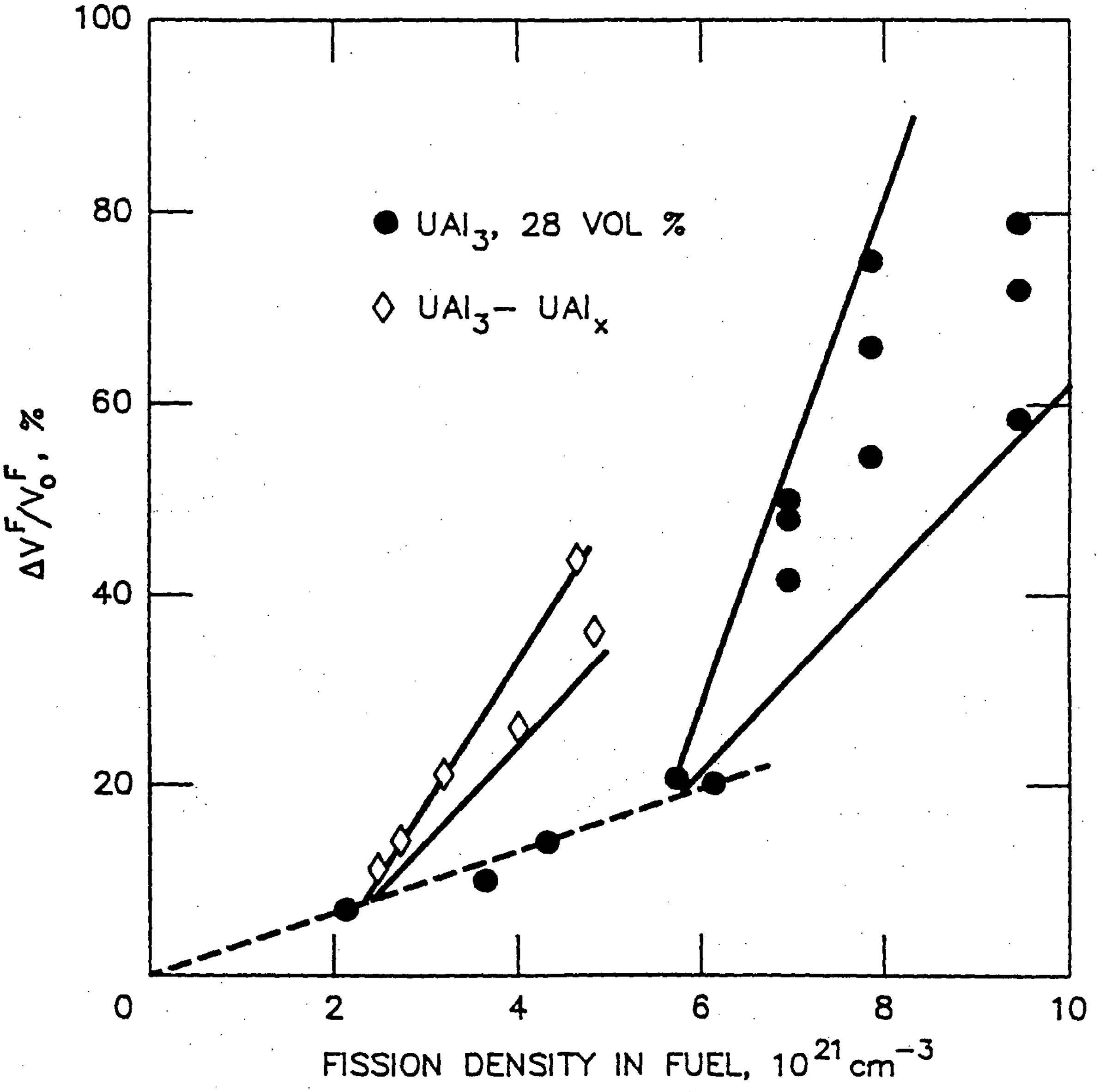

Fig. 14. Swelling of UAl_x Fuel Particles as a Function of Fission Density in the Particle.

U_3O_8 loadings of interest for the HWR-NPR. In the absence of additional data and/or analysis of existing data, a limit of 1.2 × 10^{21} f/cm^3 is recommended. Based on simple analyses of the existing U_3O_8 swelling data, though, a provisional limit of 1.4 × 10^{21} f/cm^3, which is believed to have high probability of being confirmed, is recommended for design considerations. The limits recommended for use during design are at or above the peak fission density which might be expected in the HWR-NPR, based on preconceptual design studies.

5.2 Blistering

Blisters on the surface of a fuel tube or plate occur when gases, from fission or other sources, collect at the meat-cladding interface with a pressure great enough to raise locally the cladding away from the fuel meat. Typically, blisters are from 1 to 5 mm in extent; however, in some cases they may cover a much larger area. Although used in a seemingly interchangeable manner in the literature, in this report blistering refers to a separation at the meat-cladding interface and breakaway swelling refers to a separation in the fuel meat. Blistering occurs at elevated temperatures, where the cladding has lost much of its strength. If a fuel tube were to blister during operation, transfer of heat from the fuel meat to the coolant might be severely disrupted, especially if the thermal conductivity of the meat were low. As will be discussed in Section 7, there is also the possibility that a small amount of fission gas might be released.

The resistance of a fuel tube or plate to blistering is established by measuring the blister threshold temperature, or the temperature in a series of sequential anneals at which the tube or plate first blisters. In the typical blister test the sample is held at temperature for 30 to 60 min during each annealing step. The blister temperature undoubtedly is a function of the time-temperature history of the sample during the test. For example, the 25-wt% alloy which was reported in Section 4.3, pp. 36-40, of Appendix A to have blistered after 5 h at 550°C would probably have exhibited a higher blister threshold temperature in the standard blister test because the total time at temperature would have been less. The blister threshold temperature provides an indication of the ability of the fuel to withstand short periods (of the order of an hour) of operation at high temperature without failure.

No blister threshold temperature data (based on the standard test) were found for U-Al alloy fuel. The emphasis in postirradiation testing appeared to be on long-term annealing tests, as discussed in Section 5.1. Based on that discussion, breakaway swelling rather than conventional blistering appears to be the likely failure mode during high-temperature irradiation.

Uranium aluminide dispersion fuel with no B_4C in the meat typically exhibits blister temperatures of 550°C or higher. In many cases blistering is preceded by cracking of the matrix, especially when B_4C poison is present. The He gas from the $^{10}B(n,\alpha)$ reaction provides enough additional pressure to decrease the blister temperature by 50 to 100°C. Blister temperatures for fuel plates and elements with typical ATR fuel meat compositions are listed in Table 17, p. 60, and Fig. 20, p. 61, of Appendix C. The quadratic fit shown in Fig. 20 must not be used outside the range of the data. Blister temperatures for UAl_x miniplates are summarized in Table XI.

Blistering of U_3O_8 dispersion fuel tubes or plates is typically preceded by cracking of the fuel (reaction-product) particles. Blister temperatures for U_3O_8-Al fuel tubes irradiated at SRS are shown in Fig. 30, p. 60, of Appendix B. They range from ~400 to ~600°C, which is in agreement with data for miniplates summarized in Table XI and for HFIR elements.[74] The presence of B_4C poison in the aluminum filler portion of the fuel meat of plates in the outer HFIR element results in the lowering of the blister threshold temperature by from 100 to 200°C. Both Richt et al.[74] (for U_3O_8 dispersion fuel) and Dienst et al.[17] (for UAl_x dispersion fuel) noted that the higher the irradiation temperature, the more blister resistant the fuel. Apparently, the higher irradiation temperatures allow the fuel-matrix reaction to occur more completely during irradiation. Consequently, a smaller amount of reaction, which releases fission gases, occurs during the blister test. It is interesting to note that highly loaded U_3O_8 plates irradiated during the RERTR Program exhibited consistently higher blister threshold temperatures than those measured during previous development programs. Perhaps the explanation lies in accelerated reaction due to an elevated irradiation temperature resulting from the low thermal conductivity of the highly loaded meat, as discussed above.

Blisters on fuel tubes and plates containing U-Al alloy, UAl_x dispersion, or U_3O_8 dispersion fuel meat have been found to result predominantly from fission gas or He coming from the interior of the fuel meat. Another type of blistering is most prevalent for U_3Si_2 dispersion fuels. For these fuels blisters tend to form first at the periphery of the fuel meat. Micrographic investigation has shown that these blisters are associated with oxidized fuel. These fuel particles, which oxidized before or during plate rolling, produce a nonbonded area and apparently break up under the pressure of fission gas at high temperatures and release the fission gas to form the blister. Similar blisters caused by oxidized fuel particles have been found outside the fuel zone of UAl_x dispersion fuel plates irradiated during the RERTR Program. Blister temperatures are typically in the 525 to >550°C range for U_3Si_2 dispersion fuels without B_4C in the fuel meat. As for the UAl_x and U_3O_8 dispersion fuels, the presence of B_4C in the U_3Si_2 fuel meat resulted in a reduction of the blister threshold temperature by ~100°C.

In summary, the data from many tests indicate that the intermetallic dispersion fuels (UAl_x and U_3Si_2) with no B_4C in the meat tend to blister at temperatures around 550°C. Blister temperatures for U_3O_8 dispersion fuel tend to be of the order of 100°C lower. The addition of B_4C to the fuel meat of any dispersion fuel results in the lowering of the blister temperature of that fuel by ~100°C. No conventional blister temperature data were found for U-Al alloy fuel since breakaway swelling appears to be the high-temperature failure mode.

6. BEHAVIOR UNDER ACCIDENT CONDITIONS

As stated in the introduction, a database for fuel behavior under severe accident conditions is being developed at ANL under another task. However, some pertinent information has been found during the literature searches performed for the present study. The references and the type of information available are noted below with no comment.

A summary of transient tests on fuel typical of that used in the SRS reactors is found in Section 5.2, pp. 41-45, of Appendix A. Effects on the fuel of destructive tests in the SPERT I reactor for a plate-type U-Al alloy core are described in Ref. 75. The fuel plate damage that occurred in the SPERT I tests was compared to that experienced in the SL-1 accident, the Borax I tests, and a fuel melting incident in the Westinghouse Test Reactor (WTR). The results of a detailed metallurgical examination of temperature transition zones in an MTR U-Al alloy fuel element which experienced extensive melting due to flow channel blockage are reported in Ref. 42. The results of tests of sections of a HFIR (U_3O_8 dispersion) fuel plate in TREAT are summarized in Section 5.2, p. 63,, of Appendix B.

No data exist for the behavior of U_3Si_2 dispersion fuel under transient melting conditions.

7. FISSION PRODUCT RELEASE

An excellent summary of the information available before 1982 on fission product release from research and test reactor fuels, both from out-of-reactor experiments and from reactor accidents, is contained in Ref. 37. Brief summaries of results of more recent experiments on U-Al alloy and U_3O_8 dispersion fuel samples, carried out at the Hanford Engineering Development Laboratory (HEDL) for SRS,[76,77] are given in Section 6, pp. 46-48, of Appendix A and in Section 6, pp. 63-64, of Appendix B. The U-Al alloy samples originally contained 33.6 wt% U, and the U_3O_8 samples originally contained 28.7 wt% U (34.0 wt% U_3O_8). The burnup of the samples was ~52%. The release fraction data for ^{129}I and ^{137}Cs are tabulated as functions of temperature and atmosphere in Tables XII and XIII. Krypton releases were also measured, but there is considerable scatter in the data and the calculated Kr inventory values apparently are low; therefore, these data have not been reproduced here. The author of the HEDL reports states that it is likely that the Kr release is total for Cs releases above 15 to 20%.

REFERENCES

1. J. E. Matos, J. R. Deen, and R. J. Cornella, "Fuel Selection Support Study/Neutronics," Argonne National Laboratory Report ANL/NPR-90/001 (October 1989).

2. A. Travelli, "The RERTR Program: A Progress Report," Proc. 1986 Int. Mtg. on Reduced Enrichment for Research and Test Reactors, Gatlinburg, Tennessee, November 3-6, 1986, Argonne National Laboratory Report ANL/RERTR/TM-9 (CONF-861185), pp. 3-12 (May 1988).

3. J. L. Snelgrove, G. L. Copeland, and G. L. Hofman, "Postirradiation Examination of Fuel Elements from the ORR Demonstration," in *Proc. XIIth Int. Mtg. on Reduced Enrichment for Research and Test Reactors, Berlin, 10-14 September 1989*, G. Thamm and M. Brandt, Eds., Konferenzen des Forschungszentrums Jülich, Band 4, Forschungszentrum Jülich GmbH, Jülich, Germany, pp. 151-160 (1991).

4. U.S. Nuclear Regulatory Commission, "Safety Evaluation Report Related to the Evaluation of Low-Enriched Uranium Silicide-Aluminum Dispersion Fuel for Use in Non-Power Reactors," U.S. Nuclear Regulatory Commission Report NUREG-1313 (July 1988).

5. C. D. West, "Overview of the ANS Project," Trans. Am. Nucl. Soc. **57**, 288-289 (October 1988).

6. W. C. Thurber, and R. J. Beaver, "Dispersion of Uranium Carbides in Aluminum Plate-Type Research Reactor Fuel Elements," Oak Ridge National Laboratory Report ORNL-2618 (November 5, 1959).

7. W. C. Francis, Ed., "Annual Progress Report on Reactor Fuels and Materials Development for FY 1965," Phillips Petroleum Company-Atomic Energy Division Report IDO-17154 (February 1966).

8. H. E. Hootman, Westinghouse Savannah River Company, personal communication (January 1990).

9. J. R. Deen, personal communication (March 1990).

10. B. S. Borie, "Crystal Structure of UAl_4," J. of Metals (Trans. AIME) **3**, 800-802, (1951).

11. O. J. C. Runnalls and R. R. Boucher, "Transformations in UAl_4 and $PuAl_4$," Trans. of the Metallurgical Society of AIME **233**, 1726-1732, (September 1965).

12. G. W. Gibson, "The Development of Powdered Uranium-Aluminide Compounds for Use as Nuclear Reactor Fuels," Idaho Nuclear Corporation Report IN-1133 (December 1967).

13. R. Boucher, "Études des Alliages Aluminum-Uranium Application à la Transformation à l'État Solide $UAl_3 \rightarrow UAl_4$, J. Nucl. Mater. **1**, 13-27 (1959).

14. L. R. Aronin and J. L. Klein, "Use of a Density (Specific Volume) Method as a Sensitive Absolute Measure of Alloy Composition, and Its Application to the Aluminum-Uranium System," Nuclear Metals, Inc., Report NMI-1118 (October 29, 1954).

15. T. I. Jones, I. J. McGee, and L. R. Norlock, "Some Properties of Aluminum-Uranium Alloys in the Cast, Rolled and Annealed Conditions," Atomic Energy of Canada Limited Report AECL-1215 (June 1960).

16. T. I. Jones, K. N. Street, J. A. Scoberg, and J. Baird, "Relation Between Microstructure and Thermal Conductivity in Aluminum-Uranium Alloys," Canadian Metallurgical Quarterly **2** (No. 1), 53-72 (January-March 1963).

17. W. Dienst, S. Nazaré, and F. Thümmler, "Irradiation Behaviour of UAl_x-Al Dispersion Fuels for Thermal High Flux Reactors," J. Nucl. Mater. **64**, 1-13 (1977).

18. J. Gómez, R. Morando, E. E. Pérez, D. R. Giorsetti, G. L. Copeland, G. L. Hofman, and J. L. Snelgrove, "Postirradiation Examination of High-U-Loaded Low-Enriched U_3O_8, UAl_2, and U_3Si Test Fuel Plates," Proc. 1984 Int. Mtg. on Reduced Enrichment for Research and Test Reactors, Argonne, Illinois, October 15-18, 1984, Argonne National Laboratory Report ANL/RERTR/TM-6 (CONF 8410173), pp. 86-104 (July 1985).

19. L. G. Miller and J. M. Beeston, "Extended Life Aluminide Fuel Final Report," EG&G Idaho, Inc., Report EGG-2441 (June 1986).

20. M. H. Rand and O. Kubaschewski, *Thermochemical Properties of Uranium Compounds*, Oliver and Boyd, London (1963), as quoted in Ref. 22.

21. F. Thümmler, H. E. Lilienthal, and S. Nazaré, "UAl_2-Al Instead of UAl_3-Al in Fuel-Element Plates for Advanced Test-Reactors," Powder Metallurgy **12**, (No. 23), 1-22 (1969).

22. J. L. Gregg, R. S. Crouse, and W. J. Werner, "Swelling of UAl_3-Al Compacts," Oak Ridge National Laboratory Report ORNL-4056 (January 1967).

23. G. L. Hofman, G. L. Copeland, and J. E. Sanecki, "Microscopic Investigation into the Irradiation Behavior of U_3O_8-Al Dispersion Fuel," Nucl. Tech. **72**, 338-344 (March 1986).

24. H. B. Peacock, "Technical Review of the U-Al Casting and U_3O_8-Al Powder Metallurgy Core Manufacturing Processes," I. E. du Pont de Nemours and Company Report DPST-82-537 (May 24, 1982).

25. M. M. Martin, A. E. Richt, and W. R. Martin, "Irradiation Behavior of Aluminum-Base Dispersion Fuels," Oak Ridge National Laboratory Report ORNL-4856 (May 1973).

26. G. L. Copeland and M. M. Martin, "Development of High-Uranium-Loaded U_3O_8-Al Fuel Plates," Nucl. Tech. **56**, 547-552 (1982).

27. O. Kubaschewski, E. L. Evans, and C. B. Alcock, *Metallurgical Thermochemistry*, Pergamon Press, Oxford, pp. 205-209 (1967).

28. P. Chiotti and J. A. Kateley, "Thermodynamic Properties of Uranium-Aluminum Alloys," J. Nucl. Mater. 32, 135-145 (1969).

29. J. K. Fink, R. Simms, and B. A. Brock, "Material Properties for HWR-NPR Severe Accident Studies," Argonne National Laboratory Report ANL/NPR-90/005 (March 1990).

30. M. W. Chase, Jr., C. A. Davies, J. R. Downey, Jr., D. J. Fruip, R. A. McDonald, and A. N. Syverud, *JANAF Thermochemical Tables*, Third Ed., American Institute of Physics, New York (1986).

31. F. L. Oetting, M. H. Rand, and R. J. Ackermann, *The Chemical Thermodynamics of Actinide Elements and Compounds: Part 1, The Actinide Elements*, pp. 14-20, 45, 74-81, International Atomic Energy Agency, Vienna (1976).

32. I. Barin, O Knacke, and O. Kubaschewski, *Thermochemical Properties of Inorganic Substances, Supplement*, Springer-Verlag, Heidelberg (1977).

33. I. Baron and O. Knacke, *Thermochemical Properties of Inorganic Substances*, Springer-Verlag, Heidelberg (1973).

34. R. K. Williams, R. S. Graves, R. F. Domagala, and T. C. Wiencek, "Thermal Conductivities of U_3Si and U_3Si_2-Al Dispersion Fuels," in *Thermal Conductivity*, Vol 19, D. W. Yarbrough, Ed., Plenum Publishing Corporation, pp. 271-278 (1988).

35. J. L. Bates, "Thermal Diffusivity of MTR-ETR Type Fuel Plates," Battelle Northwest Laboratory Report BNWL-CC-456 (1966), as analyzed by R. R. Hobbins, EG&G Idaho, Inc., unpublished information (1973).

36. D. L. McElroy, Oak Ridge National Laboratory, unpublished information (1971).

37. D. Stahl, "Fuels for Research and Test Reactors, Status Review: July 1982," Argonne National Laboratory Report ANL-83-5 (December 1982).

38. S. Nazaré, G. Ondracek, and F. Thümmler, "Investigations on UAl_x-Al Dispersion Fuels for High-Flux Reactors," J. Nucl. Mater. **56**, 251-259 (1975).

39. G. W. Gibson and O. K. Shupe, "Annual Progress Report on Fuel Element Development for FY 1961," Phillips Petroleum Company-Atomic Energy Division Report IDO-16727 (March 9, 1962).

40. W. R. Martin and J. R. Weir, "Mechanical Properties of X8001 and 6061 Aluminum Alloys and Aluminum-Base Fuel Dispersion at Elevated Temperatures," Oak Ridge National Laboratory Report ORNL-3557 (February 1964).

41. G. W. Gibson and W. C. Francis, "Annual Progress Report on Fuel Element Development for FY 1962," Phillips Petroleum Company-Atomic Energy Division Report IDO-16799 (August 15, 1962).

42. G. W. Gibson, M. J. Graber, and W. C. Francis, "Annual Progress Report on Fuel Element Development for FY 1963," Phillips Petroleum Company-Atomic Energy Division Report IDO-16934 (November 25, 1963).

43. G. O. Hayner and J. O. Dittmer, "A Comparison of the Compressive Yield Strengths of Irradiated and Unirradiated Standard ETR Fuel Plates at Various Temperatures," in *Reactor Engineering Branch Annual Report—Fiscal Year 1969*, E. D. Covington, Ed., Idaho Nuclear Corporation Report IN-1335, pp. 69-72 (November 1969).

44. J. O. Dittmer, "A Study of the Compressive Properties of Aluminum Clad Composite Nuclear Reactor Fuel Plates," M.S. Thesis, Idaho State University, 1969, unpublished.

45. M. J. Graber, W. F. Zelezny, and G. W. Gibson, "Annual Progress Report on Reactor Fuels and Materials Development for FY 1964," Phillips Petroleum Company-Atomic Energy Division Report IDO-17037, pp. 16-20 (November 1964).

46. J. D. Fleming and J. W. Johnson, "Aluminum-U_3O_8 Exothermic Reactions," Nucleonics **2** (No. 5), 84-87 (May 1963).

47. H. B. Peacock, "Study of the U_3O_8-Al Thermite Reaction and Strength of Reactor Fuel Tubes," E. I. du Pont de Nemours & Company Report DP-1665 (August 1983).

48. A. E. Pasto, G. L. Copeland, and M. M. Martin, "Quantitative Differential Thermal Analysis Study of the U_3O_8-Al Thermite Reaction," Ceramic Bulletin **61**, No. 4, 491-496 (1982).

49. J. E. Marra and H. B. Peacock, "Reactions During the Processing of U_3O_8-Al Cermet Fuels," Westinghouse Savannah River Company Report DP-1776 (January 1990).

50. E. A. Aitken, personal communication (February 26, 1990).

51. G. V. Samsonov, Ed., *The Oxide Handbook*, 2nd Ed., IFI/Plenum Data Company, New York, pp. 72, 401 (1982).

52. D. Okrent, personal communication (February 20, 1990).

53. D. A. Powers, Sandia National Laboratories, unpublished information presented at SRS (July 1987).

54. L. W. Gray, "Unexpected Meltdown of Scrap Uranium-Aluminum Cermet Cores During Outgassing," Nuclear Safety **15**, 455-460 (1974).

55. L. W. Gray and H. B. Peacock, "A Differential Thermal Analysis Study of the Effect of Tramp Impurities on the Exothermic U_3O_8-Al Reactions," E. I. du Pont de Nemours & Company Report DP-1770 (December 1989).

56. W. Krug, E. Groos, J. Seferiadis, and G. Thamm, "Final Results of Test-Irradiations with LEU-Plates at KFA Jülich," Proc. 1988 Int. Mtg. on Reduced Enrichment for Research and Test Reactors, San Diego, California, September 19-22, 1988, Argonne National Laboratory Report ANL/RERTR/TM-13 (CONF-8809221), pp. 155-181 (June 1993).

57. J. M. Beeston, L. G. Miller, K. R. Brown, and D. M. McGinty, "ELAF Failed Fuel Plate Examination," EG&G Idaho, Inc., Informal Report EGG-SE-6696 (October 1984).

58. J. L. Snelgrove, "Qualification Status of LEU Fuels," Proc. 1987 Int. Mtg. on Reduced Enrichment for Research and Test Reactors, Buenos Aires, Argentina, September 28-October 1, 1987, Comisión Nacional de Energía Atómica, Buenos Aires, pp. 195-203 (September 1990).

59. D. F. Sears, L. N. Herbert, and K. D. Vaillancourt, "Status of LEU Fuel Development and Conversion of NRU," in *Proc. XIIth Int. Mtg. on Reduced Enrichment for Research and Test Reactors, Berlin, 10-14 September 1989*, G. Thamm and M. Brandt, Eds., Konferenzen des Forschungszentrums Jülich, Band 4, Forschungszentrum Jülich GmbH, Jülich, Germany, pp. 161-174 (1991).

60. M. F. Marchbanks in *Metallurgy and Materials Science Branch Annual Report Fiscal Year 1970*, W. C. Francis, Ed., Idaho Nuclear Corporation Report IN-1437, pp. 38-53, 62-66 (November 1970).

61. J. M. Beeston, R. R. Hobbins, G. W. Gibson, and W. C. Francis, "Development and Irradiation Performance of Uranium Aluminide Fuels in Test Reactors," Nucl. Tech. **49**, 136-149 (1980).

62. W. C. Francis and R. A. Moen, Eds., "Annual Progress Report on Reactor Fuels and Materials Development for FY 1966," Phillips Petroleum Company-Atomic Energy Division Report IDO-17218 (November 1966).

63. V. A. Walker, M. J. Graber, G. W. Gibson, "ATR Fuel Materials Development Irradiation Results, Part II," Phillips Petroleum Company-Atomic Energy Division Report IDO-17157 (June 1966).

64. M. M. Martin, A. E. Richt, and W. R. Martin, "Irradiation Behavior of Aluminum-Base Dispersion Fuels," Oak Ridge National Laboratory Report ORNL-4856 (May 1973).

65. E. Pérez, C. Kohut, D. Giorsetti, G. Copeland, and J. Snelgrove, "Irradiation Performance on CNEA UAl_x and U_3O_8 Miniplates," Proc. Int. Mtg. on Reduced Enrichment for Research and Test Reactors, 24-27 October 1983, Tokai, Japan, Japan Atomic Energy Research Institute Report JAERI-M 84-073, pp. 67-76 (May 1984.)

66. J. L. Snelgrove, R. F. Domagala, T. C. Wiencek, and G. L. Copeland, "Fuel Development Activities of the U.S. RERTR Program," Proc. Int. Mtg. on Reduced Enrichment for Research and Test Reactors, 24-27 October 1983, Tokai, Japan, Japan Atomic Energy Research Institute Report JAERI-M 84-073, pp. 34-42 (May 1984.)

67. M. F. Hrovat and H. W. Hassel, "Recent Status of Development and Irradiation Performance for Plate Type Fuel Elements with Reduced ^{235}U Enrichment at NUKEM," Proc. Int. Mtg. on Reduced Enrichment for Research and Test Reactors, 24-27 October 1983, Tokai, Japan, Japan Atomic Energy Research Institute Report JAERI-M 84-073, pp. 95-99 (May 1984.)

68. G. L. Copeland and J. L. Snelgrove, "Examination of Irradiated High-U-Loaded U_3O_8-Al Fuel Plates," Proc. Int. Mtg. on Research and Test Reactor Core Conversions from HEU to LEU Fuels, Argonne, Illinois, November 8-10, 1982, Argonne National Laboratory Report ANL/RERTR/TM-4 (CONF-821155), pp. 79-87 (September 1983).

69. G. Thamm, E. Groos, and W. Krug, "LEU-Fuel Testing at KFA-Jülich Under the German AF-Program—Plate Irradiation and PIE," Proc. 1987 Int. Mtg. on Reduced Enrichment for Research and Test Reactors, Buenos Aires, Argentina, September 28-October 1, 1987, Comisión Nacional de Energía Atómica, Buenos Aires, pp. 182-194 (September 1990).

70. E. Groos, W. Krug, J. Seferiadis, and G. Thamm, "LEU-Plate Irradiation at FRJ-2 (DIDO) Under the German AF-Programme," in *Reduced Enrichment for Research and Test Reactors—Proc. Int. Mtg., Petten, The Netherlands, October 14-16, 1985*, P. von der Hardt and A. Travelli, Eds., D. Reidel, pp. 313-325 (1986).

71. W. Krull, "Enrichment Reduction Activities for the FRG-1 and FRG-2 Research Reactors," Proc. 1988 Int. Mtg. on Reduced Enrichment for Research and Test Reactors, San Diego, California, September 19-22, 1988, Argonne National Laboratory Report ANL/RERTR/TM-13 (CONF-8809221), pp. 273-281 (June 1993).

72. H. Sakai, T. Iwai, A. Sakakura, M. Saito, R. Oyamada, A. Yamamoto, and Y. Okamoto, "Post-Irradiation Examination of LEU Miniplates in the JMTR," Proc. 1986 Int. Mtg. on Reduced Enrichment for Research and Test Reactors, Gatlinburg, Tennessee, November 3-6, 1986, Argonne National Laboratory Report ANL/RERTR/TM-9 (CONF-861185), pp. 185-200 (May 1988).

73. G. L. Hofman, "Fission Gas Bubbles in Uranium Aluminide Fuels, " Nucl. Tech. **77**, 110-115 (April 1987).

74. A. E. Richt, R. W. Knight, and G. M. Adamson, Jr., "Postirradiation Examination and Evaluation of the Performance of HFIR Fuel Elements," Oak Ridge National Laboratory Report ORNL-4714 (December 1971).

75. J. Dugone and D. D. Wieland, "Fuel Plate Experience During the SPERT I Destructive Test Series with an Aluminum-Clad Plate-Type Core," Phillips Petroleum Company-Atomic Energy Division Report IDO-16885 (July 24, 1963).

76. R. E. Woodley, "The Release of Fission Products from Irradiated SRP Fuels at Elevated Temperature—Data Report on the First Stage of the SRP Source Term Study," Hanford Engineering Development Laboratory Report HEDL-7598 (June 1986).

77. R. E. Woodley, "Release of Fission Products from Irradiated SRP Fuels at Elevated Temperatures—Data Report on the Second Stage of the SRP Source Term Study," Hanford Engineering Development Laboratory Report HEDL-7598 (March 1987).

78. G. W. Parker, G. E. Creek, C. J. Barton, W. J. Martin, and R. A. Lorenz, "Out-of-Pile Studies of Fission-Product Release from Overheated Reactor Fuels at ORNL, 1955-1965," Oak Ridge National Laboratory Report ORNL-3981 (July 1967).

79. T. Shibata, T. Tamai, M. Hayashi, J. C. Posey, and J. L. Snelgrove, "Release of Fission Products from Irradiated Aluminide Fuel at High Temperatures," Nucl. Sci. and Eng. **87**, 405-417 (1984).

80. J. C. Posey, "Release of Fission Products from Miniature Fuel Plates at Elevated Temperatures," Proc. Int. Mtg. on Research and Test Reactor Core Conversions from HEU to LEU Fuels, Argonne, Illinois, November 8-10, 1982, Argonne National Laboratory Report ANL/RERTR/TM-4 (CONF-821155), pp. 117-133 (September 1983).

81. F. Sakurai, Y. Komori, J. Saito, B. Komukai, H. Ando, H. Nakata, A. Sakakura, S. Niiho, M. Saito, and Y. Futamura, "Progress in Safety Evaluation for the JMTR Core Conversion to LEU Fuel," in *Proc. XIIth Int. Mtg. on Reduced Enrichment for Research and Test Reactors, Berlin, 10-14 September 1989*, G. Thamm and M. Brandt, Eds., Konferenzen des Forschungszentrums Jülich, Band 4, Forschungszentrum Jülich GmbH, Jülich, Germany, pp. 269-280 (1991).

82. M. Saito, Y. Futamura, H. Nakata, H. Ando, F. Sakurai, N. Ooka, A. Sakakura, M. Ugajin, and E. Shirai, "Further Data of Silicide Fuel for the LEU Conversion of JMTR," paper presented at the Int. Symp. on Research Reactor Safety, Operations and Modifications, Chalk River, Ontario, Canada, October 23-27, 1989.

83. Y. Komori, Japan Atomic Energy Research Institute, personal communication (November 1989).

84. R. A. Lorenz, "Fission Product Release Experiments," paper presented at the ANS Workshop on Safety of Uranium-Aluminum Fuel Reactors, Idaho Falls, Idaho, March 15, 1989.

85. G. C. Rodrigues and A. P. Gouge, "Reprocessing RERTR Silicide Fuels," E. I. du Pont de Nemours & Company Report DP-1657 (May 1983).

86. U.S. Department of Energy, "Receipt and Financial Settlement Provisions for Nuclear Research Reactor Fuels," Federal Register **51**(32), 5754-5756 (February 18, 1986) and Federal Register **51**(42), 7487 (March 4, 1986).

Snelgrove

Reprint from

Materials Science and Technology

A Comprehensive Treatment

Edited by R. W. Cahn, P. Haasen and E. J. Kramer

Chapter 2

Dispersion Fuels

by G. L. Hofman and J. L. Snelgrove

from Volume 10 A

Nuclear Materials, Part 1

edited by B. R. T. Frost

Published by
VCH Verlagsgesellschaft mbH
P. O. Box 10 11 61, D-69451 Weinheim
Federal Republic of Germany

VCH

2 Dispersion Fuels

Gerard L. Hofman and James L. Snelgrove

Argonne National Laboratory, Argonne, IL, U.S.A.

With an Appendix by Brian Frost

List of Symbols and Abbreviations

a	change in fractional fuel meat volume per unit fission density or burnup
b	fraction of as-fabricated porosity consumed during irradiation
B	burnup
c	change in fractional fuel meat volume multiplying Arrhenius term in TRIGA fuel swelling correlation
C_p	heat capacity
ΔC_p	additional heat capacity of a compound
d	fuel particle diameter
f	fissions (in unit)
F	fission density
i	fuel phase
k	Boltzmann constant
n	neutrons (in unit)
q	activation energy in Arrhenius term in TRIGA fuel swelling correlation
T	temperature
T_0	initial temperature
V, V_{meat}	original (unirradiated) volume of fuel meat in a fuel plate or rod
V_a	volume fraction of matrix material in fuel meat
V_f	volume fraction of theoretical-density fuel particles in fuel meat
V_p	volume fraction of porosity in fuel meat
V_{um}	volume fraction of undamaged matrix material
ΔV	change in volume of fuel meat
ΔV_F	change in volume of fuel particles
W_f	weight fraction of uranium in fuel particles
W_m	weight fraction of fuel particles in fuel meat
W_u	weight fraction of uranium in an alloy fuel
x	stoichiometric variable

α	coefficient of linear thermal expansion
α	alpha-particle
α, β, γ, δ	phases
λ_m	fission fragment recoil range in matrix material
ϱ_a	density of matrix aluminum
ϱ_f	density of fuel compound; density of alloy fuel
ϱ_m	density of fuel meat
ϱ_u	uranium density in fuel meat

ANL	Argonne National Laboratory (Argonne, IL)
ATR	advanced test reactor (at INEL)
AUC	ammonium uranyl carbonate
DTA	differential thermal analysis
ETR	engineering test reactor (at INEL)
GA	General Atomics Corporation
GT	Georgia Institute of Technology (Georgia Tech., Atlanta, GA)

HEU	highly enriched uranium (usually ~93 wt.% ^{235}U)
HFIR	high flux isotope reactor (at ORNL)
HTGR	high-temperature gas-cooled reactor
INEL	Idaho National Engineering Laboratory (Idaho Falls, ID)
LEU	low-enriched uranium (<20 wt.% ^{235}U)
MEU	medium-enriched uranium (35–45 wt.% ^{235}U)
MHTGR	modular high-temperature gas cooled reactor
MTR	material testing reactor (at INEL)
MWe	megawatt electric
NUKEM	NUKEM GmbH (Hanau, Federal Republic of Germany)
ORNL	Oak Ridge National Laboratory (Oak Ridge, TN)
ORR	Oak Ridge research reactor (at ORNL)
RERTR	reduced enrichment research and test reactor (program)
SEM	scanning electron microscope
SRL	Savannah River Laboratory (Aiken, SC)
SRS	Savannah River Site (Aiken, SC)
SS	stainless steel
TRIGA	training, research, isotope production – General Atomics (reactor)
XRD	X-ray diffraction

and 23 wt.%, fully enriched Al–U alloy fuel plates irradiated from 13 to 83% burnup showed thickness changes in the range of −1 to +4%. It is not known to what extent oxidation of the cladding was taken into account in the quoted thickness changes. Gibson and Francis (1962) also indicate that tests of up to 50 wt.% Al–U alloy fuels at temperatures up to 177 °C and burnups up to 50% produced no apparent dimensional or microstructural changes. Gibson (1963) reports density change data for fully enriched 45-wt.%-U, 3-wt.%-Si plates irradiated in the MTR. After about 3.0×10^{27} f m^{-3} (~80% ^{235}U burnup), the plate density had decreased by approximately 2.4%, indicating about 12% swelling of the meat, or around 40% swelling of the fuel phase. Based on this latter experiment it appears that the Al–U phase in Al–U alloy fuel swells at a rate of approximately 4 vol.% per 10^{27} f m^{-3}. No evidence of fission gas bubbles in the fuel phase has been found at magnifications of up to 500 ×, and no break-away swelling has been reported.

2.8.2.2 Uranium Aluminides (UAl_x)

The development of fuel plates for a generation of high flux reactors presented fabrication problems with Al–U alloy fuel at the required high uranium loadings. Although one of the leading reactors of this kind, the HFIR in Oak Ridge, eventually was fueled with U_3O_8–Al plates, successful development work on UAl_x–Al powder dispersions for the ATR in Idaho resulted in the selection of this fuel for the ATR as well for as many other research reactors.

The selection of aluminide fuel powder was based on the very stable irradiation behavior of the same precipitate phases existing in the heretofore used Al–U alloy fuels. Experience has borne out this expectation. Dispersion fuels of UAl_x (primarily UAl_3 with varying fractions of UAl_2 and UAl_4) in aluminum matrix and cladding have shown excellent high-burnup stability and absence of break-away swelling and blistering or pillowing (Beeston, 1980; Dienst, 1977).

Attempts to increase the uranium loading either to increase burnup capability or to allow a reduction in ^{235}U enrichment through the use of UAl_2 (Thümmler, 1969; Dienst, 1977) rather than UAl_x have likewise been successful. Even irradiation tests with hypostoichiometric UAl_2, that is, UAl_2 powder containing a certain amount of uranium–aluminum solid solution phase have shown similar excellent behavior (Gómez et al., 1985). The expectation that the metallic uranium solid solution phase would, during irradiation, react with the matrix aluminum to form a stable UAl_4 or UAl_3 phase proved to be right, and resulted in higher fuel loadings than possible with UAl_x alone due to fabrication limits on the volume fraction of fuel. In fact, almost the entire meat of the test fuel plates was converted to aluminide during irradiation, as shown in Fig. 2-29, yet no abnormal swelling or plate deformations were observed.

Because of the wide application of aluminide dispersions, several studies have examined the effects of swelling on fuel plate performance (Martin et al., 1973; Beeston et al., 1980). These studies concluded that as-fabricated fuel meat porosity or void volume generally accommodates the increased atomic volume of the fission products and that the growth or swelling of the meat could be represented by a correlation like Eq. (2-22). However, deviations from the correlation might occur due to other factors, such as reaction of the fuel and the matrix. In fact this reaction does occur, as shown by postirradiation X-ray diffraction

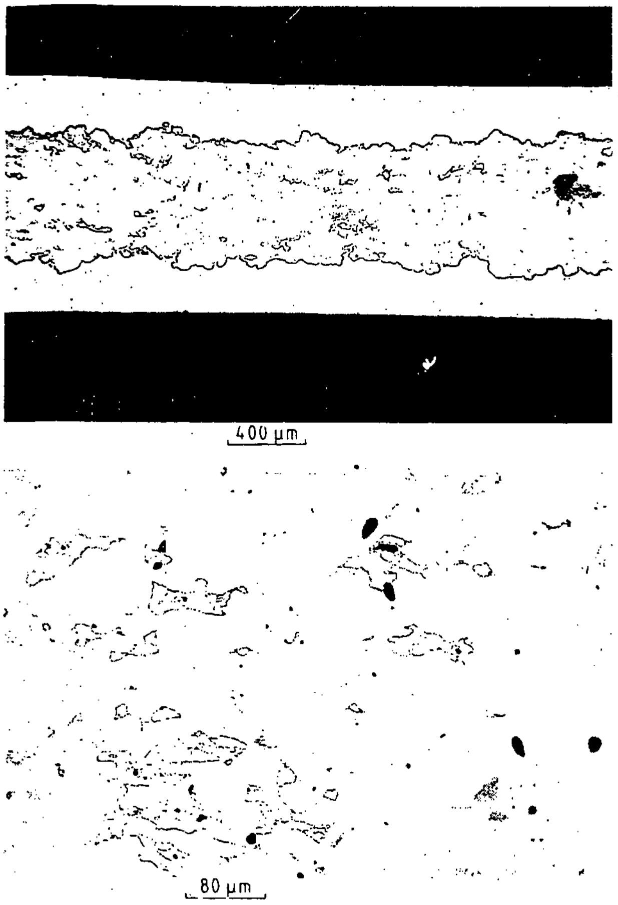

Figure 2-29. Postirradiation micrographs of highly loaded, highly burned UAl_2 - Al fuel plate, showing virtually complete elimination of the matrix aluminum in the meat through fuel–matrix reaction (Goméz et al., 1985).

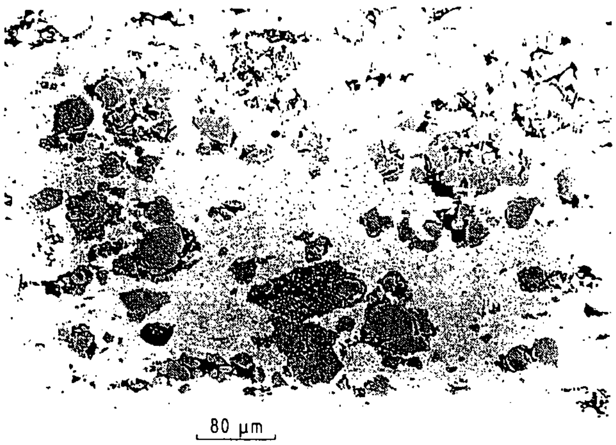

Preirradiation

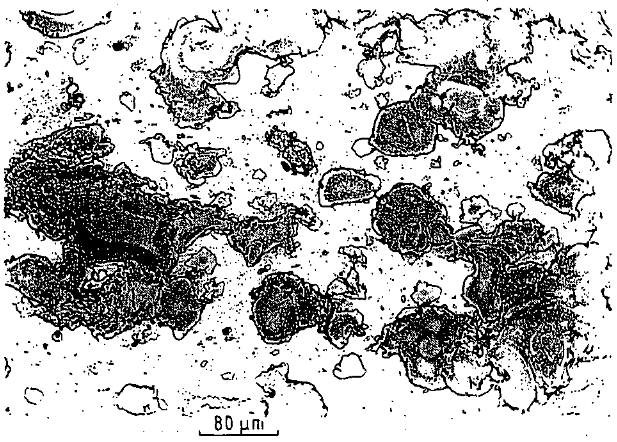

Postirradiation

Figure 2-30. UAl_x powder metallurgical dispersion before and after irradiation.

(Richt et al., 1962) and by metallography (illustrated in Figs. 2-30 and 2-31). However, calculation shows that the volume change resulting from the reaction is very small.

Large gas bubble formation appears to be suppressed by the accommodation of the gaseous atoms (Xe and Kr) in the UAl_x fuel particle, that is, in solution and, probably, in very small bubbles. Indeed, high-magnification scanning microscopy of high-burnup aluminide particles found no evidence of fission gas bubbles in any of the three phases present, as shown in Fig. 2-31 (Hofman, 1987).

Swelling data from experimental irradiations of typical ATR fuel meat compositions are shown in Fig. 2-32 (Beeston et al., 1980). Some of the swelling values in Fig. 2-32 are averages for samples having the same uranium concentration and fission density. The solid line, representing a least squares fit to the twenty-four data points, goes through the origin, indicating that there is no accommodation of the swelling fuel particle by the as-fabricated porosity. In this case the explanation is undoubtedly that the pressure of the He generated by neutron capture in the ^{10}B burnable poison kept the voids from closing. This ex-

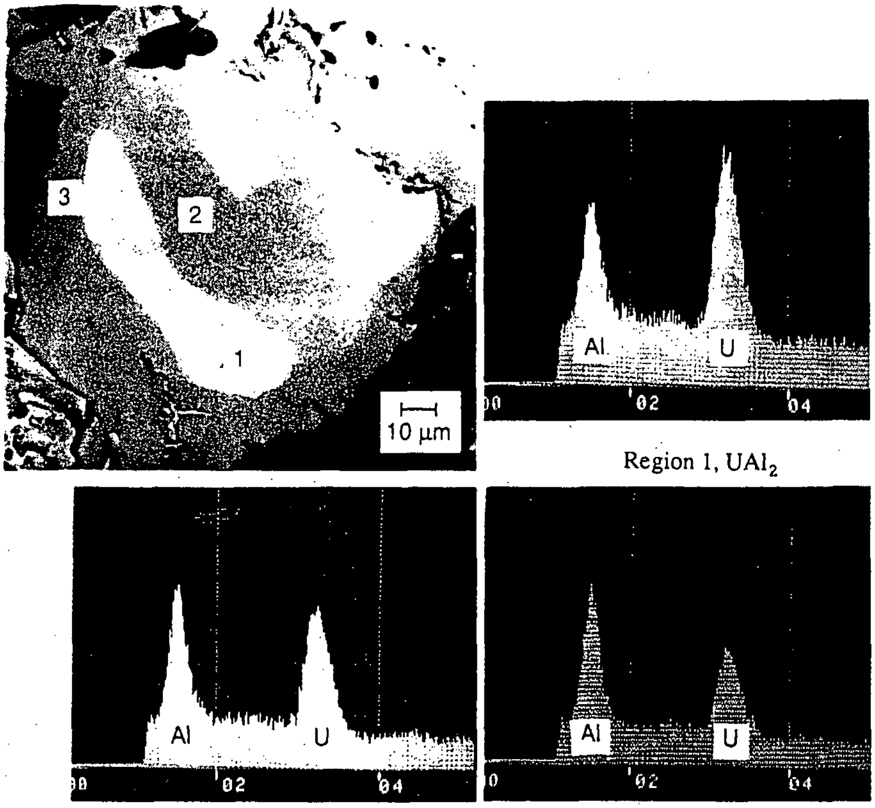

Region 1, UAl_2

Region 2, UAl_3

Region 3, UAl_4

Figure 2-31. Examination of original UAl_x grains for UAl_2 (1), UAl_3 (2), UAl_4 (3), and U. There is no indication of free uranium in the grain.

planation is supported by the fact that the two high-burnup samples with swelling values well below the curve had a low initial boron content.

Analyses of swelling data for fuel plates for which estimates of the residual porosity could be made from photomicrographs allowed the calculation of the swelling of the aluminide fuel phases, shown in Fig. 2-33. Although there is considerable scatter in these data, they indicate a two-stage swelling behavior similar in nature to that

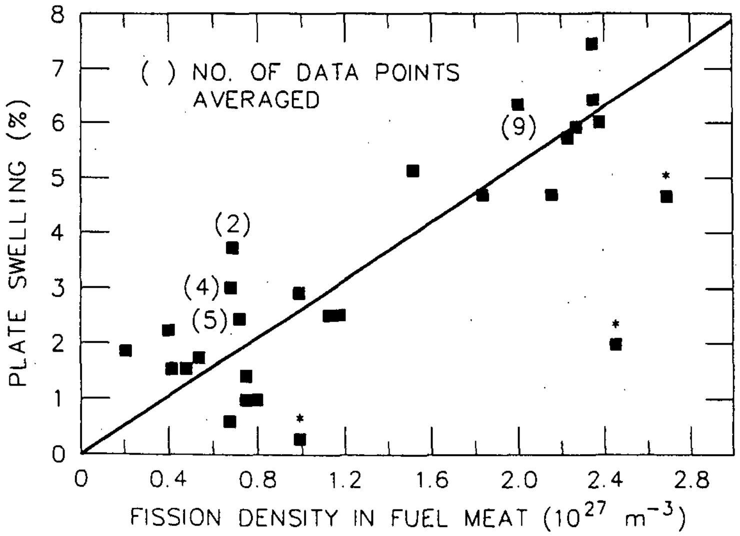

Figure 2-32. Swelling of uranium aluminide fuel plates as a function of fission density (Whitacre, 1990). *: Plates with highest as-fabricated porosity and lowest B_4C content.

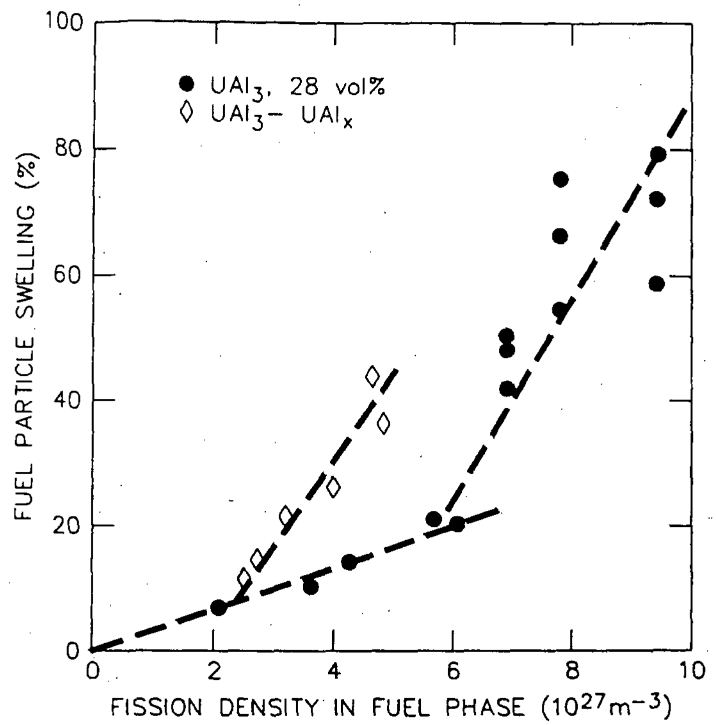

Figure 2-33. Swelling of UAl$_x$ fuel particles as a function of fission density in the particle. Solid symbols: high fission rate; open symbols: low fission rate.

observed in UO_2, as well as a fission rate effect similar to that observed for U_3Si_2 (see Sec. 2.8.2.3).

2.8.2.3 High-Density Fuel Compounds

Whereas the hitherto-discussed uranium compounds provide satisfactory material for dispersion fuel for even the highest flux reactors when highly enriched uranium is used, their uranium density is often too low for utilization as reduced-enrichment fuel. As shown in Table 2-1, there are several very-high-density uranium compounds suitable for the customary powder metallurgical fabrication of aluminum fuel plates or rods. One of these, U_3Si, has been extensively tested and is being used as a dispersion fuel in rod form in Canadian test reactors (Wood et al., 1982). Unfortunately, irradiation tests have shown the densest of

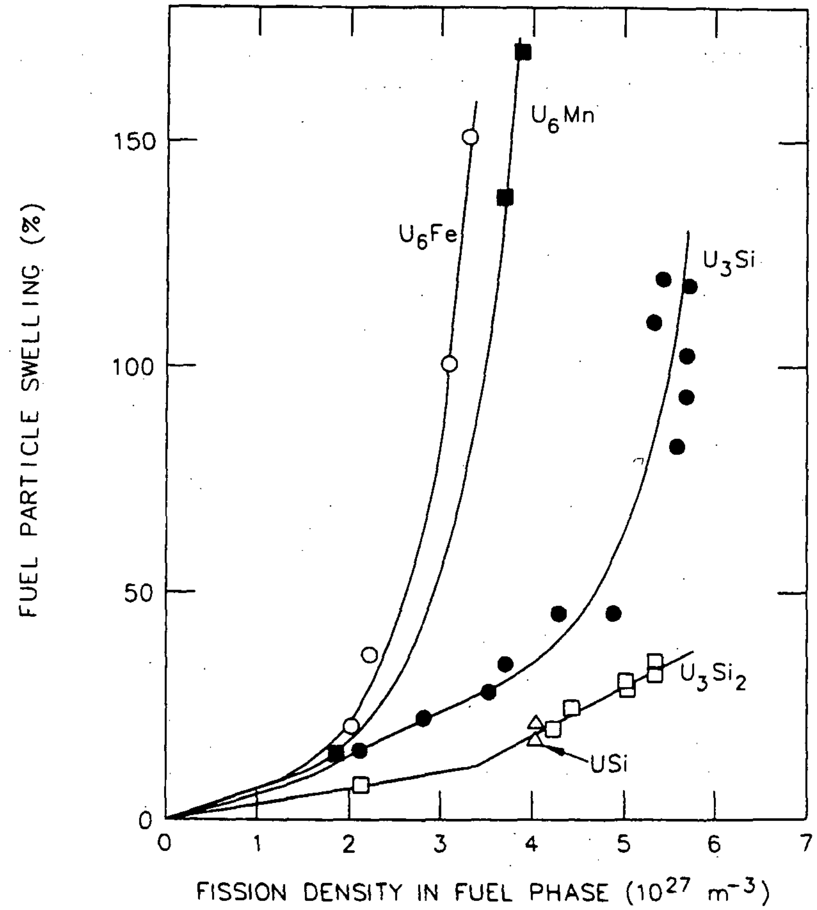

Figure 2-34. Swelling of various high- and medium-density dispersion fuel particles as a function of fission density.

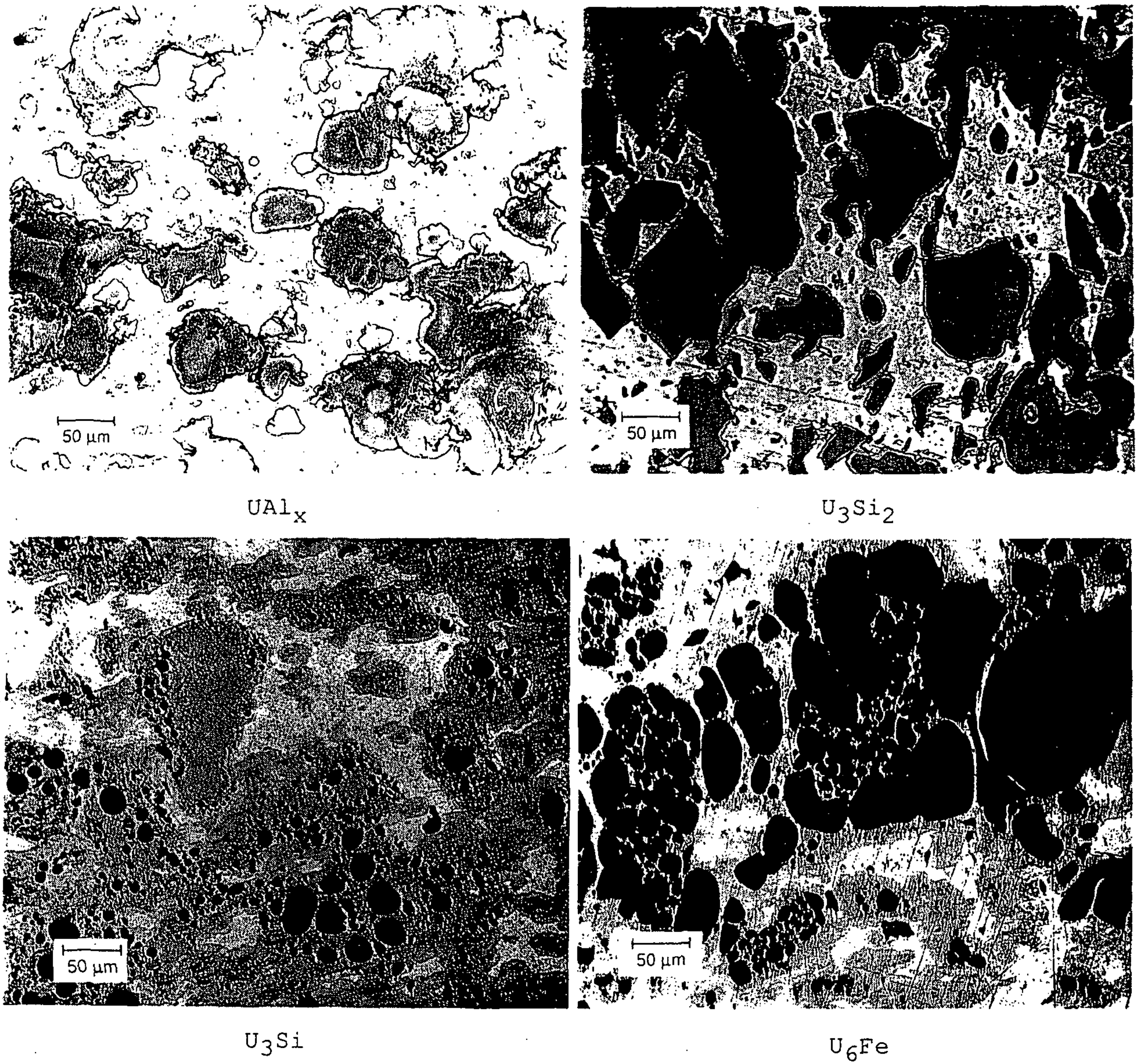

UAl_x U_3Si_2

U_3Si U_6Fe

Figure 2-35. Comparison of postirradiation microstructure of various dispersion fuel particles at several burnups showing absence of gas bubbles in UAl_x and U_3Si_2 and large interconnecting bubbles in U_3Si and U_6Fe.

these compounds to have unstable swelling behavior for most plate applications.

A comparison of the swelling of various high-density compounds tested during the RERTR program is presented in Fig. 2-34. It is clear that the very-high-density compounds such as U_6Fe, and, to a lesser extent, U_3Si exhibit undesirably high swelling rates at low or moderate fission densities. On the other hand, the medium-density compounds, U_3Si_2 and USi, appear to have a more stable swelling behavior. The reason for the difference in swelling behavior lies again in the manner in which fission gas bubble formation proceeds during irradiation.

Metallographic sections shown in Fig. 2-35 illustrate the difference in bubble morphology between, on the one hand, high-swelling compounds where bubbles grow very large and eventually interlink and, on the other hand, U_3Si_2 where bubbles are too small to be seen at the same magnification. At first glance, the irradiation behav-

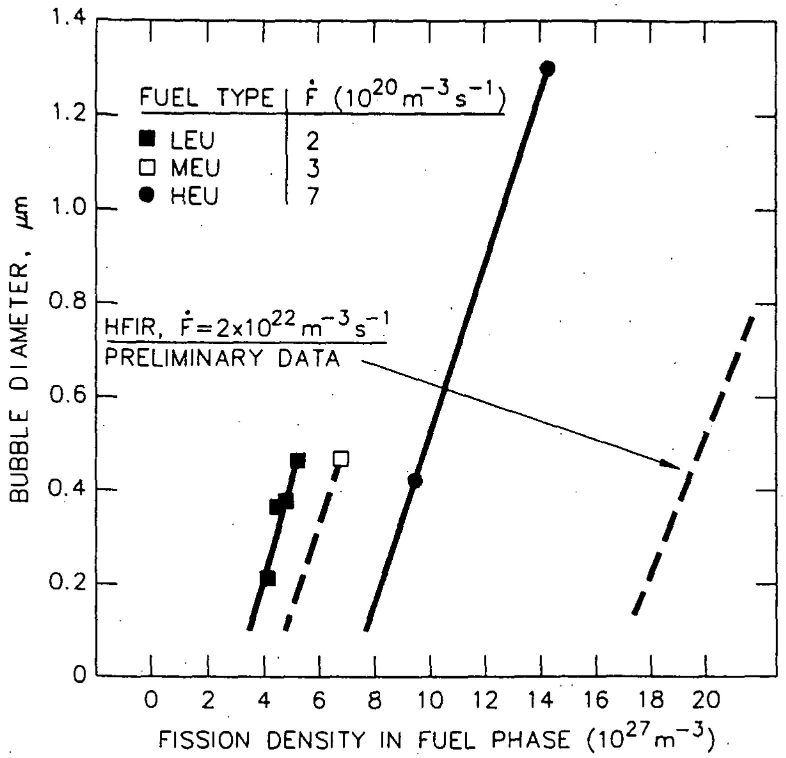

Figure 2-41. Fission gas bubble diameter as a function of fission density and fission rate, including recent (preliminary) data.

plate swelling than in dispersions without burnable poison.

2.8.3 Summary

The foregoing discussion suggests that the swelling behavior of dispersion fuels may be generalized as follows: There is an initial linear stage with a low swelling rate of approximately $3\pm1\%\,\Delta V$ per 10^{27} f m^{-3}. This stage may endure to high fission densities in certain compounds, for example, U_3Si_2, UAl_x, or UO_2. At a fission density that depends on irradiation conditions such as fission rate and temperature, a second linear rate of approximately $8\pm2\%$ ΔV per 10^{27} f m^{-3} commences. This stage appears to be associated with formation of fission gas bubbles on microstructural features such as subgrain boundaries or dislocation networks. Both stages may be considered to represent stable swelling. A third stage, which may occur in certain fuel compounds or fuel–matrix combinations and which is characterized by fission gas bubble linkup and coarsening in either the fuel particles, fuel–matrix reaction products, and/or radiation-damaged matrix material, represents unstable, or break-away, swelling. Break-away swelling renders certain compounds unsuitable for most practical applications, unless sufficient mechanical restraint can be provided, and places definite burnup and/or fuel loading limits on others.

It appears that the "inherently" stable swelling compounds can be used to extremely high fission densities or burnups and that their use in dispersion fuels is limited only by fabricability.

Recoil damage to matrix material, seen as a serious performance issue for steel and ceramics, is evidently not detrimental to the irradiation performance of stable-swelling compounds dispersed in aluminum.

2.9 Additional Properties of Irradiated Fuel

2.9.1 Blister Threshold Temperature

Blisters on the surface of a fuel tube or plate occur when gases, from fission or other sources, collect at the meat-cladding interface with a pressure great enough to locally raise the cladding away from the fuel meat. Typically, blisters are from 1 to 5 mm in extent; however, in some cases they may cover a much larger area. Although used in a seemingly interchangeable manner in the literature, in this chapter blistering refers to a separation at the meat-cladding interface, and break-away swelling (discussed in Sec. 2.8) refers to a separation in the fuel meat. Blistering occurs at elevated temperatures, where the cladding has lost much of its strength. If a fuel plate were to blister during operation, transfer of heat from the fuel meat to the coolant might be severely disrupted, especially if the thermal conductivity of the meat were low. As will be discussed later, there is also the possibility that a small amount of fission gas might be released.

The resistance of a fuel tube or plate to blistering is established by measuring the blister threshold temperature, or the temperature in a series of sequential anneals at which the plate first blisters. In the typical blister test the sample is held at temperature for 30 to 60 min during each annealing step. The blister temperature undoubtedly is a function of the time–temperature history of the sample during the test. However, the blister threshold temperature provides an indication of the ability of the fuel to withstand short periods (of the order of an hour) of operation at high temperature without failure.

No blister threshold temperature data (based on the standard test) were found for Al–U alloy fuel. Uranium aluminide dispersion fuel with no boron in the meat typically exhibits blister temperatures of 550 °C or higher. In many cases blistering is preceded by cracking of the matrix, especially when boron is present. The He gas from the $^{10}B(n, \alpha)$ reaction provides enough additional pressure to decrease the blister temperature by 50 to 100 °C.

Blistering of U_3O_8 dispersion fuel plates is typically preceded by cracking of the fuel (reaction-product) particles. Blister temperatures for U_3O_8–Al fuel plates typically range from 450 to 550 °C. The presence of boron poison in the fuel meat results in the lowering of the blister threshold temperature by at least 100 °C. Both Richt et al. (1971) (for U_3O_8 dispersion fuel) and Dienst et al. (1977) (for UAl_x dispersion fuel) noted that the higher the irradiation temperature, the more blister resistant the fuel. Apparently, higher irradiation temperatures allow the fuel–matrix reaction to occur more completey during irradiation. Consequently, a smaller amount of reaction, which releases fission gases, occurs during the blister test. It is interesting to note that highly loaded U_3O_8 plates irradiated during the RERTR program exhibited consistently higher blister threshold temperatures than those measured during previous development programs. Perhaps the explanation lies in accelerated reaction due to an elevated irradiation temperature resulting from the low thermal conductivity of the highly loaded meat.

Blisters on fuel plates containing UAl_x or U_3O_8 dispersion fuel meat have been found to result predominantly from fission gas or He coming from the interior of the fuel meat. Another type of blistering is most prevalent for U_3Si_2 dispersion fuels. For these fuels blisters tend to form first at the periphery of the fuel meat. Micrographic investigation has shown that these blisters are associated with oxidized fuel. These fuel particles, which oxidized before or during plate rolling, produce a nonbonded area and apparently break up under the pressure of fission gas at high temperatures and release the fission gas to form the blister. Similar blisters caused by oxidized fuel particles have been found outside the fuel zone of UAl_x dispersion fuel plates irradiated during the RERTR program. Blister temperatures are typically in the 525 to > 550 °C range for U_3Si_2 dispersion fuels without boron in the fuel meat. As for the UAl_x and U_3O_8 dispersion fuel, the presence of boron in the U_3Si_2 fuel meat resulted in a reduction of the blister threshold temperature by approximately 100 °C.

2.9.2 Fission Product Release

The principal danger to the general public from a severe nuclear reactor accident comes from the release of radioactive fission products. In order to predict the consequences of such an accident, one must know the amount of fission products released from the fuel and the rate of release. Parker et al. (1967), Graber et al. (1966), Posey (1983), Shibata et al. (1984), Woodley (1986, 1987), and Saito et al. (1989) have performed measurements of fission product release from aluminum-based dispersion fuels. Stahl (1982) provided an excellent summary of the information available before 1982, both from out-of-reactor experiments and from reactor accidents. Taleyarkhan (1990) performed a detailed statistical analysis of most of the available data.

Fission gases, being inert, are more easily released than other fission products. Studies of fission gas release from UAl_x, U_3O_8, and U_3Si dispersion fuels performed by Shibata et al. (1984) and Posey (1983) during the RERTR program showed that fission gas is first released through microcracks which develop during the process of blister formation. A greater amount of gas was released when the cladding began to melt. Essentially all of the gas had been released from these fuels by 650 °C, undoubtedly because the structure of the fuel particles was disrupted by reaction of the fuel and the matrix. Francis and Moen (1966) obtained similar results for UAl_x and U_3O_8. Parker et al. (1967) found that most of the fission gas was released during the first two minutes at temperature and that above approximately 3% burnup the amount of burnup did not affect the release fractions. Behavior of the volatile fission products, principally iodine, cesium, and tellurium, is much more complicated. Temperature, time, and atmosphere affect their release fractions. Taleyarkhan (1990) has provided correlations for the release fractions of the noble gases and the volatile fission products as a function of temperature.

The release of fission products from TRIGA fuel has also been studied. Fission gas release rates are very low during irradiation at normal operating temperatures (Simnad, 1980).

2.10 Appendix: Coated Particle Fuels

2.10.1 The System

The high-temperature gas-cooled reactor (HTGR) uses helium as the coolant, graphite as the moderator, and coated fuel particles dispersed in graphite as the core material. This combination allows very high fuel burnup, high specific power, and high-temperature operation. Furthermore,

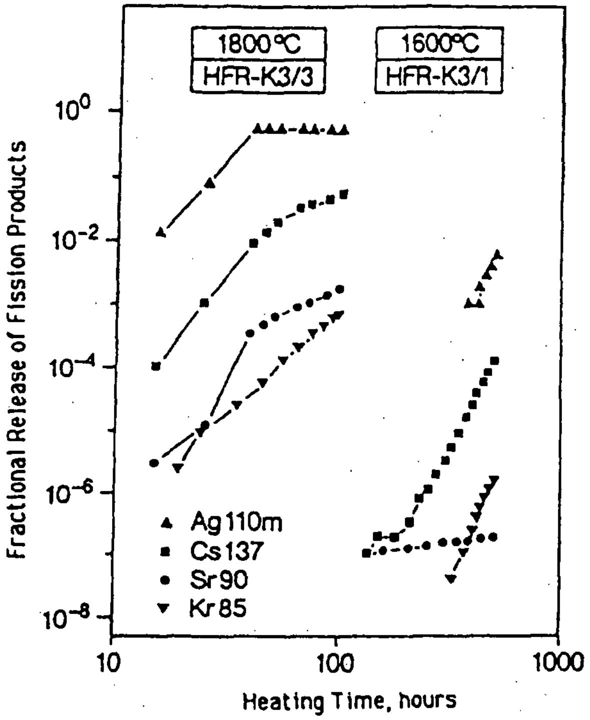

Figure 2-45. Fission product release from typical irradiated HTGR fuel when exposed to constant temperatures (1600 °C or 1800 °C) for various times.

cause for concern because they may diffuse through the coatings at normal operating temperatures; these elements are cesium, strontium, and silver. Silver, in particular, seems to diffuse through SiC at temperatures as low as 1250 °C. This is believed to be a grain boundary diffusion process. Such effects have led to the development of getters, placed within the particles, to capture excess oxygen in oxide fuels and to capture certain fission products and stop them from migrating. The ultimate goal is a combined oxygen–fission product getter. In general, the oxides or carbides of the more reactive elements – such as aluminum and zirconium – appear to be effective getters.

2.11 References

Aitken, E. A. (1990), personal communication.

ANL (Argonne Natl. Lab.) (Ed.) (1964a), *Reactor Devel. Program Prog. Rep.* Argonne, IL: ANL (ANL-6860), p. 97.

ANL (Argonne Natl. Lab.) (Ed.) (1964b) *Reactor Devel. Program Prog. Rep.* Argonne, IL: ANL (ANL-6880), p. 72.

Aronin, L.R., Klein, J. L. (1954), *Use of a Density (Specific Volume) Method as a Sensitive Absolute Measure of Alloy Composition, and Its Application to the Aluminum–Uranium System.* Cambridge, MA: Nuclear Metals, Inc. (NMI-1118).

Baker, L., Bingle, J. D. (1964), in: *Chem. Eng. Divis. Semiannu. Rep., Jan.–June 1964.* Argonne, IL: ANL (ANL-6900), pp. 298–303.

Baker, L., Bingle, J. D., Warchal, R., Barnes, C. (1964), in: *Chem. Eng. Divis. Semiannu. Rep., July–Dec. 1963.* Argonne, IL: ANL (ANL-6800), pp. 390–402.

Barin, I., Knacke, O. (1973), *Thermochemical Properties of Inorganic Substances.* Heidelberg: Springer-Verlag.

Barin, I., Knacke, O., Kubaschewski, O. (1977), *Thermochemical Properties of Inorganic Substances,* Supplement. Heidelberg: Springer-Verlag.

Barney, W. K., Wemple, B. D. (1958), *Metallurgy of Irradiated UO_2-Containing Fuel Elements,* Schenectady, NY: Knolls Atomic Power Lab. (KAPL-1836).

Beeston, J. M., Hobbins, R. R., Gibson, G. W., Francis, W. C. (1980), *Nucl. Technol. 49,* 136–149.

Beeston, J. M., Miller, L. G., Brown, K. R., McGinty, D. M. (1984), *ELAF Failed Fuel Plate Examination.* Idaho Falls, ID: EG & G Idaho, Inc. (EGG-SE-6696).

Berman, R. M. (1960), *An X-Ray Diffraction Study of Irradiated Fluorite-Type Materials.* Pittsburgh, PA: Westinghouse (WAPD-BT-21), p. 33–42.

Berman, R. M. (1963), *Nucl. Sci. Eng. 16,* 315–328.

Berman, R. M., Bleiberg, M. L., Yeniscavich, W. (1960), *J. Nucl. Mater. 2,* 129–140.

Bethune, B. (1969), *J. Nucl. Mater. 31,* 197–202.

Billington, D. S. (1956), *Int. Conf. on the Peaceful Uses of Atomic Energy,* Vol. 7, P/744. New York: United Nations, pp. 421–432.

Bleiberg, M. L., Yeniscavich, W., Gray, R. G. (1961), *Effect of Burnup on Certain Ceramic Fuel Materials,* Pittsburgh, PA: Westinghouse (WAPT-T-1274).

Bleiberg, M. L., Berman, R. M., Lustman, B. (1963), *Radiation Damage in Reactor Materials.* Vienna: IAEA, pp. 319–428.

Bloch, J. (1962), *J. Nucl. Mater. 6,* 203.

Borie, B. S. (1951), *J. Met. (Trans. AIME) 3,* 800–802.

Boucher, R. (1959), *J. Nucl. Mater. 1,* 13–27.

Chase, M. W., Jr., Davies, C. A., Downey, J. R., Jr., Fruip, D. J., McDonald, R. A., Syverud, A. N. (1986), *JANAF Thermochem. Tables,* 3rd. ed. New York: American Institute of Physics.

Chiotti, P., Kateley, J. A. (1969), *J. Nucl. Mater. 32,* 135–145.

Copeland, G. L., Martin, M. M. (1982), *Nucl. Technol. 56,* 547–552.

Copeland, G. L., Snelgrove, J. L. (1983), *Proc. Int. Mtg. on Research and Test Reactor Core Conversions from HEU to LEU Fuels, Argonne, IL, Nov. 8–10, 1982*. Argonne, IL: ANL (ANL/RERTR/TM-4, CONF-821155), pp. 79–87.

Cordfunke, E. H. P., Konings, R. J. M. (Eds.) (1990), *Thermochemical Data for Reactor Materials and Fission Products*. Amsterdam: North-Holland, pp. 669–671.

Crawford, J. H., Wittels, M. C. (1954), *1st Geneva Conf. Peaceful Uses At. Energy*, Vol. 7, P/753. New York: United Nations, pp. 654–665.

Davies, N. F., Forrester R. E. (1970), *Effects of Irradiation on Hydrided Zirconium–Uranium Alloy*. Canoga Park, CA: Atomics International (AI-AEC-12963).

Dienst, W., Nazaré, S., Thümmler, F. (1977), *J. Nucl. Mater. 64*, 1–13.

Dittmer, J. O. (1969), M.S. Thesis, Idaho State University, unpublished.

Domagala, R. F., Wiencek, T. C., Snelgrove, J. L., Homa, M. I., Heinrich, R. R. (1986), *Am. Ceram. Soc. Bull. 65*, 1164–1170.

Fleming, J. D., Johnson, J. W. (1963 a), *Trans. Am. Nucl. Soc. 6*, 158–159.

Fleming, J. D., Johnson, J. W. (1963 b), *Nucleonics 2 (No. 5)*, 84–87.

Flowers, B. H. (1974), *Proc. BNES Int. Conf.*, London, 1973. London: British Nuclear Energy Society.

Fortescue, P. (1957), *Nucl. Power 2*, 381.

Gibson, G. W. (1963), in: *Annu. Prog. Rep. on Fuel Element Development for FY, 1963:* Gibson, G. W., Graber, M. J., Francis, W. C. (Eds.). Idaho Falls, ID: Phillips Petroleum Company – Atomic Energy Division (IDO-16934), pp. 25–26.

Gibson, G. W. (1967), *The Development of Powdered Uranium–Aluminide Compounds for Use as Nuclear Reactor Fuels*. Idaho Falls, ID: Idaho Nuclear Corporation (IN-1133).

Gibson, G. W., Francis, W. C. (1962), *Annu. Prog. Rep. on Fuel Element Development for FY, 1962*. Idaho Falls, ID: Phillips Petroleum Company – Atomic Energy Division (IDO-16799), pp. 9–15, 91.

Gibson, G. W., Shupe, O. K. (1962), *Annu. Prog. Rep. on Fuel Element Development for FY, 1961*. Idaho Falls, ID: Phillips Petroleum Company – Atomic Energy Division (IDO-16727), pp. 18–20, 38–43.

Gimple, M. L., Huntoon, R. T. (1957), *Properties of Aluminum–Uranium Alloys Containing 16 to 45 Percent Uranium*. Aiken, SC: DuPont (DP-256).

Gómez, J., Morando, R., Pérez, E. E., Giorsetti, D. R., Copeland, G. L., Hofman, G. L., Snelgrove, J. L. (1985), *Proc. 1984 Int. Mtg. on Reduced Enrichment for Research and Test Reactors*. Argonne, IL: ANL (ANL/RERTR/TM-6, CONF 8410173), pp. 86–104.

Graber, M. J. (1963), in: *Annu. Prog. Rep. on Fuel Element Development for FY, 1963:* Gibson, G. W., Graber, M. J., Francis, W. C. (Eds.). Idaho Falls, ID: Phillips Petroleum Company – Atomic Energy Division (IDO-16934), pp. 21–25.

Graber, M. J. (1964), in: *Annu. Prog. Rep. on Reactor Fuels and Materials Development for FY, 1964:* Graber, M. J., Zelenzy, W. F., Gibson, G. W. (Eds.). Idaho Falls, ID: Phillips Petroleum Company – Atomic Energy Division (IDO-17037), pp. 16–22.

Graber, M. J., Zukor, M., Gibson, G. W. (1966), in: *Annu. Prog. Rep. on Reactor Fuels and Materials Development for FY, 1966:* Francis, W. C., Moen, R. A. (Eds.). Idaho Falls, ID: Phillips Petroleum Company – Atomic Energy Division (IDO-17218), pp. 52–58.

Gray, L. W., Kerrigan, W. J. (1978), *Exothermic Reactions Leading to Unexpected Meltdown of Scrap Uranium–Aluminum Cermet Cores During Outgassing*. Aiken, SC: DuPont (DP-1485).

Gray, L. W., Peacock, H. B. (1989), *A Differential Thermal Analysis Study of the Effect of Tramp Impurities on the Exothermic U_3O_8–Al Reactions*. Aiken SC: DuPont (DP-1770).

Gregg, J. L., Crouse, R. S., Werner, W. J. (1967), *Swelling of UAl_3–Al Compacts*. Oak Ridge TN: ORNL (ORNL-4056).

Gulden, T. D., Harmon, D. P., Stansfield, O. M. (1975), *Physical Metallurgy of Reactor Fuel Elements*. London: The Metals Society, pp. 341–351.

Hick, H., Graham, L. W., Nabielek, H., Rowland, P. R., Faircloth, R. L., Brown, P. E. (1975), *Gas-Cooled Reactors*. Vienna: IAEA, I, 203.

Hobbins, R. R. (1973), unpublished.

Hofman, G. L. (1986 a), *Nucl. Technol. 72*, 338–344.

Hofman, G. L. (1986 b), *J. Nucl. Mater. 140*, 256–263.

Hofman, G. L. (1987), *Nucl. Technol. 77*, 110–115.

Hofman, G. L. (1993), *Proc. 1988 Int. Mtg. on Reduced Enrichment for Research and Test Reactors, San Diego, CA, Sept. 19–22, 1988*. Argonne, IL: ANL (ANL/RERTR/TM-13, CONF-8809221), pp. 92–110.

Holden, A. N. (1967), *Dispersion Fuel Elements*. New York: Gordon and Breach Science Publ.

Hrovat, M. F., Hassel, H. W. (1983 a), *Proc. Int. Mtg. on Research and Test Reactor Core Conversions from HEU to LEU Fuels, Argonne, IL, Nov. 8–10, 1982*. Argonne, IL: ANL (ANL/RERTR/TM-4, CONF-821155), pp. 171–182.

Hrovat, M. F., Huschka, H., Koch, K. H., Nazaré, S., Ondracek, G. (1983 b), *Proc. Int. Mtg. on Dev., Fab., and Application of Reduced Enrichment Fuels for Research and Test Reactors*, Argonne, IL, *Nov. 12–14, 1980*. Argonne, IL: ANL (ANL/RERTR/TM-3, CONF-801144), pp. 201–221.

IAEA (1990), *Gas Cooled Reactor Design and Safety*, Tech. Rep. Ser. No. 312. Vienna: IAEA.

Issorow, S. (1957), *J. Met. (Trans. AIME) 9*, 1236–1239.

Jesse, A., Ondracek, G., Thümmler, F. (1971), *Powder Metall. 14*, 289.

Jones, T. I., McGee, I. J., Norlock, L. R. (1960), *Some Properties of Aluminum–Uranium Alloy in the Cast, Rolled and Annealed Conditions*. Chalk River, ON: AECL (AECL-1215).

Jones, T. I., Street, K. N., Scoberg, J. A., Baird, J. (1963), *Can. Metall. Q. 2 (No. 1)*, 53–72.

Kangilaski, M. (1966), *The Effect of Nuclear Radiation on Dispersion Fuel Materials*. Columbus, OH: Radiation Effects Information Center, Battelle Memorial Institute (REIC-40).

Keller, D. L. (1961), *Nucleonics 21*, 48.

Kim, C. K., Kuk, I. H. (1992), *Proc. Int. Mtg. Reduced Enrichment Res. Test Reactors, Jakarta, Indonesia, Nov. 2–6, 1991*. Jakarta: BATAN, in press.

Krug, W., Groos, E., Seferiadis, J., Thamm, G. (1993), *Proc. 1988 Int. Mtg. Reduced Enrichment Res. Test Reactors, San Diego, CA, Sept. 19–22, 1988*. Argonne, IL: ANL (ANL/RERTR/TM-13, CONF-8809221), pp. 155–181.

Kubaschewski, O., Evans, E. L., Alcock, C. B. (1967), *Metall. Thermochem.* Oxford: Pergamon Press, pp. 205–209.

Lacy, C. E., Leary, E. A. (1958), *Irradiation Performance of Highly Enriched Fuel*. Schenectady, NY: Knolls Atomic Power Laboratory (KAPL-1952).

Lambert, J. D. B. (1968), in: *Metall. Soc. Confs.*, Vol. 42: Holden, A. N. (Ed.). New York: Gordon and Breach.

Lillie, A. F. (1973), *Zirconium Hydride Fuel Element Performance Characteristics*. Canoga Park, CA: Atomics International (AI-AEC-13084).

Marra, J. E., Peacock, H. B. (1990), *Reactions During the Processing of U_3O_8–Al Cermet Fuels*. Aiken, SC: Westinghouse Savannah River Company (DP-1776).

Martin, M. M., Richt, A. E., Martin, W. R. (1973), *Irradiation Behavior of Aluminum-Base Dispersion Fuels*. Oak Ridge, TN: ORNL (ORNL-4856).

Martin, W. R., Weir, J. R. (1964), *Mechanical Properties of X8001 and 6061 Aluminum Alloys and Aluminum-Base Fuel Dispersion at Elevated Temperatures*. Oak Ridge, TN: ORNL (ORNL-3557).

Miller, L. G., Beeston, J. M. (1986), *Extended Life Aluminide Fuel Final Rep.* Idaho Falls, ID: EG&G Idaho, Inc. (EGG-2441).

Mondolfo, L. F. (1976): *Aluminum Alloys: Structure and Properties*. London: Butterworth.

Nazaré, S. (1984), *J. Nucl. Mater. 124*, 14–24.

Nazaré, S., Ondracek, G., Thümmler, F. (1970), *UAl_3–Al as Dispersion Fuel for High Flux Reactors*. Karlsruhe: Kernforschungszentrum Karlsruhe GmbH (KfK 1252), p. 59.

Nazaré, S., Ondracek, G., Thümmler, F. (1975), *J. Nucl. Mater. 56*, 251–259.

Oetting, F. L., Rand, M. H., Ackermann, R. J. (1976), in: *The Chemical Thermodynamics of Actinide Elements and Compounds*, Part 1: *The Actinide Elements*. Vienna: IAEA, pp. 14–20, 45, 74–81.

Parker, G. W., Creek, G. E., Barton, C. J., Martin, W. J., Lorenz, R. A. (1967), *Out-of-Pile Studies of Fission-Product Release from Overheated Reactor Fuels at ORNL, 1955–1965*. Oak Ridge, TN: ORNL (ORNL-3981).

Pasto, A. E., Copeland, G. L., Martin, M. M. (1982), *Ceram. Bull. 61, No. 4*, 491–496.

Peacock, H. B. (1983 a), *Study of the U_3O_8–Al Thermite Reaction and Strength of Reactor Fuel Tubes*. Aiken, SC: DuPont (DP-1665).

Peacock, H. B. (1983 b), *Proc. Int. Mtg. Reduced Enrichment Res. Test Reactors, Oct. 24–27*, 1983. Tokai, Jpn.: JAERI (JAERI-M 84-073), pp. 77–84.

Peacock, H. B. (1990 a), *Properties of U_3O_8–Aluminum Cermet Fuel.* Aiken, SC: Westinghouse Savannah River Co. (WSRC-RP-89-981, Rev. 1).

Peacock, H. B. (1990 b), personal communication.

Peacock, H. B., Frontroth, R. L. (1989), *Properties of Aluminum–Uranium Alloys*. Aiken, SC: Westinghouse Savannah River Co. (WSRC-RP-89-489), pp. 30–31, 41.

Posey, J. C. (1983), in: *Proc. Int. Mtg. on Research and Test Reactor Core Conversions from HEU to LEU Fuels, Argonne, IL, Nov. 8–10, 1982*. Argonne, IL: ANL (ANL/RERTR/TM-4, CONF-821155), pp. 117–133.

Rest, J., Hofman, G. L. (1990), in: *Fundamental Aspects of Inert Gases in Solids:* Donnelly, S. E., Evans, J. M. (Eds.). New York: Plenum Press.

Richt, A. E., Knight, R. W., Adamson, G. M. (1971), *Postirradiation Examination and Evaluation of the Performance of HFIR Fuel Elements*. Oak Ridge, TN: ORNL (ORNL-4714).

Richt, A. E., Leiten, C. F., Beaver, J. (1962), in: *Res. Reactor Fuel Element Conf., Gatlinburg, TN, Sept. 17–19, 1962*, Vol. 2. Oak Ridge, TN: USAEC (TID-7642), pp. 469–488.

Runnalls, O. J. C., Boucher, R. R. (1965), *Trans. Met. Soc., AIME 233*, 1726–1732.

Saito, M., Futamura, Y., Nakata, H., Ando, H., Sakurai, F., Ooka, N., Sakakura, A., Ugajin, M., Shirai, E. (1989), *Further Data of Silicide Fuel for the LEU Conversion of JMTR*, presented at: *Int. Symp. Research Reactor Safety, Operations and Modifications, Chalk River, Ontario, Canada, Oct. 23–27, 1989*. Vienna: IAEA (IAEA-SM-310/59P).

Saller, H. A. (1956), *Int. Conf. on the Peaceful Uses of Atomic Energy*, Vol. 9, P/562. New York: United Nations, pp. 214.

Samoilov, A. G., Kashtanov, A. I., Volkov, V. S. (1965), Engl. Translation: Aladjem, A. (1968), *Dispersion-Fuel Nuclear Reactor Elements*. Jerusalem: Israel Program for Scientific Translations.

Samsonov, G. V. (Ed.) (1978), Engl. Translation, revised and corrected: Johnston, R. K. (1982), *The Oxide Handbook*, 2nd ed. New York: IFI/Plenum Data Co., pp. 20–31.

Sears, D. F. (1993), *Proc. Int. Mtg. on Reduced Enrichment for Research and Test Reactors, Newport,* *RI, Sept. 23–27,* 1990. Argonne, IL. ANL (ANL/RERTR/TM-18, CONF-9009108), pp. 33–42.

Sheldon, R. I., Peterson, D. E. (1989), *Bull. Alloy Phase Diagrams 10 (2),* 165–171.

Shepherd, L. R., Brown, P. E., Nabielek, H. (1982), *Gas-Cooled Reactors Today,* Vol. II. London: British Nuclear Energy Society, p. 123.

Shibata, T., Tamai, T., Hayashi, M., Posey, J. C., Snelgrove, J. L. (1984), *Nucl. Sci. Eng. 87,* 405–417.

Shimizu, H. (1965), *The Properties and Irradiation Behavior of* U_3Si_2. Canoga Park, CA: Atomics International (NAA-SR-10621).

Simnad, M. T. (1971), *Fuel Element Experience in Nuclear Power Reactors.* New York: Gordon and Breach.

Simnad, M. T. (1972), *Review of UZr-Hydride Driver Fuel Elements for Thermionic Reactors.* San Diego, CA: General Atomic Company (Gulf-GA-A11075).

Simnad, M. T. (1980), *The* $U-ZrH_x$ *Alloy: Its Properties and Use in TRIGA Fuel.* San Diego, CA: General Atomic Company (E-117-833).

Simnad, M. T., Foushee, F. C., West, G. B. (1976), *Nucl. Technol. 28,* 31–56.

Snelgrove, J. L. (1992), *Heat Transfer – San Diego 1992, AIChE Symp. Ser. No. 288,* Vol. 88. New York: AIChE, pp. 305–314.

Snelgrove, J. L., Domagala, R. F., Hofman, G. L., Wiencek, T. C., Copeland, G. L., Hobbs, R. W., Senn, R. L. (1987), *The Use of* U_3Si_2 *Dispersed in Aluminum in Plate-Type Fuel Elements for Research and Test Reactors.* Argonne, IL: ANL (ANL/RERTR/TM-11), pp. 22–23.

Stahl, D. (1982), *Fuels for Research and Test Reactors, Status Review: July 1982.* Argonne, IL: ANL (ANL-83-5).

Stewart, H. B., Dahlberg, R. C., Goeddel, W. V., Trauger, D. B., Kasten, P. R., Lotts, A. L. (1972), in: *Proc. 4th Int. Conf. on the Peaceful Uses of Atomic Energy,* Vol. 4. Vienna: IAEA, p. 433.

Taleyarkhan, R. P. (1990), *Proc. Int. Topical Mtg. on Safety, Status and Future of Non-Commercial Reactors and Irradiation Facilities, Boise, ID, Sept. 30 – Oct. 4, 1990,* La Grange Park, IL: American Nuclear Society, pp. 371–380.

Thümmler, F., Lilienthal, H. E., Nazaré, S. (1969), *Powder Metall. 12 (No. 23),* 1–22.

Thurber, W. C., Beaver, R. J. (1959), *Development of Silicon-Modified 48 wt.% U–Al Alloys for Aluminum Plate-Type Fuel Elements.* Oak Ridge, TN: ORNL (ORNL-2602).

Thurber, W. C., McQuilkin, F. R., Long, E. L., Osborn, M. F. (1964), *Irradiation Testing of Fuel for Core B of the Enrico Fermi Fast Breeder Reactor.* Oak Ridge, TN: ORNL (ORNL-3709).

Toft, P., Jensen, A. (1986), in: *Reduced Enrichment for Research and Test Reactors – Proc. of an Int. Mtg., Petten, The Netherlands, Oct. 14–16, 1985:* von der Hardt, P., Travelli, A. (Eds.). Dordrecht, The Netherlands: D. Reidel Publishing Co., pp. 373–381.

Une, K., Nogita, K., Kashibe, S., Imamura, M. (1992), *J. Nucl. Mater. 188,* 65–72.

Walker, C. T., Kameyama, T., Kitajima, S., Kinoshita, M. (1992), *J. Nucl. Mater. 188,* 73–79.

Werner, W. J., Barkman, J. R. (1967), *Characterization and Production of* U_3O_8 *for the High Flux Isotope Reactor.* Oak Ridge, TN: ORNL (ORNL-4052).

Whitcare, R. F. (1990), *The* UAl_x *Fuel Dispersion System.* Idaho Falls, ID: EG&G Idaho, Inc. (EGG-PRP-8783, Rev. 2).

Williams, R. K., Graves, R. S., Domagala, R. F., Wiencek, T. C. (1988), in: *Thermal Conductivity,* Vol. 19: Yarbrough, D. W. (Ed.). New York: Plenum Publishing Corporation, pp. 271–278.

Wood, J. C., Foo, M. T., Berthiaume, L. C. (1982), in: *Proc. Int. Mtg. on Research and Test Reactor Core Conversions from HEU to LEU, Argonne, IL, Nov. 8–10, 1982.* Argonne, IL: ANL (ANL/RERTR/TM-4, CONF-821155), pp. 57–74.

Woodley, R. E. (1986), *The Release of Fission Products from Irradiated SRP Fuels at Elevated Temperature – Data Report on the First Stage of the SRP Source Term Study.* Hanford, WA: HEDL (HEDL-7598).

Woodley, R. E. (1987), *Release of Fission Products from Irradiated SRP Fuels at Elevated Temperatures – Data Report on the Second Stage of the SRP Source Term Study.* Hanford, WA: HEDL (HEDL-7598).

Yeniscavich, W., Bleiberg, M. L. (1960), in: *Bettis Technical Review.* Pittsburgh, PA: Westinghouse Electric Company (WAPD-BT-20), pp. 1–21.

Zelenzy, W. F. (1964), in: *Annu. Prog. Rep. on Reactor Fuels and Materials Development for FY, 1964:* Graber, M. J., Zelenzy, W. F., Gibson, G. W. (Eds.). Idaho Falls, ID: Phillips Petroleum Company-Atomic Energy Division (IDO-17037), pp. 2–9.

General Reading

Frost, B. R. T. (1982), *Nuclear Fuel Elements – Design, Fabrication and Performance.* Oxford: Pergamon Press.

Holden, A. N. (1967), *Dispsersion Fuel Elements.* New York: Gordon and Breach.

Holden, A. N. (Ed.) (1968), *High-Temperature Nuclear Fuels.* New York: Gordon and Breach.

Holden, R. B. (1966), *Ceramic Fuel Elements.* New York: Gordon and Breach.

Samoilov, A. G., Kashtanov, A. I., Volkov, V. S. (1965), Engl. Translation: Aladjem, A. (1968), *Dispersion-Fuel Nuclear Reactor Elements.* Jerusalem: Israel Program for Scientific Translations.

DEVELOPMENT AND IRRADIATION PERFORMANCE OF URANIUM ALUMINIDE FUELS IN TEST REACTORS

FUELS

KEYWORDS: *dispersion nuclear fuels, test reactors, uranium alloys, aluminum alloys, fuel plates, fabrication, performance*

J. M. BEESTON, R. R. HOBBINS, G. W. GIBSON, and
W. C. FRANCIS* *EG&G Idaho, Inc., P.O. Box 1625*
Idaho Falls, Idaho 83401

Received July 9, 1979
Accepted for Publication December 19, 1979

Uranium aluminide powder production, fuel plate fabrication development, and irradiation performance of more than 1700 fuel elements during 10 yr of operational service at Idaho National Engineering Laboratory are discussed. The UAl_x dispersion fuel system has performed well in extended service in the high flux test reactors. The anticipated benefits of the powder dispersion form—accommodation of fission products in deliberate voidage, structural tolerance of fission gas, and dispersion of burnable poisons—have been realized. The operating limit for the Advanced Test Reactor fuel elements is presently set at 2.3×10^{21} fiss/cm^3 of core—a burnup of >500 000 MWd/MTU.

The growth or swelling of uranium aluminide fuel plates at up to 2.4×10^{21} fiss/cm^3 is proportional to the fission density, but the proportionality constant depends on the temperature, core porosity, and fuel loading with 93% enriched uranium. For a fuel loading of 4.3×10^{21} U atoms/cm^3, the growth corresponds to 0.11% per % burnup. The blister test as a criterion for impending fuel plate failure due to swelling appears adequate, and the blister temperature at fission densities of 2.7×10^{21} fiss/cm^3 of core is ~720 K.

I. INTRODUCTION

Prior to the development of the uranium aluminide (UAl_x dispersion) fuel system, the uranium aluminum alloy system had performed very reliably in the Materials Test Reactor (MTR) and the Engineering Test Reactor (ETR) at the Idaho National Engineering Laboratory (INEL), as well as in other reactors throughout the world. Three limitations precluded the direct application of the alloy for the high flux, high power Advanced Test Reactor (ATR) at INEL:

1. Fabrication and reprocessing techniques did not allow a high enough fuel content.
2. Swelling of the fuel limited the burnup.
3. A need existed to distribute uniformly small amounts of ^{10}B (burnable poison) in the plates.

Fuel consisting of uranium oxide powder dispersed in aluminum had been developed for the High Flux Isotope Reactor and the ATR (Ref. 1); however, concern with regard to exothermic reaction of the uranium oxide and aluminum[2] with subsequent initiation of aluminum-water (steam) reactions prompted development starting in 1962 at INEL of the uranium aluminide dispersion UAl_x fuel system.[3-5]

Several features of the UAl_x dispersion fuel system contribute to its extended performance capability in the high flux reactors:

1. The powder dispersion allows voidage to be fabricated into the fuel matrix for accommodation of the increased volume of fission products.
2. Burnable poisons can be readily dispersed in the fuel matrix.
3. The structure has exceptional tolerance for fission gas, with attendant high blister temperatures.

After powder uranium aluminides were developed for use in the ATR, they were subsequently used to fuel the MTR and ETR. The technology was further developed in Europe and the material is now used as the fuel for the French-German High-Flux Reactor.[6-] In the U.S., powder uranium aluminide fuels are being

---

*Retired.

used in other reactors. The material currently is in use in the Missouri University Research Reactor, the Massachusetts Institute of Technology Reactor-II, and the Ford Nuclear Reactor at the University of Michigan. Current work at INEL on this material seeks to develop even higher fuel loadings using lower enrichments of uranium aimed at providing greater safeguards for nonproliferation.

The purpose of this paper is to describe the material and fabrication development, and review the irradiation performance of the uranium aluminide dispersion system during 10 yr of operational service at INEL.

II. DEVELOPMENT AND FABRICATION EXPERIENCE

As shown in Table I, there are three uranium aluminide compounds with greatly differing properties. For a given uranium loading, the use of UAl_2 results in the lowest volume of hard brittle particles dispersed in the aluminum matrix in the fuel plate cores, and hence promotes the homogeneous dispersion of fuel particles within the fuel plate core during the fabrication of the fuel plates.

However, the early work in the development of a method for the preparation of uranium aluminide powders showed that fuel powders rich in UAl_2 were highly pyrophoric, while those rich in UAl_3 were only moderately pyrophoric. Moreover, either UAl_2 or UAl_3 reacts with an excess of aluminum at moderate temperatures to form UAl_4. Thus, the finished fuel plate cores, ready for reactor use, contain UAl_3 and UAl_4 as the fuel compound.[11]

It is difficult, if not impossible, to prepare pure uranium aluminide compounds by melting operations. The pure compounds can be prepared by the use of uranium hydride,[12] but this is not a commercially acceptable method for the preparation of nuclear reactor fuel materials because of the difficulties encountered in reprocessing the scrap materials, and because of the costs and hazards.

In a melting operation the scrap can be easily remelted. Due to the great differences between uranium and aluminum in melting temperatures and densities, care must be taken during the melting operation to ensure that complete alloying is achieved. In addition, uranium, aluminum, and the uranium aluminides are all highly reactive materials. To ensure that the final product is nuclear grade, precautions must be taken to prevent contamination of the fuel materials with oxygen, nitrogen, iron, copper, carbon, or any other detrimental foreign elements.

TABLE I

Properties of Uranium Aluminides (Ref. 10)

Compound	Theoretical Density (g/cm^3)	Uranium Content (g/cm^3)	Melting Point (K)	Crystal Structure
UAl_2	8.14	6.64	1863	FCC
UAl_3	6.80	5.08	1623	Simple cubic
UAl_4	6.06	4.16	1003	Orthorhombic

Since the uranium aluminides are friable materials, powders can readily be produced from the alloy castings by the use of conventional jaw crushers and hammer mills. The particles are sized by the use of metallic screens with oversize and undersize materials being recycled.

Compared to most commercial metallurgical operations, these powders are prepared on a very small scale. The size of the uranium aluminide powder operations is restricted by the high cost, high strategic value, and low demand for the fuel materials. In addition, nuclear criticality control and safeguarding problems tend to restrict the scale of operations.

A flow chart for a typical method for the preparation of the uranium aluminide powder is shown in Fig. 1. Table II shows the properties, both specified and typical, of powders produced by the process outlined in Fig. 1.

Figure 2 is a flow chart showing the method used for incorporating the fuel powders into finished plates. The process used is based on the well-established picture-frame process that has been used for more than 25 yr to produce aluminum-clad nuclear reactor fuel element plates. The fuel plate cores are made by powder metallurgy techniques instead of the formerly used wrought U-Al alloy. Fuel loading of 1.49 g $^{235}U/cm^3$ of core translates into 31 vol% of UAl_3 powder in the plate cores. Four to eleven percent voids are incorporated in the ATR fuel plate cores. As noted subsequently, these voids are important to the satisfactory performance of the fuel elements since they participate in reducing the swelling.

When making highly loaded aluminum-clad fuel plates with either wrought or powder metallurgy cores, core thickening (dogboning) has always been a problem. This proved to be the case when fabricating ATR fuel plates. The problem has been solved by use of shaped cores and improved inspection techniques. The original fuel plate fabrication process used core compacts with square corners and edges. The fuel plates had extremely thin cladding at the leading and trailing ends of the fuel plate cores. By changing the core compact to provide for tapered compact ends, the cladding was made uniform in thickness and the dogboning effect was reduced.

To ensure that the thin cladding problem remained under control, an ultrasonic inspection device was developed.[13] This machine, referred to as a

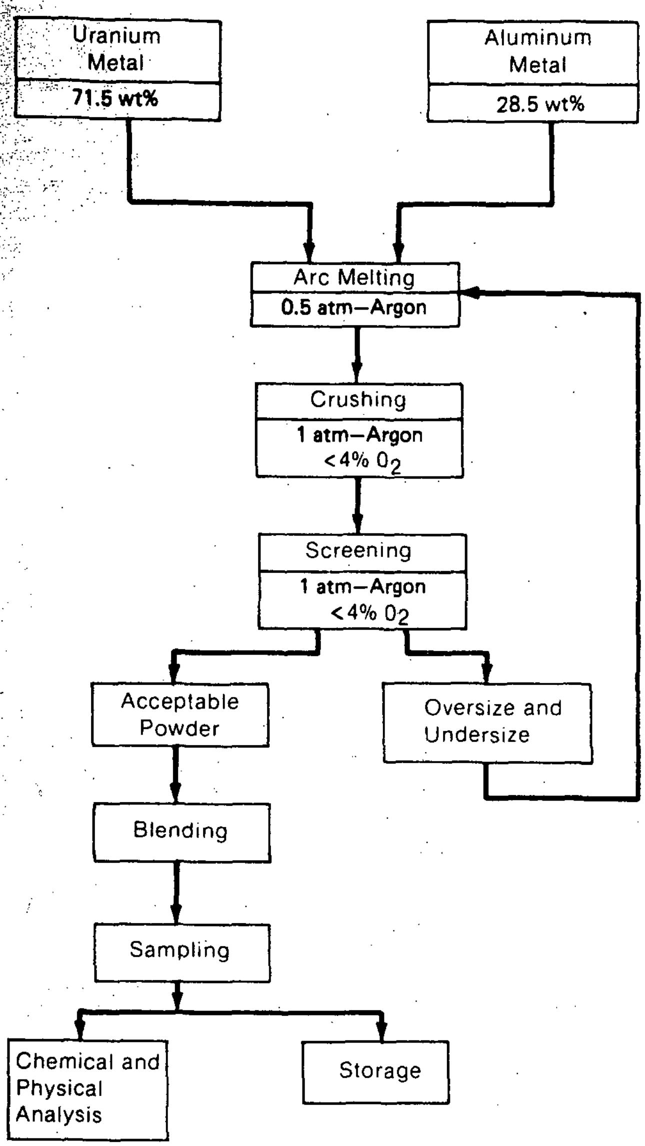

Fig. 1. Flow chart of uranium aluminide powder production process.

"min-clad gauge," has the ability to determine that at least 0.22 mm of cladding is covering the plate core. This device has been highly effective in detecting leak-prone fuel plates.

III. PERFORMANCE

Over 1700 plate-type uranium aluminide fuel elements have been operated in INEL test reactors (ATR, ETR, MTR) in the past 10 yr. Several measures of performance are mechanical and nuclear stability, radioactivity release, and fuel burnup. Two failure modes postulated with extended burnup of plate-type elements are

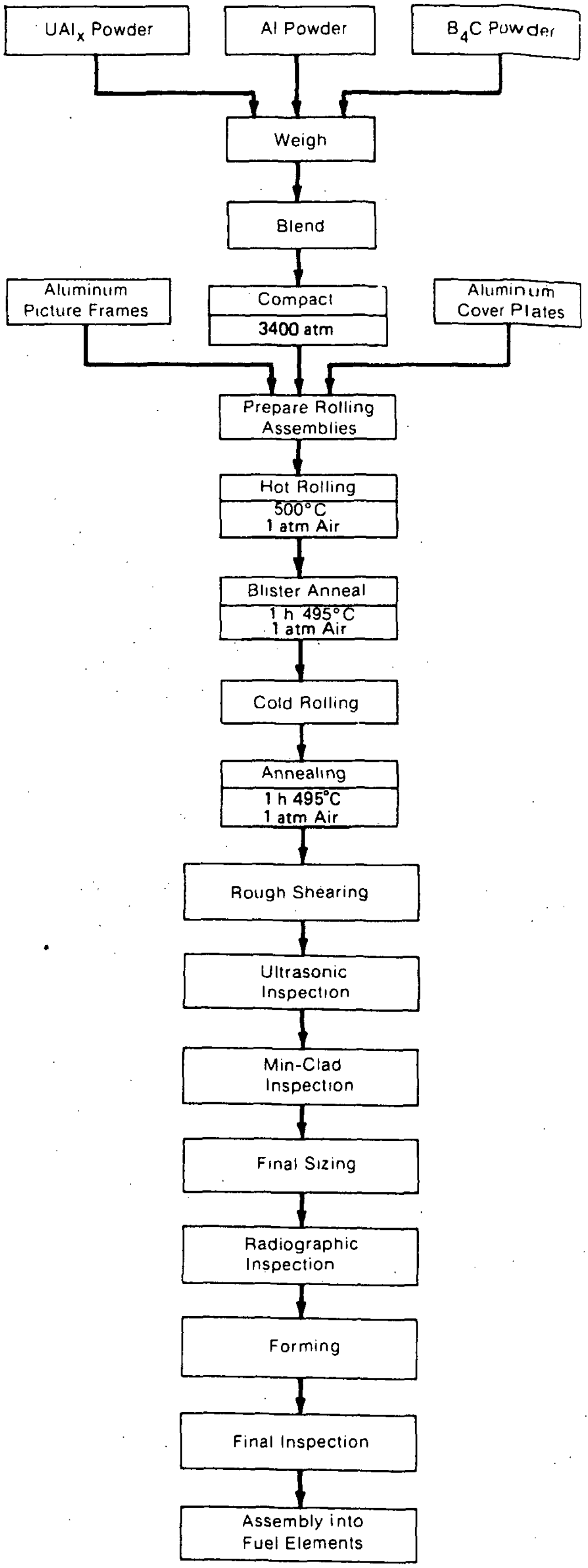

Fig. 2. Flow chart of a fuel plate production process.

TABLE II

Properties of Uranium Aluminide (UAl_x) Powder and Core Compacts

	Specified	Typical
Isotopic Composition:		
^{235}U content	93.0 ± 1.0 wt%	93.19
^{238}U content	6.0 ± 1.0 wt%	5.37
^{236}U content	0.3 ± 0.2 wt%	0.44
^{234}U content	1.2 maximum wt%	1.00
Chemical Composition:		
Uranium	69.0 ± 3.0 wt%	71.28
Oxygen	0.60 wt% maximum	0.25
Carbon	0.18 wt% maximum	0.05
Nitrogen	0.045 wt% maximum	0.032
Hydrogen	0.020 wt% maximum	0.005
Nonvolatile matter	99.0 wt% minimum	99.9
Easily extracted fatty and oily matter	0.2 wt% maximum	0.09
EBC[a]	30 ppm maximum	<6
Physical Properties:		
Particle size, U.S. standard mesh	−100 + 325 mesh = 75% minimum	76.0
	−325 mesh = 25% maximum	24.0
Crystalline constituents—by x-ray diffraction	50% UAl_3 minimum no unalloyed U	6% UAl_2 63% UAl_3 31% UAl_4
For ATR zone loaded core fuel loading, g ^{235}U/cm^3 core (maximum) wt% UAl_3 in core	1.0, 1.30, 1.60	46.4 54.4 62.8
Uranium concentration, U atom/cm^3 of core (maximum)		2.76×10^{21} 3.58×10^{21} 4.41×10^{21}

[a] EBC = equivalent boron content.

1. buckling due to axial compressive loads developed either from thermal stresses or irradiation growth stresses
2. blistering due to excessive fission gas buildup.

During inspection no difficulties have been encountered due to the presence of loose plates, and measurements for nuclear stability have not revealed any fuel element instability.

Of the 1700 fuel elements, 48 have been found to contain blistered fuel plates, nearly all during the first years of ATR operation. The investigations revealed that the blisters were associated with thin cladding over the ends of the plate cores. None of these plates had been "min-clad" inspected. The corrosion of the aluminum cladding and fuel particles close to the surface as a result of the high heat flux, 0.95 to 4.73×10^6 W/m^2 (0.3 to 1.5×10^6 Btu/h·ft^2), exposed small areas of the plate cores to the reactor coolant. The corrosion products produced in the reaction of both fuel core and cladding with coolant water occupied more volume than the original materials. Thus, small pimples or blisters were produced on the plate surfaces. The growth of these pimples was a slow process so that only small amounts of fission products were released. Consequently, the operation of the reactor was not interrupted.

The operating life of the fuel elements in the ATR is determined by the burnup limit. Fuel burnup is sometimes expressed as percent of the ^{235}U isotope fissioned, or percent of the total uranium, as well as the total fissions per unit volume (fission density). In this paper, the number of fissions per unit fuel plate core volume will be taken as the basic parameter. The reactor burnup limit has been extended in steps to a fission density of 2.3×10^{21} fiss/cm^3 of core. The burnup extensions were made possible as a result of the favorable irradiation performance data, some of which is presented herein. The data consist of postirradiation measurements, both destructive and nondestructive, made on fuel elements and on sample fuel plates.

III.A. Growth and Swelling

Fission results in solid and gaseous atom products. A potential exists for growth and swelling, both from these products and from chemical reactions that occur between the fuel and matrix. [Growth is defined as a change in shape with small change in volume, while swelling is defined as a change in volume (decrease in immersion density).] In the uranium aluminide fuel system, the differentiation of the amount of growth and swelling due to the mechanisms of atomic volume increase (two atoms replacing one), and displacement damage—defects, voids, vacancies, and interstitials—has not been accomplished. The swelling due to bubble formation (gas atom agglomeration) and volume changes from chemical reactions is not great in uranium aluminide fuels. Because of constraints in the fuel plates, growth of the fuel plate core occurs only in the thickness direction. It is recognized that the irradiation temperature has an influence on the swelling, and must be taken into account. For purposes of this paper, growth and swelling are treated together except for gas agglomeration (bubble formation).

Various studies[9,14-16] have been made of these effects on fuel plate or sample performance, and considerable experience with fuel element performance has been obtained. The swelling or growth due to atomic fission products either in solution or in precipitates is not easy to distinguish from incipient gaseous swelling. The gaseous atoms (krypton and xenon) constitute ~15% of the fission products, and it will be shown (Sec. III.C) that they are principally in *solution* in the microstructure. The *solid* fission product swelling would be expected to be proportional to the fission density less any volume accommodation from fuel core porosity. The accommodation of solid fission products in the core porosity appears to be related to the core temperature and fission rate.

It has been postulated[5,16] that fuel core porosity or void volume accommodates the increased atomic volume of the fission products so that the growth or swelling ($\Delta V/V$) can be given by

$$\frac{\Delta V}{V}\,\% = 6.4\%\, F/10^{21}\ \mathrm{fiss/cm^3} - Vp \quad , \qquad (1)$$

where

F = fission density (fiss/cm^3 of core)

Vp = core porosity or void volume (%).

It was, however, recognized that positive or negative swelling deviations might occur due to other factors. It was calculated[16] that complete reaction of UAl_3 to UAl_4 in a 63% UAl_3-Al matrix would result in a volume decrease of ~0.3%. Gas bubble formation appears[5] to be suppressed by the accommodation of the gaseous atoms (helium, xenon, and krypton) in the UAl_4 fuel particle, i.e., in solution. The swelling data[14,17-19] from four fuel elements and sixteen samples are represented by an empirical equation obtained by least-squares linear regression. The data are given in Table III and plotted in Fig. 3. The fission density has been corrected to the Nd(145 + 146) monitor (the most accurate monitor).[20] Some of the swelling values were averaged before being placed in the table (those for the same U-atom concentration and fission densities). The averaging reduced the scatter for core thickness measurements used in determining the vol% swelling. The empirical equation for 24 data points is given as

$$\frac{\Delta V}{V}\,\% = 2.6\%\, F/10^{21}\ \mathrm{fiss/cm^3\ of\ core} \quad ,$$

where the constants have been rounded to the nearest 0.1, hence the first term "a" of the linear equation $\Delta V/V = a + bF$ reduces to zero.

For high fuel loading plates (4.3×10^{21} U atoms/cm^3 of core) this swelling corresponds to 0.11 vol%/% burnup. A similar value was obtained[9] on sample fuel plates at low burnup (1.5×10^{21} fiss/cm^3 of core) and low temperature (343 K instead of 423 to 473 K). The constant (2.6% instead of 6.4%) corresponds to a relative atomic volume increase of 1.2, instead of 3.04 calculated in Ref. 5, which indicates (since two atoms are replacing one) that gas is not agglomerating. Another indication that gas is not agglomerating will be given in Sec. III.B. The burnup is proportional to fission density for constant fuel loading (Fig. 4), and hence the value of swelling (0.11%/% burnup) will vary with fuel loading. Although there appears to be an effect of core porosity on accommodation of the solid fission products, the growth begins at fission densities at

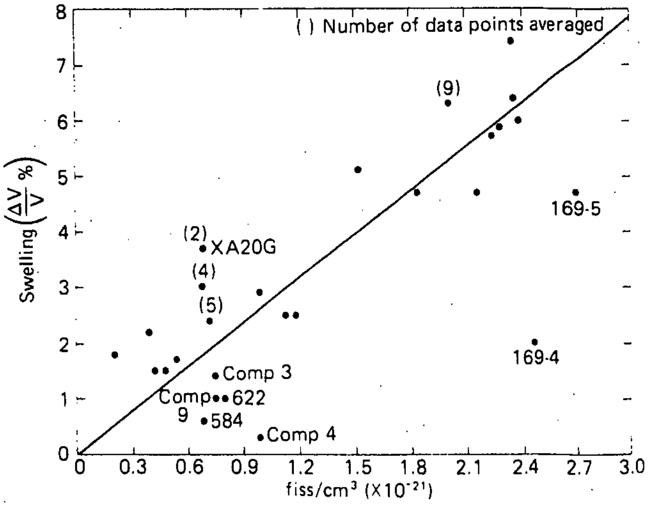

Fig. 3. Swelling of uranium aluminide fuel plates as a function of fission density.

TABLE III

Growth and Swelling of Fuel Plate Core and Samples

Element and Sample Number	U atom/cm^3 ($\times 10^{-21}$)	Fission Density ($\times 10^{-21}$)	Irradiation Temperature (K)	Core Porosity (vol%)	Swelling $\left(\frac{\Delta V}{V}\%\right)$	Reference
Comp 3	2.48	0.75	423-473	10.5	1.4	17
Comp 4	3.32	1.0	423-473	14.0	0.3	17
Comp 9	2.48	0.75	423-473	10.5	1.0	17
584	3.40	0.68	423-473	4.6	0.6	18
587	3.40	1.52	423-473	4.6	5.1	18
621	3.65	1.18	423-473	4.1	2.5	18
622	3.65	0.80	423-473	6.2	1.0	18
623	3.65	1.13	423-473	4.5	2.5	18
625	3.65	0.48	423-473	4.5	1.5	18
169-11	3.38	2.16	373-473	8.4	4.7	19
169-12	3.39	2.27	373-473	8.4	5.9	19
169-19	2.65	1.84	373-473	6.6	4.7	19
169-36	3.34	2.35	373-473	7.9	6.4	19
169-37	3.34	2.38	373-473	7.8	6.0	19
169-38	3.39	2.34	373-473	7.0	7.4	19
169-39	3.35	2.23	423-473	7.5	5.7	19
XA8G	2.69	0.72	423-473	3-11	2.4[a]	14
XA8G	3.39	0.99	423-473	3-11	2.9	14
XA20G	3.39	0.21	423-473	3-11	1.8	14
XA8G	2.69	0.40	423-473	3-11	2.2	14
XA8G	4.10	0.68	423-473	3-11	3.0[a]	14
XA8G	3.39	0.54	423-473	3-11	1.7	14
XA8G	4.10	0.42	423-473	4-11	1.5	14
Fuel elements						
XA130K&A135K	4.25	2.0	423-473	5.94	6.3[a]	19
169-4	4.22	2.46	423-473[b]	11.6	2.0	19
169-5	4.20	2.69	423-473[b]	12.0	4.7	19
XA20G	3.39	0.69	423-473	3-11	3.7[a]	14

[a] Averages of growth data on fuel elements where fission density is within 0.15 × 10^{21} fiss/cm^3.

[b] Temperature range is for fission densities between 1.2 × 10^{21} fiss/cm^3 and value given.

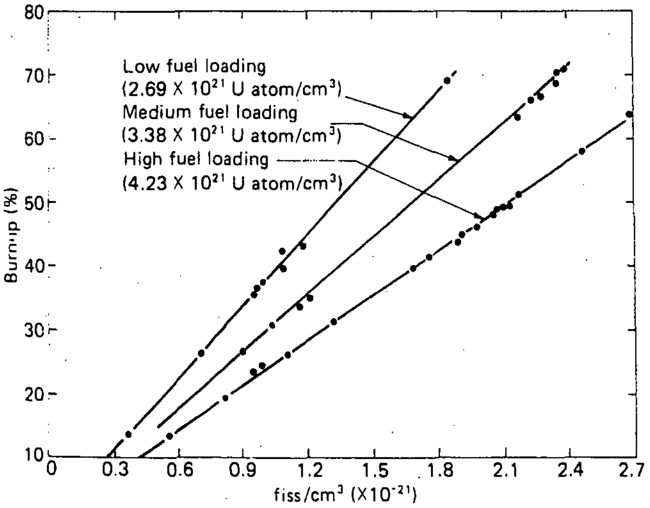

Fig. 4. Burnup of uranium aluminide fuel plate cores with different fuel loadings as a function of fission density.

which the pores have not filled. For example, for the core porosity of 4.6%, swelling by Eq. (1) should start at a fission density of 0.72 × 10^{21} fiss/cm^3, and, at higher core porosity, swelling should start at higher fission densities; however, Eq. (2) indicates swelling starts with fissioning.

Several parameters affect the scatter in the data of Fig. 3. These are

1. irradiation temperature (however, the data have been selected to be in a narrow temperature range, 373 to 473 K)
2. fuel loading (atom U/cm^3 of core)
3. core porosity.

The data in Fig. 3 and Table III indicate that increasing core porosity tends to reduce swelling. Three data points (169-4, 169-5, Comp 4), which have swelling values that lie well below the least-squares linear regression curve in Fig. 3, correspond to samples with high initial porosity (>11.6%) according to Table III. An effect of fuel loading is apparent from a regression analysis of the 17 data points in Table III at constant fuel loading. The analysis of these 17 points increased the correlation coefficient from 0.90 to 0.93 and decreased the standard error of estimate of Eq. (2). Figure 5, a plot of values of known core density and porosity of individual fuel plates, indicates that at constant core density the porosity increases with increased fuel loading. This relationship tends to reduce the scatter in Table III and Fig. 3 due to different fuel loadings.

Three data points from Table III and Fig. 3 (the last three in Table III) have not been included in the regression analysis for Eq. (2). If these three points are included, the curve is rotated clockwise, giving a positive swelling at zero fissioning (which is not realistic) and a lower slope. A statistical tolerance limit test (one-sided tolerance limit for normal distribution) was used to show that these three points lie beyond the values at which with 90% confidence 90% of the population will lie, hence it is probable that a factor other than that for the other 24 data points is influencing the swelling behavior of these samples. Examination of the porosity indicates that it is the likely factor. Two of the points have higher porosity than most of the data while the third is a composite (average of several samples). Hence, it is probable that the factor that reduces the swelling at high fission densities is the pore volume, which accommodates the solid fission products during the slowing down process of the fission fragments, i.e., the core behavior is plastic provided the temperature and fission rate are high enough.

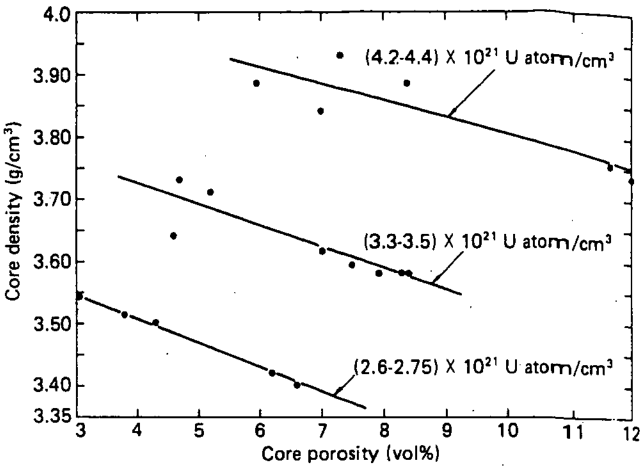

Fig. 5. Core density and porosity of uranium aluminide fuel plates with different fuel loadings.

III.B. Blister Testing

Postirradiation blister testing has been used as a criterion for predicting failure of the fuel elements. The assumption is that, as the concentration of the gaseous atoms (helium, xenon, krypton) increases and the pores or voids become filled, the temperature at which breakaway swelling occurs is decreased. The criterion should be conservative since, under irradiation, gaseous atoms in bubbles undergo resolution from the slowing down process of the fission fragments.[21,22,23] Resolution of fission gas bubbles up to 300 Å (30 nm) in diameter was reported[21] in UO_2 when irradiated at 373 K. The release of gas to the boundaries was shown[22] to be controlled by the irradiation resolution of bubbles. For the aluminide fuel the resolution mechanism will also apply and the blister temperature in-reactor should be equal to or greater than in postirradiation tests.

The postirradiation blister temperatures are given in Table IV and a least-squares regression analysis with proposed 2σ and 3σ limit curves is given in Fig. 6. The proposed limit curves are extended to a higher fission density from the fission density at the minimum value of the polynomial. The polynomial is given as

$$T_B = 905 - 139.9\,F - 44.8\,F^2 \quad , \tag{3}$$

where

F = units of 10^{21} fiss/cm^3

T_B = blister temperature in K.

Thus, up to a fission density of 2.7 X 10^{21} fiss/cm^3, the potential for swelling from gaseous atoms as measured in a blister test is not strongly influenced by burnup in the uranium aluminide fuels. The polynomial fit to the data gave a higher correlation coefficient (0.705) than either linear (0.04) or logarithmic regression analysis (−0.15), both of which indicated no drop-off in the blister temperature at high fission density. It is not physically realistic that the blister temperature would increase at fission densities beyond 1.5 X 10^{21} fiss/cm^3, hence it is

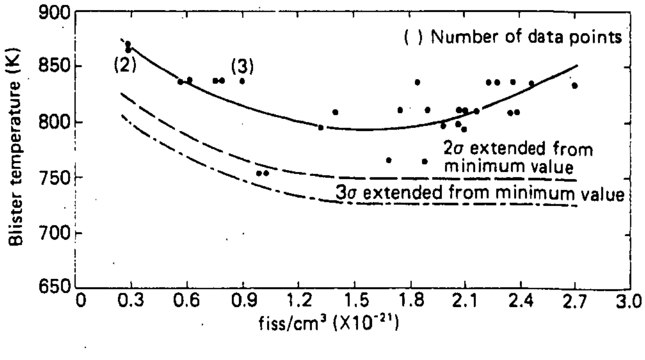

Fig. 6. Blister temperatures of uranium aluminide fuel plates as a function of fission density.

TABLE IV

Blister Temperatures for Fuel Elements and Samples

Element	Sample Number	^{235}U atom/cm^3 (X10^{-21})	Total U atom/cm^3 (X10^{-21})	Burnup (%)	Fission Density [fiss/cm^3 of core (X10^{-21})]	Temperature (K)
XA3G	2-21	2.50	2.69	37.0	0.98	755
	7-0	3.81	4.10	14.2	0.61	838
	7-7	3.81	4.10	18.8	0.79	838
	7-14	3.81	4.10	21.3	0.89	838
	7-21	3.81	4.10	21.3	0.89	838
	7-28	3.81	4.10	21.3	0.89	838
	7-35	3.81	4.10	18.0	0.75	838
	7-42	3.81	4.10	13.3	0.56	838
	15-25	3.81	4.10	33.3	1.40	810
	16-21	3.16	3.40	30.5	1.03	755
XA8G	7-T	3.81	4.10	6.7	~0.28	871
UAl$_x$-7F	11-T	3.81	4.10	6.7	~0.28	866
	11-B	3.81	4.10	6.7	~0.28	866
XA130K	0-7	3.96	4.26	13.2	0.56	---
	0-6	3.96	4.26	26.1	1.11	---
	0-5	3.96	4.26	39.7	1.69	767
	0-4	3.96	4.26	44.1	1.88	767
	0-3	3.96	4.26	46.2	1.97	800
	0-2	3.96	4.26	48.4	2.06	800
	0-1	3.96	4.26	49.8	2.12	---
XA135K	5-2	3.95	4.23	19.4	0.82	---
	5-3	3.95	4.23	31.3	1.32	797
	5-4	3.95	4.23	41.4	1.75	813
	5-5	3.95	4.23	44.9	1.90	813
	5-6	3.95	4.23	48.8	2.07	813
	5-7	3.95	4.23	51.4	2.17	813
	5-1	3.95	4.23	49.3	2.09	797
Sample	169-4	3.88	4.22	58.3	2.46	838
	169-5	3.86	4.20	64.0	2.69	838
	169-11	3.11	3.38	63.9	2.16	811
	169-12	3.11	3.39	67.0	2.27	838
	169-19	2.44	2.65	69.4	1.84	838
	169-36	3.11	3.34	70.4	2.35	838
	169-37	3.11	3.34	71.3	2.38	811
	169-38	3.14	3.39	69.0	2.34	811
	169-39	3.12	3.35	66.6	2.23	838

believed that the polynomial fit in the region beyond 1.5×10^{21} fiss/cm^3 is due to the limited amount of data. The limiting curves for 2σ and 3σ were extended as horizontal lines from the minimum values in Fig. 6.

The behavior in the blister tests whose gas atom concentration in the fuel core increases with fission density will be discussed. A gas atom concentration of 1 gas atom per 100 core atoms at a fission density of 2.1×10^{21} fiss/cm^3 of core was measured (Table V) by dissolution and mass spectrography.

With a model for gas behavior in UO_2 at low fuel temperatures, Nelson[23] indicates that the mobility of the inert gas atoms will be controlled by diffusion, the value of which is on the order of 10^{-17} cm^2/s. Nelson concludes that 50% of the gas is in bubbles and 50% in dynamic solution, and that the predominant mechanism by which gas reaches the grain boundaries is by atomic diffusion. In aluminide fuels the diffusion coefficient of helium gas in aluminum at 473 K is also ~10^{-17} cm^2/s (Ref. 24), and for xenon and krypton would be less. The blister behavior indicates that all of the gas is in dynamic solution at reactor shutdown since increasing gas concentration (fission density) does not reduce the blister temperature. Since the blister test is conducted by heating for 30 min in 30 K increments until blistering occurs, the nucleation rate of bubbles, instead of the diffusion rate, must be controlling the

TABLE V

Fission Gas Content

Sample	Tagged Atoms $\left(\frac{\text{fission gas}}{\text{fission}}\right)$	Total Atoms $\left(\frac{\text{fission gas}}{\text{fission}}\right)$	Total U atom/cm^3 of core ($\times 10^{-21}$)	Burnup (%)	Fission Density [fiss/cm^3 core ($\times 10^{-21}$)]	Fission Gas Atom Concentration $\left(\frac{\text{atom gas}}{\text{atom core}}\right)$
ENDF/V	0.1056	0.2727	---	---	---	---
XA130K#2	0.1085	0.3170	4.26	48.431	2.06	0.0105
XA130K#7	0.1068	0.2997	4.26	13.158	0.56	0.0029

blister temperature. For example, postirradiation annealing tests were run on UO_2, U_3O_8, and UAl_x fuel core plates. The results in Fig. 7 show the changes in core densities caused by 30-min incremental anneals.[5] The UO_2 plate blistered at the first temperature increment and the matrix cracked as a result of irradiation swelling. The U_3O_8 plates resisted blistering until the aluminum cladding had lost the major part of its strength (as a result of elevation of temperature), thus indicating that gross fuel particle-aluminum matrix separation had not occurred on this set of plates. The UAl_x plates showed the greatest resistance to blistering. Thus, the UO_2 behaved as if an appreciable amount of the gas (perhaps 50% as suggested by Nelson[23]) was in bubbles, while the U_3O_8 and UAl_x behaved as if all the gas were in dynamic solution.

The blister behavior of the UAl_x suggests that blisters should first form at boundaries at which nucleation would be enhanced, such as the pores that are added to accommodate the solid fission products.

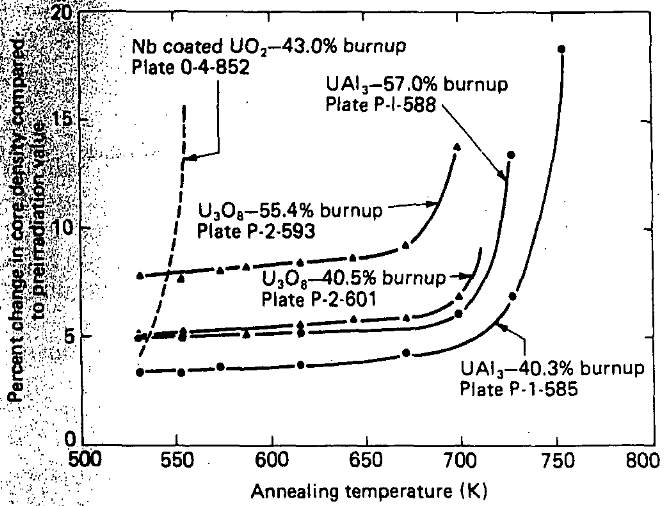

Fig. 7. Postirradiation annealing results of uranium aluminide plates compared with uranium oxide fuel plates.

Evidence of this behavior has been observed—blisters have formed at fabrication flaws or at the pores in low temperature and low fission rate regions on the fuel plates. The plates would be more susceptible to this type of failure if a gas concentration were built up (from nuclear reactions) before the pores were closed by the plastic core behavior. This evidence has been observed in some regions of plates where low temperatures and low fission rates prevail (for example, at the top or the bottom of the reactor core). Such evidence is shown in Figs. 8a and 8b.

III.C. Gas Content and Behavior

The principal gaseous atoms in nuclear fuels are krypton, xenon, helium, and hydrogen. The krypton and xenon are fission products and the helium and hydrogen are principally other nuclear reaction products from boron and impurities. The gas content is responsible for the swelling and blister behavior and some of the radioactive gaseous isotopes also affect reactor performance in that they are found in the stack release gases. The source of the fission gases, i.e., from tramp uranium or from fuel, is a broad subject, but the containment of the fission gases within the fuel plate core is a function of the gas retention behavior of the aluminide fuel and the aluminum cladding. A number of studies have been reported[5,25,26] that describe the gas retention behavior of the aluminide fuels. The gas retention has been attributed to the defect structure of UAl_4 (although UAl_3 also retains the gas) and to the porosity.

Fission gas retention in the fuel plate core, as indicated by the high gas concentrations reported in Table V (0.0105 represents 1 gas atom in 100 core atoms) has been confirmed in other ways.

First, two punchings from an ATR fuel plate were analyzed for krypton and xenon by mass spectrometry. One punching was in a low and the other in a high burnup portion of the plate. The punchings were chemically dissolved and the gases collected. The analysis was made for the isotopes by adding known quantities of ^{78}Kr and ^{129}Xe. The burnup

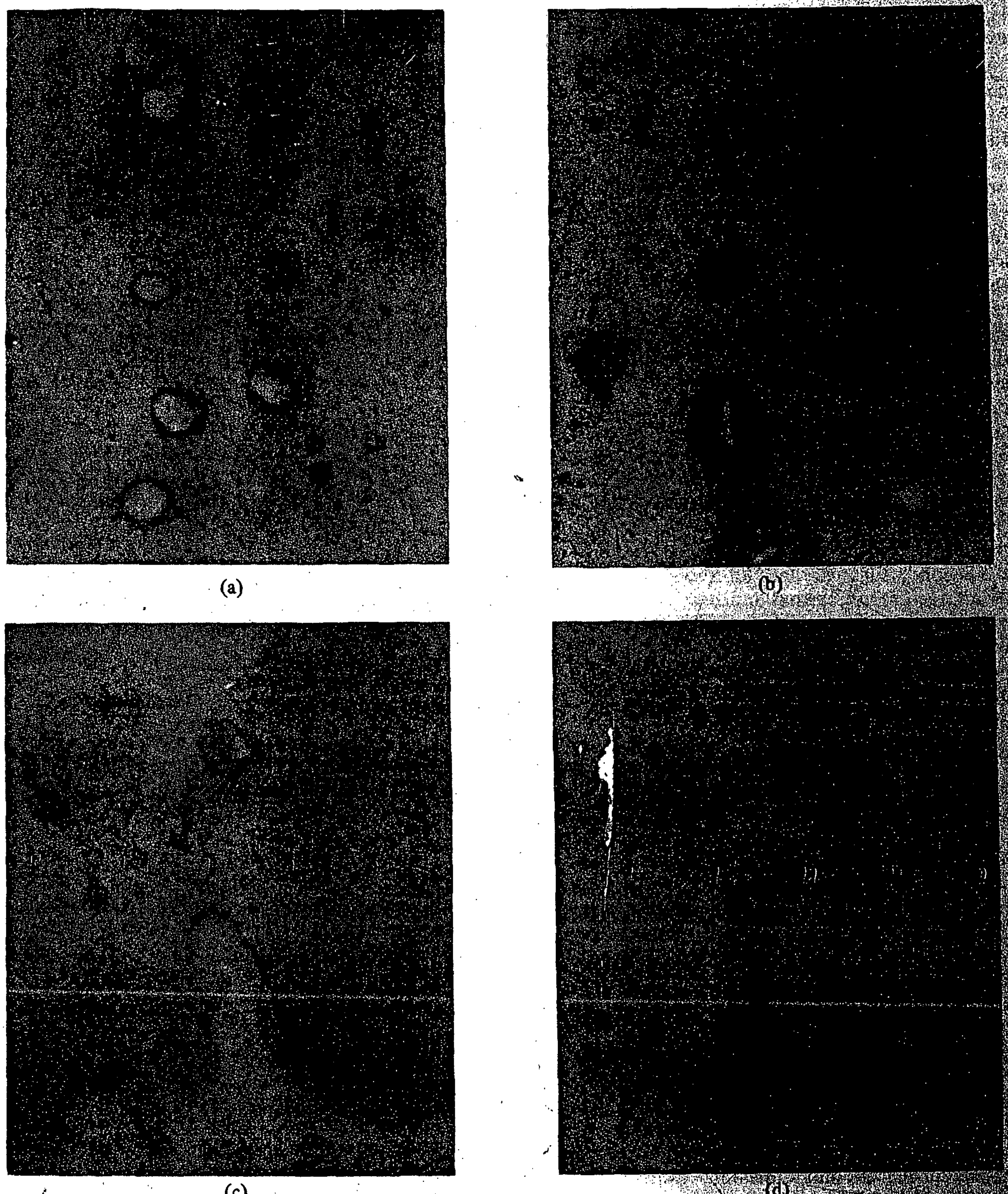

(a) (b)

(c) (d)

Fig. 8. Microstructures from three fuel element plates with various burnups: (a) and (b) a high porosity plate, (c) and (d) high fuel loading plates.

a. Fuel core—1.05×10^{21} fiss/cm^3. Pores = 10 to 20 μm diam. Immersion density = 3.05 g/cm^3. P.L. 500X.

b. Fuel core—0.67×10^{21} fiss/cm^3. Pores = 15 to 40 μm diam. Immersion density = 2.76 g/cm^3. B.F. 500X.

c. Fuel core—2.17×10^{21} fiss/cm^3. Pores = 10 μm diam. Immersion density = 3.09 g/cm^3. B.F. 500X.

d. Fuel core—1.11×10^{21} fiss/cm^3. Pore = 10 μm diam. Immersion density = 3.13 g/cm^3. B.F. 500X.

monitor used was Nd(145 + 146) (Ref. 20). The fission yields for the calculations were taken from the July 1977 Evaluated Nuclear Data Files (ENDF/B-V) compilation. The tagged atoms (the sum of which have small grow-in or burnout cross section) of the fission gas in Table V consist of Kr(83 + 84 + 86) plus Xe(131 + 132). The sum of these five gas nuclides should make a reliable indicator of burnup, which when compared with the burnup determined from Nd(145 + 146) would indicate any fission gas loss from the punchings.[27] The sums of the atoms of these five gaseous nuclides are divided by the total number of fissions as determined for Nd(145 + 146) and the results are given in Table V. The value of the ratio of fission gas per fission from ENDF/B-V is also given in Table V. The ratio for the low burnup punching is higher than the ENDF/B-V ratio by 1%, and that for the high burnup punching is higher by 3%. This difference is on the order of the errors of measurement. This close agreement between the yields of the gaseous nuclides and the yield of Nd(145 + 146) demonstrates that the loss of gas from the punchings was very small.

Second, Figs. 8c and 8d show that the microstructures of low burnup and high burnup fuel plate cores are not appreciably different, although the fission gas atom concentration in the high burnup punching is 1 gas atom in 100 core atoms while that of the low burnup is 1 gas atom in 345 atoms. It was seen in Fig. 6 that the threshold blister temperature is not appreciably different for these two burnups.

Third, it was found in an annealing experiment[25] that the principal release of fission gas from fuel pellets of UAl_4 or UAl_3 occurred at temperatures corresponding to the isothermal transformation in the U-Al phase system (for UAl_4 the major release was >1003 K and for UAl_3, it was ~1548 K). In annealing tests on aluminum-clad UAl_x dispersion-type fuel plates, the major part of the fission gas is released above the solidus temperature ~858 K of the cladding material[26] (at 873 to 943 K, ~99% of the Kr + Xe gas atoms are released with <1% released upon dissolution). The liquid aluminum undoubtedly reacts with the UAl_4 to release the fission gas at a lower temperature than the 1003 K peritectic temperature of UAl_4.

The gas atoms are thus retained in the irradiated fuel core structure, and do not agglomerate appreciably during 30-min annealing tests until a temperature of 720 K is reached.

III.D. Buckling Failure

Buckling due to axial compressive loads developed either from thermal stresses or irradiation growth stresses has not been detected in the ATR fuel elements or plates. In ETR fuel elements in which flat fuel plates were pinned instead of roll swaged to side plates so that axial slippage was restricted, some buckling was observed.

Thermal stresses are restricted by standard reactor operating practices. The result is that plate cores plastically flow before the plates buckle under loadings produced from differential thermal expansion. The buckling resistance is produced by bending stresses in the cladding. Under initial irradiation, in the ATR environment, the fuel plates heat up to 420 to 450 K while the side plates, heated by gamma absorption, operate at ~330 K (Ref. 15). This temperature differential results in a compressive loading on the fuel plates that produces a potential for yielding or buckling. The criteria for thermal stress loads that restrict yielding to the edges of the plates is evaluated by calculating thermal conditions at which the yield strength would be exceeded.

The irradiation swelling shown in Fig. 3 is expected to be isotropic, and would be ~6% at a fission density of 2.3×10^{21} fiss/cm^3 of core. This swelling represents a potential for yielding or buckling greater than from the thermal stress. However, the dimensional change is not isotropic. Because of the restraint in planar directions produced by the cladding, the dimensional change is virtually all in the thickness direction. The planar growth restraint results in compressive loading in the fuel core and tensile loading of the cladding material. Inasmuch as general stress conditions may have an effect on swelling, this compressive loading of the fuel core may provide a reason for the blister temperatures assuming the parabolic shape or leveling off as in Fig. 6, since annealing of the residual stresses might affect the nucleation mechanism. It has been shown[28,29] that tensile stress enhances swelling in irradiated steels, and it has been assumed[30] that compression stress reduces the swelling. Thus, a contributing factor for swelling in blister tests may be the temperature at which the residual compressive stress is relieved.

It is standard operating practice to require that the calculated thermal stress, for the operating conditions in the center half-span of the fuel plates, be at some margin below the unirradiated and irradiated yield strength of the fuel plate composite throughout the cycle. Some typical limiting strength values[19,31] are given in Table VI. The compressive yield strength values from the thinner cladding composite plates and the higher wt% UAl_3 fuel cores tend to be higher. There is an effect of irradiation initially to reduce the strength of the composite cold-worked plates (Type 1100-H12), and increase the strength of the Type 6061-0 plates. The limiting strength values (at minus sigma for more than one test) should be conservative since they include effects of irradiation, thick annealed cladding, and a low UAl_3 content fuel core.

TABLE VI

Typical Values Selected for Limiting Thermal Stress

Material	Temperature (K)	Limiting Strength (MPa)	Measured Compressive Yield Strength (MPa)	
			Unirradiated	Irradiated
ATR type 6061-0 clad	367 (200°F)	96	98.5	---
100-mil plate	422 (300°F)	90	91.0	---
35 wt% UAl_3	478 (400°F)	79	81.1	---
	533 (500°F)	44	44.8	---
50-mil 51 wt% UAl_3	478 (400°F)	---	---	120.6
3 to 14 × 10^{20} fiss/cm^3	533 (500°F)	47	47.3	82.7
	589 (600°F)	---	---	68.9
ETR type 1100-H12 clad				
35 wt% UAl_x	422 (300°F)	48	107	48.3
50-mil plate, unirradiated and	578 (400°F)	48	83	48.3
irradiated to 2 to 14 × 10^{20} fiss/cm^3	533 (500°F)	42	61	42.0

III.E. Release of Gases

The release of radioactive fission gases to the primary cooling water is detected by monitoring the stack gases. The subject is pertinent to the performance of fuel elements. The release of radioactive gases appears to be divided into two categories:

1. a background release that comes from tramp uranium, diffusion of the fission gases, and argon in the water
2. a release that comes from defected fuel elements (leakers, etc.).

The question of the irradiation enhancement of diffusion has been examined[32] and it appears that irradiation does not increase the diffusion of fission gases in fuel materials.

IV. DISCUSSION

Although the amounts of growth and swelling, because of their effect on the buckling or blister failure modes, are considered to be the limiting criteria determining the service life of the fuel elements, the low swelling and the anisotropic growth behavior (growth in the thickness direction) have not limited the service life.

In examining the swelling, % $\Delta V/V$ per % burnup (fission density), evidence has been presented to show that swelling is reduced by fuel core porosity. It has been estimated[5] that the growth rate without the presence of fuel core porosity should be ~6.4% × 10^{-21} fiss/cm^3 (0.27%/% burnup for the high fuel loading). The estimate is based on relative atomic volumes of the uranium and the fission products and neglects the effects of phase changes or chemical reactions. This growth rate is more than twice that determined for the data of Fig. 3. The growth does appear, however, to be proportional to the fission density, thus indicating that gaseous swelling, at least at the breakaway point, is not occurring. The fuel core acts to absorb the increased volume of solid fission products with an attending core thickness increase and without appreciable plate thickness increase. The core thickness increase is offset by the loss of cladding thickness from corrosion.

The accommodation of fission products in the porosity in UO_2–stainless-steel fuel has also been noted.[33-36] Low density (~85% theoretical) fuel particles were shown to undergo a lower growth than higher density fuel thus exhibiting the ability to utilize the voidage provided. The matrix appeared to force the UO_2 to swell into its own voidage showing a plastic core behavior, and particle cracking was reduced.

Although the potential for buckling from the growth process is greater than that from fuel plate thermal expansion, the measured changes of free-fuel plate length and width have been insignificant, and plate thickness has increased only ~25 to 50 μm over several measurements. The increase in core thickness can be explained by the plastic flow of the fuel core, accommodation of the solid fission products, and reaction with the matrix. The cladding has higher strength than the fuel core material, hence a tensile stress in the cladding and compressive stress in the fuel core with the displacements from the fission fragments causes the fuel core to yield plastically.

These compressive stresses in the fuel core may contribute to the low swelling and high blister temperatures.

V. CONCLUSIONS

1. The UAl_x dispersion fuel system has performed well in extended service in the high flux test reactors. The anticipated benefits of the powder dispersion form–accommodation of fission products in deliberate voidage, structural tolerance of fission gas, and effective dispersion of burnable poisons–have been realized. The operating limit for ATR fuel elements is presently set at 2.3×10^{21} fiss/cm^3 of core–a burnup of over 500 000 MWd/MTU.

2. The growth or swelling of uranium aluminide fuel plates at up to 2.4×10^{21} fiss/cm^3 is proportional to the fission density, but the proportionality constant depends on the temperature, core porosity, and fuel loading with 95% enriched uranium. For a fuel loading of 4.3×10^{21} U atom/cm^3 the growth corresponds to 0.11%/% burnup.

3. The blister test as a criterion for impending fuel failure due to swelling appears adequate, and the blister temperature at fission densities of 2.7×10^{21} fiss/cm^3 of core is ~720 K, at the 2σ value, a margin of 260 K greater than the peak operating temperature of the plates in the ATR.

4. The fission gas is principally retained in the fuel plate core.

5. Buckling as a failure mode for ATR fuel plates has not been observed, and the operating practice of limiting the calculated thermal stress values to a margin less than the yield strength appears adequate to prevent this failure mode.

6. Release of radioactive fission gas to the primary cooling water appears to be adequately prevented by cladding of uniform thickness (>0.2 mm).

ACKNOWLEDGMENT

This work was supported by U.S. Department of Energy Contract EY-76-C-07-1570.

REFERENCES

1. D. O. HOBSON, R. L. HEESTAND, and C. F. LEITTEN, Jr., "Fabrication Development of U_3O_8-Aluminum Composite Fuel Plate for the Advanced Test Reactor," ORNL-3644, Oak Ridge National Laboratory (1964).

2. J. D. FLEMING and J. W. JOHNSON, "Aluminum-U_3O_8 Exothermic Reactions," *Nucleonics*, **21**, 84 (1963).

3. G. W. GIBSON and W. C. FRANCIS, "Annual Progress Report on Fuel Element Development for FY-1962," IDO-16799, Idaho Operations Office Atomic Energy Commission (1962).

4. G. W. GIBSON, M. J. GRABER, and W. C. FRANCIS, "Annual Progress Report on Fuel Element Development for FY-1963," IDO-16934, Idaho Operations Office, Atomic Energy Commission (1963).

5. W. C. FRANCIS, Ed., "Annual Progress Report on Reactor Fuels and Materials Development for FY-1965," IDO-17154, Idaho Operations Office, Atomic Energy Commission (1966).

6. F. THÜMMLER, S. NAZARÉ, and G. ONDRACEK, "The Technology of UAl_3-Al Irradiation Test Plates," *Powder Metall.*, **10**, 264 (1967).

7. A. JESSE, G. ONDRACEK, and F. THÜMMLER, "Preliminary Studies of the Fabrication of UAl_4-Al Test-Plates by Powder-Metallurgical Techniques," *Powder Metall.*, **14**, 289 (1971).

8. S. NAZARÉ, G. ONDRACEK, and F. THÜMMLER, "Investigations on UAl_x-Al Dispersion Fuels for High Flux-Test Reactors," *J. Nucl. Mater.*, **56**, 251 (1975).

9. W. DIENST, S. NAZARÉ, and F. THÜMMLER, "Irradiation Behavior of UAl_x-Al Dispersion Fuels for Thermal High Flux Reactors," *J. Nucl. Mater.*, **64**, 1 (1977).

10. H. S. KALISH et al., "Uranium Alloys," in *Reactor Handbook*, Vol. I, *Materials*, p. 174, C. R. TIPTON, Ed., Interscience Publishers, Inc., New York (1960).

11. G. W. GIBSON, "The Development of Powdered Uranium-Aluminide Compounds for Use as Nuclear Reactor Fuels," IN-1133, Idaho Nuclear Company (1967).

12. H. J. EDING and E. M. CARR, "High Purity Uranium Compounds–Final Report," ANL-6339, Argonne National Laboratory (1961).

13. C. R. MIKESELL and D. C. ERDMAN, "Ultrasonic Examination System for Nuclear Fuel Plates," presented at 1971 National Fall Conference, American Society for Nondestructive Testing, Detroit, Michigan (October 18-21, 1971).

14. M. J. GRABER, G. O. HAYNER, R. R. HOBBINS, and G. W. GIBSON, "Performance Evaluation of Core II and III Advanced Test Reactor Fuel Elements," ANCR-1027, Aerojet Nuclear Company (1971).

15. M. L. GRIEBENOW, Ed., "ATR Extended Burnup Program," ANCR-1015, Aerojet Nuclear Company (1971).

16. M. M. MARTIN, A. E. RICHT, and W. R. MARTIN, "Irradiation Behavior of Aluminum-Base Fuel Dispersions," ORNL-4856, Oak Ridge National Laboratory (1973).

17. M. J. GRABER, G. W. GIBSON, V. A. WALKER, and W. C. FRANCIS, "Results of ATR Sample Fuel Plate

Irradiation Experiment," IDO-16958, Idaho Operations Office, Atomic Energy Commission (1964).

18. V. A. WALKER, M. J. GRABER, and G. W. GIBSON, "ATR Fuel Materials Development Irradiation Results–Part II," IDO-17157, Idaho Operations Office, Atomic Energy Commission (1966).

19. Unpublished Internal Data, EG&G Idaho, Inc.

20. W. J. MAECK, R. L. TROMP, F. A. DUCE, and W. A. EMIL, "Isotope Correlation Studies Relative to High Enrichment Test Reactor Fuels," ICP-1156, Idaho Chemical Programs, Allied Chemical Corp. (1978).

21. A. D. WHAPHAM, "Electron Microscope Observations of the Fission-Gas Bubble Distribution in UO_2," *Nucl. Appl.*, **2**, 123 (1966).

22. R. M. CORNELL, M. V. SPEIGHT, and B. C. MASTERS, "The Role of Bubbles in Fission Gas Release from Uranium Dioxide," *J. Nucl. Mater.*, **30**, 170 (1969).

23. R. S. NELSON, "The Stability of Gas Bubbles in an Irradiation Environment," *J. Nucl. Mater.*, **31**, 153 (1969).

24. C. J. SMITHELLS, Ed., *Metals Reference Book*, 5th ed., Butterworth and Co. Ltd., London (1976).

25. W. C. FRANCIS, "Metallurgy and Materials Science Branch Annual Report Fiscal Year 1970," IN-1437, Idaho Nuclear Company (1970).

26. W. C. FRANCIS and R. A. MOEN, "Annual Progress Report on Reactor Fuels and Materials Development for FY-1966," IDO-17218, Idaho Operations Office, Atomic Energy Commission (1966).

27. W. J. MAECK, W. A. EMEL, L. L. DICKERSON, J. E. DELMORE, J. H. KELLER, F. A. DUCE, and R. L. TROMP, "Discrepancies and Comments Regarding ^{235}U and ^{239}Pu Thermal Fission Yields and the Use of ^{148}Nd as a Burnup Monitor," ICP-1092, Idaho Chemical Programs, Allied Chemical Corp. (1976).

28. H. R. BRAGER, F. A. GARNER, and G. L. GUTHRIE, "The Effect of Stress on the Microstructure of Neutron Irradiated Type 316 Stainless Steel," *J. Nucl. Mater.*, **66**, 301 (1977).

29. J. F. BATES and E. R. GILBERT, "Experimental Evidence for Stress Enhanced Swelling," *J. Nucl. Mater.*, **59**, 95 (1976).

30. J. P. FOSTER and J. E. FLINN, "TC-160-18 Analysis of SA304L Capsule Residual Stress Data," *Cladding-Duct Materials Development Program Quarterly Technical Progress Letter* (July-Sep. 1978).

31. G. O. HAYNER, J. O. DITTMER, and R. D. PHIPPS, "A Determination of the Compressive Properties of Irradiated Nuclear Fuel Plates," *Trans. Am. Nucl. Soc.*, **12**, 559 (1969).

32. J. LETEURTRE and Y. QUERÉ, *Irradiation Effects in Fissile Materials Series of Defects in Crystalline Solids*, pp. 102-103, Elsevier North-Holland, Inc., New York (1972).

33. C. E. WEBER and H. H. HIRSCH, "Dispension Type Fuel Elements," in *Progress 12 Nuclear Energy*, Series V, *Metallurgy and Fuels*, H. M. FINNISTON and J. P. HOWE, Eds., McGraw-Hill Book Company, New York (1956).

34. J. D. B. LAMBERT, "Irradiation Study of UO_2-Stainless Steel and $(Pu,U)O_2$-Stainless Steel Cermet Fuels in Rod and Plate Geometry," *Proc. Conf. High Temperature Nuclear Fuels*, Delevan, Wisconsin, October 1966, CONF-661003-18, **42**, 237, American Institute of Mining and Metallurgical Engineers (1968).

35. D. H. GURINSKY, G. P. PANCER, and R. B. HOLDEN, "Studies on a Fuel for an Ordered Bed Reactor," *Conf. High Temperature Nuclear Fuels*, Delevan, Wisconsin, October 1966, CONF-661003-18, **42**, 467, American Institute of Mining and Metallurgical Engineers (1968).

36. M. J. GRABER and G. W. GIBSON, "Irradiation Testing of Fuel for the Mark I Core of the Argonne Advanced Research Reactor," IN-1160, Idaho Nuclear Company (1968).

Appendix B

De Walsche

Massachusetts Institute of Technology
Nuclear Reactor Laboratory
(Cambridge, MA, USA)

Institut National des Sciences et Techniques Nucléaires
CEN Saclay, CEA
(Gif-sur-Yvette, FRANCE)

Prediction of the Oxidation of the Fuel Clad and Consequences for the MITR Research Reactor

Research supervised by
Dr. J. Bernard
Dr. L.W. Hu
Mr. T. Newton

Cédric De WALSCHE **June1997**

ACKNOWLEDGEMENT

I would like to express my greatest gratitude to Dr. J. Bernard, Dr. L.W. Hu and T. Newton for their help and their guidance during this research. They always encouraged my work, provided me all the information I required and this experience at the Massachusetts Institute of Technology would not have been possible without their collaboration.

I also wish to express my appreciation to D. Brochard at the 'Commissariat a l'Energie Atomique' who allowed me to live this enriching experience and always provided me for help when needed.

TABLE OF CONTENTS

1. Introduction

The aim of this report is to present the work carried out during the internship that took place between April and June 1997 at MIT Nuclear Reactor Laboratory.

MIT Nuclear Reactor Laboratory is a part of the MIT Nuclear Engineering Department, which also includes:

- Laboratory for Accelerator Beam Applications
- Radiofrequency Accelerator Laboratory
- Nuclear Magnetic Resonance Laboratory
- Plasma Fusion Center
- Nuclear Reactor Laboratory

The MIT nuclear research reactor can be used by universities, industries and hospitals, for irradiation and experiment purposes. A notable example of reactor utilization is the program by Massachusets General Hospital to perfect the neutron capture treatment of glioblastoma (brain cancer). Other research fields are the applications of neutron activation analysis, biomedical research, neutron physics, nuclear physics, solid state physics or radiation effects...

1.1. Description of the MIT research reactor (MITR)

The MIT research reactor is a tank type reactor. It has an outer tank for the heavy water reflector and is cooled and moderated by light water. Originally, it was cooled and moderated by heavy water too but the present design allowed to increase significantly the thermal neutron flux in the reflector region where the experimental beam ports are located.
Designed to operate primarily at a rated power of 5 MW, MITR uses highly enriched (93%) uranium in the form of uranium aluminide (UAl_x). The core contains 24 rhombic shaped fuel element assemblies and 3 dummy elements (which can be sample assemblies). Each fuel assembly consists of 15 fuel plates. Fins along the aluminum fuel cladding allow to improve the heat exchange between the fuel and the coolant.
One regulating rod and six shim blades are used to control the rate of fission in the core. At 5MW, the reactor operates with a thermal flux of around 5.10^{13} $n.cm^{-2}.s^{-1}$, at a low temperature (<55°C) and at an atmospheric pressure.

1.2. Objectives of the study

The current license of MIT reactor will expire in 1999. In order to obtain a new license and improve its research capabilities, a large redesign effort is underway.
In the process of redesigning the reactor to increase the power to 10 MW (MITR-III), studies are being made about the extension of fuel element fission density limit. The Nuclear Regulatory Commission asked about the corrosion of the cladding and the effects of the oxide layer building on the surface of the finned clad.
The following questions were asked in 1991 ([1]):

- Do the new predictions of the oxide thickness lead to fuel temperatures above limits previously analyzed and approved for normal operation?
- Does the oxide thickness affects reactor responses to rapid insertions of reactivity?
- Can the oxide clog the grooves between the clad fins and if it is the case what are the consequences?

Besides, it was added that the value of the oxide thermal conductivity should be 1.3 Btu/hr-°F-ft instead of 2.0 Btu/hr-°F-ft as had been assumed in the previous studies.
The aim of the present study is to try to clarify these points, to predict the oxide layer thickness and its effects on the heat transfer in the core, and to determine if the oxide layer formation may have an influence on the fuel burn-up limit. As no precise study about this subject had been performed at MITR laboratory until now, it was asked for a physical description of the oxide building too, an interesting question being the influence of the pH.

1.3. Organization of this report

Chapter 2: Bibliographical research
First, a bibliographical research was performed in order to understand the physical mechanisms leading to the building of the oxide layer, to identify the important parameters influencing this phenomenon and to find the appropriate way to predict the oxide thickness and its effects.

Chapter 3: Effects of the oxide layer on the clad thermal behavior
Two-dimensional computations were performed to investigate the influence of the oxide layer on the heat exchange between the clad and the coolant. The results were compared with the one-dimensional analysis proposed by Taborda ([2]).
Sensitivity studies were also performed.

Chapter 4: Calculation of the oxide layer thickness in the hot channel
Correlations found in the literature were used to compute the distribution of the oxide layer in the hot channel that was identified as the critical area where the thickest oxide layer could be found.

Chapter 5: Influence of the oxide growth on the coolant velocity
The influence of the oxide formation on the coolant flow was investigated on the conservative assumption that no dissolution of the reacting aluminum occurred during the oxidation.

Chapter 6: Transient analysis
The initial steady state 2-dimensional program was adapted to study the influence of the oxide in the case of a rapid insertion of reactivity.

Chapter 7: Conclusions and recommandations

2. Bibliographical Research / Description of the oxide layer building

2.1. General behavior of the oxidation process

The fuel cladding of the MIT reactor consists of A-6061 aluminum. This material is a widely used medium-strength wrought Al-Mg-Si alloy. It typically contains 1% Mg, 0.6% Si, 0.25%Cr and 0.25% Cu.
Although aluminum is inherently highly reactive, it is resistant to significant oxidation because of the thin, highly protective product film formed under most exposures. This film remains less than one micrometer or so in thickness for all practical purposes in gaseous oxidants. The corrosion behavior in aqueous media, however, is known to be more complex, and reaction rates can vary from nil to rapid, depending upon the thermal, chemical and physical environment.
According to Godard [3], the rate of growth decreases with time and depends on the temperature, the oxygen content of the water, the ions present and the pH. As the MITR primary coolant is pure, the influence of aggressive ions like chlorides or copper is not to be expected. As far as the velocity of the fluid is concerned, it would have little influence in the pH range 4.5 to 7. Since MITR coolant pH is around 6-6.3, the fluid velocity is not to be considered as a determining factor.
The Pourbaix diagrams below are showing the nature of the oxidation products as a function of the potential and the pH. As we can see, the protective oxide of aluminum is being formed for pH values between 4 and 10 at 25°C, 3 to 8.5 at 60°C and 2.5 to 7 at 100°C. Outside this range of values, the corrosion of aluminum becomes intense since the oxide film loses its protective role and is dissolved quickly. Inside this range, the oxide film is stable and the oxide growth is relatively slow. The pH of the coolant in MITR is around 6-6.3 and no temperatures higher than 80°C are expected in normal conditions, so that the passivity requirements are fulfilled.

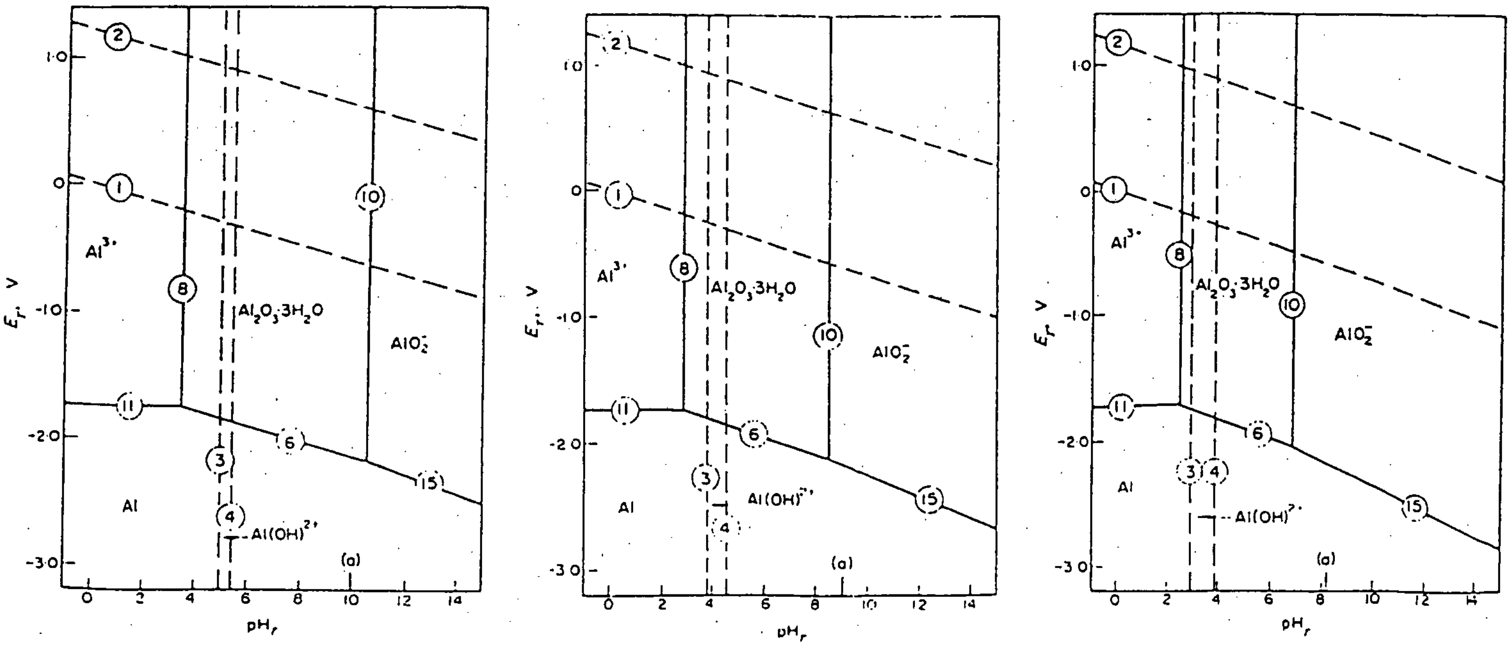

25°C

60°C

100°C

Figure 2.1 - Potential-pH diagrams for the Al-H_2O system at different temperatures [11]

Despite the presence of the oxide layer that acts as a protection against corrosion, cations and anions still diffuse across the oxide, which explains why the oxide thickness still increases and why a part of the reacting aluminum is dissolved in the coolant, as reported by Griess ([5],[6]) and Pawel ([8],[9]). Besides, one can understand that a temperature increase will make the ions diffusion easier hence an increase of the oxide growth. The pH will also affect the ion diffusion as ions, like H^+ and OH^- , have an important role in the corrosion mechanisms.

2.2. Nature of the oxide product

Several hydrated oxides of aluminum are known to exist in hydrothermal systems. These include gibbsite and bayerite $Al_2O_3.3H_2O$, boehmite and diaspore $Al_2O_3.H_2O$ and corundum Al_2O_3. According to Griess ([5]), boehmite is the substance that must be expected in MITR conditions. Other authors report that the nature of the oxide film is bayerite. According to Mac Donald ([11]), this lack of agreement is due to the tendency of the various oxides to exist as metastable phases. This behavior is particularly relevant to the corrosion of aluminum at temperatures below 150°C where it has generally been found that the passivating film consists of bayerite or boehmite rather than the thermodynamically stable gibbsite. The formation of these metastable products is in keeping with the following series of transformations:

$Al+3\ H_2O \rightarrow Al(OH)_3\ \text{(amorphous)} +3H^+$
$2\ Al(OH)_3 \rightarrow Al_2O_3.H_2O\ \text{(boehmite)}+2\ H_2O$
$Al_2O_3.H_2O\ \text{(boehmite)} + 2\ H_2O \rightarrow Al_2O_3.3H_2O\text{(bayerite)}$
$Al_2O_3.3H_2O\ \text{(bayerite)} \rightarrow Al_2O_3.3H_2O\ \text{(gibbsite)}$

The initial corrosion product $Al(OH)_3$ transformation into boehmite is fast while it has been found that transformations into bayerite and gibbsite are extremely slow.
The most recent experimental studies on the corrosion of 6061 aluminum under reactor heat transfer conditions were performed at Oak Ridge National Laboratory ([8]) in the corrosion loop specially designed for the Advanced Nuclear Source (ANS) project. The product film consisted mainly of boehmite.
Yet, the Idaho National Engineering Laboratory ([12]) reports to have identified amorphous aluminum oxide and bayerite on Advanced Test Reactor (ATR) and Engineering Test Reactor (ETR) fuel plate cladding at normal operating conditions, even at temperatures that would result in the formation of boehmite out of the reactor.

2.3. Effect of the pH

During the ANS corrosion tests, Pawel & al ([8]) report that at low coolant pH values (4.5-5.0) and "low" coolant inlet temperatures (<57°C), a thin iron-rich layer was generally found on the outer surface of the boehmite. The iron was thought to come from the piping corrosion and to act as a barrier against the diffusion of the oxidizing agents. Higher pH values (≅6) yielded comparatively high growth rates and little, if any, iron enrichment of the outer boehmite layer. The absence of iron in high pH cases would be due to the behavior change of iron solubility which is a function of the temperature and of the pH.

Besides, Pawel observed that a region of high pH sensitivity existed, leading to striking changes in rate as the pH is increased from slightly less than 5 to slightly more than 5. He also noticed that the effect of the pH was more important when the temperature increased.

These effects are illustrated by figures 2 and 3. The rate factor on the y-axis corresponds to the measured rate constant divided by the constant predicted by the 'correl 2' correlation established for a pH of 5. The 'correl 2' correlation was specially developed for the ANS design (see 2.4.1).

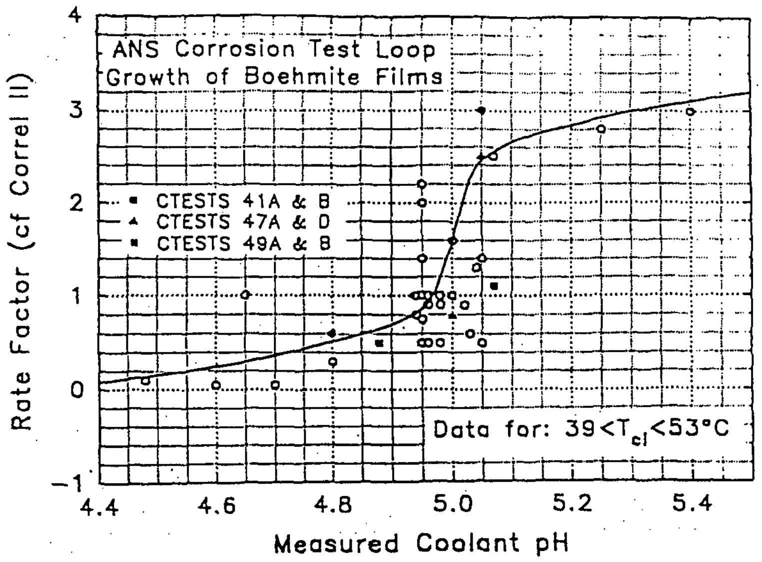

Figure 2.2 Rate constant for low inlet bulk temperatures (39-53°C) - ANS corrosion tests [7]

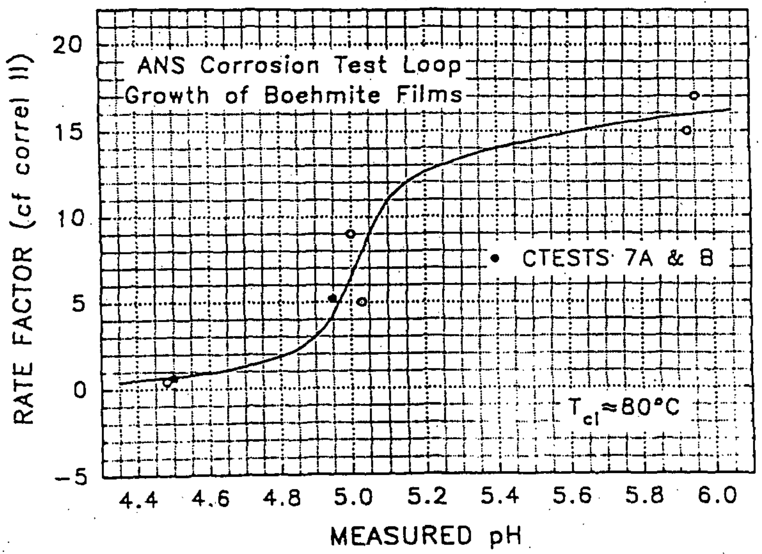

Figure 2.3 Rate constant for a high inlet bulk temperatures (80°C) - ANS corrosion tests [7]

As the high pH tends to increase the corrosion rate and the film growth., test reactors using aluminum clads, such as the High Flux Brookhaven Reactor, the Missouri University Research Reactor, etc, maintain the coolant pH at about 5 during normal operations.

The pH is generally lowered by use of nitric acid. In Brookhaven ([13]), the acid is continuously replenished to account for the removal by the resins in the primary loop purification system. The pH control and regulation is based on conductivity. The resins are replaced every 5-7 months.

2.4. Correlations used to predict the oxide film thickness in nuclear reactor conditions

2.4.1. Description

The complexity of the mechanisms leading to the oxide formation explains why laboratories developed empirical correlations to predict the oxide layer growth in nuclear reactor conditions. No satisfactory theoretical model seems to exist until today.

The correlations found in the literature are generally based on data found in ex-reactor conditions which approximately follow the common general equation:

$$\frac{dx}{dt} = \frac{k}{x^n}$$

where

x=film thickness (μm)
t=time (hour)
k=rate constant (μm^{n+1}/hr)
n=constant (mechanism number)

Many oxidation systems seem to follow this simple rate equation, with n=1 or 0.

The integrated equation takes the form:

$$x_t = \left[x_0^{n+1} + (n+1)kt\right]^{1/(n+1)}$$

where

x_t=film thickness at time t
x_0=film thickness at time t=0

The oldest correlation, developed by Griess ([6]), has been widely used to predict the extent of aluminum corrosion under various reactor conditions. It was obtained from a set of ex-reactor loop experiments, mostly 10 to 20 days in length, conducted with an average heat flux of 5.3 MW/m^2, average coolant velocity of 78°C. Griess correlation can be written in the form:

$$x_t = \left[x_0^{1.28535} + 1.28535\,kt\right]^{0.778}$$

k ($\mu m^{1.28535}$/h) is the rate constant and is given by an Arhenius type law:

$$k=1.2538.10^5 \exp(-Q/T_{x/c})$$

where

Q=5912.6 K

$T_{x/c}$=interface temperature (K)
T=time (h)

Although the heat flux is not a variable in this correlation, Griess remarked that at 1.6 MW/m^2, the oxide growth rate was about half of that observed at heat fluxes of 3 to 6MW/m^2.

This observation explains why Kritz considered the heat flux as a variable for his correlation. He proposed the same expression as Griess with:

$$k = 8.686\,\Phi^{1.2835}\exp(-2416.5 / T_{x/c}) \quad \mu m^{1.28535} / h \qquad [8]$$

where Φ=heat flux, MW/m^2

A recent correlation for certain ANS data, called "ANS Correlation II" (Correl 2) is:

$$x_t = \left[x_0^{1.351} + 1.351\,kt\right]^{0.74}$$

where

$$k=6.992.10^5 \exp(-7592/(T_{x/c}+10\Phi))$$

A limiting requirement of these correlations is that the pure coolant water pH be maintained around 5 by adding nitric acid. According to Griess observations, k should be multiplied by 3.6 for higher pH values between 5.7 and 7.

The following table summarizes the conditions in which each correlation was established.

Correlation	Aluminum alloy	Coolant velocity (m/s)	Inlet temperature (°C)	Bulk temperature (°C)	Oxide/coolant interface temperature (°C)	Heat flux (MW/m^2)	pH
Griess	6061-1100	10.7-15.5	66-94	66-120	136-174	3.20-6.30	5-7
Kritz	1100	9-15	-	-	90-140	0.057-5.70	5-5.20
Correl 2	6061	25-28	39-49	45-82	95-200	6.20-20.00	5

It is important to note that in each case, the studied aluminum cladding was non-finned. Besides, the investigated range for the heat flux was generally much higher than in MITR (less than 1MW/m^2 for MITR-III)

2.4.2. Comparison

During ANS corrosion loop tests, the different correlations quoted above were compared. It was found that the predictions varied widely from a correlation to another, which justified the development of "Correl 2" correlation for own ANS purposes. A few tests were performed on 8001 Al, whose behavior turned out to be very similar to 6061 Al.

Figure 4 below illustrates the results obtained on 8001 Al with a high coolant pH (6±0.2), an inlet bulk temperature of 65°C, a heat flux of 1.0 MW/m^2 and an oxide/coolant temperature of 111°C (for a slightly pressurized system). The oxide thickness is determined by the temperature drop across the film by assuming the boehmite conductivity of 2.25 W/mK. This test appears as one of the ANS tests the closest to MITR

conditions, especially as far as the pH and the heat flux are concerned. The coolant pH during the early part of this test was about 5.8, increasing to about 6.2 in the latter stages. According to Pawel, the increasing pH has probably influenced the film growth kinetics so that the usual decreasing rates found in the other tests (cf figure [2.4]) is not observed. It seems indeed that the growth rate suddenly changes after ≅850 hrs.
According to this result that shows a seemingly good agreement between the experimental data and the Griess and Kritz correlations, it would be tempting to use them for MITR-III oxide film calculations, even if the oxide/coolant temperature is higher than the expected value. On the contrary, the "Correl 2" correlation seems to underestimate significantly the oxide growth for low heat flux values like in MITR.

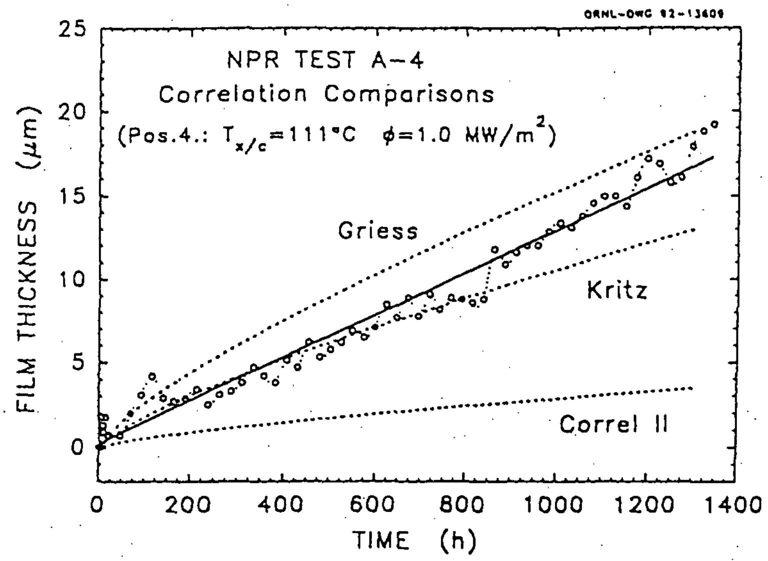

Figure 2.4 Experimental film growth and comparison to classical correlations [9]
Heat flux of 1MW/m^2 - Oxide/coolant temperature=111°C

2.5. Oxide thickness limits

The question is to know what is the maximum oxide thickness which can be accepted for MITR-III conditions.
The two potential major fuel assembly problems for common reactors are the structural failure due to overheating of the fuel plates, and the fission product release after spallation, that is the flaking or sloughing of some significant fraction of the oxide layer that can lead to clad deterioration.

2.5.1. Oxide thermal effects

The oxide film represents an added thermal resistance that leads to an increased temperature in the fuel and in the aluminum clad.
Although aluminum melts at about 660°C, it begins to soften significantly at approximately 450°C, which can be considered as the maximum temperature guaranteeing the cladding integrity. Besides, Beeston&al ([19]) report that the temperature limit for the UAl_x fuel is about 470°C. This temperature corresponds to a

fuel blistering due to excessive fission gas buildup and is valid for UAl_x fuels up to fission densities of 2.7×10^{21} fissions per cm^3 (the current burn up limit for UAl_x fuel is 1.8×10^{21}).

In high flux reactors, one cmay fear that the fuel temperature limit be exceeded, because of the high heat flux values and the low oxide thermal conductivity (2.25W/mK according to Griess). For MITR III, though, the maximum heat flux value is about $1MW/m^2$, so that the expected temperatures in the clad and the fuel for usual values of oxide film thickness (around 50 μm at most) should remain very far from the limits.

Yet, the presence of the oxide film may have an effect on the heat transfer performance of the finned cladding, as Taborda ([2) and Para ([14]) remarked. This point will be investigated more precisely in chapter 3.

2.5.2. Spallation.

An important issue of engineering concern is the spallation of the oxide film.

Spallation results in a very rough surface (in comparison to unspalled regions), and tends to decrease the average oxide thickness and therefore the thermal resistance imposed by the oxide film. However, particularly for 6061 Al, this phenomenon may increase the resistance to heat flow and threaten the integrity of the cladding since it is often accompanied by structural damage of the aluminum in the form of blisters or subsurface reaction products and voids. It could eventually lead to fission gas release in the coolant.

According to Yoder ([15]), spallation may be associated with the migration of hydrogen released during the oxidation process which leads to rapid intergranular corrosion.

Pawel & al([8]), for experiments performed on 6061 Al at high heat fluxes (6-20 MW/m^2) and coolant velocities (to 28m/s), insisted that spallation was due to stresses by thermal gradients and found that no spallation was observed until the temperature difference across the oxide film, ΔT, reached a certain range. The minimum value for which spallation occurred was 119K, even if the experimental range of ΔT was wide.

Griess ([5],[6]) reported spallation for several alloys at about 2mils (50 μm), which, according to Yoder, corresponds to roughly the same temperature drops in the oxide.

2.6. Conclusions for MITR-III

The bibliographical investigations show that it is impossible to predict the oxide layer buildup in a reactor by a theoretical model. Yet, three empirical correlations, used for in-reactor prediction of aluminum oxidation, are available.

The characteristics of MIT reactor that make the applicability of these correlations difficult to predict are:

- its high pH (6-6.3).
- its low coolant velocity (<4.5 m/s)
- the presence of fins on the fuel clad

To take the pH effect into account, a correction factor of 3.6 for the oxide growth rate constant k (2.4.1) is to be used in the Griess and Kritz correlations. Besides, a correction factor of 4.5 is proposed in the current study for "Correl2" correlation by extrapolating linearly the results showed in figure 2.2 for a pH of 6.3.

Although the mechanisms leading to oxide spallation are still not totally understood, an oxide thickness limit of 2mils (50μm), as proposed by Griess, allows to prevent any spallation phenomenon. This value can seem to be very conservative, since the heat flux in MITR-III is very low in comparison with Griess or Pawel tests and the actual temperature drop in the oxide film is far below the spallation temperature drop of 113°C proposed by Pawel. This is all the more true as the low fluid velocity (around 4m/s at most) should

reduce the risks of spallation. Still, this conservatism is supposed to reflect the uncertainties linked to the high pH effects and the finned geometry of the fuel cladding.
Besides, the finned geometry of the clad should not affect the availability of the correlations used as long as the oxide film is thin enough. As the fins width and length is 10 mils (0.25 mm), a 2 mil thickness limit seems to be appropriate too.

3. Effect of the oxide layer on the heat transfer in MITR clad

3.1. Introduction

MITR fuel elements consist of finned plates held by two side plates. The fuel is highly enriched (93%) uranium aluminum alloy clad with 15 mils of 6061 aluminum. 10 mil high rectangular fins extend the heat transfer area of the cladding surface, allowing high power density without nucleate boiling in the core channels.

For a system as shown in figure 3.1 subjected to a constant heat flux q_B at the back surface to be convected into a coolant, a heat balance yields:

$$q_B = h\,(T_W - T_b)$$

where h is the convection coefficient
T_W is the exposed plate surface temperature
T_b is the coolant bulk temperature

The presence of the fins (figure 3.2) requires introduction of a correcting factor η_0, called "surface effectiveness", which represents the ratio of the heat dissipated by a finned surface to the heat dissipated by an unfinned surface at the same conditions of temperature and heat transfer coefficients:

$$q_B = \eta_0\, h\,(T_W - T_b)$$

The question is to determine η_0 in the case of a finned clad covered by an oxide layer.

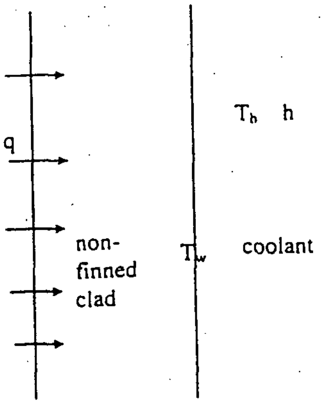

Figure 3.1

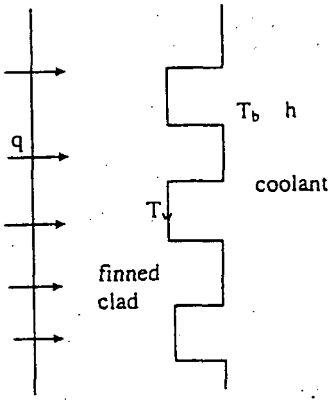

Figure 3.2

3.2. One dimensional analysis

Taborda ([2]) has proposed the following one dimensional analysis for MITR-II.

3.2.1. Fin without oxide layer

If the heat convected through the fin is considered as a one-dimensional conduction problem, the profile of temperature changing only with x along the length as in figure 3.3, an energy balance in an element of thickness dx of the fin can be made, assuming a steady state:

$$-(k \operatorname{div} T)\ A\,dx + h\,(T - T_b)\,P\,dx = 0.$$

[diffused energy + convected energy = 0]

or $\dfrac{d^2\theta}{dx^2} = m^2\theta$

where

k is the conductivity
P=2(2t+w) is the perimeter of the fin
A=2tw is the fin surface area
$m^2 = \dfrac{hP}{kA} \approx \dfrac{h}{kt}$ for $w >> t$
$\theta(x)=T(x)-T_b$

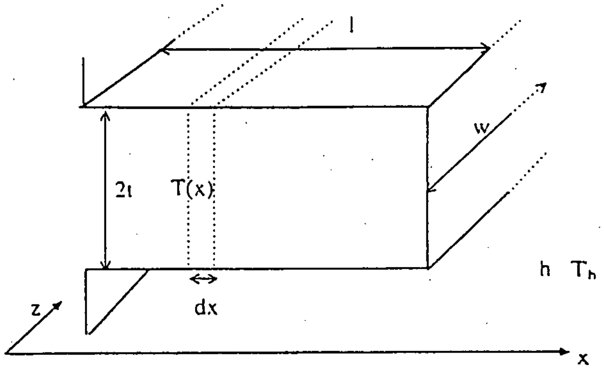

figure 3.3

Considering the boundary conditions $\begin{cases} \theta(x=0) = T_w - T_b = \theta_w \\ -k \left.\dfrac{d\theta}{dx}\right|_{x=l} = h\ \theta|_{x=l} \end{cases}$, the solution is:

$$\theta(x) = \theta_w\ \frac{\cosh m(l - x) + mt \sinh m(l - x)}{\cosh ml + mt \sinh ml}$$, where $\theta_w = T_w - T_B$

The total heat dissipated by the fin is:

$$Q_{fin} = -kA\left.\frac{d\theta}{dx}\right|_{x=0} = \theta_w \sqrt{hkAP}\ \frac{\sinh ml + mt \cosh ml}{\cosh ml + mt \sinh ml}$$

Let us introduce the fin efficiency η_f, defined as the ratio of the heat dissipated by the fin to the heat dissipated if the entire fin surface was at the base temperature T_w:

$$\eta_f = \frac{1}{m(l + t)}\ \frac{\sinh ml + mt \cosh ml}{\cosh ml + mt \sinh ml}$$

As the magnitude of mt is small, we can make the following approximation:

$$\eta_f = \frac{1}{m(l+t)}\ \frac{\sinh ml \cosh mt + \sinh mt \cosh ml}{\cosh ml \cosh mt + \sinh mt \sinh ml} \approx \frac{\tanh m(l+t)}{m(l+t)}$$

This approximation represents an error of only 0.2% for the following values:
h=10000
l=2.54e-4
t=l/2

The concept of fin efficiency can be used to model the surface effectiveness. Indeed, the heat flux q_B is dissipated either by a fin or by the base of the clad and an energy balance yields:

$$q_B A_B = h\,\theta_w(\eta_r A_f + A_u)$$

where A_f=2tw is the area of the finned part of the clad and A_u =2uw is the area of the unfinned part, A_B=A_f+A_u.

$$\text{We deduce: } \eta_0 = \frac{\eta_f A_f + A_u}{A_B} \approx \frac{\dfrac{\tanh m(l+t)}{m} + u}{u+t} \quad \text{for } mt \ll 1$$

Besides, the resolution of the heat equation in the internal region of the plate allows to express the temperatures in the clad as a linear function of x.

$$\begin{cases} \Delta\theta = \dfrac{d^2\theta}{dx^2} = 0,\ x \le g \\ \theta(x=0) = \theta_B = T_B - T_w \\ q_B = \eta_0 h \theta_w \end{cases} \text{, hence } \begin{cases} \theta = \theta_w + \theta_B(1 - x/g),\ \ x \le g \\ \theta_w = \dfrac{q_B}{\eta_0 h} \\ \theta_B = q_B\left(\dfrac{1}{h\eta_0} + \dfrac{g}{k}\right) \end{cases}$$

3.2.2. Effect of the oxide layer

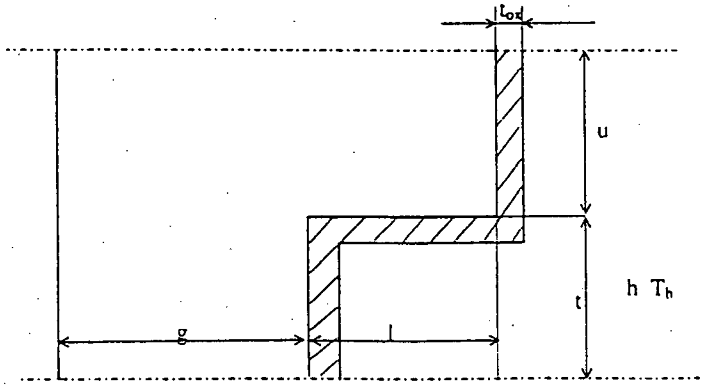

figure 3.4

If we consider now a fin covered by a thin uniform oxide layer (cf figure 3.4), whose thickness and conductivity respectively are t_{ox} and k_{ox}, the same heat balance as previously made for a clean fin yields:

$-(k \operatorname{div} T)\, A\, dx + \dfrac{(T - T_b)}{\frac{1}{h} + \frac{t_{ox}}{k_{ox}}} P\, dx = 0$, if we neglect the longitudinal heat conduction through the oxide layer.

Defining an equivalent convection coefficient $h' = \dfrac{1}{\frac{1}{h} + \frac{t_{ox}}{k_{ox}}}$ and a parameter $m' = \sqrt{\dfrac{h'P}{kA}}$, and by analogy to the case without oxide layer, the same solution applies for θ and η_f', the new fin effectiveness:

$$\theta(x) = \theta_w \frac{\cosh m'(l - x) + m't \sinh m'(l - x)}{\cosh m'l + m't \sinh m'l}$$

$$\eta_f' = \frac{1}{m'(l + t)} \frac{\sinh m'l + m't \cosh m'l}{\cosh m'l + m't \sinh m'l} \approx \frac{\tanh m'(l + t)}{m'(l + t)}$$

Still assuming a monodimensional conduction, the presence of the oxide layer can be considered as a simple additional thermal resistance at the fin base:

$$k_{ox} \frac{T_w - T_c}{t_{ox}} = h(T_c - T_b)$$

The same analysis as previously applies, and by analogy:

$$q_B A_B = h\, \theta_c (\eta_r' A_f + A_u), \text{ where } \theta_c = T_c - T_b$$

Hence, we have:

$$q_B = h'\eta_0'\theta_w \text{ and } \eta_0' = \eta_f' \frac{A_f}{A_B} + \frac{A_u}{A_B} = \frac{\tanh m'(l + t)}{m'(u + t)} + \frac{u}{t + u}$$

where η_0' is the surface effectiveness for an equivalent convection coefficient $h' = \dfrac{1}{\frac{1}{h} + \frac{t_{ox}}{k_{ox}}}$.

3.2.3. 1-dimensional results

The following 1-dimensional results are obtained for the Griess oxide conductivity of 2.25 W/m^{2}K
Still according to Griess observations (high flux reactor), it was assumed that the oxide thickness was equal to the transformed aluminum thickness. According to Griess, it means that approximately 50% of the reacting aluminum atoms are dissolved in the coolant, as boehmite density is lower than aluminum density.
We can observe a decrease of the fins efficiency for increasing values of the heat transfer coefficient. It is due to the fact that a higher value for h represents a better cooling of the fin and a decrease in the temperature along the fin. This temperature reduction means a higher heat flux at the fin base and thus a lower surface effectiveness. The selected values for h, from 20000W/m^{2}K to 40000W/m^{2}K, are supposed to cover the range of values expected for MITR-III.
The effect of the oxide layer thickness is more surprising as 1-dimensional analysis predicts that the presence of the oxide film tends to increase the surface effectiveness. The oxide would have a positive effect on the heat transfer within the clad by favoring the heat release in the fin.

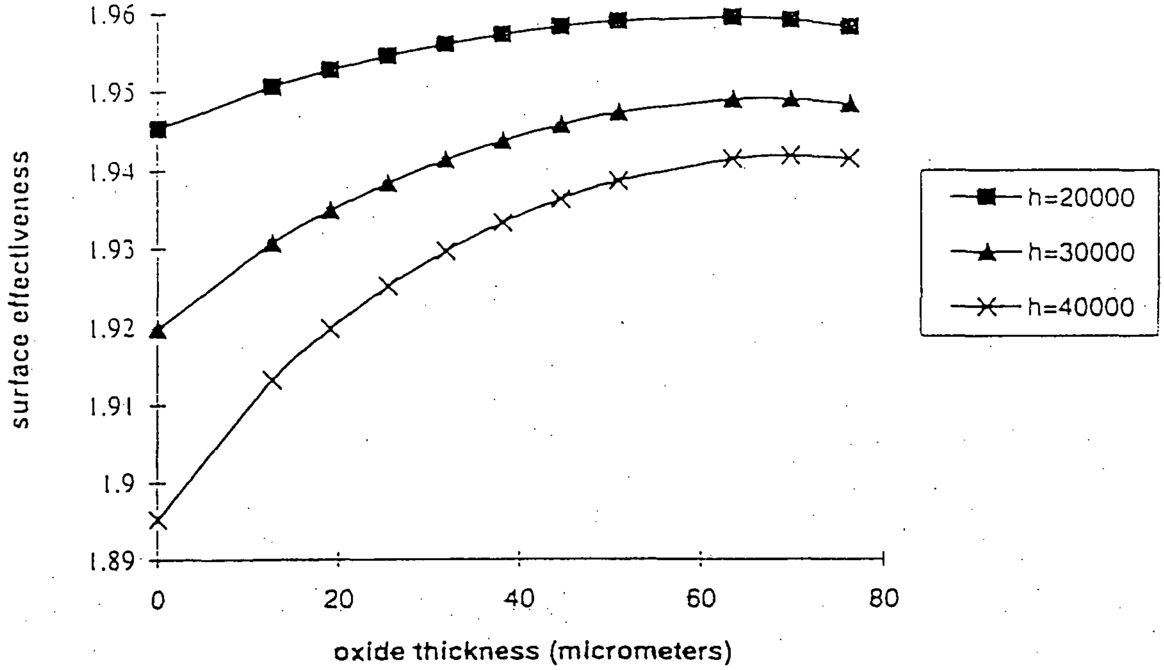

Figure 3.5 Surface effectiveness predicted by the 1-dimensional analysis

3.3. TWO DIMENSIONAL STEADY STATE CALCULATION

3.3.1. Presentation

The previous analysis had assumed a flat temperature distribution in the transverse direction. Although according to Taborda, this hypothesis can be justified by the high value of aluminum conductivity , it was thought that the presence of an oxide layer with a very low conductivity might challenge this hypothesis. Two-dimensional finite-difference calculation has been performed to check the validity of one-dimensional equations and to interpret the influence of the oxide layer thickness more precisely.

3.3.2. Equations and modeling

Consider a part of the clad with an oxide layer subjected to a heat flux q, as shown in figure 3.6. We assume a uniform coolant (heat transfer coefficient h, bulk temperature T_b) and symmetry conditions at lower and upper borders, which means that we neglect the axial variations of the back heat flux. The steady state temperature profile is a solution of the following equations:

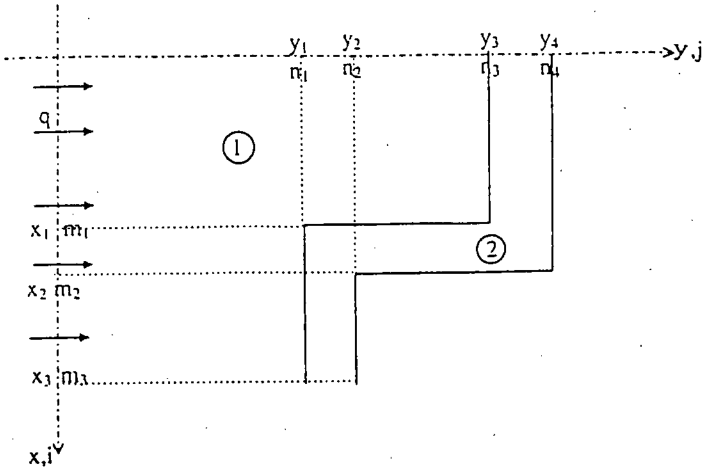

figure 3.6

Local equation:

$$\Delta T = \frac{\partial^2 T}{\partial x^2} + \frac{\partial^2 T}{\partial y^2} = 0$$

Upper boundary condition:

$$-k_1\left(\frac{\partial T}{\partial x}\right)_{x=0} = 0$$

Lower boundary condition:

$$-k_1\left(\frac{\partial T}{\partial x}\right)_{x=x_3} = 0$$

Continuity conditions between medium 1 (aluminum) and medium 2 (oxide):

- for $x = x_1, y_1 < y < y_3$

  $T_1 = T_2$ (no thermal resistance between aluminium and oxide)

  $$-k_1\left(\frac{\partial T}{\partial x}\right)_1 = -k_2\left(\frac{\partial T}{\partial x}\right)_2 \quad \text{(heat flux continuity)}$$

- for $y = y_3, 0 < x < x_1$ and for $y = y_1, x_1 < x < x_3$

  $T_1 = T_2$ (no thermal resistance between aluminium and oxide)

  $$-k_1\left(\frac{\partial T}{\partial y}\right)_1 = -k_2\left(\frac{\partial T}{\partial y}\right)_2 \quad \text{(heat flux continuity)}$$

Boundary conditions at the interface oxide layer / coolant fluid:

- for $y = y_4, 0 < x < x_2$ and for $y = y_2, x_2 < x < x_3$

  $$h(T_2 - T_b) = -k_2\left(\frac{\partial T}{\partial y}\right)_2$$

- for $x = x_2, y_2 < y < y_4,$

  $$h(T_2 - T_b) = -k_2\left(\frac{\partial T}{\partial x}\right)_2$$

The subscripts 1 and 2 respectively refer to aluminum and oxide, k is the conductivity.

3.3.3. Finite-difference formulation

A first finite-difference model with constant mesh grid steps in the x and y directions was developed first. Yet, Matlab imposes a limited number of mesh points (around 700) above which the matrix inversion required for the calculation is impossible. As the "external" geometry of the clad is imposed, the number of possible values for the oxide thickness was limited. Furthermore, it was impossible to check the convergence of the results by increasing the number of mesh points and to have an estimation of the error.

It was thus decided to choose a non uniform mesh grid. The values of the step between each point in the x- and y-directions are chosen by the user.

Defining the temperature matrix $(\theta_{i,j})$ where $\theta_{i,j}$ is the temperature on the node located on the i-th line and the j-th column, a heat balance can be made on the control volume surrounding the point (i,j) (figure 3.7). As there is no energy production and as we assume a steady state, it yields:

$$Q_x|_E + Q_x|_W + Q_y|_S + Q_y|_N = 0$$

or

$$-k\frac{\theta_{i,j+1}-\theta_{i,j}}{\Delta y_j}\overline{\Delta x} - k\frac{\theta_{i,j-1}-\theta_{i,j}}{\Delta y_{j-1}}\overline{\Delta x} - k\frac{\theta_{i+1,j}-\theta_{i,j}}{\Delta x_i}\overline{\Delta y} - k\frac{\theta_{i-1,j}-\theta_{i,j}}{\Delta x_{i-1}}\overline{\Delta x} = 0$$

$$\text{where} \quad \begin{cases} \overline{\Delta x} = \dfrac{\Delta x_i + \Delta x_{i-1}}{2} \\ \overline{\Delta y} = \dfrac{\Delta y_j + \Delta y_{j-1}}{2} \end{cases}$$

This relation corresponds to the local heat equation and is valid for a uniform conductivity k.

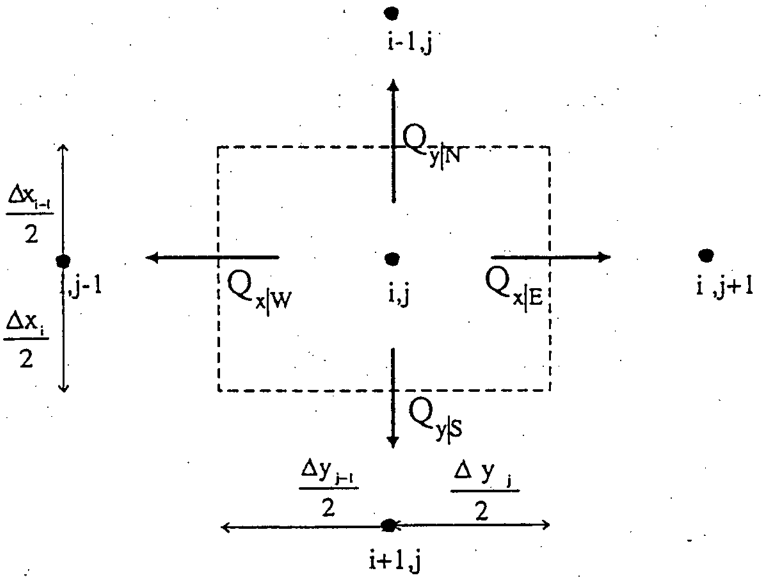

Figure 3.7

The boundary conditions are obtained the same way by a heat balance on each finite control volume surrounding the concerned node. As an instance, let us consider the upper-right convection boundary, ie j=n4 and 1<i<m2.

We can write again that the heat entering the control volume is globally equal to zero:

$$Q_x|_W + Q_y|_N + Q_y|_S + Q_x|_E = 0$$

where $Q_x|_W = -k\dfrac{\theta_{i,j-1} - \theta_{i,j}}{\Delta y_{j-1}}\overline{\Delta x}$

$$Q_y|_N = -k\frac{\theta_{i+1,j} - \theta_{i,j}}{\Delta x_i}\Delta y_{j-1}$$

$$Q_y|_S = -k\frac{\theta_{i-1,j} - \theta_{i,j}}{\Delta x_{i-1}}\Delta y_{j-1}$$

$$Q_x|_E = h(\theta_{i,j} - T_b)\overline{\Delta x}$$

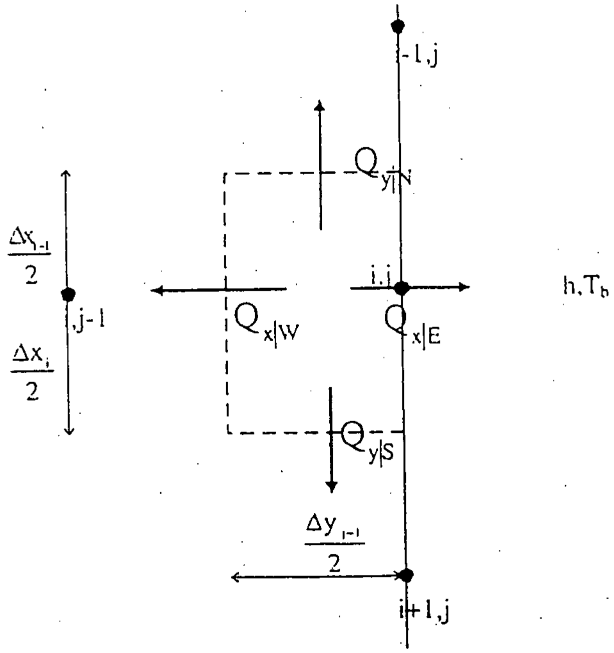

figure 3.8

Similar heat balances for the other boundary conditions of the problem were performed. One will notice that it is necessary to use specific conditions for the "corners" for the heat flux being conservative. The results are the following:

Node localization	Equation
Interior node	$(\frac{\overline{\Delta x}}{\Delta y_j} + \frac{\overline{\Delta x}}{\Delta y_{j-1}} + \frac{\overline{\Delta y}}{\Delta x_i} + \frac{\overline{\Delta y}}{\Delta x_{i-1}})\theta_{i,j} - \frac{\overline{\Delta x}}{\Delta y_j}\theta_{i,j+1} - \frac{\overline{\Delta x}}{\Delta y_{j-1}}\theta_{i,j-1} - \frac{\overline{\Delta y}}{\Delta x_i}\theta_{i+1,j} - \frac{\overline{\Delta y}}{\Delta x_{i-1}}\theta_{i-1,j} = 0$ $\overline{\Delta x} = \frac{\Delta x_i + \Delta x_{i-1}}{2}$ and $\overline{\Delta y} = \frac{\Delta y_j + \Delta y_{j-1}}{2}$
Upper right convection boundary + Lower right convection boundary $2 \le i \le m_2-1$, $j=n_4$ $m_2+1 \le i \le m_3-1$, $j=n_2$	$(\frac{\overline{\Delta x}}{\Delta y_j} + \frac{\overline{\Delta y}}{\Delta x_i} + \frac{\overline{\Delta y}}{\Delta x_{i-1}} + Bi)\theta_{i,j} - \frac{\overline{\Delta x}}{\Delta y_j}\theta_{i,j+1} - \frac{\overline{\Delta y}}{\Delta x_i}\theta_{i+1,j} - \frac{\overline{\Delta y}}{\Delta x_{i-1}}\theta_{i-1,j} = Bi\ T_b$ $Bi = \frac{h\overline{\Delta x}}{k_2}$ $\overline{\Delta x} = \frac{\Delta x_i + \Delta x_{i-1}}{2}$ and $\overline{\Delta y} = \frac{\Delta y_{j-1}}{2}$
Medium right convection boundary $i=m_2$, $n_2+1 \le j \le n_4-1$	$(\frac{\overline{\Delta x}}{\Delta y_j} + \frac{\overline{\Delta x}}{\Delta y_{j-1}} + \frac{\overline{\Delta y}}{\Delta x_{i-1}})\theta_{i,j} - \frac{\overline{\Delta x}}{\Delta y_j}\theta_{i,j+1} - \frac{\overline{\Delta x}}{\Delta y_{j-1}}\theta_{i,j-1} - \frac{\overline{\Delta y}}{\Delta x_{i-1}}\theta_{i-1,j} = Bi\ T_b$ $Bi = \frac{h\overline{\Delta y}}{k_2}$, $\overline{\Delta y} = \frac{\Delta y_j + \Delta y_{j-1}}{2}$ and $\overline{\Delta x} = \frac{\Delta x_{i-1}}{2}$

Left boundary (constant surface heat flux q in the y direction) j=1, $2 \le i \le m_3-1$	$(\frac{\overline{\Delta x}}{\Delta y_j} + \frac{\overline{\Delta y}}{\Delta x_i} + \frac{\overline{\Delta y}}{\Delta x_{i-1}})\theta_{i,j} - \frac{\overline{\Delta x}}{\Delta y_j}\theta_{i,j+1} - \frac{\overline{\Delta y}}{\Delta x_i}\theta_{i+1,j} - \frac{\overline{\Delta y}}{\Delta x_{i-1}}\theta_{i-1,j} = q\frac{\overline{\Delta x}}{k_1}$ $\overline{\Delta y} = \frac{\Delta y_j}{2}$ and $\overline{\Delta x} = \frac{\Delta x_i + \Delta x_{i-1}}{2}$
Upper boundary (no heat flux in the x direction) i=1, $2 \le j \le n_4-1$	$(\frac{\overline{\Delta x}}{\Delta y_j} + \frac{\overline{\Delta x}}{\Delta y_{j-1}} + \frac{\overline{\Delta y}}{\Delta x_i})\theta_{i,j} - \frac{\overline{\Delta x}}{\Delta y_j}\theta_{i,j+1} - \frac{\overline{\Delta x}}{\Delta y_{j-1}}\theta_{i,j-1} - \frac{\overline{\Delta y}}{\Delta x_i}\theta_{i+1,j} = 0$ $\overline{\Delta x} = \frac{\Delta x_i}{2}$ and $\overline{\Delta y} = \frac{\Delta y_j + \Delta y_{j-1}}{2}$
Lower boundary (no heat flux in the x direction) $i=m_3$, $2 \le j \le n_2-1$	$(\frac{\overline{\Delta x}}{\Delta y_j} + \frac{\overline{\Delta x}}{\Delta y_{j-1}} + \frac{\overline{\Delta y}}{\Delta x_{i-1}})\theta_{i,j} - \frac{\overline{\Delta x}}{\Delta y_j}\theta_{i,j+1} - \frac{\overline{\Delta x}}{\Delta y_{j-1}}\theta_{i,j-1} - \frac{\overline{\Delta y}}{\Delta x_{i-1}}\theta_{i-1,j} = 0$ $\overline{\Delta x} = \frac{\Delta x_{i-1}}{2}$ and $\overline{\Delta y} = \frac{\Delta y_j + \Delta y_{j-1}}{2}$
Upper right and lower right interface aluminum/oxide $j=n_3$, $2 \le i \le m_1-1$ $j=n_1$, $m_1+1 \le i \le m_3-1$	$(k_2\frac{\overline{\Delta x}}{\Delta y_j} + k_1\frac{\overline{\Delta x}}{\Delta y_{j-1}} + \overline{k_j}\frac{\overline{\Delta y}}{\Delta x_i} + \overline{k_j}\frac{\overline{\Delta y}}{\Delta x_{i-1}})\theta_{i,j} - k_2\frac{\overline{\Delta x}}{\Delta y_j}\theta_{i,j+1} - k_1\frac{\overline{\Delta x}}{\Delta y_{j-1}}\theta_{i,j-1}$ $- \overline{k_j}\frac{\overline{\Delta y}}{\Delta x_i}\theta_{i+1,j} - \overline{k_j}\frac{\overline{\Delta y}}{\Delta x_{i-1}}\theta_{i-1,j} = 0$ $\overline{\Delta x} = \frac{\Delta x_i + \Delta x_{i-1}}{2}$, $\overline{\Delta y} = \frac{\Delta y_j + \Delta y_{j-1}}{2}$, $\overline{k_j} = \frac{\Delta y_{j-1}k_1 + \Delta y_j k_2}{\Delta y_{j-1} + \Delta y_j}$
Medium interface aluminum/oxide $i=m_1$, $n_1+1 \le j \le n_4-1$	$(\overline{k_i}\frac{\overline{\Delta x}}{\Delta y_j} + \overline{k_i}\frac{\overline{\Delta x}}{\Delta y_{j-1}} + k_2\frac{\overline{\Delta y}}{\Delta x_i} + k_1\frac{\overline{\Delta y}}{\Delta x_{i-1}})\theta_{i,j} - \overline{k_i}\frac{\overline{\Delta x}}{\Delta y_j}\theta_{i,j+1} - \overline{k_i}\frac{\overline{\Delta x}}{\Delta y_{j-1}}\theta_{i,j-1}$ $- k_2\frac{\overline{\Delta y}}{\Delta x_i}\theta_{i+1,j} - k_1\frac{\overline{\Delta y}}{\Delta x_{i-1}}\theta_{i-1,j} = 0$ $\overline{\Delta x} = \frac{\Delta x_i + \Delta x_{i-1}}{2}$ and $\overline{\Delta y} = \frac{\Delta y_j + \Delta y_{j-1}}{2}$, $\overline{k_i} = \frac{\Delta x_{i-1}k_1 + \Delta x_i k_2}{\Delta x_{i-1} + \Delta x_i}$
Upper left corner For i=1, j=1	$(\frac{\overline{\Delta x}}{\Delta y_j} + \frac{\overline{\Delta y}}{\Delta x_i})\theta_{i,j} - \frac{\overline{\Delta x}}{\Delta y_j}\theta_{i,j+1} - \frac{\overline{\Delta y}}{\Delta x_i}\theta_{i+1,j} = q\frac{\overline{\Delta x}}{k_1}$ $\overline{\Delta x} = \frac{\Delta x_i}{2}$ and $\overline{\Delta y} = \frac{\Delta y_j}{2}$
Lower left corner For $i=m_3$, j=1	$(\frac{\overline{\Delta x}}{\Delta y_j} + \frac{\overline{\Delta y}}{\Delta x_{i-1}})\theta_{i,j} - \frac{\overline{\Delta x}}{\Delta y_j}\theta_{i,j+1} - \frac{\overline{\Delta y}}{\Delta x_{i-1}}\theta_{i,j} = q\frac{\overline{\Delta x}}{k_1}$ $\overline{\Delta x} = \frac{\Delta x_i}{2}$ and $\overline{\Delta y} = \frac{\Delta y_j}{2}$

Upper right corner for the aluminum (interface Al/Al2O3) For $i=1$, $j=n_3$	$(k_2 \frac{\overline{\Delta x}}{\Delta y_j} + k_1 \frac{\overline{\Delta x}}{\Delta y_{j-1}} + \overline{k_j} \frac{\overline{\Delta y}}{\Delta x_i})\theta_{i,j} - k_2 \frac{\overline{\Delta x}}{\Delta y_j}\theta_{i,j+1} - k_1 \frac{\overline{\Delta x}}{\Delta y_{j-1}}\theta_{i,j-1}$ $- \overline{k_j} \frac{\overline{\Delta y}}{\Delta x_i}\theta_{i+1,j} = 0$ $\overline{\Delta x} = \frac{\Delta x_i}{2}$ and $\overline{\Delta y} = \frac{\Delta y_j + \Delta y_{j-1}}{2}$, $\overline{k_j} = \frac{\Delta y_{j-1} k_1 + \Delta y_j k_2}{\Delta y_{j-1} + \Delta y_j}$
Medium right corner for Al (external corner Al/Al2O3) For $i=m_1$, $j=n_3$	$(k_2 \frac{\overline{\Delta x}}{\Delta y_j} + \overline{k_i} \frac{\overline{\Delta x}}{\Delta y_{j-1}} + k_2 \frac{\overline{\Delta y}}{\Delta x_i} + \overline{k_j} \frac{\overline{\Delta y}}{\Delta x_{i-1}})\theta_{i,j} - k_2 \frac{\overline{\Delta x}}{\Delta y_j}\theta_{i,j+1} - \overline{k_i} \frac{\overline{\Delta x}}{\Delta y_{j-1}}\theta_{i,j-1}$ $- k_2 \frac{\overline{\Delta y}}{\Delta x_i}\theta_{i+1,j} - \overline{k_j} \frac{\overline{\Delta y}}{\Delta x_{i-1}}\theta_{i-1,j} = 0$ $\overline{\Delta x} = \frac{\Delta x_i + \Delta x_{i-1}}{2}$ and $\overline{\Delta y} = \frac{\Delta y_j + \Delta y_{j-1}}{2}$ $\overline{k_j} = \frac{\Delta y_{j-1} k_1 + \Delta y_j k_2}{\Delta y_{j-1} + \Delta y_j}$ and $\overline{k_i} = \frac{\Delta x_{i-1} k_1 + \Delta x_i k_2}{\Delta x_{i-1} + \Delta x_i}$
Medium medium corner (internal corner Al/Al2O3) For $i=m_1$, $j=n_1$	$(\overline{k_i} \frac{\overline{\Delta x}}{\Delta y_j} + k_1 \frac{\overline{\Delta x}}{\Delta y_{j-1}} + \overline{k_j} \frac{\overline{\Delta y}}{\Delta x_i} + k_1 \frac{\overline{\Delta y}}{\Delta x_{i-1}})\theta_{i,j} - \overline{k_i} \frac{\overline{\Delta x}}{\Delta y_j}\theta_{i,j+1} - k_1 \frac{\overline{\Delta x}}{\Delta y_{j-1}}\theta_{i,j-1}$ $- \overline{k_j} \frac{\overline{\Delta y}}{\Delta x_i}\theta_{i+1,j} - k_1 \frac{\overline{\Delta y}}{\Delta x_{i-1}}\theta_{i-1,j} = 0$ $\overline{\Delta x} = \frac{\Delta x_i + \Delta x_{i-1}}{2}$ and $\overline{\Delta y} = \frac{\Delta y_j + \Delta y_{j-1}}{2}$ $\overline{k_j} = \frac{\Delta y_{j-1} k_1 + \Delta y_j k_2}{\Delta y_{j-1} + \Delta y_j}$ and $\overline{k_i} = \frac{\Delta x_{i-1} k_1 + \Delta x_i k_2}{\Delta x_{i-1} + \Delta x_i}$
Lower right corner for Al For $i=m_3$, $j=n_1$	$(\overline{k_i} \frac{\overline{\Delta x}}{\Delta y_j} + k_1 \frac{\overline{\Delta x}}{\Delta y_{j-1}} + \overline{k_j} \frac{\overline{\Delta y}}{\Delta x_i} + k_1 \frac{\overline{\Delta y}}{\Delta x_{i-1}})\theta_{i,j} - \overline{k_i} \frac{\overline{\Delta x}}{\Delta y_j}\theta_{i,j+1} - k_1 \frac{\overline{\Delta x}}{\Delta y_{j-1}}\theta_{i,j-1}$ $- \overline{k_j} \frac{\overline{\Delta y}}{\Delta x_i}\theta_{i+1,j} - k_1 \frac{\overline{\Delta y}}{\Delta x_{i-1}}\theta_{i-1,j} = 0$ $\overline{\Delta x} = \frac{\Delta x_{i-1}}{2}$ and $\overline{\Delta y} = \frac{\Delta y_j + \Delta y_{j-1}}{2}$, $\overline{k_j} = \frac{\Delta y_{j-1} k_1 + \Delta y_j k_2}{\Delta y_{j-1} + \Delta y_j}$
Upper right corner for Al2O3 For $i=1$, $j=n_4$	$(\frac{\overline{\Delta x}}{\Delta y_{j-1}} + \frac{\overline{\Delta y}}{\Delta x_i} + Bi)\theta_{i,j} - \frac{\overline{\Delta x}}{\Delta y_{j-1}}\theta_{i,j-1} - \frac{\overline{\Delta y}}{\Delta x_i}\theta_{i+1,j} = Bi \ T_b$ $Bi = \frac{h\overline{\Delta x}}{k_2}$, $\overline{\Delta x} = \frac{\Delta x_i}{2}$ and $\overline{\Delta y} = \frac{\Delta y_{j-1}}{2}$

Medium right corner for Al2O3 For $i=m_2, j=n_4$	$(\frac{\overline{\Delta x}}{\Delta y_{j-1}} + \frac{\overline{\Delta y}}{\Delta x_{i-1}} + Bi)\theta_{i,j} - \frac{\overline{\Delta x}}{\Delta y_{j-1}}\theta_{i,j-1} - \frac{\overline{\Delta y}}{\Delta x_{i-1}}\theta_{i-1,j} = Bi\ \ T_b$ $Bi = h\frac{\overline{\Delta x} + \overline{\Delta y}}{k_2}$ $\overline{\Delta x} = \frac{\Delta x_{i-1}}{2}$ and $\overline{\Delta y} = \frac{\Delta y_{j-1}}{2}$
Medium-medium (internal) corner for Al2O3 For $i=m_2, j=n_2$	$(\frac{\overline{\Delta x}}{\Delta y_{j-1}} + \frac{\overline{\Delta y}}{\Delta x_{i-1}} + Bi)\theta_{i,j} - \frac{\Delta x_{i-1}}{2\Delta y_j}\theta_{i,j+1} - \frac{\overline{\Delta x}}{\Delta y_{j-1}}\theta_{i,j-1} - \frac{\Delta y_{j-1}}{2\Delta x_i}\theta_{i+1,j}$ $- \frac{\overline{\Delta y}}{\Delta x_{i-1}}\theta_{i-1,j} = Bi\ \ T_b$ $Bi = h\frac{\Delta x_i + \Delta y_j}{2k_2}$ $\overline{\Delta x} = \frac{\Delta x_i + \Delta x_{i-1}}{2}$ and $\overline{\Delta y} = \frac{\Delta y_j + \Delta y_{j-1}}{2}$
Lower right corner for Al2O3 For $i=m_3, j=n_2$	$(\frac{\overline{\Delta x}}{\Delta y_{j-1}} + \frac{\overline{\Delta y}}{\Delta x_{i-1}} + Bi)\theta_{i,j} - \frac{\overline{\Delta x}}{\Delta y_{j-1}}\theta_{i,j-1} - \frac{\overline{\Delta y}}{\Delta x_{i-1}}\theta_{i-1,j} = Bi\ \ T_b$ $Bi = \frac{h\overline{\Delta x}}{k_2}$ $\overline{\Delta x} = \frac{\Delta x_{i-1}}{2}$ and $\overline{\Delta y} = \frac{\Delta y_{j-1}}{2}$

By defining the vector $T = (\theta_{1,1}, \theta_{1,2}, \ldots, \theta_{1,n4}, \ldots, \theta_{i,j}, \ldots, \theta_{m3,n2})$ and the appropriate matrix M, all these relations can be written in the form:

$$M\,T = V$$

M can easily be inverted with Matlab so that we can find the approximate temperature distribution in the clad.

A problem is now to define the surface effectiveness since the temperature on the surface of the oxide is not uniform as in the 1-dimensional case. The maximum temperature at the interface oxide/coolant has a particular importance as it determines the onset of nucleate boiling and can be used to predict the oxide growth under conservative assumptions.
That is why we define:

$\eta_{min} = \frac{q_B}{h(T_{c\,max} - T_b)}$ where $T_{c\,max}$ is the maximum temperature on the oxide surface.

We also use

$\eta_{av} = \frac{q_B}{h(T_{c\,av} - T_b)}$ where $T_{c\,av}$ is the average temperature on the clad fin base.

We assume a uniform oxide distribution along the fin surface. Still basing on Griess observations, the oxide thickness is supposed equal to the corroded metal thickness.

3.3.4. Program validation

3.3.4.1. Test calculations

A series of test calculations were performed in order to check the validity of the written finite difference program.

- The analogy with the 1-dimensional case was checked with a maximum width t and a minimum length l for the fin. The surface effectiveness tended towards 1 and the maximum temperature gradient in the y-direction tended towards 0, which corresponds to a flat temperature profile as in the 1-dimensional case with the corresponding temperature drops.
- The surface effectiveness tended towards its maximum value (2, which is the ratio between the clad outer surface and the back surface) when the conductivity was increased and when the convection coefficient was decreased. This behavior was predictable as an increase of the conductivity tends to homogenize the temperature in the clad and a decrease of the convection coefficient tends to decrease the temperature drop through the fin.
  On the contrary, the surface effectiveness tended towards 1 when we increased the convection coefficient.

- Finally, for every calculation, the heat flux entering the clad by the back surface was found equal to the heat flux going out by the clad/coolant interface.
  It was also checked that the calculated efficiencies were independent from the surface back heat flux (q or q_B) and from the coolant bulk temperature T_b.

3.3.4.2. Mesh grid choice

The choice of the mesh grid was a complex question, as the number of nodes was limited by Matlab ability to invert the system matrix M. Sensitivity studies about the choice of $\Delta x(i)$ and $\Delta y(j)$ were performed. It was found that it was possible to take a relatively large step in the aluminum regions without influencing the results. On the contrary, the choice of a thinner step in the oxide region had more importance, as the conductivity and so the temperature changes are more important in the oxide region.
Besides, the temperature gradients in the x-direction (parallel to the back surface) were found to be relatively important and justified the choice of a thinner step in the x direction.
As the most important effect of the oxide is expected for a maximum oxide thickness, the step configuration in the "aluminum region" ($0<i<n1$, $n2<i<n3$, $0<j<m1$, $m2<j<m3$) was defined with an oxide thickness of 2 mils and was globally conserved for the other configurations.
By taking a y-step of $\frac{1}{3}$ mil and an x-step of $\frac{1}{8}$ mil for the other (i,j) values, where the presence of the oxide imposed higher temperature gradients, it was established that quite precise results were obtained.
The following table shows the results obtained for h=30000 and a 2mil oxide film. It illustrates the influence of the steps Δx and Δy in the "oxide region" ($n1<j<n2$, $n3<j<n4$, $m1<i<m2$).

Δx	Δy	η_{av}	η_{min}
$\frac{2}{3}$ mil	$\frac{1}{8}$ mil	1.718	1.528

½ mil	⅛ mil	1.718	1.530
⅖ mil	⅛ mil	1.717	1.532
⅓ mil	⅛ mil	1.717	1.533
⅕ mil	⅛ mil	1.717	1.534
⅓ mil	½ mil	1.718	1.530
⅓ mil	⅙ mil	1.717	1.533
⅓ mil	⅛ mil	1.717	1.533
⅓ mil	1/12 mil	1.717	1.534

These results allow to estimate the accuracy of the results to about 2.10^{-3}or 0.15%.
The figure 3.9 presents the mesh grid used for the calculation with a 2 mil oxide layer.
For the other oxide thickness values, a minimum step of ⅙ mil and ⅛ mil (respectively in the x and y direction) was taken. Actually, the step was generally thinner, so as to obtain the most precise result.

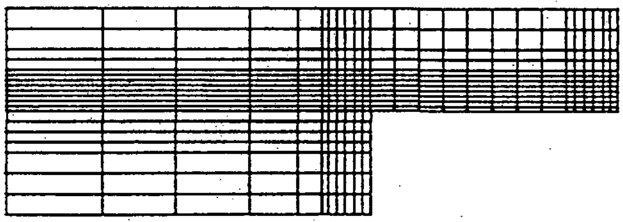

Figure 3.9 – Mesh grid used for a clad with 2 mil oxide layer

3.3.4.3. Comparison with other authors

Taborda ([2) had performed finite difference calculations on the fin clad. The resolution method chosen was a point-successive iteration over-relaxation instead of a matrix inversion. His conclusion was that the one-dimensional equations offered results that were accurate enough compared to the 2-dimensional analysis.
Yet, the range of values for h investigated by Taborda was quite different from the values expected for MITR-III (5000-10000 instead of 20000-30000). Besides, Taborda investigated the behavior of the clad with a crud oxide deposit whose conductivity he considered equal to 3.5 W/mK. So Taborda took a conductivity twice as high as the value proposed by Griess and he considered that the oxide was an additional layer on the clad surface while it should be considered as formed *in* the aluminum clad.
Besides, the definition considered for the surface effectiveness in Taborda's 2-dimensional computations was unclear, and the values of the heat flux entering the clad and the heat flux going out were slightly different, due to the numerical method used. That is why Taborda's calculations of the clad with an oxide layer are difficult to compare.

For the appropriate mesh points, h=5678 W/m^2K and no oxide layer, the results are similar though:

	η(1 dimensional)	η_{av}	η_{min}
Taborda	1.985	1.983 ?	
Present study	1.985	1.983	1.979

Para [14] performed clad 3-dimensional calculations with FLUENT. Like Taborda, he assumes an additional crud layer rather than an oxide layer building up in the clad. Besides, the surface effectiveness he calculates is based on the wall temperature, that is the mean temperature at the fin base.

For h=25000 (average value for FLUENT 3D calculations), the results are the following:

	η(based on the average temperature on the fin clad base)	η_{min}
Para	1.952	
Present study	1.928	1.911

The difference may be due to 3-D effects and to the definition of the effectiveness.

3.3.5. Calculation results

3.3.5.1. Comparison with 1-dimensional results

An important difference was found with the one-dimensional predictions. The results showed that this difference rose when increasing the heat transfer coefficient and the oxide thickness. 1-D predictions always overestimated the surface effectiveness values. This error reached up to 20% for η_{av} and 30% for η_{min} for h $\cong 30000 W/m^2K$ which is a typical value for MITR-III.
The following figure presents the results obtained for a 1.5 mil oxide thickness.

Figure 3.10 Computed surface effectiveness - Comparison between 1-D and 2-D results

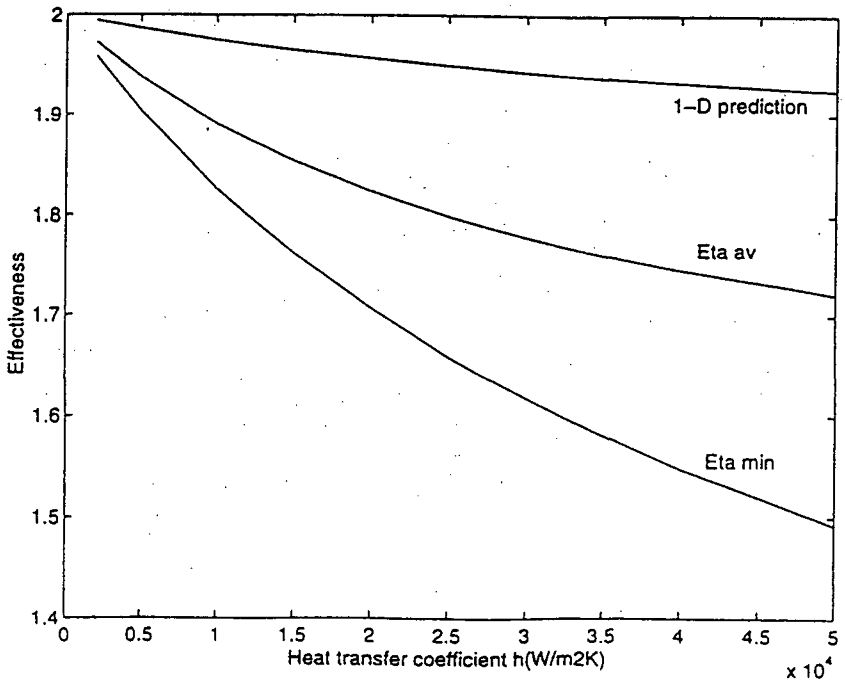

The presence of the oxide layer was found to favor the energy release by the fin base (non-finned part of the clad) rather than by the fin itself. So that an increase in the oxide thickness, as well as an increase in the heat transfer coefficient value, led to higher maximum temperatures on the fin base and lower fin tip temperatures.

In order to understand the important error made under one-dimensional assumptions, the heat circulation in the clad was investigated. The figure 3.11 represents the heat flux distribution for a clad covered by a 2 mil oxide film. It tends to prove that it is impossible to neglect the two-dimensional effects, especially in the presence of the oxide film that acts as a thermal barrier and creates important gradients in the x-direction by diverting the heat flux to the fin.

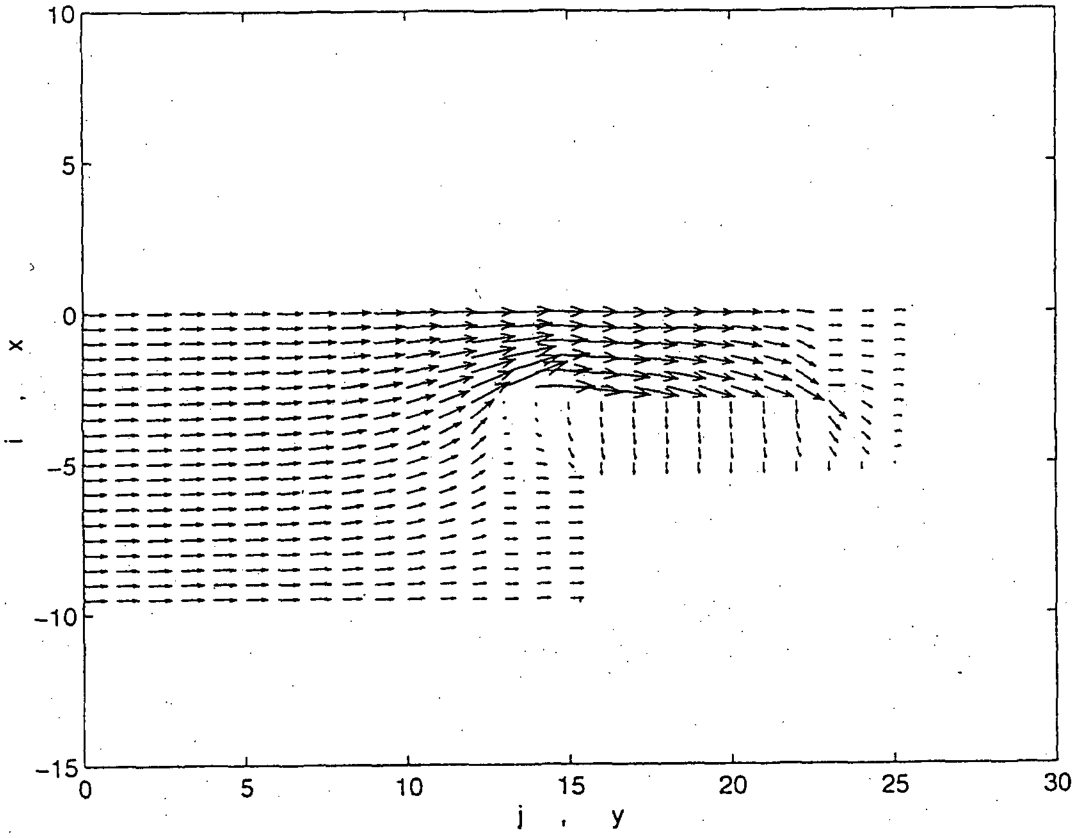

Figure 3.11 2-D heat fluxes in the clad with a 2 mil oxide layer - h=25000MW/m^{2}K

3.3.5.2. Effects of the heat transfer coefficient and of the oxide thickness on the surface effectiveness

η_{av} and η_{min} are represented as functions of h and e (oxide thickness) in figures 3.12 and 3.13. They show that the oxide debases the heat exchange between the clad and the coolant. At h=30000W/m^{2}K, η_{min} switches from 1.89 for a non-oxidized clad down to 1.53 in the presence of a 2 mil oxide layer.

In order to use these values in subsequent calculations, we performed least-square regressions with Matlab to write the effectiveness in the form:

figure 3.12 Minimum surface effectiveness for different oxide layers

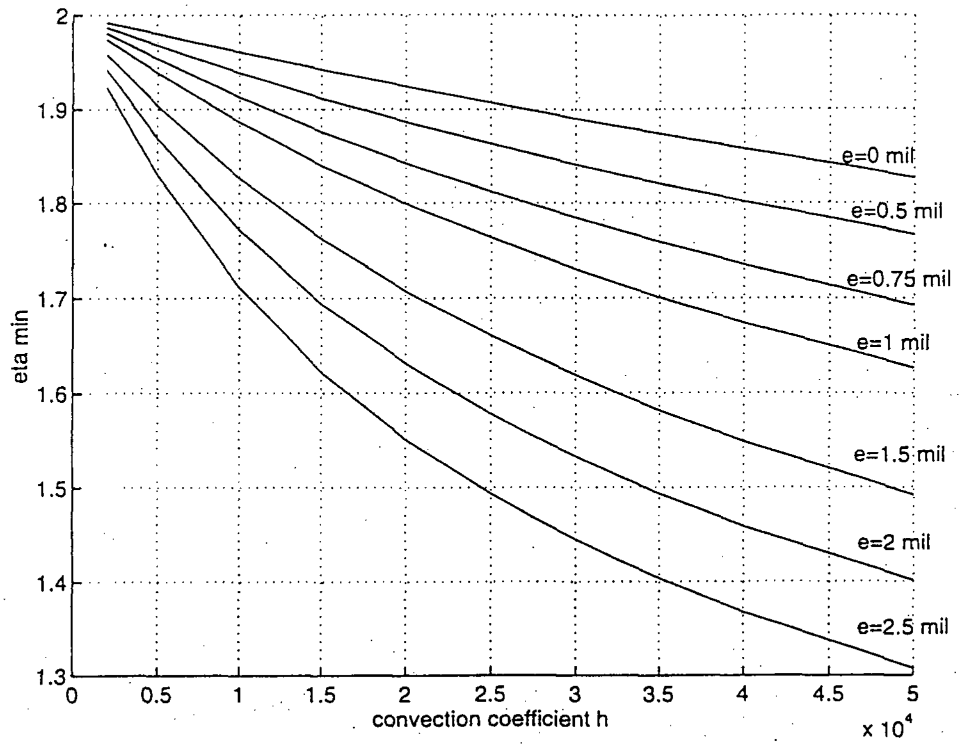

figure 3.13 Average surface effectiveness (clad base) for different oxide layers

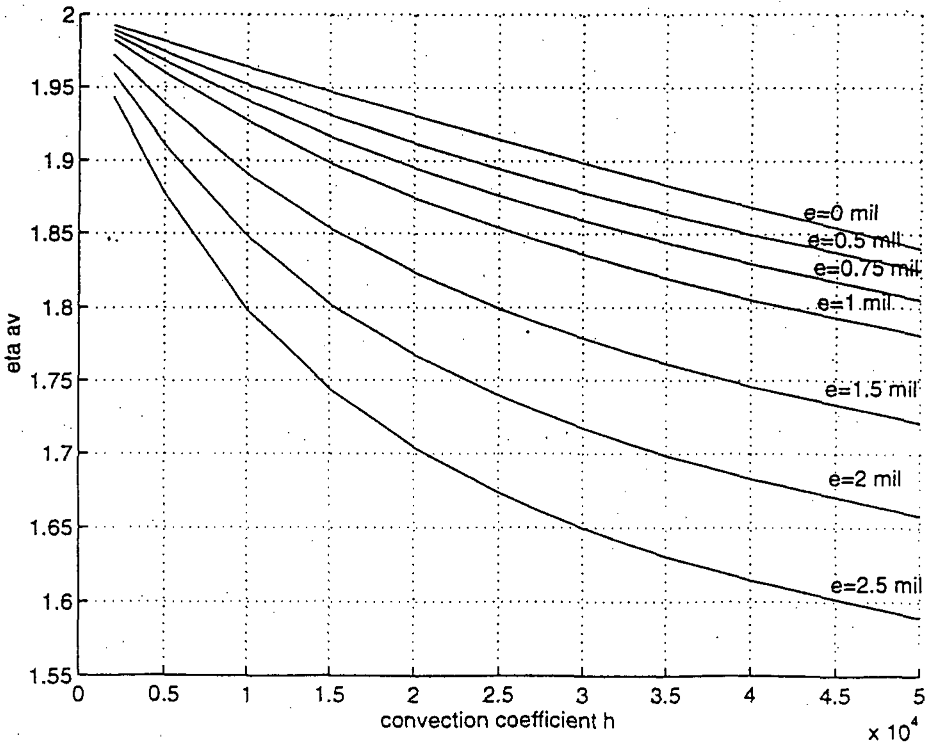

$\eta = p_1(e) + p_2(e)\exp(p_3(e)\ h)$

h (W/m^{2}K)
e (mils)

Although satisfactory for η_{av}, this formula did not predict η_{min} accurately. This was due to the location change of the maximum temperature point on the surface clad from (i=m3, j=n2) to the interior corner (i=m2,j=n2) (cf figure 3.6) which occurred when the oxide thickness reached about 0.25 mil.
Yet, η_{min} can be well predicted by:

$\eta = p_1(e) + p_2(e)h + p_3(e)\exp(p_4(e)\ h)$

The values of the parameters p_i are given in the appendix 1.

The local effectiveness, which can be defined as $\eta = \frac{q}{h(T - T_b)}$, where T is the local temperature at the surface, was found to vary widely along the lateral edge of the fin in the presence of a thick oxide film. Local effectiveness variations were quite low when no oxide was formed on the clad. The figures 3.13, 3.14 and 3.15 represent the profile of the local effectiveness along the clad surface and illustrate the temperature heterogeneity due to the oxide film. For an oxide thickness of 2 mils and a heat transfer coefficient of 30 000 W/m^{2}K, the surface effectiveness varied from 1.52 to 3.75 along the lateral edge of the fin. It varied from 1.9 to 2.1 for a non-oxidized clad.
This means that temperature differences of a few Celsius degrees are to be expected between the clad base and the fin tip, which could lead to the oxide film being thicker at the fin base than at the fin tip.

3.3.6. Sensitivity studies

3.3.6.1. Oxide distribution

The previous remark incited to study the case of a non-uniform distribution of the oxide along the clad surface. Assuming a conservative value of 0.5 MW/m^2 for the heat flux and a heat transfer coefficient of 30 000 MW/m^{2}K, a temperature difference of about 7°C would exist between the fin tip and the fin base. This difference of temperature implies an oxide growth rate difference between the two extremities of the fin. In the same conditions and for bulk temperatures of 40-70°C., the ratio of the oxide growth rate at the fin tip by the growth rate at the fin base is approximately equal to 0.75, according to Griess correlation.
Therefore, the two following oxide distributions were compared for h=30000MW/m^{2}K:

	Case 1	Case2	Case3	Case4	Case5
Oxide thickness (mils)	Fin tip: 1.5 Fin edge: 1.8 Fin base: 2	Fin tip:1.8 Fin edge:1.9 Fin base:2	Fin tip: 2 Fin edge: 2 Fin base: 2	Fin tip: 1.8 Fin edge: 1.8 Fin base: 1.8	Fin tip: 1.5 Fin edge: 1.5 Fin base: 1.5
η_{av}	1.819	1.760	1.718	1.743	1.824
η_{min}	1.605	1.564	1.531	1.570	1.707

Figure 3.13 Surface effectiveness variations along the fin tip (h=30000W/m^{2}K)

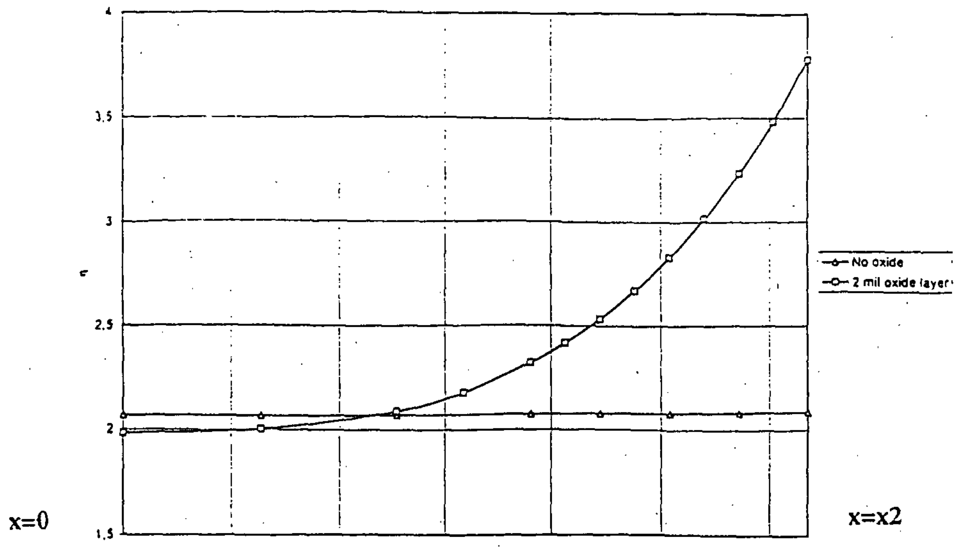

Figure 3.14 Surface effectiveness variations along the lateral fin edge(h=30000W/m^{2}K)

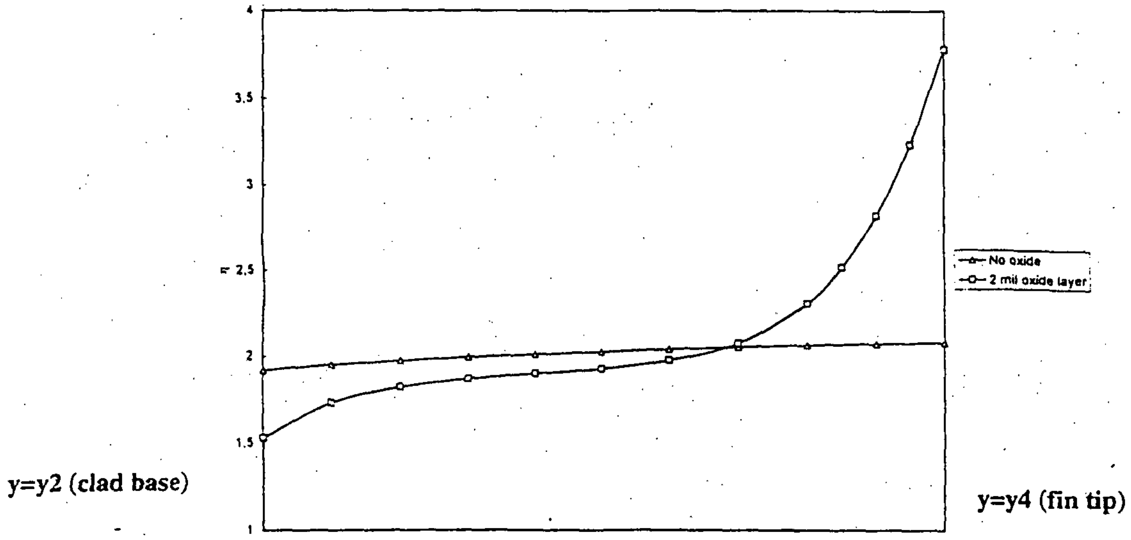

Figure 3.15 Surface effectiveness variations along the clad base (h=30000W/m^{2}K)

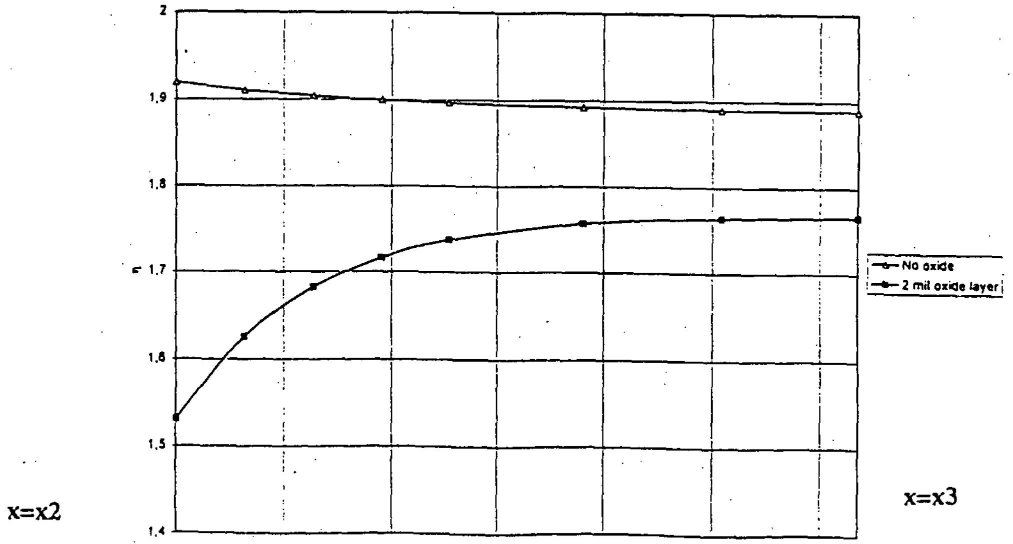

As can be seen, assuming a lower thickness distribution leads to a significant improvement of the surface effectiveness, even in the case 2, where a low heterogeneity was assumed.
Conservative results will be obtained if we suppose that the oxide thickness distribution is uniform and equal to the maximum thickness on the clad, as assumed in chapter 4.

3.3.6.2. Corroded oxide thickness

The previous calculations assumed that the thickness of corroded metal was equal to the oxide film thickness, so that the external geometry of the clad was conserved. This implies that a part of the reacting aluminum be dissolved in the coolant. Assuming that the corrosion product is boehmite ant no aluminum is dissolved, the ratio $\frac{\text{volume of oxide}}{\text{volume of corroded aluminum}}$ is about 2.0 (cf chapter 5), which means that, for an oxide thickness of 2mils, the corroded metal thickness is only 1 mil. The consequences of the resulting clad swelling were calculated for e=2mils, h=30000MW/m^{2}K:

	Initial case	No dissolution
η_{av}	1.718	1.761(+2.5%)
η_{min}	1.531	1.569 (+2.5%)
Percentage of heat released by the fin	70.9%	73.0%

The "no dissolution" hypothesis leads to wider dimensions for the aluminum part of the clad, which favors the heat release by the fin and explains the observed improvement.
Conservative values are expected with the initial hypothesis.

3.3.6.3. Aluminum conductivity

The aluminum conductivity varies with the temperature and the nature of aluminum. The conductivity of pure aluminum is 204-206 W/mK. The conductivity of Alloy 6061 would be a bit higher (217-221W/mK [16]).

k_{Al}(W/mK)	200	206	220
η_{av}	1.718	1.712	1.725
η_{min}	1.531	1.534	1.537

As seen in results above obtained for e=2mils , h=30000W/m^2 and for different values of the conductivity, , the value of 200 W/mK considered for all the calculations leads to slightly conservative results (a maximum relative difference of 0.4% exists for η_{min}). A higher value of the aluminum conductivity favors the heat release by the fin.

3.3.7. Conclusions

The surface effectiveness of the clad was found to be a decreasing function of the heat transfer coefficient and of the oxide thickness, so that for significant oxide films (above 0.2 mils), the oxide thickness influence cannot be neglected.
The 1-dimensional analysis does not seem to be valid and underestimates the influence of the oxide and of the heat transfer coefficient.
The hypothesis of a uniform oxide formation driven by the maximum temperature on the clad surface will lead to conservative results.
The penetration of the oxide into the clad influences the fins efficiency. We assume for the following that the oxide thickness equals the dissolved metal thickness and believe that it should be a sufficient hypothesis to obtain conservative results.

All the calculations assumed constant properties for the coolant (h and T_b). We did not take into account the temperature variations of the coolant along the fins. Logically, the coolant should be slightly warmer in the grooves, which should lead to overestimate the surface effectiveness in the present calculations. Although we believe that the flow is turbulent enough to homogenize the temperature in the coolant, this point should be studied more precisely.

4. Calculation of the oxide distribution in the hot channel

Matlab computations were performed in order to determine the distribution of oxide along the hot channel. As a matter of fact, as the oxide growth increases with the temperature at the oxide/coolant interface, the maximum thickness and the maximum effects on the clad temperature are to be expected in the hot channel. The aim of this calculation is to compare the predictions of each of the correlations available to predict the maximum oxide film thickness in the core and to give an idea about the oxide distribution.
The presence of the oxide film causes a decrease of the clad surface effectiveness, thus an increase in the oxide/coolant temperature. This temperature increase leads to a change in the correlation parameters so that the oxide growth cannot be simply determined a priori. That is why the current results took into account the growth rate variations with the time.

4.1. Geometry of the channel

The surface of each side of MITR fuel plates is increased by 110 fins whose dimensions are 0.254 mm thick and 0.254 mm high. The cross sectional view of the channel is represented below:

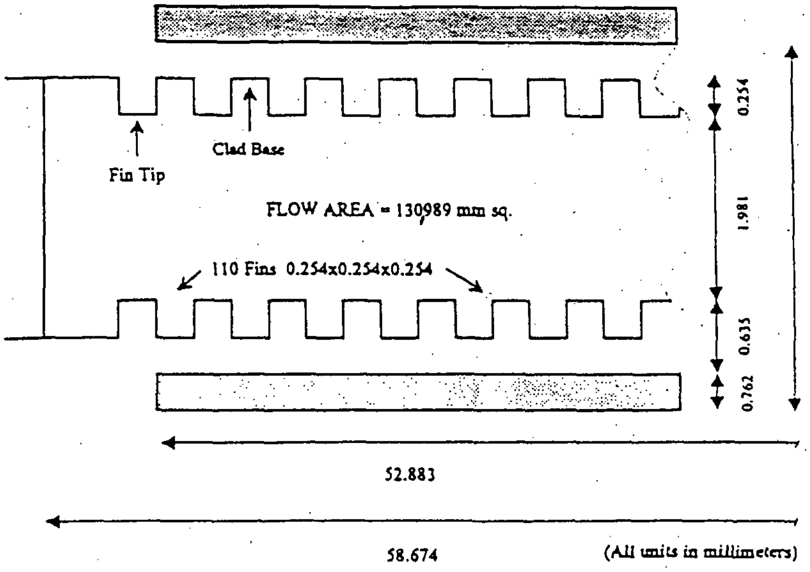

figure 4.1 Cross sectional view of a flow channel and finned fuel plates

4.2. Modeling choices

4.2.1. Principles

The used Matlab program consists in resolving for each hot channel element i characterized by a heat flux value q_i:

$$q_i = \eta_i h_i (T_{w_i} - T_{b_i})$$

where the subscript i refers to the i-element, η represents the surface effectiveness, T_b is the bulk coolant and T_w is the wall temperature.

The value considered for $T_{b\,i}$ is the mean value between the temperature at the inlet of the channel element i and the temperature at the outlet. It depends on the heat flux distribution, on the velocity and of the coolant temperature at the channel inlet, T_{inlet}.

The velocity is considered equal to the mean velocity in the core and is given as the global flow rate divided by the total flow area. This represents a conservative assumption as the velocity in the hot channel is a bit higher than in the average channel, which should favor the heat transfer between the clad and the coolant.

4.2.2. Oxide growth correlations

Griess, Kritz and "Correl 2" correlations were used to predict the oxide growth. The correction factor of 3.8, recommended by Griess in the case of a high pH, is used in Griess and Kritz correlations. A pH correction factor of 4.5 is used for "Correl 2", following an extrapolation of the figure 2.2.

The heat flux used in the correlation is the maximal heat flux at the clad surface (ie q / η_{min}).

As we explained, the oxide growth constant is expected to change with time, and is recalculated at every time step.

4.2.3. Heat transfer coefficient correlation

The modified Seider-Tate correlation was used to calculate the heat transfer coefficient,

$$Nu = 0.023\, Re^{0.8}\, Pr^{0.4} \left(\frac{\mu_b}{\mu_w} \right)^{0.14} (1 + \alpha(Z))$$

$$\alpha(Z) = \begin{cases} \dfrac{1.12 D_e}{Z} & \text{for } Z < 400\,\text{mm} \\ 0 & \text{for } Z > 400\,\text{mm} \end{cases}$$

where

$Nu = \dfrac{hD_e}{k}$ is the Nusselt number of the bulk coolant

h is the heat transfer coefficient (W/m^2K)

D_e is the hydraulic equivalent diameter of the channel

k is the thermal conductivity of the bulk coolant (W/mK)
$Re = \frac{\rho v D_e}{\mu}$ is the Reynolds number of the bulk coolant
Pr is the Prandtl number of the bulk coolant
v is the fluid velocity in the channel
ρ is the volumic mass of the bulk coolant
μ is the dynamic viscosity of the coolant at the bulk temperature (b subscript) or at the wall temperature (w subscript).
Z is the axial height

According to Parra ([14]), this correlation is valid in the range 0.7<Pr<120, and L/De>60, where L represents the channel height, and is more precise than the Dittus-Boelter or the Colburn correlations. It allows to take into account entrance effects which enhance the heat transfer coefficient in the coolant channel entrance region.

4.2.4. Surface effectiveness

The 1-dimensional expression for the surface effectiveness was initially used. When it became obvious that this solution led to overestimate dangerously the surface effectiveness, the 2-dimensional computation results were introduced in the form of a table of values which gave the surface effectiveness as a function of the heat transfer coefficient and the oxide thickness. Cubic interpolations between the data were performed to determine the surface effectiveness.
The used data were the values of the minimum surface effectiveness computed in chapter 3.

4.2.5. Heat flux distribution

The heat flux distribution in the hot channel, at the early life of the fuel, was previously calculated by Bhutta ([17]).
We assume the same heat flux distribution (cf figure 4.2) during the whole history of the core, until the fission density limit of 2.3 10^{21} fissions/cm^3 be reached at the hottest point. This hypothesis logically leads to a conservative assumption for the calculation of the maximum oxide thickness. Indeed, the heat flux flattening, which must be observed during the fuel burn-up, would contribute to a reduction of the hot point temperature and would lead to a more homogeneous oxide growth rate. Besides, we do not take into account the fuel management program and the fuel element inversions, which makes our hypotheses obviously very conservative.
A simple calculation allows to determine the burn-up limit in hours, assuming a constant power of 10 MW and a power release of 200 MeV per fission. It is equal to 7030 hours.

4.3. Results

4.3.1. Maximum oxide thickness

After 7030 hours of normal operation at 10 MW (average heat flux q= 0.45 MW/m^2), the results depended widely on the values of the flow rate and of the temperature at the channel inlet. The following tables give the maximum thickness predicted by the different correlations in mils. If the thickness limit of 2 mils is exceeded, the result is the maximum time t (in hours), at which the oxide thickness limit is reached.

	Flow rate of 2500gpm	Flow rate of 2750gpm	Flow rate of 3000gpm	Flow rate of 3250gpm	Flow rate of 3500gpm
T_{inlet}=40°C	6500<t<6600	1.89	1.73	1.60	1.49
T_{inlet}=45°C	5200<t<5300	5900<t<6000	6600<t<6700	1.94	1.81
T_{inlet}=50°C	4300<t<4400	4700<t<4800	5200<t<5300	5700<t<5800	6200<t<6300
T_{inlet}=55°C	3500<t<3600	3800<t<3900	4200<t<4300	4600<t<4700	4900<t<5000
T_{inlet}=60°C	2800<t<2900	3100<t<3200	3400<t<3500	3700<t<3800	3900<t<4000

Maximum oxide thickness (mils=25.4μm) in the hot channel and maximum times predicted by Griess correlation

	Flow rate of 2500gpm	Flow rate of 2750gpm	Flow rate of 3000gpm	Flow rate of 3250gpm	Flow rate of 3500gpm
T_{inlet}=40°C	1.35	1.32	1.29	1.27	1.25
T_{inlet}=45°C	1.46	1.43	1.41	1.38	1.37
T_{inlet}=50°C	1.58	1.55	1.53	1.51	1.49
T_{inlet}=55°C	1.72	1.69	1.66	1.64	1.63
T_{inlet}=60°C	1.86	1.83	1.81	1.79	1.77

Maximum oxide thickness (mils=25.4μm) in the hot channel predicted by Kritz correlation

	Flow rate of 2500gpm	Flow rate of 2750gpm	Flow rate of 3000gpm	Flow rate of 3250gpm	Flow rate of 3500gpm
T_{inlet}=40°C	0.23	0.21	0.19	0.17	0.16
T_{inlet}=45°C	0.29	0.26	0.23	0.21	0.20
T_{inlet}=50°C	0.35	0.32	0.29	0.26	0.24
T_{inlet}=55°C	0.44	0.39	0.35	0.33	0.30
T_{inlet}=60°C	0.53	0.48	0.44	0.40	0.38

Maximum oxide thickness (mils=25.4μm) in the hot channel predicted by "Correl 2" correlation

The Griess correlation predicts that the oxide thickness limit of 2mils will be exceeded unless a low value of the inlet temperature and a high value of the flow rate are guaranteed. It must be reminded, though, that these calculations used conservative hypotheses about the heat flux. Besides, the fuel disposition is supposed to be modified according to the fuel management program, so that the oxide growth should be slowed down when moving the fuel from the hot channel to another one.

Figure 4.2
Surface heat flux q(W/m^2),
Z is proportional to the axial height (Z=1 is the core inlet, Z=10 is the core outlet)

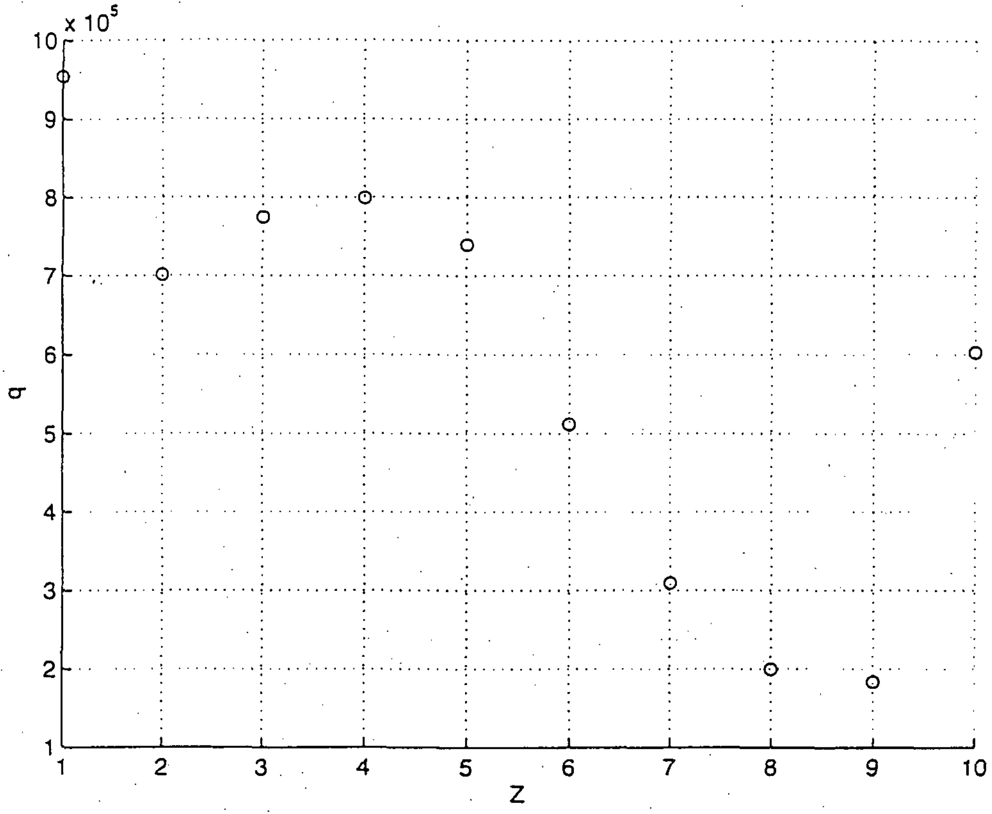

Figure 4.3

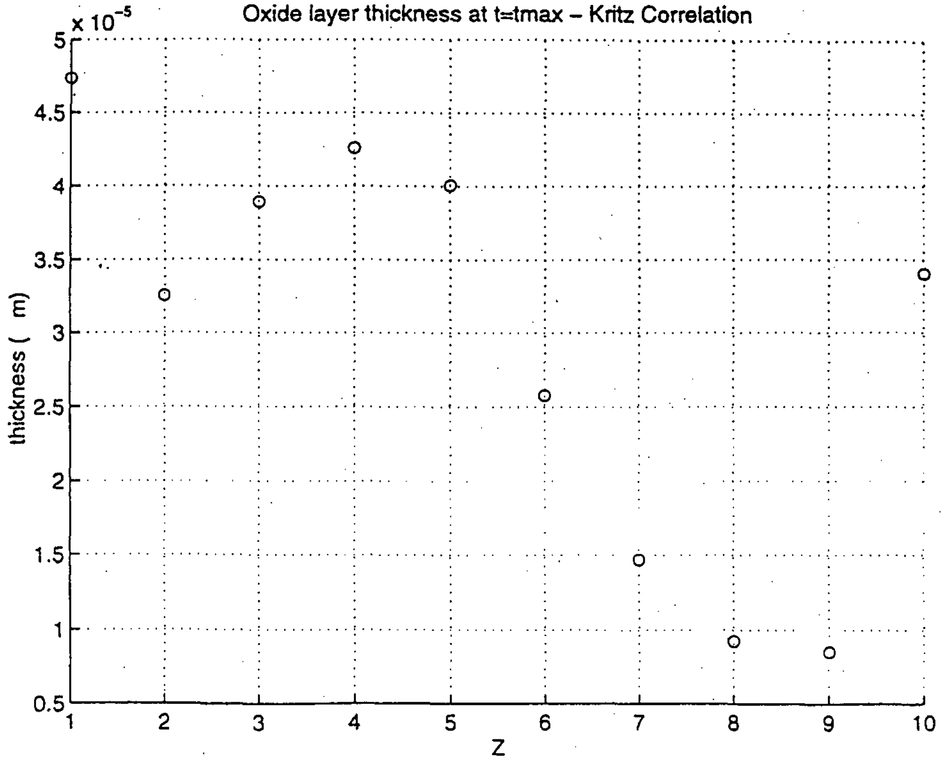

Figure 4.4

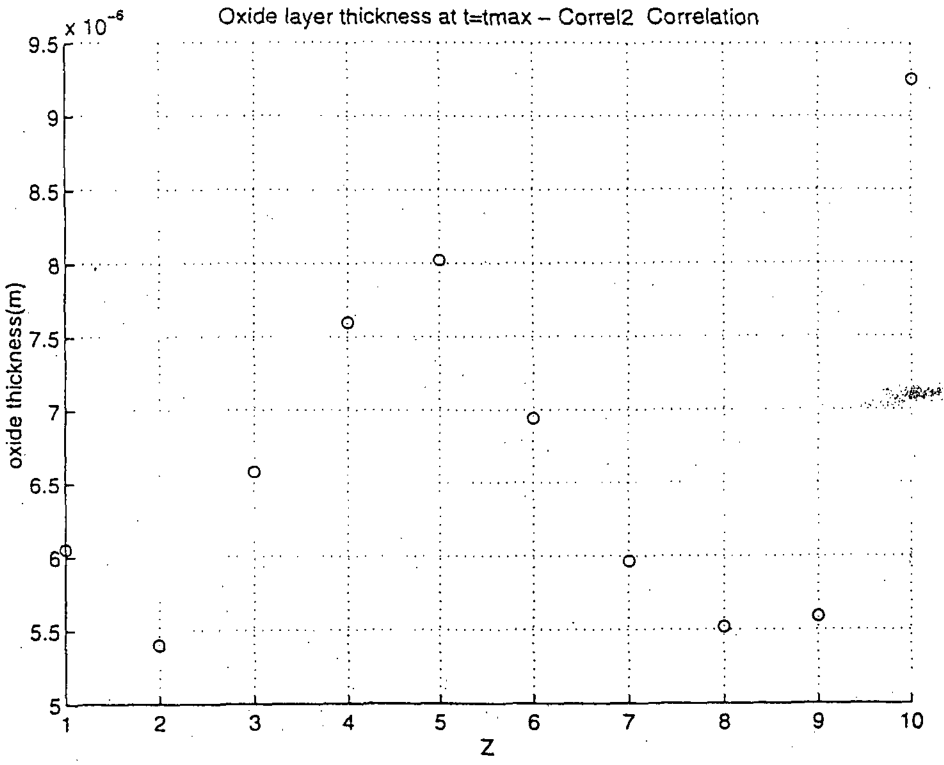

Figure 4.5

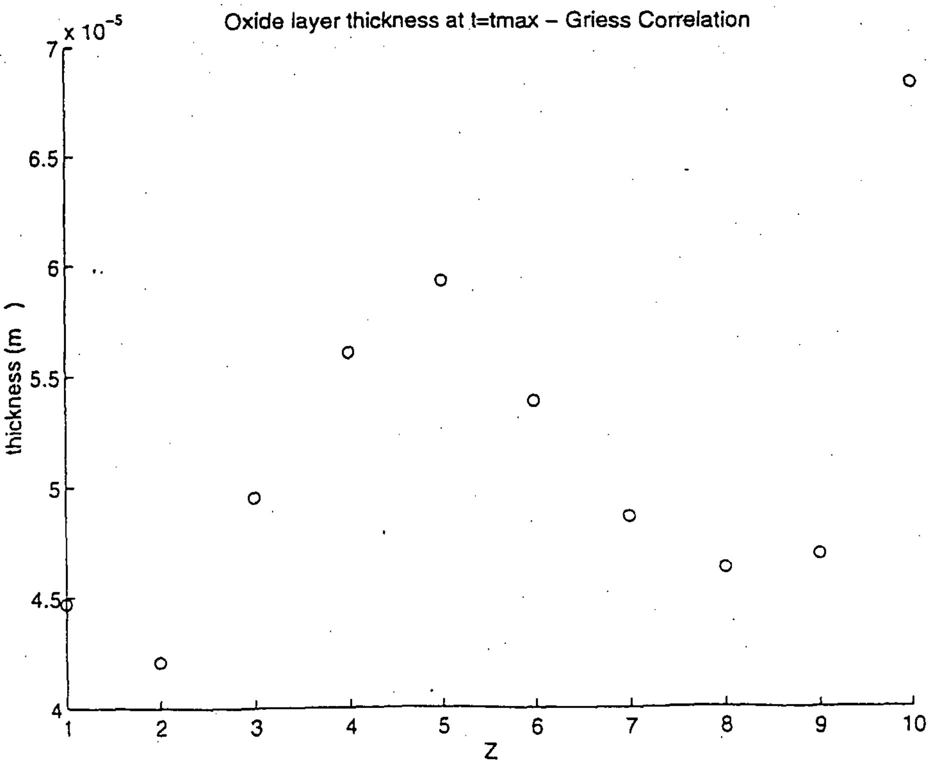

Above all, the Griess correlation is known to predict very conservative values, so that the results obtained by the Kritz correlation are more reliable. As far as the "Correl 2" correlation is concerned, the predictions are very low, which is probably due to this correlation not being valid for the low heat flux and high pH conditions of MITR-III.

4.3.2. Oxide distribution

Figures 4.2 4.3 4.4 give the calculated oxide distribution in the hot channel, in the worst case, that is for a maximum inlet temperature of 60°C and a minimum flow rate (2500gpm) and at the maximum time (7030 hours or 2900 hours for the Griess correlation). For the calculation, the channel was divided in 10 elements and Z, which is proportional to the axial height, represents the number of each element.

Once again, the results vary widely from a correlation to another. Griess and Correl 2 predict a maximum oxide layer at the outlet of the channel (Z=10), where the bulk temperature and the surface temperature are maximal, while the Kritz correlation locates the maximum oxide thickness at the channel inlet (Z=1) where the heat flux is the highest. The oxide distribution globally follows the heat flux profile along the channel and appears very heterogeneous.

4.3.3. Oxide thermal effect

The presence of the oxide results in a lower clad surface effectiveness , which leads to a wall temperature increase illustrated in figure 4.5. The maximum temperature increase compared to a configuration with no oxide is less than 4 °C. The global maximum surface temperature for all the calculations is 95 °C, which corresponds to the channel outlet temperature predicted by the Griess correlation. This value is still well below the 106°C value that corresponds to the onset of nucleate boiling.

4.3.4. Conclusions

The maximal thermal effect due to the oxide formation, as long as the oxide thickness remains less than 2 mils, is to increase the clad surface temperature by a maximum of 4°C. This temperature rise should not represent a major concern in MITR-III design, even if it cannot be neglected.

If we admit that the Kritz correlation is the most suitable to predict the oxide growth in MITR-III case, the oxide layer should not exceed the critical value of 2 mils above which film spallation could be feared. The maximum calculated oxide thickness was found equal to 1.9 mils for an extended burn-up limit of 2.3 10^{21} fissions/cm^3, a pH of 6, a core inlet temperature of 60°C, a flow rate of 2500 gpm and with conservative hypotheses on the heat flux.

Yet, the pH factor used for the present calculation was so empirical that we have doubts as to its validity for MITR case, so that we recommend a low core inlet temperature and a high flow rate for MITR-III.

A lower coolant pH, maintained below 5 by use of nitric acid would be the best solution to make sure that no risk of spallation exists.

In any case, the use of the Kritz correlation is recommended in the current MITR-II fuel management program as calculations performed in MITR-II configuration (5MW, maximum time of 11000 hours, same heat flux distribution) led to widely exceeded oxide thickness limits.

Figure 4.5

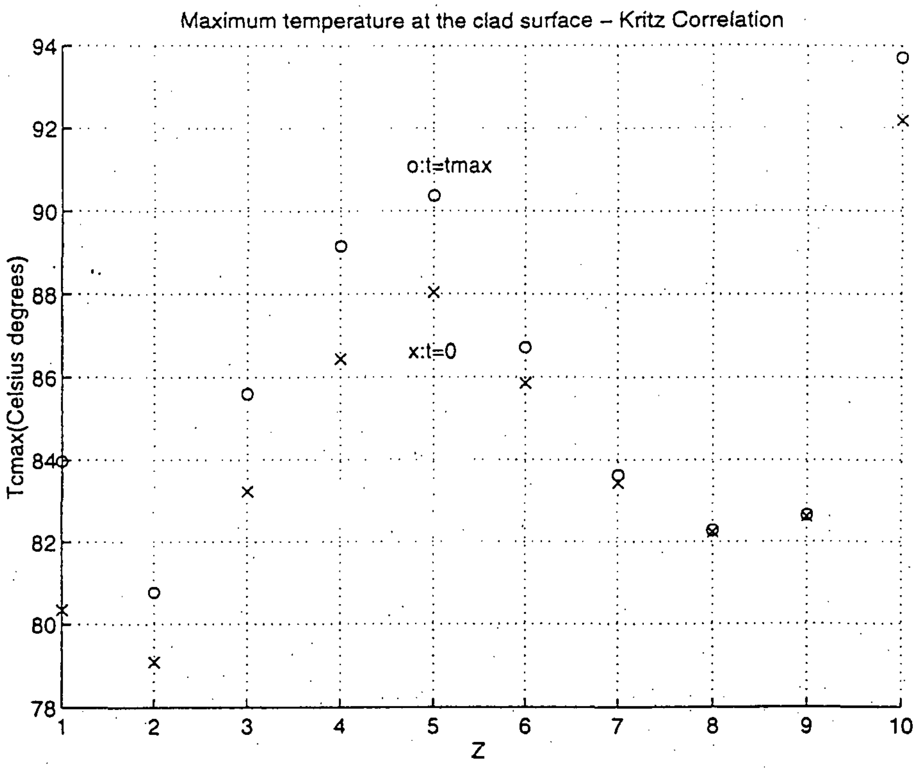
Maximum temperature at the clad surface – Kritz Correlation
Tcmax(Celsius degrees)
94
92
90
88
86
84
82
80
78
1
2
3
4
5
6
7
8
9
10
Z
o:t=tmax
x:t=0

5. Influence of the oxide growth on the coolant flow in the channel

5.1. Maximum swelling of the clad

In the previous parts, we generally made the hypothesis that the oxide thickness was equal to the corroded metal thickness, following the partial dissolution of the reacting aluminum in the coolant. Yet, if we assume that no dissolution occurs and that all the reacting aluminum remains on the clad surface, the consequence would be a partial clogging of the grooves between the fins and a global reduction of the hydraulic diameter.

If the oxide is entirely boehmite Al_2O_3-$3H_2O$, as suggested by all ex-reactor experiments, the production of one mole of oxide cones from the reaction of 2 moles of Al.

So that $\dfrac{\text{Volume of oxide}}{\text{Volume of reacting aluminium}} = \dfrac{M_{\text{boehmite}}}{\rho_{\text{boehmite}}} \dfrac{\rho_{\text{Al}}}{2M_{\text{Al}}} = 1.99$

With:

ρ_{Al}=2710kg/m^3

ρ_{boehmite}=3020kg/m^3

M_{al}=27.0g/mole

M_{boehmite}=120g/mole

We can deduce the clad maximum swelling due to the oxide formation, assuming a uniform oxide distribution as below:

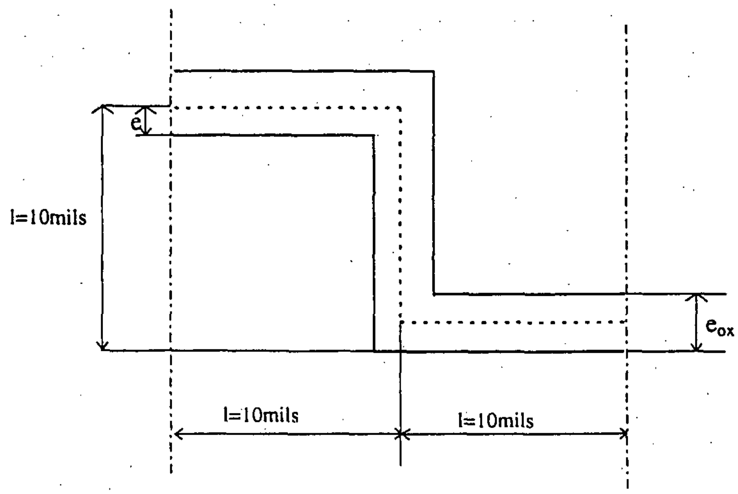

Figure 5.1

The ratio of the oxide volume by the volume of corroded metal is $\dfrac{e_{ox}(l+e)+2e_{ox}(l-e)}{el+2(l-e)e} = 1.99$.

For an oxide thickness of 2 mils, we find e=1.0 mils.

5.2. Effects on the average velocity in the channel

Such a situation would lead to a 2.4 % reduction of the channel hydraulic diameter from 2.25mm to 2.20mm and a 2.4 % reduction of the channel flow area from 131.8mm^2 to 128.7mm^2.

Assuming that the friction coefficient follows the Darcy law $\lambda = 0.316\,\mathrm{Re}^{-0.25}$, where Re is the Reynolds number, we can prove that, for a same configuration, the velocity (v) variations are bound to the hydraulic diameter (De) variations and the head loss (ΔP) variations by

$$\frac{d\Delta P}{\Delta P} + 1.75\frac{dv}{v} - 1.25\frac{dD_e}{D_e} = 0$$

So that, for an unchanged head loss, the relative velocity reduction in the channel is about 1.7%.

This value supposes that a uniform 2 mil oxide layer has formed along the considered channel, and that no dissolution of aluminum occurs and consequently must be considered as a very conservative value. We can conclude that the oxide formation should have a very small effect on the mean velocity in the core channels.

5.3. Velocity variations in the groove

It appears by intuition that, in the presence of fins, the boundary layer close to the roots of the fins is thicker, being more pronounced at the corners of the fin bases. This augmented boundary layer would increase the resistance to the heat transfer and reduce the flow velocity in the groove.

In such a case, the partial clogging of the grooves by the oxide could increase this effect.

An estimation of the boundary layer thickness comes from the **law of the wall** which gives the following expression for the dimensionless velocity u^+ in the boundary layer :

$$u^+ = \frac{1}{\kappa}\ln y^+ + C$$

where

$$u^+ = \frac{u}{u_e}\sqrt{\frac{2}{C_f}} \quad \text{and} \quad y^+ = \frac{y}{v}\sqrt{\frac{C_f}{2}}$$

u is the velocity in the boundary layer
u_e is the bulk velocity
v is the cinematic viscosity
C_f is the Darcy friction factor, given by $C_f=0.3164\,\mathrm{Re}^{-0.25}$.
κ is the Von Karman constant.
Mills ([15]) proposes κ=0.41 and C=7.44.
Defining the boundary layer thickness δ as the location where u=0.99u_e, we find the following results:

	Tb=40°C	*Tb=60°C*	*Tb=80°C*
v=3.35m/s	δ=4.6μm	δ=4.0μm	δ=3.6μm
v=4.68m/s	δ=4.0μm	δ=3.5μm	δ=3.1μm

The two values for the velocity v correspond to the mean velocity in the core channels for flow rates of 2500 and 3500 gpm.

As the distance between two fins is 254 µm with no oxide and more than 200 µm in the worst case in the presence of oxide, the dimensions of the flow space between fins remains about two orders of magnitude greater than the boundary layer. It is consequently expected that the partial clogging of the grooves will not affect the velocity, nor the heat transfer coefficient in the grooves.

6. Transient analysis

6.1. Presentation

The presence of the oxide is supposed to modify the thermal behavior of the clad in the case of a sudden heat-flux variation, following a rapid insertion of reactivity for instance. This change is due to the low conductivity of the oxide and to its slightly higher heat capacity. It is also due to the general lower performance of the fins in the presence of oxide as shown in the previous chapter.

It is important to know whether the presence of oxide can lead to exceed the temperature limit of 450°C for the clad, which corresponds to the integrity limit.

6.2. 1-dimensional hypothesis

A simple hypothesis, widely used for MITR thermal-hydraulic transient calculations consists in homogenizing the clad in the form of a 1-dimensional 20 mil flat plate.

In the case of a sudden variation of the heat flux from a constant value q_0 to another one q_1, the temperatures in the clad follow an exponential law :

$$T(t) = T_\infty + (T_0 - T_\infty)\ \exp(-t/t_c),$$

where t_C is a time constant, T_0 is the initial temperature for a heat flux q_0 and T_∞ is the temperature after an infinite time at a heat flux q_1.

In the 1-dimensional case, one can show ([16]) that:

$$t_c = \frac{L^2}{\alpha\mu^2},$$

where $\alpha = \dfrac{k}{\rho C}$ is the thermal diffusivity

k is the thermal conductivity
ρC is the heat capacity (J/m^3)
L is the plate thickness

$$\text{Besides, } \mu^2 = \left\{\begin{matrix} (\pi/2)^2 & \text{for large Biot numbers Bi} \\ \mathrm{Bi} & \text{for small Bi} \end{matrix}\right\} \approx \frac{1}{\left(\frac{2}{\pi}\right)^2 + \frac{1}{\mathrm{Bi}}},$$

where $\mathrm{Bi} = \dfrac{hL}{k}$

h is the heat transfer to coolant.

We found the following results for h=30000 MW/m^2K, which should be a characteristic value for MITR-III:

	k (W/mK)	ρC (kJ/m^3)	t_c(ms)
no oxide	200	2520	44
2 mil oxide thickness	164	2680	47

The homogenized value for k and ρC were found by still assuming a uniform oxide thickness and with the following values:

k_{Al}=200 W/mK
k_{oxide}=2.25W/mK
ρ_{Al}=2710 kg/m^3
ρ_{oxide}=3020 kg/m^3
C_{al}=930kJ/kg
C_{oxide}=1100kJ/kg (boehmite [11]).

These results would tend to show that the influence of the oxide on a thermal transient in the clad is small and can be neglected in a first approximation.

6.3. Finite difference formulation

As the first part showed unexpected differences between the 1-dimensional and the 2-dimensional results, the steady state finite difference program was adapted for transients to obtain a Crank-Nicholson method, which has the advantage of being unconditionnally stable (unlike the explicit method) and is known to give more accurate results than fully explicit or implicit methods for a given mesh size.

Like previously, we write heat balances on finite control volumes, which yields for an interior node:

$$\alpha(Q_x^{n+1}|_E + Q_x^{n+1}|_W + Q_y^{n+1}|_S + Q_y^{n+1}|_N) + (1-\alpha)(Q_x^{n}|_E + Q_x^{n}|_W + Q_y^{n}|_S + Q_y^{n}|_N) + \overline{(\Delta x \Delta y)}\rho_1 C_1 \frac{\theta_{i,j}^{n+1} - \theta_{i,j}^{n}}{\Delta t} = 0$$

where α=0.5 for a Crank-Nicholson method,

$Q_x^n|_E$ represents the heat passing through the eastern face of the control volume in the x-direction, at the time step n, so that $Q_x^n|_E = -k_1 \overline{\Delta x} \frac{\theta_{i,j+1}^{n} - \theta_{i,j}^{n}}{\Delta y_j}$ (see figure 3.7)

T had been previously defined as $(\theta_{1,1}\ \theta_{1,2} \ldots \theta_{1,n4}\ \theta_{2,1} \ldots)^T$.
The matrix M characterizing the steady-state problem MT=V (cf chapter 3.3.3) may be easily modified to characterize the new system of equations.
In a first step, we multiply the appropriate lines of M by k_1 or k_2, so that the elements of the vector M'T, where M' is the modified matrix, represent the heat powers exiting the control volumes (i,j). V' is then deduced by multiplying the lines of V by the same coefficients so that MT=V and M'T=V' are two equivalent problems.

For each node (i,j), we define $p_{i,j} = \frac{C_{i,j}}{\Delta t}$, where $C_{i,j}$ is the heat capacity of the control volume surrounding the node (i,j). This heat capacity has to be calculated for every control volume type.

We can then build the matrix P defined by $PT = (p_{1,1}\theta_{1,1} \ \ p_{1,2}\theta_{1,2} \cdots p_{m_3,n_2}\theta_{m_3,n_2})^T$.

Assuming that the same boundary conditions as in the steady-state problem are fulfilled, the transient finite element problem then becomes:

$$(\alpha M'+P)T^{n+1} + ((1-\alpha)M'-P)T^n = V'^n$$

where $T^n = (\theta^n_{1,1} \ \ \theta^n_{1,2} \ldots \theta^n_{m3,n2})$ is the temperature distribution in the clad at the time step n.

Thus the transient problem can be explicitely solved by Matlab, :

$$T^{n+1} = AV'^n - BT^n$$

where $A=(\alpha M'+P)^{-1}$ and $B=A((1-\alpha)M'-P)$,

Heat flux data, varying with n, appear in V'^n.

6.4. Validation tests

After an infinite time, it was checked that the time dependent temperature distribution converges to the solution given by the steady-state program.
Besides, least square regressions still performed with Matlab allowed to check the values given by the 1-dimensional analysis in chapter 6.2 in the case of a homogenized clad.
For h=30000 W/m^{2}K, the time constant corresponding to the maximum temperature in the clad was found to be 42.7 ms with no oxide and 46 ms with a 2 mil oxide film, which is relatively closed to the theoretical values.

6.5. Results

6.5.1. Time constants

Least square regressions performed on the maximum temperature in the clad after a small heat flux change (0.1MW/m^2) gave the results presented in figure 6.1 . For a bad heat exchange between the clad and the coolant, it is physically more difficult for the fluid to drain off the energy stored in the clad after the heat flux increase. That is why a lower heat transfer coefficient leads to significantly higher time constants, as 1-dimensional expressions foresee.
We can notice important differences with the time constant values predicted by the homogeneous plate model (figure 6.2). First, the time constant without oxide is twice lower than that calculated under the hypothesis of a homogeneous clad, which means that the real clad thermal inertia is much lower than that generally assumed. Moreover, the oxide formation consistently increases the thermal inertia of the clad, leading to a higher time constant: 37.8 ms at h=30000W/m^{2}K for a 2 mil oxide film, instead of 22.2 ms with no oxide.
The time constant for the maximum temperature at the clad surface was a bit higher (respectively 40.5 ms and 23.5 ms). This difference can be interpreted as the transport time of the energy from the inner part of the clad to the surface. It is logically increased in the presence of oxide.

Figure 6.1

Time constants (Maximum temperature in the clad)
2-dimensional computations

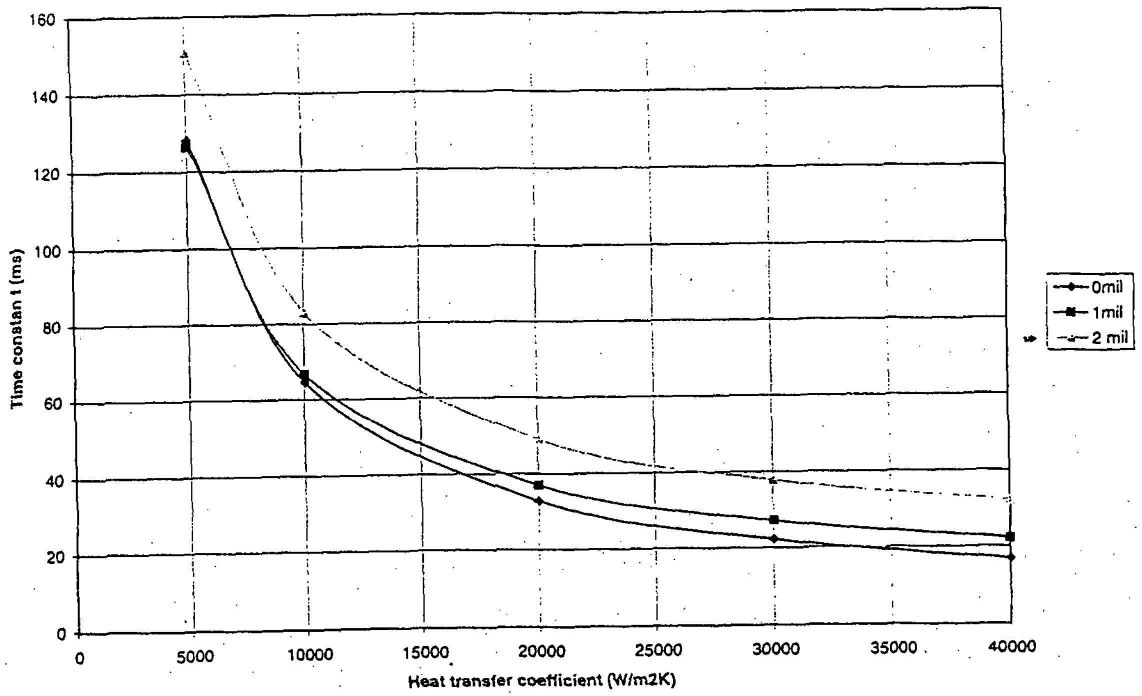

Figure 6.2

Time constants (Maximum temperature in the clad)
Homogeneous clad hypothesis

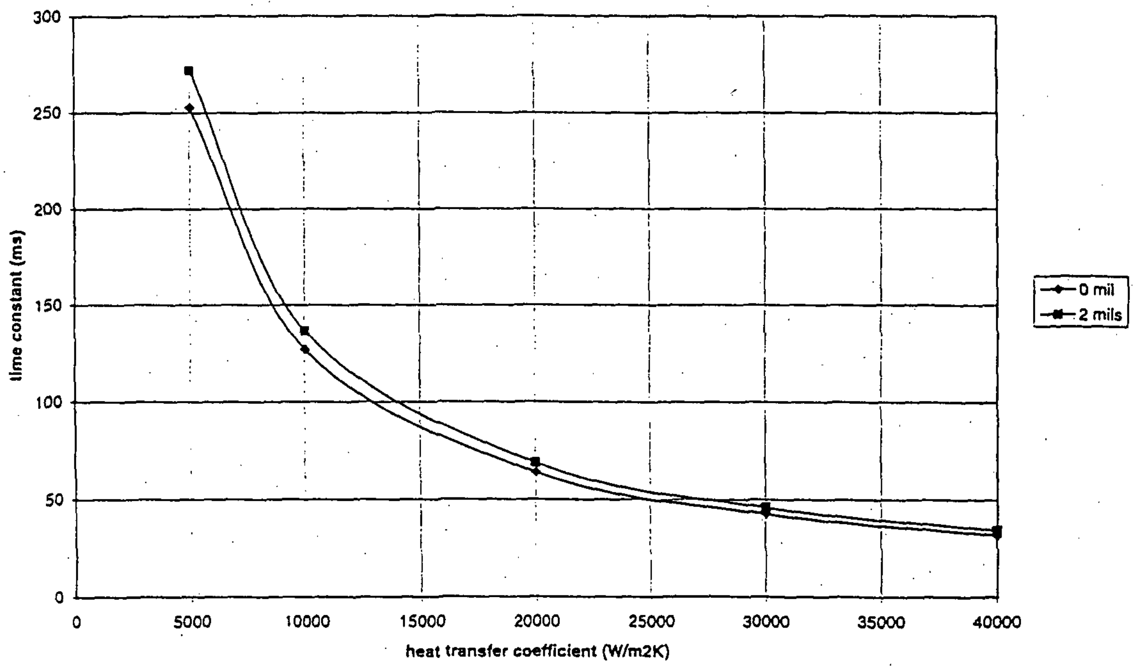

6.5.2. Thermal behavior for a rapid insertion of reactivity

In order to illustrate better the influence of the oxide on a reactivity insertion scenario, we exploited a result by Dutto&Evo ([20]) who used the Paret code to investigate the most penalizing case of reactivity insertion in the MITR II. A reactivity step insertion of 2$ at a low initial power of 10 kW led to the power peak represented in figure 6.3.

We assumed the same power peak to compute the evolution of the maximum temperature in the clad at the hot spot. As the used model is limited to the behavior of the clad itself, we had to assume a constant heat transfer coefficient as well as a constant coolant temperature, so that our results must be considered as a sensitivity study. A constant hot spot factor of 2.2 was assumed for the heat flux, which is the steady state value computed by Bhutta ([17]).

First, the hypothesis of a homogeneous clad was used to compute the temperature evolution in the clad. Dutto&Evo had precisely used this hypothesis, which leads to double the exchange surface to take into account the presence of the fins. In order to translate this hypothesis in our calculation, we divided by two the hot channel factor. The result was a peak temperature of 165°C with no oxide layer and 161°C with a 2 mil oxide film (cf figure 6.3). The calculation was performed for T_b=40°C and h=30000 W/m^{2}K and the maximum temperature increase of 120°C due to the reactivity insertion corresponds fairly well to the temperature increase in the clad predicted by Dutto&Evo (around 110°C).

On the contrary, the 2-dimensional calculations resulted in a worrying peak temperature increase up to 300°C for a 2 mil oxide thickness and a still high temperature of 250°C with no oxide (cf figure 6.4).

The higher temperature peak obtained for the 2-dimensional hypothesis is probably due to the finned clad having a lower thermal inertia than the homogeneous non-finned clad (cf time constants). When adding an oxide layer, we increase the thermal inertia, but the surface effectiveness is lowered, which explains the higher peak temperature obtained.

The reduction of the heat transfer to h=10000W/m^{2}K logically resulted in higher temperatures (up to 300-320°C) but the influence of the oxide was lower (a few degrees only).

6.6. Conclusions

We found a disagreement between the 'homogenized clad' model and our 2-dimensional finned clad model, which would tend to prove that the homogeneous hypothesis, which has been commonly used for the transient analysis of the MITR, is not valid for MITR-III.

At h=30000W/m2K, the presence of a 2mil oxide thickness resulted in a significant increase of the peak temperature (50°C). Yet, our results still predict temperatures well below the 450°C limit.

As in the steady state analysis, higher values for the heat transfer coefficient lead to a increase the oxide influence.

Yet, we must not overlook the simplicity of our modeling, which does not take into account the heat transfer exchange between the clad and the coolant, nor the presence of the fuel or 3-dimensional effects. The real problem is much more intricate.

Figure 6.3
Maximum temperature in the clad - 2-dimensional computations

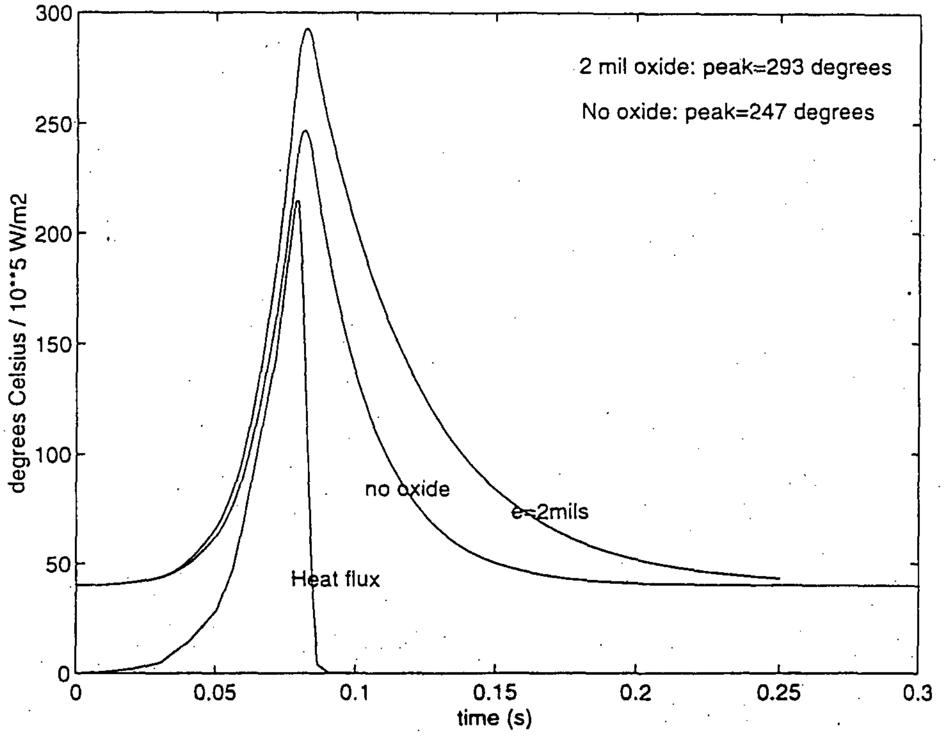

Figure 6.4

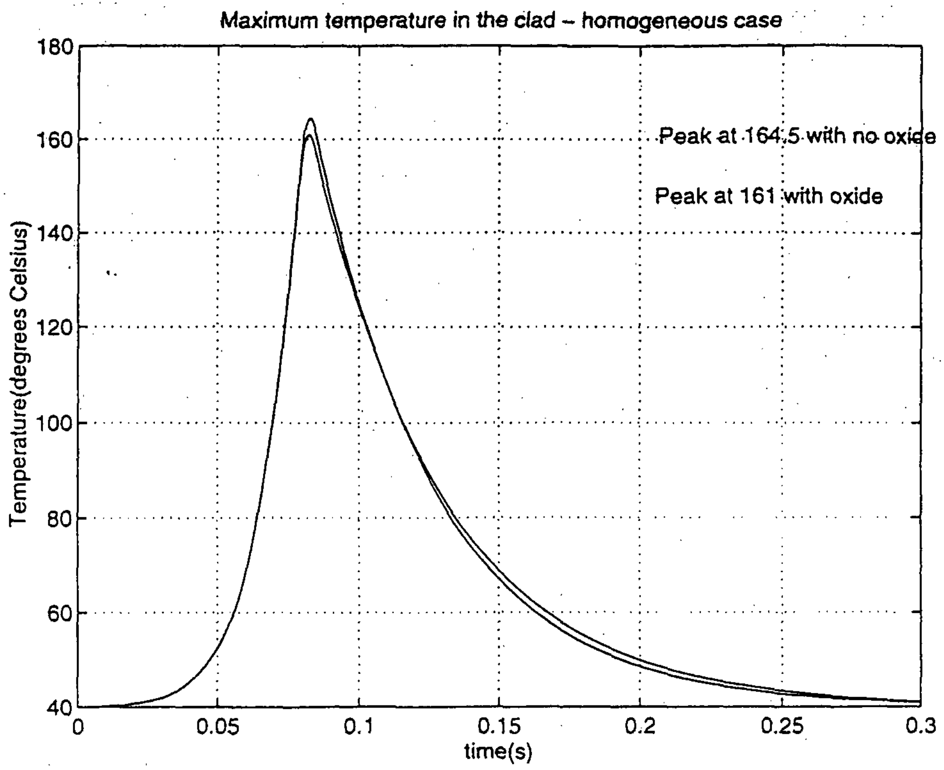

7. Conclusions and recommendations

The 2-dimensional calculations performed on the fuel clad tended to prove that a more conservative margin must be considered to determine the maximum temperature at the surface of the finned clad for high values of the heat transfer coefficient as foreseen for the MITR-III reactor, and to take into account the presence of a layer of aluminum oxide at the clad surface.
An oxide thickness limit of 2 mils should prevent cases of spallation, which could lead to the release of radioactive gas in the primary water. The Kritz correlation predicts that this limit should not be exceeded, even for an extended fuel burn-up limit of 2.3 10^{21} fissions/cm^3, while the Griess correlation leads to unacceptable values.
Yet it is difficult to be sure of the validity of this correlation because of the high pH value of the primary water in the MITR reactor. A pH regulation by use of nitric acid would allow to maintain a lower pH value (below 5) and to reduce significantly the oxide formation.
In other respects, an experimental ex-reactor program could allow to check the validity of the Kritz correlation and/or prove that no case of spallation is to be feared.
The use of the Kritz correlation in the fuel management program is recommended.

As far as the effects of the oxide layer are concerned, we found a maximum temperature increase at the clad surface of less than 4°C in the hot channel for an operation power of 10 MW.
As long as its thickness is less than 2 mils, the oxide should have a very limited influence on the primary water flow in the channels.
Yet, its influence in case of a reactivity insertion accident should be more important than foreseen by the usual 'heterogeneous clad' approximation. The temperature limit of 450°C should not be exceeded, though.
The very different behavior noticed between the homogeneous 1-dimensional clad hypothesis and the 2-dimensional clad would justify further investigation.

BIBLIOGRAPHICAL REFERENCES

[1] Request for additional information by the United Stets Regulatory Commission, January 14, 1991.

[2] J.A Taborda-Romero, *Design of MITR-II Fuel Plates:Heat Transfer in Longitudinal Finned Narrow Channels,* M.S. Thesis, MIT Departement of Nuclear Engineering, Sept. 1971.

[3] H.P Godard, W.B. Jepson, M.R. Bothwell, R.L. Kane, *The Corrosion of Light Metals,* John Wiley & Sons, Inc,1967.

[4] J.C. Griess, H.C. Savage, T.H. Mauney, J.L English, J.G. Rainwater, *Effect of Heat Flux on the Corrosion of Aluminum by Water. Part II. Influence of Water Temperature, Velocity and pH on Corrosion-Product Formation,* ORNL-3056, Union Carbide Corp., Oak Ridge Natl. Lab., Feb 1961.

[5] J.C. Griess and al.,. *Effect of Heat Flux on the Corrosion of Aluminum by Water Part III. Final Report on Tests Relative to the High-Flux Isotope Reactor,* ORNL-3230, Union Carbide Corp., Oak Ridge Natl. Lab., Dec 1961.

[6] J.C. Griess, H.C. Savage, J.L. English, *Effect of Heat Flux on the Corrosion of Aluminum by Water. Part IV. Tests Realtive to the Advanced Test Reactor and Correlation with Previous Results.* , ORNL-3541, Union Carbide Corp., Oak Ridge Natl. Lab., Feb 1964.

[7] S. J. Pawel, D. K. Felde, R. E. Pawel, *Influence of Coolant pH on Corrosion of 6061 Aluminum Under Reactor Heat Transfer Conditions,,* ORNL/TM-13083, Union Carbide Corp., Oak Ridge Natl. Lab., October 1995.

[8] R. E. Pawel, G. L. Yoder, D. K. Felde, B. H. Montgommery, M. T. McFee, *The Corrosion of 6061 Aluminum Under Heat Transfer Conditions in the ANS Corrosion Test Loop, Oxydation of Metals,* Vol.36, Nos 1/2, 1991.

[9] R.E Pawel, D.K. Felde, J.A Clinard, T.A Thornton, *The Corrosion Behavior of 8001 Al Under Heat Transfer Conditions in an Aqueous Loop System,* ORNL/NPR-92/65, Oak Ridge Natl. Lab.

[10] R.E Pawel, D.K. Felde, M.T. McFee, *The Development of an Improved Correlation for Corrosion Product Growth on Aluminum Alloy Fuel Cladding for the Advanced Neutron Source.*

[11] D.D. Mac Donald, P. Butler, *The Thermodynamics of the Al-Water System at Elevated Temepratures,* Corrosion Sc., 1973, vol.13, pp 259-274

[12] *Report of the Advanced Neutron Source (ANS) Aluminum Cladding Corrosion Workshop, November 16-17, 1988, Idaho Falls, Idaho,* CONF-8811203, Oak Ridge Natl. Lab.

[13] e-mail by K. White (HFBR) to T. Courau, 1996.

[14] Parra, J.A., *The Physics and Engineering Upgrade of the MIT Research Reactor,* Ph.D. Thesis, MIT Nuclear Engineering Department, April 1993.

[15] G.L. Yoder, N.C.J. Chen, D.K. Felde, W.R. Nelson, R.E. Pawel, *The Effect of Aluminum Corrosion on the Advanced Neutron Source Reactor Fuel Design,* Nuclear Engineering and Design 136 (1992) 401-408, North Holland.

[16] A.F. Mills, *Heat Transfer*, R.R. Donneley&Sons, Irwin, 1992.

[17] B. Bhutta, report on MCMP calculations, MIT Nuclear Reactor Lab.,1996.

[18] K.A. Lucas, H. Clarke, *Corrosion of Aluminum-Based Matrix Composite*, Research Studies Press Ltd, John Wiley&Sons Inc., 1993.

[19] J.M. Beeston, R.R. Hobbins, G.W. Gibson, W.C.Francis, *Development and Irradiation Performance of Uranium Aluminide Fuels in Test Reactor,* Nuclear Technology, Vol 49, June 1980.

[20] J.B. Dutto, T. Evo, *Investigation of the Paret Code to Evaluate Safe Reactivity Limits for the MITR II Reactor*, Report, MIT Nuclear Reactor Laboratory, 1994.

APPENDIX 1

```
Values of p(1), p(2), p(3), p(4), etamin=p(1)+p(2)*h+p(3)*exp(p(4)*h)

e(mil)  p(1)               p(2)              p(3)             p(4)
0.00   1.8605010e+00  -2.0162631e-06   1.3963113e-01  -1.4592113e-05
0.10   1.8267363e+00  -1.5850129e-06   1.7335863e-01  -1.5330724e-05
0.15   1.8186180e+00  -1.4279620e-06   1.8145320e-01  -1.6021888e-05
0.25   1.8062708e+00  -1.1699121e-06   1.9372838e-01  -1.7509670e-05
0.35   1.7937893e+00  -1.3981472e-06   2.0619439e-01  -1.7910801e-05
0.50   1.7794194e+00  -1.7061679e-06   2.2051593e-01  -2.2293530e-05
0.75   1.7520198e+00  -2.3146956e-06   2.4776036e-01  -2.9724734e-05
1.00   1.7241165e+00  -2.8448090e-06   2.7535175e-01  -3.6753076e-05
1.50   1.6596023e+00  -3.9296169e-06   3.3854280e-01  -4.9466156e-05
2.00   1.6023398e+00  -4.4150916e-06   3.9344200e-01  -6.1079958e-05
2.50   1.5409483e+00  -4.9501131e-06   4.5114290e-01  -7.1517684e-05


Values of p(1), p(2), p(3), etaav=p(1)+p(2)*exp(p(3)*h)

e(mil)     p(1)            p(2)            p(3)
0.00   1.3451977e+00   6.5474158e-01  -5.6032905e-06
0.10   1.5008278e+00   4.9905168e-01  -7.8042616e-06
0.15   1.5492427e+00   4.5059942e-01  -8.8775188e-06
0.25   1.6146930e+00   3.8505340e-01  -1.1052148e-05
0.35   1.6572083e+00   3.4740145e-01  -1.3295599e-05
0.50   1.6912399e+00   3.0810652e-01  -1.6646046e-05
0.75   1.7130506e+00   2.8557376e-01  -2.2420642e-05
1.00   1.7120526e+00   2.8548030e-01  -2.8034554e-05
1.50   1.6769716e+00   3.1705721e-01  -3.8319891e-05
2.00   1.6301483e+00   3.5876435e-01  -4.7981864e-05
2.50   1.5720452e+00   4.0977805e-01  -5.6747397e-05
```

Appendix 2

Answers to the Nuclear Regulatory Commission Request (ref [1])

1. *Compare directly the predicted oxide thickness for extended burn-up with the oxide thickness assumed in the FSAR for the presently approved burn-up. Discuss whether the new predictions lead to fuel temperatures above limits previously analyzed and approved for normal operation.*

Cf chapter 4.
According to the present study, a maximum thickness of 1.9 mils for the oxide layer thickness should not be exceeded in MITR-III. According to Griess, no risk of spallation or clad deterioration is to fear below this limit. The calculations used the Kritz correlation with the correcting factor proposed by Griess to take into account the high pH of MITR and is valid for a low flow rate hypothesis (2500 gpm) and a high core inlet temperature (60°C) hypothesis. The calculation took into account the increase of the wall temperature due to the oxide formation . The maximum temperature increase obtained was inferior to 4°C and the wall temperature never exceeded 94°C in the hot channel.
The 2 mil limit to prevent risks of spallation is probably very conservative though. Indeed, according to recent studies ([8,15]), spallation is linked to thermal stress and should not occur for a temperature drop of less than 113°C in the oxide layer, a value which will never be reached in MITR as the heat flux is too low ($1MW/m^2$ at the hot spot for a 10 MW power). A maximum clad temperature increase of 15°C must be expected in the presence of a 2 mil oxide thickness, according to 2-dimensional complementary results, so that the clad temperature will remain very far from the integrity temperature limit (450°C).

2. *Oxide thickness also affects responses to rapid insertions of reactivity, and ,perhaps, other MIT accident scenarios. Please review and re-analyze all potential accidents and discuss whether FSAR conclusions would remain valid with the projected increases in oxide thickness.*

Cf chapter 6.
It is usually assumed for transient analyses that the clad is a homogenized non-finned plate. If the same hypothesis is assumed in the presence of a 2mil oxide layer, the oxide influence should be relatively small and would even lead to lower peak temperatures in the case of a reactivity insertion scenario.
Yet, 2-dimensional modeling revealed that the influence of the oxide layer should lead to higher temperatures. For a 2$ reactivity insertion scenario, the peak temperature was estimated to 290°C, while it was around 250°C for a clad with no oxide. The obtained temperatures remain far away from the clad structural integrity limit of 450°C, though.

3. *The increased oxide thickness will decrease the hydraulic diameter of the grooves. This will result in increased pressure losses due to friction and to decreased coolant velocities in the grooves. Please provide analyses of the impact of these changes on hot channel factors, and assess to what extent the decreased coolant velocities affect the oxide build-up or other crud deposition in the grooves. Unless justification can be provided that grooves do not become clogged, please provide analyses of fuel*

temperature conditions both in steady state and potential accident scenarios with the grooves filled with oxide.

Cf chapter 5.
In the worst case (no dissolution of the reacting aluminum in the coolant), a 2 mil boehmite layer would represent a reduction of the hydraulic diameter by 2.2%. This is a very conservative value, though, as a part of the reacting aluminum should be dissolved in the coolant.
On the same assumption, the space between the fins would be reduced from 10 mils to 8 mils (>200μm). As the boundary layer thickness is less than 5 μm for MITR-III, it is expected that this reduction would have a very limited influence on the coolant velocity in the groove.

4. The thermal conductivity assumed for the oxide on the fuel plates appears to be inconsistent. The response o the request for information dated 11/28/89 satets a thermal conductivity of 2.0 Btu/hr-°F-ft. The conductivity used will influence fuel plate temperatures, transient response to accidents, and additional oxide growth since the oxide-aluminum interface temperature controls oxide growth. Please justify the use of the 2.0 Btu/hr-°F-ft value in your analyses, or re-analyze reactor behavior with the Griess value of 1.3 Btu/hr-°F-ft.

All the present study assumed the Griess value of 1.3 Btu/hr-°F-ft for the conductivity of the oxide.

Appendix C

MathCAD for RAI #4.15

Natural Convection CHF for the MITR

$g := 9.8$

$\rho f := 953$ $\rho g := 0.75$ $hf := 448.47 \cdot 10^{3}$ $hg := 2686.9 \cdot 10^{3}$ $\sigma := 64 \cdot 10^{-3}$ $Tsat := 107$

(properties for P=0.13 MPa, 3 meters under water) $\mu f := 260 \cdot 10^{-6}$ $cpf := 4200$

$$\lambda := \left[\frac{\sigma}{(\rho f - \rho g) \cdot 9.8}\right]^{0.5}$$

$Aht\_1side := 0.031757$

$Aht := Aht\_1side \cdot 2 \cdot 1.9 \cdot 15 \cdot 22$

$Axs := 22 \cdot 15 \cdot 1.2490 \cdot 10^{-4}$ $W := 5.588 \cdot 10^{-2}$

$R := 0.697 + 0.00063 \cdot \frac{0.5683}{2.1864 \cdot 10^{-3}}$ $R = 0.861$

$$q\_CHF(G, DT\_sub) := 0.005 \cdot (hg - hf) \cdot [\lambda \cdot \rho g \cdot (\rho f - \rho g) \cdot 9.8]^{0.5} \cdot \left[\frac{G}{[\lambda \cdot \rho g \cdot (\rho f - \rho g) \cdot 9.8]^{0.5}}\right]^{0.611} \cdot \left[1 + \frac{5000}{\frac{G}{[\lambda \cdot \rho g \cdot (\rho f - \rho g) \cdot 9.8]^{0.5}}} \cdot DT\_sub \cdot \frac{cpf}{(hg - hf)}\right]$$

(Sudo et al, 1993)

SAR Eq (4-30)

$$q\_CHF3 := 0.7 \cdot \frac{Axs}{Aht} \cdot (hg - hf) \cdot [\lambda \cdot \rho g \cdot (\rho f - \rho g) \cdot 9.8]^{0.5} \cdot \frac{\sqrt{\frac{W}{\lambda}}}{\left[1 + \left(\frac{\rho g}{\rho f}\right)^{0.25}\right]^{2}}$$

(minimum CHF heat flux due to blocked channel)

$q\_CHF3 = 2.353 \times 10^{4}$

Appendix D

- Study for RAI 4.16

Journal of NUCLEAR SCIENCE and TECHNOLOGY, 23[1], pp. 73~82 (January 1986).

TECHNICAL REPORT

Experimental Study of Incipient Nucleate Boiling in Narrow Vertical Rectangular Channel Simulating Subchannel of Upgraded JRR-3

Yukio SUDO*, Keiichi MIYATA**, Hiromasa IKAWA*
and Masanori KAMINAGA*

* *Japan Atomic Energy Research Institute*
** *Nippon Kokan K. K.*

Received May 15, 1985
Revised July 23, 1985

Experiments were carried out with a vertical rectangular channel simulating a subchannel of the upgraded JRR-3 fuel element, in order to investigate the validity and the error of the correlations predicting the superheat at the onset of nucleate boiling. These correlations were used in the core thermal-hydraulic design of the upgraded JRR-3. As the results, the following were made clear: ① The existing Bergles-Rohsenow correlation gives a good prediction for the relationship of heat flux *vs.* superheat at the onset of nucleate boiling, with the error of about 1 K against the lower limits of the measured superheat. ② There are no significant differences in the characteristics of the relationship of heat flux *vs.* superheat at the onset of nucleate boiling between upflow and downflow. ③ There are no significant differences in the histories of relationship of heat flux *vs.* superheat from the forced convection single-phase flow to the subcooled boiling between increasing heat flux and decreasing heat flux, with little overshoot of superheat at the onset of nucleate boiling both in the upflow and in the downflow.

KEYWORDS: incipient nucleate boiling, vertical rectangular channel, forced convection, subcooled boiling, upflow, downflow, hysteresis, ONB temperature, heat flux, superheating

I. INTRODUCTION

The problem which is addressed to in this study is of the incipient nucleate boiling in a narrow vertical rectangular channel simulating a subchannel of the upgraded Japan Research Reactor-3 (JRR-3). The Japan Atomic Energy Research Institute (JAERI) is planning to remodel the existing research reactor, JRR-3 from 10 to 20 MWt with 20% low enriched uranium (LEU) fuel to primarily provide much higher thermal neutron fluxes and adequate neutron flux sources for beam experiments. The upgraded JRR-3 is designed to be a light water moderated and cooled, beryllium and heavy water reflected, pool-type reactor.

A key design criterion was set up for the core thermohydraulics so that the fuel may have enough safety margin under the condition of normal operation in which the core is cooled by either the natural convection or the forced convection. Heat generated in the core is removed by the natural convection cooling mode due to a natural circulation be-

---

* *Tokai-mura, Ibaraki-ken 319-11.*
** *No. 1-1-2, Marunouchi, Chiyoda-ku, Tokyo 100.*

tween the core and the reactor pool through a valve up to 200 KW and by the forced convection cooling mode with the downward core flow up to 20 MW. The criterion is that nucleate boiling should be avoided anywhere in the core in order to give enough margin against the burnout of the fuel even at the hottest spot in the core, to avoid any flow instability induced by partial boiling and to obtain stable neutron fluxes for experiments. For this criterion, the margin of the fuel surface temperature against the onset of nucleate boiling (ONB) temperature was evaluated and secured in the core thermohydraulic design, using so-called hot channel factors⁽¹⁾. The ONB temperature was determined by the following two simultaneous equations:

Bergles & Rohsenow

$$q=1.76\times10^{-3}\cdot P^{1.156}\left\{\frac{9}{5}(T_w-T_s)\right\}^{2.83/P^{0.0234}} \qquad (1)$$

$$q=0.023\,Re^{0.8}\,Pr^{0.4}\frac{k}{D_e}\{(T_w-T_s)+(T_s-T_b)\}. \qquad (2)$$

Equation (1) was proposed by Bergles & Rohsenow⁽²⁾ as a relationship of heat flux q *vs.* superheat ΔT_s $(=T_w-T_s)$ at the onset of nucleate boiling for water, and Eq. (2) was proposed by Dittus & Boelter⁽³⁾ for the forced convection single-phase flow. The ONB temperature T_{ONB} and the ONB heat flux q_{ONB} are obtained as an intersecting point of Eqs. (1) and (2), as shown in **Fig. 1**.

Equation (2) gives higher heat flux with higher water velocity, that is, higher Reynolds number and higher inlet water subcooling (T_s-T_b). Therefore, the intersecting point of Eqs. (1) and (2) gives higher heat flux and superheat at the onset of nucleate boiling with higher water velocity and inlet water subcooling. This is a remarkable feature of the conditions of the onset of nucleate boiling predicted by Eqs. (1) and (2). In Fig. 1 are also illustrated the following theoretical predictions which were obtained by Davis & Anderson⁽⁴⁾ from the postulation of Hsu⁽⁵⁾.

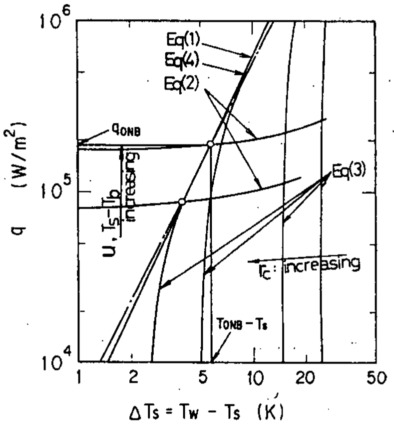

Fig. 1 Determinations of heat flux q and superheat ΔT_s at incipient nucleate boiling

$$T_{\mathrm{ONB}}-T_s=\frac{2\sigma T_s}{h_{fg}\gamma_g}\cdot\frac{1}{r_c}+\frac{q_{\mathrm{ONB}}\,r_c}{k} \qquad (3)$$

for the given radius r_c of active cavities, and

Davis & Anderson

$$q_{\mathrm{ONB}}=\frac{h_{fg}\gamma_g k}{8\sigma T_s}(T_{\mathrm{ONB}}-T_s)^2 \qquad (4)$$

for any size of r_c. Equations (1) and (4) are in good agreement with each other as shown in Fig. 1 and fairly well predict the onset of nucleation in the experiments carried out by Bergles & Rohsenow⁽²⁾ with water flowing at velocities up to 17.5 m/s at low pressures and low temperatures and also in the experiments of Clark & Rohsenow⁽⁶⁾ at high pressures.

For the evaluation of the margin of fuel surface temperature against the ONB temperature, the precision of Eqs. (1) and (2) should have been made clear. The precision of Eq. (2) has been evaluated in the experiments with a vertical rectangular channel simulating the subchannel of the JRR-3 for both upflow and downflow⁽⁷⁾. Meanwhile, the

---

precision of E
JRR-3 becaus
nucleate boilin
The objective
ing out the e
channel of th
the JRR-3 in
characteristics
departure fror

Figure 2
the test loop,
used to invest
phase forced-c
teristics betwe
a narrow rect
is composed
0.2 m³ in vol
bypass line, a
valves, stop
simulating a s
ard fuel eleme
flow can be se
order to inve
natural convec
the forced con

The test s
The configurat
rectangular wi
similar to the
in water gap a
that of the JR
the experiment
width as the J
channel does n
are made of In
the inside of t

The heatin
channel is obt
Water tempera
O.D. thermocou
at several loca
ONB is obtaine

The temper
surface temper

precision of Eq. (1) was not always clear for the application to the subchannel of the JRR-3 because the amount of available data was small on the condition of the onset of nucleate boiling for the forced convection flow though some data have been reported(8)~(10). The objectives of this study are, therefore, (1) to estimate the error of Eq. (1) by carrying out the experiment with a vertical rectangular channel properly simulating the subchannel of the JRR-3, (2) to investigate the applicability of Eq. (1) to the subchannel of the JRR-3 in the viewpoint of safety design and at the same time, (3) to make clear the characteristics of the process from the forced convection single-phase heat transfer to the departure from the nucleate boiling (DNB) through the ONB.

II. EXPERIMENT

Figure 2 shows a schematic diagram of the test loop, which is the same as the one used to investigate the difference in single-phase forced-convection heat transfer characteristics between upflow and downflow with a narrow rectangular channel(7). The loop is composed of a water storage tank with 0.2 m^3 in volume, a recirculation line, a bypass line, a pump, flow meters, regulation valves, stop valves and a test section simulating a subchannel of the JRR-3 standard fuel element. Any of upflow and downflow can be selected in the test section in order to investigate on the upflow for the natural convection and on the downflow for the forced convection.

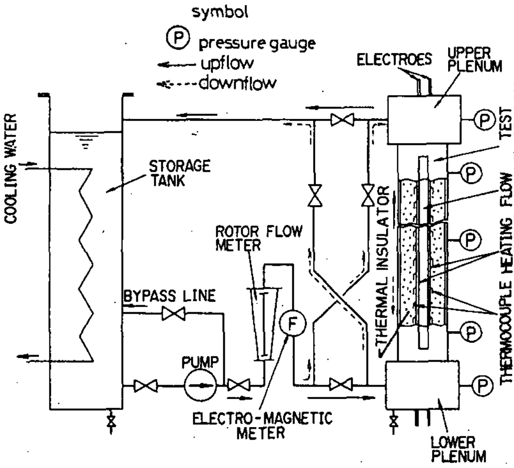

Fig. 2 Schematic diagram of experimental rig

The test section is composed of a flow channel, a lower plenum and an upper plenum. The configuration of the flow channel which is composed of adjacent two heating plates is rectangular with 50 mm in width, 2.25 mm in water gap and 750 mm in length, and is very similar to the subchannel of the JRR-3 whose configuration is 66.6 mm in width, 2.28 mm in water gap and 750 mm in length. The width of the flow channel is, thus, smaller than that of the JRR-2 subchannel. This is because the capacity of electric power supply for the experiment is not enough to realize the required maximum heat flux with the same width as the JRR-3 subchannel. It is considered that such difference in the width of flow channel does not give any significant effect on the ONB temperature. The heating plates are made of Inconel 600 with 1.0 mm in thickness. From both sides of the flow channel the inside of the flow channel can be observed through the window made of lucite.

The heating plates are heated by direct current and the heat input into the flow channel is obtained by measurements of current and voltage for each of heating plates. Water temperatures at the inlet and outlet of the flow channel are measured with 1.6 mm O.D. thermocouples inserted in the upper and lower plena. Coolant pressures are measured at several locations along the flow direction as shown in Fig. 2, and the pressure at the ONB is obtained by interpolation at the location where the ONB was observed.

The temperature of heating plates required to identify the ONB temperature is the surface temperature T_{wi} on the flow channel side. To obtain the surface temperature T_{wi}

along the flow direction, sheathed thermocouples of 0.5 mm O.D. are attached on the surface on the thermal insulator side as shown in Fig. 2 because it is difficult to attach the thermocouples on the flow channel side. Under the assumption of no heat loss into the thermal insulator, which has been confirmed in Ref. (7), T_{wi} is obtained with the local surface temperature T_{wo} of heating plate measured on the thermal insulator side, the electric power supply Q to the heating plates, thermal conductivity k of heating plates and thickness S, width W and length L of heating plates as follows:

$$T_{wi}=T_{wo}-\frac{QS}{4kWL}.$$

The error of T_{wi} is expressed with the sum of errors due to the first term T_{wo} and the second term $QS/4kWL$. The error of the first term is about 0.5 K and that of the second term is about 1.5 K at $Q=4.8\times10^4$ W, increasing linearly with the increase of Q.

The condition of ONB, that is, the superheat at ONB is considered to be affected by the properties of coolant and the surface roughness of heating plates. Therefore, in this experiment were used the pure water which is used as primary coolant in the upgraded JRR-3 and the heating plates whose surface roughness was almost the same as that of the JRR-3 fuel plate. Other factors which might affect the condition of ONB are dissolved gases and the gases trapped in the cavities on the surface of heating plates. Because the amounts of dissolved gases depend on the water temperature at a given pressure, the water temperature is selected as one of major parameters in this experiment. On the other hand, the heating plates were cooled for a long time enough before the data of the ONB conditions were taken, in order to avoid the effect of gases trapped in the cavities on the surface of the heating plates as much as possible.

The key items for instrumentation are flow rate, heat input into the flow channel, water temperatures at the inlet and the outlet of the flow channel, surface temperatures of heating plates and pressures.

Major parameters in this experiment are flow direction (upflow or downflow), heat input, flow rate, inlet water temperature and the heating condition, that is, if the channel is heated from one side or both sides. The ranges of these parameters investigated in this study are listed in **Table 1**.

Table 1 Test conditions

Flow direction	Upflow, downflow
Heating method	Both sides, one side
Velocity	0.07∼1.5 m/s
Inlet subcooling	28∼85 K
Pressure	∼1.2×10^5 Pa
Heat flux	3×10^4∼8×10^5 W/m^2

III. EXPERIMENTAL RESULTS AND DISCUSSION

1. Relationship of ONB *vs.* Surface Temperature Profiles

Figure 3 shows typical surface temperature profiles of heating plate along the flow direction together with the bulk temperature profiles of water, which were obtained for upflow at different heat fluxes under the pressure of 1.2×10^5 Pa, the water velocity of 7.3 cm/s and the inlet water temperature of 308 K. In the figure, T_w is the surface temperature of the heating plate, T_b the bulk temperature of water and T_s the saturation temperature at 1.2×10^5 Pa. It is clearly observed that the surface temperature of heating plate and the bulk temperature of water become higher with an increase of heat flux, and at the heat flux higher than 3.4×10^4 W/m^2 there occurs the region where the surface temperature becomes higher than the saturation temperature.

The arrows shown in Fig. 3 indicate the locations where the ONB was observed at

---

different hea
window on
channel. By
ONB was ob
perature T_{ON}
tified on the
profile of the
heat flux. T
by T_{ONB} in
locus of the
tained by obs
heat fluxes.
the location w
served, the su
above the satur
is almost unif
means that the
of the ONB wl
heating plate a
boiling region

2. **ONB o**

Figure 4 s
flow under the
the constant in
the figure, the
shown at diffe
ratios x/D_e f
Open symbols sh
solid symbols s
The solid line
ΔT_s given by E
the relationship
under the cond
water subcooling
and 168 for upfl
flow. The effe
heat at ONB is
and 143 as seen

In general, t
upflow and dow
than the ONB te
ing point of Eqs.
out that higher
heat for ONB wl
prediction by E
tendency that th

different heat fluxes through the window on both sides of the flow channel. By the location where the ONB was observed, the ONB temperature T_{ONB} could be easily identified on the surface temperature profile of the heating plate for each heat flux. The solid line indicated by T_{ONB} in the figure shows the locus of the ONB temperature obtained by observation at different heat fluxes. At the downstream of the location where the ONB was observed, the surface temperature is above the saturation temperature and is almost uniform while this region is considered to be a nucleate boiling region. This means that the location of the ONB obtained by observation is correspondent to the location of the ONB which is judged from the characteristics of the surface temperature profile of heating plate along the flow direction. It is clear in Fig. 3 that the length of the nucleate boiling region along the heating plate becomes longer with a further increase of heat flux.

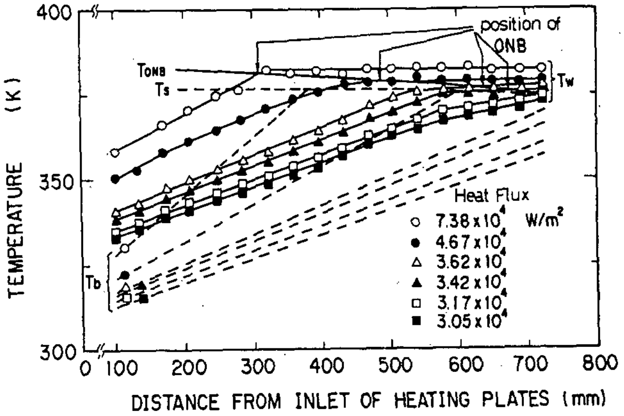

Fig. 3 Profile of surface temperature along heating plate

2. ONB on Boiling Curve

Figure 4 shows the effect of the water velocity on the ONB in both upflow and downflow under the constant pressure of 0.12 MPa and the constant inlet water subcooling of 69 K. In the figure, the relationships of q *vs.* ΔT_s are shown at different distance-to-hydraulic diameter ratios x/D_e for each constant water velocity. Open symbols show the non-boiling condition while solid symbols show the nucleate boiling condition. The solid line shows the relationship of q *vs.* ΔT_s given by Eq. (1) and the dotted lines show the relationship of q *vs.* ΔT_s given by Eq. (2) under the condition of the given pressure, inlet water subcooling and water velocity at $x/D_e=143$ and 168 for upflow and at $x/D_e=152$ for downflow. The effect of the ratio x/D_e on the superheat at ONB is rather small between $x/D_e=168$ and 143 as seen in Fig. 4.

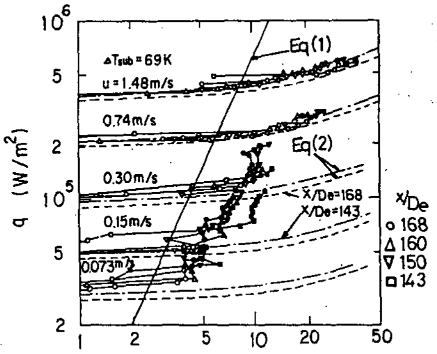

(a) upflow

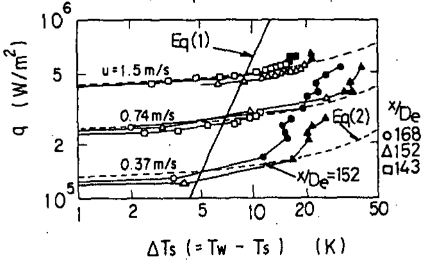

(b) downflow

Fig. 4 Effect of coolant velocity on q *vs.* ΔT_s at incipient nucleate boiling in rectangular vertical channel for upflow and downflow

In general, the ONB temperature obtained for upflow and downflow in this experiment is higher than the ONB temperature given by the intersecting point of Eqs. (1) and (2). It is also pointed out that higher water velocity gives higher superheat for ONB which is the same tendency as the prediction by Eqs. (1) and (2). Besides, the tendency that the temperature margin to the superheat predicted by Eqs. (1) and (2) becomes larger with an increase of water velocity is clearly observed especially in the upflow.

Figure 5 shows the effect of the inlet water subcooling on the ONB under the constant pressure of 0.12 MPa with the constant water velocity of 0.15 m/s for upflow and the constant water velocity of 0.74 m/s for downflow. The solid symbols show the nucleate boiling conditions and open symbols show the non-boiling conditions. It is clearly recognized that higher inlet water subcooling gives higher superheat and higher heat flux at the ONB for both upflow and downflow. This is the same tendency as Eqs. (1) and (2) predict.

It is, therefore, clear in Figs. 4 and 5 that the water velocity and the inlet water subcooling have strong effects on the condition of the ONB.

Figure 6 shows the relationship of q *vs.* ΔT_s from the forced-convection single-phase heat transfer to the departure from nucleate boiling (DNB) through the ONB for both upflow and downflow. The data were obtained by raising the heat flux stepwisely until DNB was detected with a steep increase of any of the surface temperatures of the heating plates, which were recorded on pen recorders. Once the DNB was detected, the electric power supply to the heating plates was turned off so that the heating plates might not be burnt out. The experiments were carried out under the pressure of 1.2×10^5 Pa, the inlet water subcooling of 69 K and the water velocity of 0.15 m/s for upflow and 0.37 m/s for downflow. Open symbols show the non-boiling conditions in the figure. In the figure the ONB and DNB are indicated with arrows.

Figure 6 shows the definite difference in the relationship of q *vs.* ΔT_s between the forced-convection single-phase heat transfer region and the nucleate boiling region. It should be noted here that the ratio of the DNB heat flux to the ONB heat flux is much smaller in the downflow than that in the upflow. As a major reason for this, it is point out that the flow condition in the downflow becomes oscillatory once the nucleate boiling occurs in the flow channel. In the downflow, vapor bubbles generated on the surface of the heating plates go downward as a co-current downflow, accompanied by the downward water flow. An

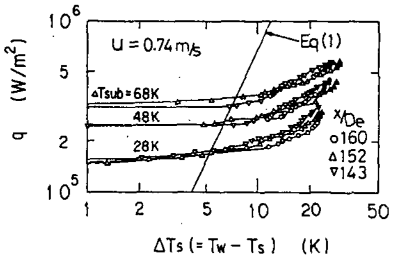

(a) downflow

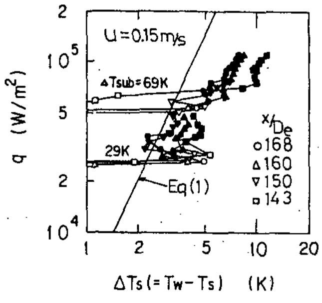

(b) upflow

Fig. 5 Effect of inlet coolant subcooling on q *vs.* ΔT_s at incipient nucleate boiling in rectangular vertical channel for upflow and downflow

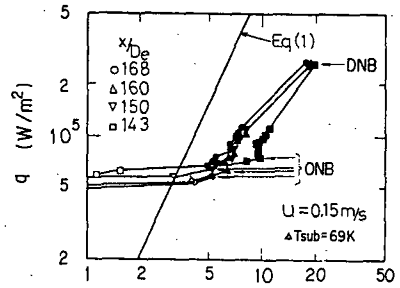

(a) upflow

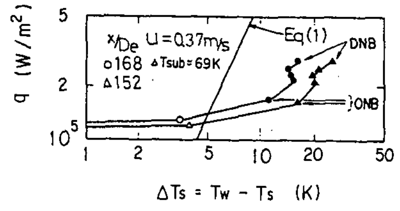

(b) downflow

Fig. 6 Relationship of q *vs.* ΔT_s in forced convection to DNB through incipient nucleate boiling for upflow and downflow increase of heat flux gives the alternative occurrence of the co-current downflow and the counter-current flow. In the counter-current flow, the vapor bubbles go upward and water goes down, and the vapor bubbles disappear or stop going upward before the vapor bubbles reach the upper end of heated length of the channel. With a further increase of heat flux, the alternate occurrence of co-current downflow and counter-current flow continues with the vapor bubbles reaching the upper end of the heated length in the counter-current flow, and at last the DNB occurs. In the upflow, on the other hand, there is no alternate occurrence of cocurrent downflow and counter-current flow but there is always a co-current upflow. Therefore, there is no oscillatory flow in the upflow. **Figure 7** shows the typical responses of the surface temperature of heating plate before ONB and just before DNB for both upflow and downflow, in order to show the above-mentioned oscillatory flow condition during the nucleate boiling in the downflow. The temperature response for downflow was obtained at $x/D_e=152$ under the pressure of 1.2×10^5 Pa, the inlet water subcooling of 69 K and water velocity of 0.37 m/s and the temperature response for upflow was obtained at $x/D_e=150$ under the pressure of 1.2×10^5 Pa, the inlet water subcooling of 69 K and the water velocity of 0.15 m/s.

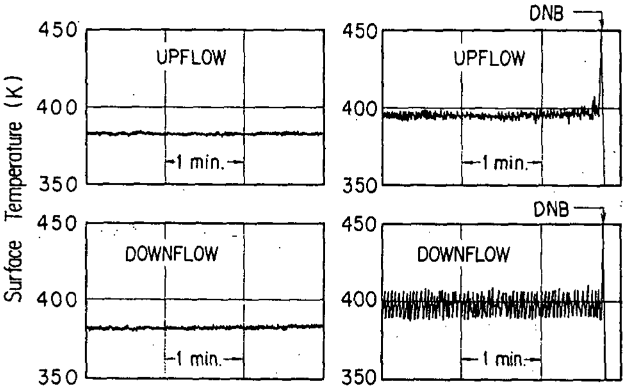

(a) Before ONB (b) Just before DNB

Fig. 7 Differences in characteristics of surface temperature responses between upflow and downflow before ONB and just before DNB

The amplitude of oscillatory temperature responses is very small within about 2.5 K in both upflow and downflow before ONB, as shown in Fig. 7(a). The oscillation amplitude is, on the other hand, about 20 K just before DNB in the downflow while that is about 5 K at the most before DNB in the upflow.

3. Hysteresis of ONB

Figure 8 shows the typical histories of the ONB between the case of increasing heat flux and the case of decreasing heat flux. They were obtained at $x/D_e=143$ and 168 for upflow under the pressure of 1.2×10^5 Pa, the inlet water subcooling of 69 K and the water velocity of 0.074 m/s. In the figures, the solid line shows the relationship of q *vs.* ΔT_s in the case that the heat flux increases while the dotted line shows the case that the heat flux decreases. The dark symbols show the nucleate boiling conditions and the open symbols the non-boiling conditions.

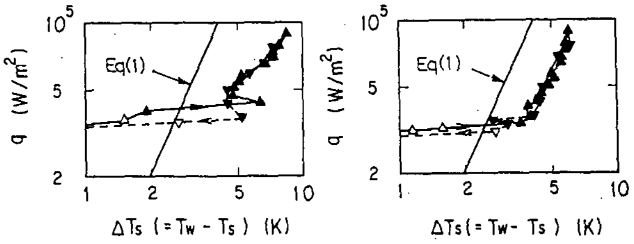

(a) $x/De=143$ (b) $x/De=168$

Fig. 8 Hysteresis of q *vs.* ΔT_s between processes in increasing and decreasing heat fluxes

It is observed that at the location of $x/D_e=143$ the history during the increase of heat flux is a little different from that during the decrease of heat flux and there exists an overshoot of superheat for ONB both during an increase of heat flux and during a decrease of heat flux. But the magnitude of difference between the histories during the increase and the decrease of heat flux is not large and the magnitude of overshoot of the superheat at ONB is also not large within 2 K at the most. At the location of $x/D_e=168$, on the other hand, there is neither significant difference in the histories between the increase and the decrease of heat flux nor significant overshoot of the superheat at ONB during both the increase and the decrease of heat flux. Therefore, it is understood that the differences in the histories between the increasing and the decreasing heat flux and the overshoot of superheat at ONB are not significant though some are observed. Meanwhile, Hino *et al.* reported that a significant difference in the histories between the increasing and the decreasing heat flux and a significant overshoot of the superheat at ONB were observed for R-113⁽⁹⁾. It should be, therefore, noted that the result obtained in this experiment for water is quite different from the result of Hino *et al.*, with respect to the hysteresis of q *vs.* ΔT_s and the overshoot of the superheat at ONB.

4. Conditions of ONB

Figure 9 shows the comparison of the experimental results obtained for both upflow and downflow in this experiment with Eqs. (1), (3) and (4), with respect to the relationship of q *vs.* ΔT_s at the onset of nucleate boiling. The conditions of the experiments are listed above the figure. From this figure and test conditions listed above the figure, it is clearly recognized that higher inlet water subcooling and higher water velocity give higher heat flux and higher superheat at the ONB. This is the same tendency as predicted by the simultaneous Eqs. (1) and (2), or the simultaneous Eqs. (4) and (2). It is also pointed out in this figure that (1) no significant difference between upflow and downflow is observed with respect to the relationship of q *vs.* ΔT_s at the ONB and (2) higher heat flux gives higher superheat at the ONB, giving a larger difference in the superheat between the measured and the prediction of Eq. (1) or (4). The former is correspondent to that there was no significant difference in the responses of the surface temperatures of the heating plate between upflow and downflow, which was described in Sec. III-2. On the latter, the previous studies with water⁽²⁾⁽⁶⁾⁽⁸⁾⁽¹⁰⁾ reported the similar results to the present experimental results, except for the tendency that a higher heat flux gives a larger difference in the superheat between the measured and the prediction of Eq. (1). It should be mentioned here that the latter tendency cannot always be observed in the case of fluids other than water, because Hino *et al.*⁽⁹⁾ reported that for R-113 the superheat at the ONB is almost constant in spite

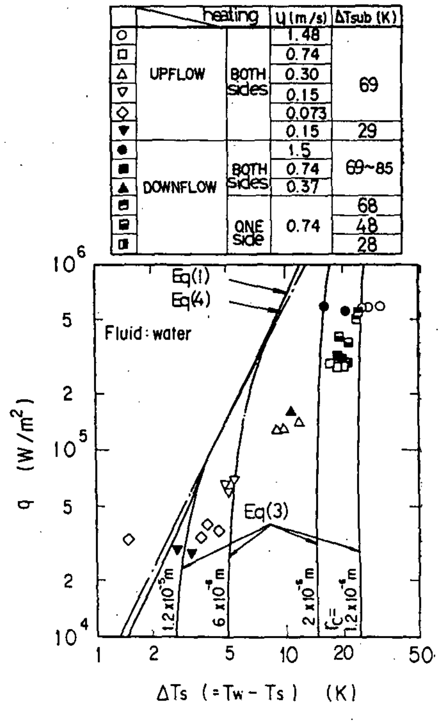

	heating		u (m/s)	ΔTsub (K)
○	UPFLOW	BOTH sides	1.48	69
□			0.74	
△			0.30	
▽			0.15	
◇			0.073	
▼			0.15	29
●	DOWNFLOW	BOTH sides	1.5	69~85
■			0.74	
▲			0.37	
◘		ONE side	0.74	68
◘				48
◘				28

Fig. 9 Comparison of present experimental data with existing predictions of q *vs.* ΔT_s at incipient nucleate boiling

of the differences in the inlet coolant subcooling and coolant velocity.

Figure 10 shows the comparison of the experimental results including the available existing data(2)(6)(8)(10) with the predictions by Eqs. (1) and (4), in order to evaluate the errors of Eqs. (1) and (4).

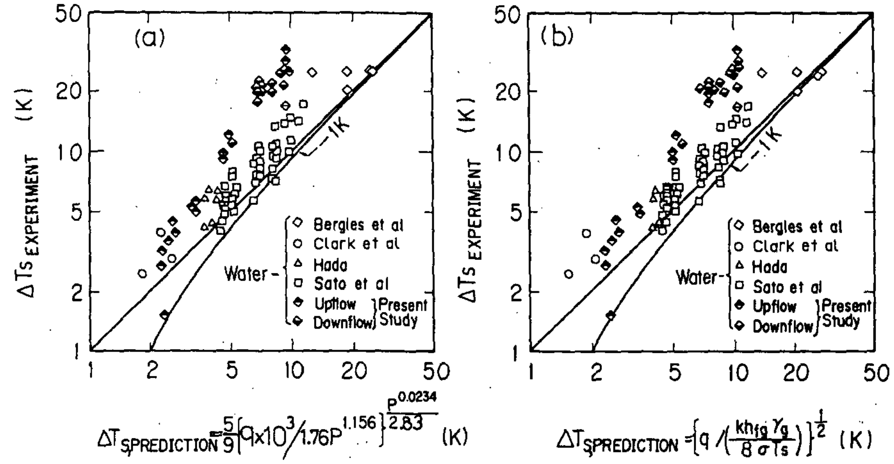

Fig. 10 Comparisons of predictions with experimental results including existing data on superheat at incipient nucleate boiling

Figure 10(a) shows the comparison of the measured superheats with the predicted superheats of Eq. (1) at the ONB for water. These experimental data include high pressure data of Clark *et al.*(6) and high water velocity data of Bergles *et al.*(2) This figure clearly indicates that the error of Eq. (1) is about −1 K against the lower limit of the measured superheats at the ONB. In the viewpoint of safety design that nucleate boiling should be avoided in the normal operation of the upgraded JRR-3, a correlation which predicts the superheat lower than the measured with a given heat flux should be used in the design and analysis of the upgraded JRR-3. Therefore, the use of Eq. (1) is recommended for the evaluation of the ONB temperature to show that there exists a margin in the fuel surface temperature against the ONB temperature. On the other hand, Fig. 10(b) shows the comparison of the measured superheats with the prediction of Eq. (4). Figure 10(b) shows that the error of Eq. (4) is also about −1 K against the lower limit of the measured superheats at the ONB. It is clear from Fig. 10(a) and (b) that Eq. (4) has the same magnitude of error against the lower limits of the measured superheats at the ONB as Eq. (1) does.

IV. CONCLUDING REMARKS

On the relationship of heat flux *vs.* superheat at the onset of nucleate boiling which is important as one of the design criteria for the core thermal-hydraulic design of the JRR-3, experiments were carried out with a vertical rectangular channel simulating a subchannel of the JRR-3 fuel element in order to investigate the validity and the error of the adopted correlation. As the results, the following were made clear:

(1) The ONB temperatures predicted by the Bergles-Rohsenow correlation (Eq. (1)) with given heat fluxes are correspondent to the lower limits of the measured ONB temperatures and therefore, the use of Eq. (1) is recommended to evaluate the ONB tem-

perature and show that there exists a margin in the fuel surface temperature against the ONB temperature.

(2) The error of Eq. (1) is within −1 K against lower limits of the measured superheat at the ONB.

(3) As the remarkable features of the ONB for water, it is pointed out that (i) there are no significant differences in the characteristics of the relationship of q *vs.* ΔT_s at the ONB between upflow and downflow, (ii) there are no significant differences in histories of relationship of q *vs.* ΔT_s from the forced convection single-phase flow to the subcooled boiling through ONB between increasing and decreasing heat flux, and (iii) the overshoot of the superheat at ONB is very small with 2 K at the most.

[NOMENCLATURE]

D_e:	Equivalent hydraulic diameter	(m)	T_b:	Bulk temperature of coolant	(K)
h_{fg}:	Latent heat of evaporation	(J/kg)	T_{ONB}:	Temperature at ONB	(K)
k:	Thermal conductivity of coolant	(W/mK)	T_s:	Saturation temperature	(K)
L:	Length of heating plate	(m)	T_w, T_{wi}:	Surface temperature of heating plate on flow channel side	(K)
P:	Pressure	(Pa)	T_{wo}:	Surface temperature of heating plate on insulator side	(K)
Pr:	Prandtl number		ΔT_s:	Superheat ($=T_w-T_s$)	(K)
q:	Heat flux	(W/m^2)	ΔT_{sub}:	Inlet water subcooling ($=T_s-T_b$)	(K)
q_{ONB}:	Heat flux at ONB	(W/m^2)	u:	Velocity of coolant	(m/s)
Q:	Electric power supply to heating plates	(W)	x:	Distance along the heating plate	(m)
Re:	Reynolds number		W:	Width of heating plate	(m)
r_c:	Critical radius of active cavity	(m)	σ:	Surface tension	(N/m)
S:	Thickness of heating plate	(m)	γ_g:	Density of vapor	(kg/m^3)

ACKNOWLEDGMENT

The authors would like to express their profound gratitude to Mr. N. Ohnishi for his continuous suggestions and encouragements during this study.

—REFERENCES—

(1) SUDO, Y., *et al.*: Core thermohydraulic design with 20% low enriched fuel for upgraded research reactor, JRR-3, *J. Nucl. Sci. Technol.*, 22[5], 565 (1985).

(2) BERGLES, A. E., *et al.*: *Trans. ASME*, Ser. C, 86[3], 365 (1964).

(3) DITTUS, F. W., *et al.*: *Univ. Calif. Pubs. Eng.*, 2, 443 (1930).

(4) DAVIS, E. J., *et al.*: *AIChE J.*, 12[4], 774 (1966).

(5) HSU, Y. Y.: *Trans. ASME, J. Heat Transfer*, 84, 207 (1962).

(6) CLARK, J. A., *et al.*: *Trans. ASME*, 76[2], 553 (1954).

(7) SUDO, Y., *et al.*: *J. Nucl. Sci. Technol.*, 22[3], 202 (1985).

(8) SATO, T., *et al.*: *Trans. JSME*, (in Japanese), 29[204], 1367 (1963).

(9) HINO, R., *et al.*: *ibid.*, Ser. B, 50[458], 2401 (1984).

(10) HADA, M.: Technical Memoranda, ISNSE, ANL, Oct. 1958 (Quoted from Ref. (7)).

Appendix E

Intentionally left blank

Appendix F

-Yu-Chih for RAI 13.3

Reduced Enrichment Test and Research Reactors (RERTR) Conference
Prague, September 23-27, 2007

VALIDATION OF THE MULCH-II CODE FOR THERMAL-HYDRAULIC SAFETY ANALYSIS OF THE MIT RESEARCH REACTOR CONVERSION TO LEU

Yu-Chih Ko‡, Lin-Wen Hu*,
‡Nuclear Science and Engineering Department, MIT
*Nuclear Reactor Laboratory, MIT, Cambridge, MA, USA 02139

Arne P. Olson and Floyd E. Dunn
RERTR Program
Argonne National Laboratory, Argonne, IL USA 60439

ABSTRACT

An in-house thermal hydraulics code was developed for the steady-state and loss of primary flow analysis of the MIT Research Reactor (MITR). This code is designated as MULti-CHannel-II or MULCH-II. The MULCH-II code is being used for the MITR LEU conversion design study. Features of the MULCH-II code include a multi-channel analysis, the capability to model the transition from forced to natural convection during a loss of primary flow transient, and the ability to calculate safety limits and limiting safety system settings for licensing applications. This paper describes the validation of the code against PLTEMP/ANL 3.0 for steady-state analysis, and against RELAP5-3D for loss of primary coolant transient analysis. Coolant temperature measurements obtained from loss of primary flow transients as part of the MITR-II startup testing were also used for validating this code. The agreement between MULCH-II and the other computer codes is satisfactory.

1. Introduction

An in-house thermal hydraulics code, MULti-CHannel-II or MULCH-II, was developed for the steady-state and loss of primary flow analysis of the MIT Research Reactor (MITR) [1,2,3]. The MULCH-II code features the multi-channel analysis, natural circulation and anti-siphon valve models, fin effectiveness model and correlations for low pressure systems. In addition, the MULCH-II code is

---

* Corresponding author: Email: lwhu@mit.edu; TEL: (617)258-5860

capable of modeling forced to natural convection during a loss of primary flow transient and calculating the safety limits and limiting safety system settings for licensing applications.

This paper presents the benchmark results of the MULCH-II code for the MITR low enrichment uranium (LEU) conversion study. The PLTEMP/ANL (version 3.0) [4] and RELAP5-3D (version 2.3.6) [5] are chosen to benchmark MULCH-II for steady state analysis and loss of primary flow transient, respectively. Furthermore, coolant temperature measurements obtained from loss of primary flow transients as part of the MITR-II startup testing were also used for the benchmark of the MULCH-II.

2. Description of the MIT Research Reactor

Figure 1 is an isometric view of the MIT Research Reactor (MITR). The MITR is a 5 MW nuclear research reactor that is owned and operated by the Massachusetts Institute of Technology to further its educational and research missions. It is currently being relicensed for 6 MW operation. The reactor uses finned plate-type fuel with aluminum clad and is cooled and moderated by light water. The longitudinal fins are 10 mils by 10 mils which doubles the heat transfer surface area. Currently the MITR uses highly enriched uranium (HEU) fuel in the form of UAl_x cermet. The fuel elements are rhomboid in shape and each contains fifteen plates. The reactor core can hold up to twenty- seven of these elements. The normal core configuration is twenty-four fuel elements with three positions available for in-core experiments.[6]

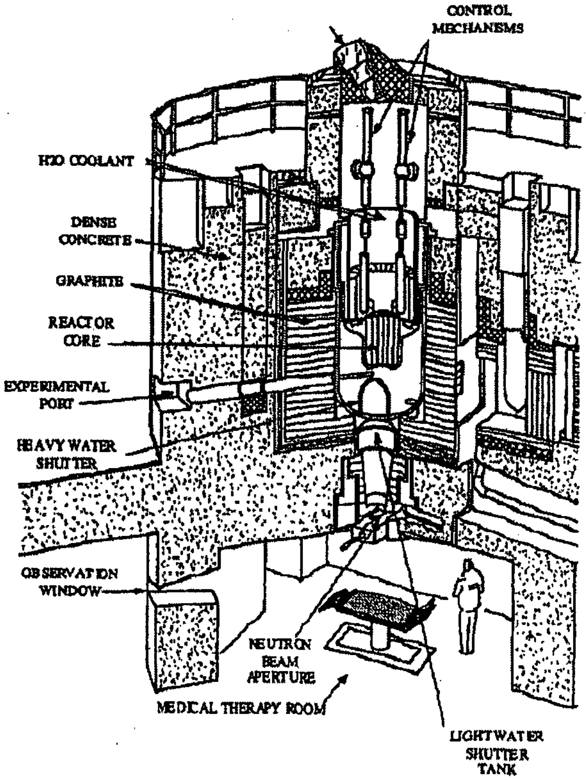

Figure 1. Isometric View of the MIT Research Reactor

Reactor control is provided by six boron-impregnated stainless-steel shim blades and one cadmium regulating rod. The core is contained in a tank of light-water and this tank is in turn surrounded by first a heavy-water and then a graphite reflector. Forced flow removes heat from the primary, heavy water, and graphite region with all heat loads being deposited in a common secondary cooling system. There are two anti-siphon valves located in the upper core tank to prevent complete drainage because of a siphon effect in the event of a break in the inlet primary piping. Four natural convection valves, that are located next to the flow guide, provide a natural circulation flow path for decay heat removal. The pressure in the system is practically atmospheric, and coolant temperature is approximately 50 °C (120 F).

3. MULCH-II benchmark study for steady-state analysis using PLTEMP/ANL

PLTEMP/ANL is developed and maintained by ANL and has been used for other conversion studies [7]. Benchmark analyses are based on a steady-state reactor power of 6 MW for the existing high enrichment uranium (HEU) core. For simplicity, in the following paragraph the terms "MULCH" and "PLTEMP" will be used instead of "MULCH-II" and "PLTEMP/ANL" code.

The fin effectiveness of the MULCH code is a multiplication factor used in conjunction with the coolant heat transfer coefficient to account for the heat transfer augmentation due to the longitudinal fins on the clad surface. Since PLTEMP v3.0 cannot include the fin effectiveness as in the case of MULCH, the plate width was increased to account for the larger heat transfer area. Regarding the heat transfer correlation, PLTEMP uses Dittus-Boelter to calculate single phase and Bergles-Rohsenow to calculate two-phase heat transfer coefficient. MULCH uses the Chen correlation to calculate both single and two-phase heat transfer coefficient.

Figure 2 is the comparison of coolant temperature. Average and hot channel temperature are both plotted in the figure. Coolant temperature is determined by energy conservation equation which is a function of power (integrated heat flux) and coolant inlet temperature. Since these parameters are the same in MULCH and PLTEMP as input parameters, as shown in Fig.2, the calculated coolant temperatures are about the same. Figure 3 is the comparison of cladding temperature. As shown in Fig. 3, the cladding temperature curves are very close between these two codes. PLTEMP predicts slightly lower cladding temperature than MULCH which is consistent with the coolant temperature difference.

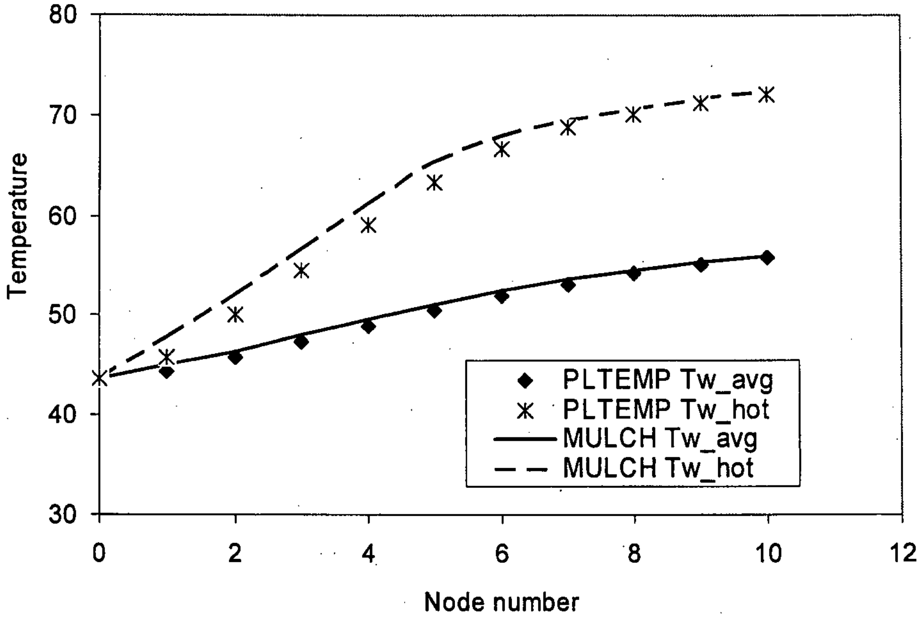

Figure 2. Comparison of coolant temperature (MULCH VS PLTEMP, steady state)

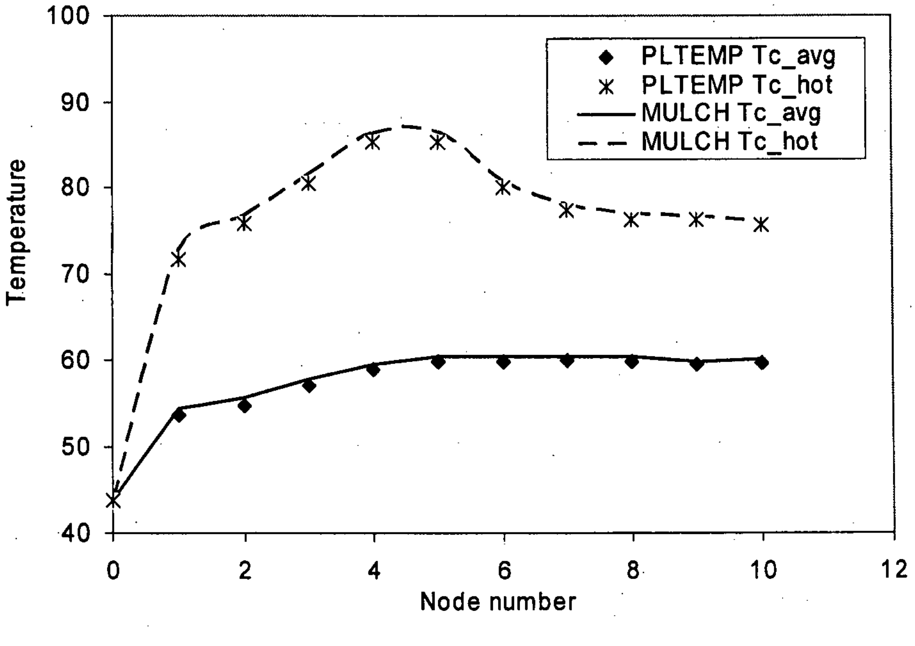

Figure 3. Comparison of cladding temperature (MULCH VS PLTEMP, steady state)

Table 1. Temperature difference* between MULCH and PLTEMP (Steady state)

	Hot Channel		Average Channel	
Node	Cladding (°C)	Coolant (°C)	Cladding (°C)	Coolant (°C)
1	1.028	2.088	0.75	0.672
2	1.03	2.105	0.804	0.631
3	1.078	2.173	0.728	0.733
4	1.198	2.261	0.736	0.739
5	1.17	1.984	0.707	0.662
6	0.755	1.205	0.653	0.633
7	0.846	0.732	0.568	0.501
8	0.757	0.525	0.581	0.351
9	0.53	0.453	0.312	0.293
10	0.465	0.319	0.351	0.27

* Temperature difference = MULCH – PLTEMP/ANL.
Clad temperature refers to the clad/crud outer surface temperature.

Table 1 summarizes the temperature differences for coolant, cladding surface and fuel for each axial node. It shows that the maximum temperature difference between MULCH and PLTEMP occurs at node 4, which is also the hottest node. Overall, MULCH predicts higher temperature of coolant, cladding and fuel. The temperature difference in the hot channel is higher than it is in the average channel due to higher heat flux. It is noted that the first five nodes have greater temperature difference than the following nodes due to bottom peaking of the power distribution. One possible cause for the discrepancy in coolant temperature is that MULCH reports maximum node temperature (e.g., coolant temperature at node outlet) while PLTEMP reports the node-average temperature. Since the difference of the coolant outlet temperatures is small (~ 0.3 °C), it is determined that both codes are consistent in calculating the coolant energy equation.

Table 2 summarizes the comparison of hot channel heat flux and heat transfer coefficient. It shows that the heat flux is exactly the same in the two codes. Since the simulation case is steady state, i.e., no boiling occurs, MULCH and PLTEMP use the same correlation for single phase heat transfer (Chen's correlation reduces to standard Dittus-Boelter during single phase flow). Therefore the values of heat transfer coefficient should be roughly the same. It should be noted that the discrepancy in cladding-coolant temperature difference is less than 4% and is consistent with that of heat transfer coefficients.

Table 2. Comparison of hot channel heat flux, temperature difference* and heat transfer coefficient (MULCH VS PLTEMP, steady state)

	Heat Flux q" (W/m^2)		Temperature Difference Tc – Tw (°C)		Heat Transfer Coefficient h (W/m^2 °C)	
Node	MULCH	PLTEMP	MULCH	PLTEMP	MULCH	PLTEMP
1	4.21E+05	4.21E+05	24.9	25.96	1.69E+04	1.62E+04
2	4.33E+05	4.33E+05	24.7	25.775	1.75E+04	1.68E+04
3	4.52E+05	4.52E+05	24.9	25.995	1.82E+04	1.74E+04
4	4.70E+05	4.70E+05	25.1	26.163	1.87E+04	1.80E+04
5	4.06E+05	4.05E+05	21.1	21.914	1.92E+04	1.85E+04
6	2.51E+05	2.51E+05	12.8	13.25	1.96E+04	1.89E+04
7	1.65E+05	1.65E+05	8.7	8.586	1.89E+04	1.92E+04
8	1.17E+05	1.17E+05	6.3	6.068	1.86E+04	1.93E+04
9	9.77E+04	9.77E+04	5.1	5.023	1.92E+04	1.94E+04
10	6.95E+04	6.95E+04	3.7	3.554	1.88E+04	1.95E+04

*Temperature Difference = cladding temperature (Tc) – coolant temperature (Tw)

4. MULCH-II benchmark study for loss of primary flow transient using RELAP5-3D

The RELAP5-3D input model for the MITR 6 MW power uprate was assembled. Analyses are based on a steady-state reactor power of 6 MW with an initial flow rate at 2000 gpm for the existing HEU core. For simplicity, the term "RELAP5" will be used instead of "RELAP5-3D" in the following description.

Figure 4 is a comparison of the simplified primary loop control volumes of MITR for MULCH and RELAP5 code for the LOF transient simulations. Anti-siphon valves (ASVs) and natural convection valves (NCVs) are also shown in the figures. Both ASV and NCV are very important components for establishing natural circulation during the loss of primary flow transients. As shown in Fig. 4, it can be found that RELAP5 divides the primary loop into more control volumes. In the RELAP5 MITR model, mixing area is split into three sub-regions and the average channel, hot channel and bypass flow are separate control volumes.

Convection heat transfer correlations are different in the MULCH and RELAP5 codes. MULCH uses Chen's correlation for both single and two-phase transfer. For RELAP5, single phase heat transfer correlations are calculated relying on evaluating forced turbulent convection, forced laminar convection, and natural convection and selecting the maximum of these three. The correlations are by Dittus-Boelter, Kays, and Churchill-Chu, respectively. Two-phase heat transfer correlations are calculated by Chen's correlation for nucleate boiling and transition boiling; by Bromley correlation for film boiling.

When a pump coast down accident occurs, the reactor will shut down automatically upon receiving a low primary coolant flow scram signal. In the loss of primary flow simulation, MULCH assumes the reactor will shut down after 2.3 seconds (one second of instrument delay time and 1.3 seconds for shim blade insertion) by a step reactivity insertion after the low flow scram setpoint is reached. For RELAP5, it is assumed that the reactor will scram by a ramp reactivity insertion with a reactivity insertion of -7.5 beta (corresponding to MITR shim bank height of 10") within one second after the scram is initiated.

There are four natural convection valves (NCVs) and two anti-siphon valves (ASVs) installed in the reactor core tank. During normal operation (forced convection), NCVs and ASVs are closed due to primary coolant pressure head. Determination of the friction loss coefficients of these ball-type check valves is given in Ref [8]. When the pressure reduces (e.g., pump coastdown), NCVs and ASVs will open. Natural convection flow is then established within the core tank because of the buoyancy force of the heated coolant in the core region. In the MULCH simulation cases, it is predicted that the NCV and ASV will open at the same time, about 4.4 seconds after the initiating event. For RELAP5, we use this timing as an assumption to force open the NCVs and ASVs at 4.4 seconds. It is reasonable since RELAP5 adopts the same pump coastdown curve as MULCH.

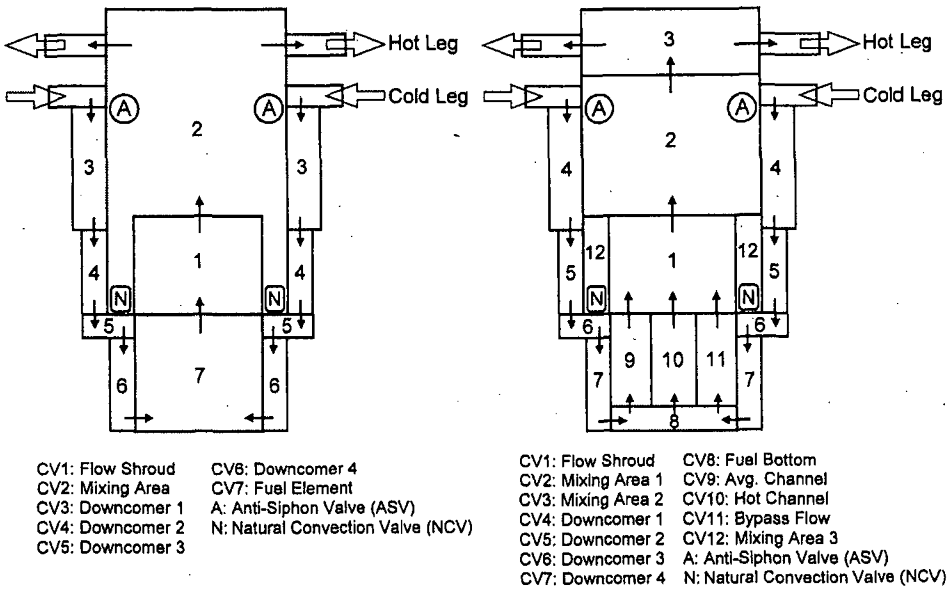

(a) MULCH-II Code

(b) RELAP5 Code

Figure 4. Primary loop control volumes for MIT reactor

Figures 5 and 6 are the calculated flow rates of ASV and NCV. In Fig.5 and Fig. 6, positive flow rate means it is an "up-flow" or "bypass flow"; if negative, it is a "down-flow" or "natural convection flow". As show in Fig. 5, the flow passing through ASV is always a down-flow during the transient. Overall, RELAP5 predicts higher ASV flow rate than the prediction of MULCH. Besides, MULCH predicts the steady state ASV flow rate of 1.37 (kg/s), which is slightly less than RELAP5's prediction. of 1.40 (kg/s). Figure 6 shows that at first, the flow passing through NCV is upward during pump coastdown. MULCH predicts flow through the NCV would become downward (natural convection flow) at 18.4 second. RELAP5 predicts the natural convection flow established at time equal to 15.0 second. For RELAP5 and MULCH, the steady-state NCV flow rates are 0.51 (kg/s) and 0.29 (kg/s) respectively.

Comparison of core flow rate is summarized in Table 3. At the beginning of the transient, MULCH predicts a higher core flow rate than RELAP5. After ASV and NCV open (at 4.4 second), the core flow rate of RELAP5 becomes greater than MULCH. Once the natural convection flow is established, the core flow rate would be steady and equal to the summation of ASV and NCV flow rate. It can be found in Table 3 that RELAP5 predicts a higher steady state core flow rate than MULCH, which is consistent with the results shown in Figs. 5 and 6.

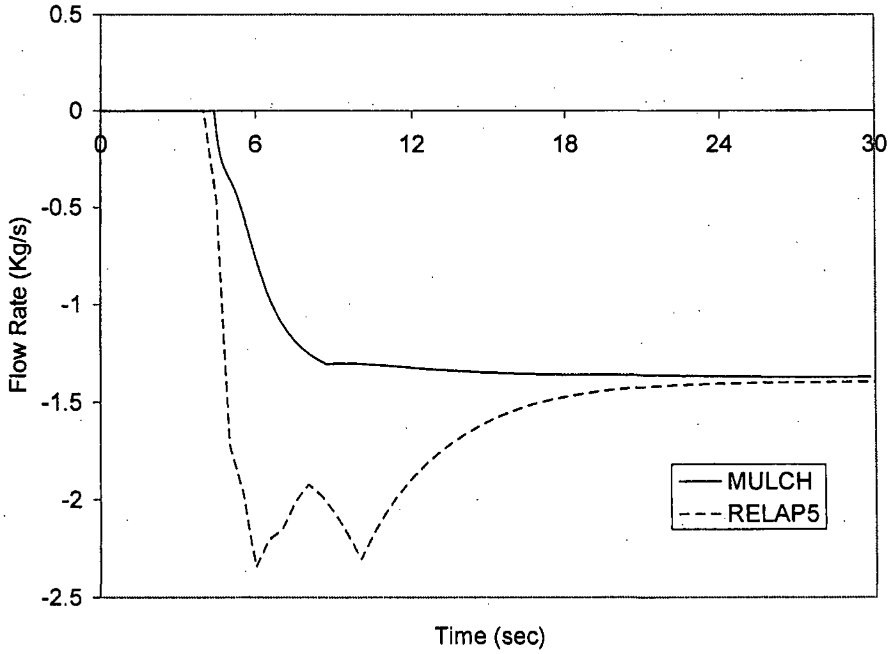

Figure 5. Comparison of ASV flow rate

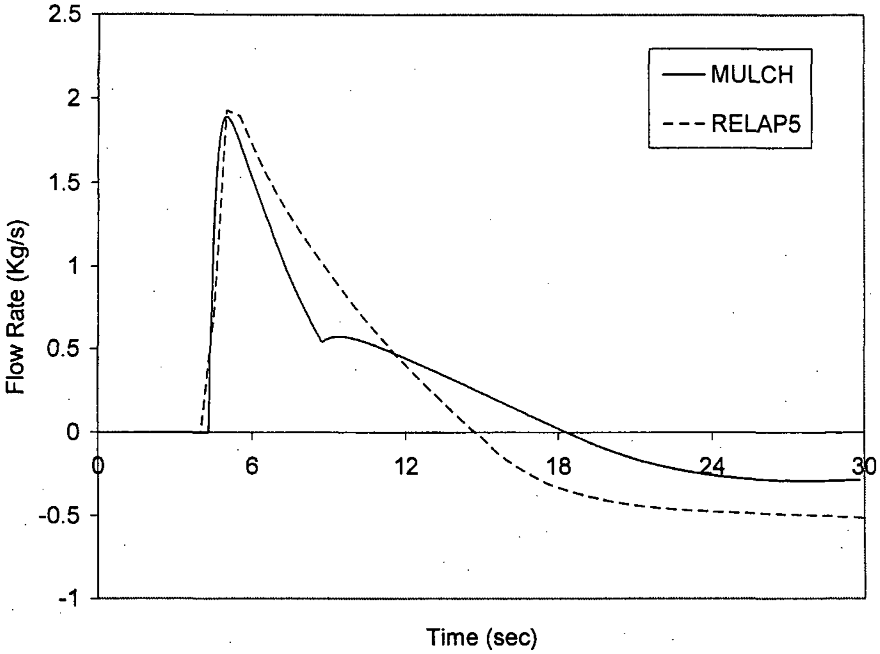

Figure 6. Comparison of NCV flow rate

Table 3. Comparison of primary flow rates through reactor core during LOF transient

Time (sec)	Core flow rate (kg/s)	
	MULCH	RELAP5
0.0	115.1	115.2
1.0	63.2	56.9
2.0	34.2	30.6
3.0	18.6	16.7
4.0	9.96	9.04
4.5	5.80	5.63
5.0	3.46	3.62
6.0	1.74	2.60
7.0	1.08	2.10
8.0	0.77	1.82
9.0	0.68	1.66
10.0	0.69	1.56
20.0	1.35	1.89
30.0	1.52	1.91

MITR-II startup test are coolant temperature measurements from compared with the predictions by MULCH and RELAP5. The loss of primary flow in MITR-II has been studied in detail by Bamdad [9]. Measured data from thermocouples TC-6, TC-7, and TC-9 are compared with the predicted values of coolant outlet temperature. Notice that the thermocouples are located in different positions. It is expected that the measured temperature would fall between the predicted average and peak temperatures (within experimental error).

Figure 7 shows the comparison of coolant temperature between MULCH and measurements. One can observe that the predicted values lie above and below the measured values. Figure 8 shows the comparison of coolant temperature between RELAP5 and measurements. It can be found that RELAP5 seems to over-predict the peak temperature. However, in general RELAP5 has good performance and the predicted trend and values are closer to the measured values.

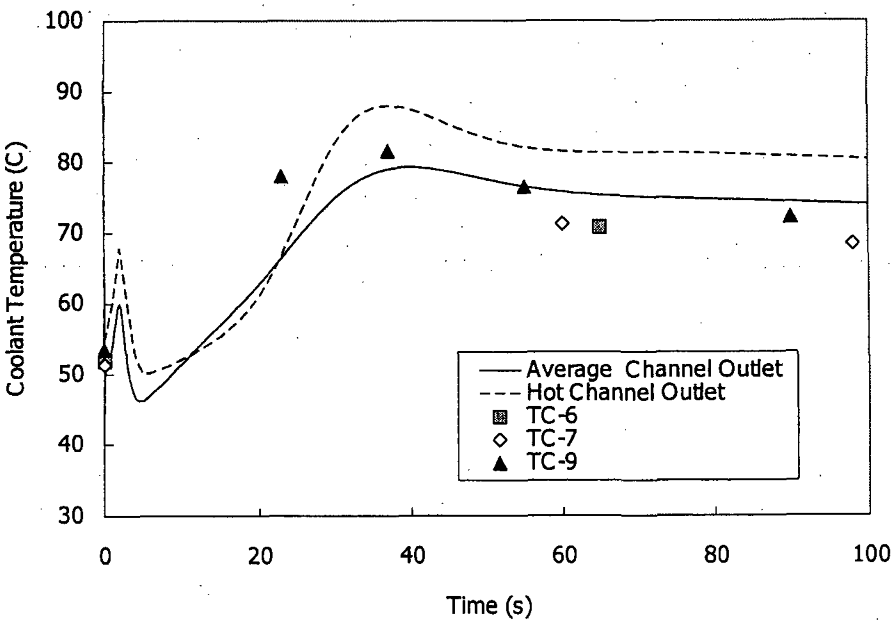

Figure 7. Comparison of coolant temperature between MULCH and measurement

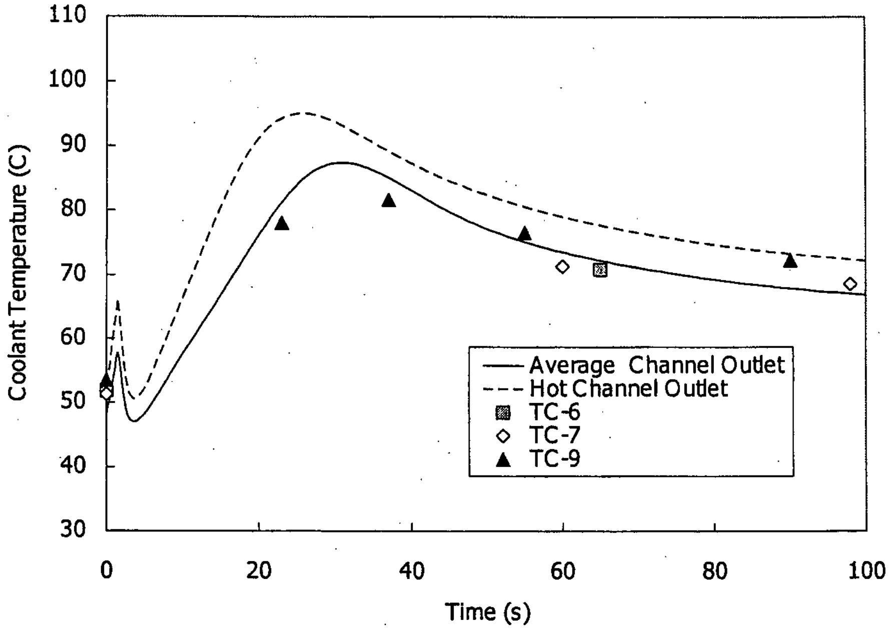

Figure 8. Comparison of coolant temperature between RELAP5 and measurement

5. Conclusions

Steady state analyses are performed by using the MULCH and PLTEMP codes. Comparison of the coolant and cladding temperatures shows that the calculated temperatures by MULCH-II code are in agreement with PLTEMP. Results of loss of primary flow transients show that RELAP5 predicts higher ASV, NCV and core flow when natural convection is established. RELAP5 also predicts that the natural convection flow will establish earlier that the prediction of MULCH.

The calculated outlet coolant temperatures are compared with measurements. Results show that RELAP5 seems to over-predict the peak temperature but the predicted trend and values match the measured values well. MULCH is less conservative than RELAP5; however it can be used for safety analysis since the predicted peak values are always higher than the experimental data.

Based on the benchmark analysis results, the MULCH code is qualified for the LEU core conversion analysis. In the future, a sensitivity study for decay power will be performed. The point kinetics model in MULCH can also be improved. It can be expected that MULCH will predict better results for loss of primary flow transient if the step reactivity insertion is replaced by a ramp reactivity insertion.

References

[1] M. J. McGuire, "An Analysis of the Proposed MITR-III Core to Establish Thermal-Hydraulic Limits at 10 MW", PhD Thesis, MIT Nucl. Eng. Dept., June 1995

[2] L.-W. Hu and J. A. Bernard, "Development and Benchmarking of a Thermal-Hydraulics Code for the MIT Nuclear Research Reactor," Proceedings of the ANS Joint International Conference on Mathematical Methods and Super-Computing for Nuclear Applications, Saratoga, NY, Oct. 5-7, 1997.

[3] L.-W. Hu and J. A. Bernard, "Thermal-Hydraulic Analysis for the Upgraded MIT Nuclear Research Reactor," *IEEE Transactions on Nuclear Science*, Vol. 45, No. 3, Part I, June 1998.

[4] Arne P. Olson and M. Kalimullah, "A Users Guide to The PLTEMP/ANL Code", Argonne National Laboratory, May 2006

[5] The RELAP5 Code Development Team, "RELAP5/MOD3 Code Manual", USA: Idaho National Engineering Laboratory, 1995.

[6] MITR Staff, "Safety Analysis Report for the MIT Research Reactor (MITR-II)", MITNE-15, Nuclear Engineering Department, Massachusetts Institute of Technology, Oct., 1970.

[7] Alireza Haghighat, Submittal Report to Cover Analyses of University of Florida Training Reactor (UFTR) conversion from HEU to LEU Fuel, University of Florida, Dec 2005

[8] Lin-Wen Hu, "Thermal Hydraulic Mixing Transients in the MIT Research Reactor Core Tank", PhD Thesis, MIT Nucl. Eng. Dept., Feb. 1996.

[9] F. Bamadad-Haghighi, "Natural convection analysis of the MITR-II during loss of flow accident, Master Thesis, MIT Nucl. Eng. Dept., August 1977

Appendix G

-Newton for RAI 13.5

NUCLEAR REACTOR LABORATORY

AN INTERDEPARTMENTAL CENTER OF
MASSACHUSETTS INSTITUTE OF TECHNOLOGY

Thomas H. Newton, Jr., Ph.D.
Associate Director for
Engineering

138 Albany Street, Cambridge, MA 02139-4296
Telefax No. (617)253-7300
Telephone No. (617)253-4211
Email: tnewton@mit.edu

Activation Analysis
Coolant Chemistry
Nuclear Medicine
Reactor Engineering

June 23, 2008

From: Tom Newton

To: File

Re: Edge coolant channel dimensions

Coolant channels along the edges of fuel elements are formed with the minimum distance between elements given by the condition where the "shoulders" for adjacent fuel elements are touching. As shown in the fuel element drawing (R3F-201-4), the shoulders of an element are 2.405" apart in both the fuel plate and side plate directions.

Calculations of the channel thicknesses as well as hydraulic diameters of different fuel element orientations are made below. Note that all dimensions listed are nominal values. Values involving fuel plates are taken from the fin tips.

Interior fuel plate coolant channels:

Spacing between interior fuel plates: 0.078"
Width of coolant channel: 2.308"
Fin height and width: 0.010"

Hydraulic diameter (D_e):
Area = (0.078 + 0.020) * 2.308 – 2 * 111 * 0.010 * 0.010 = 0.2040 in^2
Pw = ((0.078 + 0.020) + 2.308 + 2*111*0.010) * 2 = 9.252 in
D_e = 4A/Pw = 0.08820 in (0.2240 cm)

Edge fuel plate facing edge fuel plate:

Space from edge fuel plate to end of side plate: 0.044"

Distance from end of side plate to end of other side plate: 2.380"
Distance from shoulder to shoulder along same (fuel plate) axis: 2.405"

Additional gap due to shoulder: (2.405 - 2.380) / 2 = 0.0125 in

Resultant gap from edge fuel plate to shoulder: (0.044” + 0.0125”) = 0.0565 in

If fuel orientation is fuel plate-to fuel plate, total gap between fuel plates is
0.0565 + 0.0565 = 0.113”

Hydraulic diameter:
Area = (0.113 + 0.020) * 2.308 – 2 * 111 * 0.010 * 0.010 = 0.2848 in^2
Pw = ((0.113 + 0.020) + 2.308 + 2*111*0.010) * 2 = 9.322 in
D_e = 4A/Pw = 0.1222 in (0.3104 cm)

Edge fuel plate facing side plate:

Distance from side plate to side plate: 2.375”
Distance from shoulder to shoulder along side plate axis: 2.405”
Gap due to shoulder: (2.405-2.375)/2 = 0.015”

If fuel orientation is fuel plate to side plate, total gap is
0.044 + 0.0125 + 0.015 = 0.0715 in

Hydraulic diameter:
Area = (0.0715 + 0.010) * 2.308 - 111 * 0.010 * 0.010 = 0.1770 in^2
Pw = ((0.0715 + 0.010) + 2.308 + 111 * 0.010) * 2 = 6.999 in
D_e = 4A/Pw = 0.1012 in (0.2570 cm)

Grid at edge of core:

The fuel plates at the edge of the core are next to the reactor grid structure (as shown in drawings R3S-14-5 and R3S-15-4). The minimum distance from fuel plate to the core edge is made with the fuel element nozzle placed in the grid as close to the edge as possible.
Spacing from nozzle to shoulder:
(2.405 – 2.119)/2 = 0.143

Element-to-core edge grid spacing 0.245”
Gap from fuel plate to edge of core:
0.245 - 0.143 + 0.044 + 0.0125 = 0.1585 in

Hydraulic diameter:
Area = (0.1585 + 0.010) * 2.308 - 111 * 0.010 * 0.010 = 0.3778 in^2
Pw = ((0.1585 + 0.010) + 2.308 + 111 * 0.010) * 2 = 7.173 in
D_e = 4A/Pw = 0.2107 in (0.535 cm)

Thus, from the calculations given above, the interior fuel plate channels have the smallest hydraulic diameter.